Engineering Guided Polaritons and Nonlinear Light-Matter Interactions for On-Chip Photonic and Optoelectronic Devices

Manuka Piyumantha Suriyage

April 2026

THIS DISSERTATION IS SUBMITTED FOR THE DEGREE OF DOCTOR OF PHILOSOPHY OF THE AUSTRALIAN NATIONAL UNIVERSITY

Research School of Engineering College of Systems and Society

Australian National University

© Copyright by Manuka Suriyage 2026

ALL Rights Reserved

Declaration

This dissertation reports the research I conducted from August 2021 to April 2026 at the School of Engineering, College of Engineering, Computing & Cybernetics, Australian National University.

To the best of my knowledge, the material presented in this dissertation is my own original work, except where appropriate acknowledgment and referencing have been made. This work has not been previously published by others, nor has it been submitted, in whole or in part, to any university for any degree, diploma, or other qualification.

During the preparation of this thesis, generative artificial intelligence tools were used only in a limited and clearly defined manner to assist with grammar checking, language refinement, and improvement of sentence clarity in text that I had already drafted. Generative AI was not used to develop the core research questions, formulate the methodology, generate or analyse data, interpret results, or produce the original scientific arguments and conclusions presented in this thesis.

All substantive intellectual content, including the research design, analysis, discussion, and conclusions, is my own work. Any use of generative AI has been appropriately acknowledged in accordance with ANU academic integrity expectations, and all AI-assisted text was carefully reviewed, verified, and revised by me before inclusion. I take full responsibility for the final content of this thesis and confirm that the work submitted represents my own original research and writing.

Manuka Piyumantha Suriyage

April 2026

Acknowledgement

Completing this PhD has been one of the most challenging journeys of my life, and I would not have reached this point without the support of many people around me. I am deeply grateful to my supervisors, mentors, colleagues, friends, and family for their guidance, patience, encouragement, and belief in me throughout this journey. Their support helped me through the difficult moments and made the achievements along the way all the more meaningful. This thesis is not only the result of my own efforts, but also a reflection of the kindness and generosity of those who stood by me. I would like to sincerely thank all of them for being part of this important chapter of my life.

I am especially grateful to my primary supervisor and panel chair, Prof. Yuerui (Larry) Lu, for his constant guidance, encouragement, and support throughout my PhD. His insight, high standards, and belief in my potential have shaped not only this research but also the way I now think about science. I have learned a great deal from his approach to research, problem-solving, and turning ideas into meaningful outcomes. I truly appreciate the many opportunities, resources, and advice he generously provided along the way. His mentorship has had a lasting impact on both my academic journey and my personal growth. I would also like to sincerely thank the rest of my supervisors, Prof. Yuri Kivshar and Dr. Jiri Janousek, for their constant guidance and support throughout this journey. I am equally grateful to A/Prof. Daria Smirnova, who, as one of my supervisors, has taught me a great deal during the final year of my PhD through our collaboration on different projects. It has been a true honour and privilege to work closely with each of them, and their support, knowledge, and encouragement have meant a great deal to me. The opportunity to learn from such remarkable researchers is something I will always value and carry with me.

I would also like to acknowledge my collaborators for their contribution towards the completion of this thesis. My thanks go to Qingyi Zhou and Prof. Zongfu Yu from University of Wisconsin-Madison, A/Prof. Daria and her students Lingxiao Li and E. Smolina, Dr. Chi Li and Dr. Haoran Ren from Monash University, A/Prof. Domenico de Ceglia from University of Brescia, and A/Prof Marco Centini from SAPIENZA University of Rome. I would like to extend my special thanks to Dr. Adrian Cernescu from Neaspec and AttoCube for guiding me throughout my PhD with my measurements. I also want to extend my gratitude to all the staff at the Australian National Fabrication Facility ACT Node, including Dr. Kaushal Vora, Dr. Li Li, Dr. Naiyin Wang, Ms. Gayatri Vaidya, Dr. Olivier Lee Cheong Lem, and Ms. Sue Berkeley for their support on ANFF equipments, technical discussions, and generous help.

Next, I would like to sincerely thank my wonderful colleagues and lab mates for making this journey more enjoyable and far less lonely. More than just colleagues, Dr. Yilin Tang and Dr. Xueqian Sun have been a constant source of help, encouragement, and support throughout my PhD. I am also very grateful to Dr. Yi, Dr. Sharidya, Dr. Boqing, Hao, Shuyao, Luke, Ruosi, Dr. Bowen, Johnson, and Wengkai, for their kindness, support, and the many moments of help and friendship along the way. Working alongside

all of them has been a truly valuable part of my PhD experience. I am deeply grateful for the financial support I received through the ANU PhD Scholarship, which made my doctoral studies possible. I would also like to sincerely acknowledge the ANU College of Systems and Society (CSS) for supporting both my scholarship and living expenses throughout the PhD, which was essential to the successful completion of this program. In addition, I would like to thank the CSS HDR administrative team and the Engineering School administration team for their continuous support in helping manage the many practical aspects of my projects. Their behind-the-scenes assistance kept everything running smoothly and contributed greatly to making this journey far more manageable and rewarding.

I would also like to warmly thank my friends at Graduate House and the Sri Lankan community for making life here feel like home. Their friendship, care, and sense of togetherness helped ease the distance from my family and home country, and they truly became a second family to me during this time. I would also like to thank my badminton and cricket community for being such a positive and refreshing part of my life during this demanding PhD journey. In the middle of deadlines, stress, and long research days, they gave me moments of joy, laughter, and balance that I truly needed. Spending time with them was more than just a distraction, it was a source of energy, friendship, and relief that helped me stay grounded throughout this journey.

I would also like to sincerely thank Prof. Damith Herath, who has been both a mentor and like an elder brother to me from the very beginning of my time here. His care, guidance, and constant support have meant a great deal to me, and I am truly grateful for the way he looked out for me throughout this journey. I would also like to extend my heartfelt thanks to the entire University of Canberra (UC) robotics team for their friendship, support, and encouragement along the way. Having them around made this journey much warmer, more enjoyable, and far less difficult.

I would also like to express my heartfelt gratitude to Bhanuka, Hiruna, Anjalie, and Asiri Aiyya, who have been much more than friends to me throughout my time in Australia. They welcomed me into their lives and treated me as part of their own family, giving me a sense of belonging and warmth despite being so far away from home. Their kindness, care, generosity, and constant support have meant more to me than words can express, especially during the most challenging moments of my PhD journey. Whether through their encouragement, the time we spent together, or simply knowing that I had people I could always count on, they made my life in Australia feel much more like home. I will always cherish the wonderful memories we have shared and remain deeply grateful for the love and friendship they have given me.

Last, but certainly not least, I would like to express my deepest gratitude and my everlasting sincere thanks to my parents, my sisters, and my girlfriend for standing by me and supporting me through every stage of this journey, especially during the most difficult times. My parents have been the strongest foundation in my life, and the sacrifices they made to raise me, support my education, and believe in

my dreams without hesitation are far beyond anything I can ever repay. The values they instilled in me from childhood, along with their constant love, strength, and encouragement, carried me through this entire PhD journey more than words can express. I am equally grateful to my sisters and my girlfriend for their patience, understanding, and unwavering emotional support, which gave me comfort and strength whenever I needed it most. No amount of thanks would ever be enough to match all that they have done for me, but I hope they know that this achievement belongs to them as much as it does to me.

Publications

1. **Manuka Suriyage*,** Qingyi Zhou*, Hao Qin, Xueqian Sun, Zhuoyuan Lu, Stefan A. Maier, Zongfu Yu & Yuerui Lu. Long-propagating ghost phonon polaritons enabled by selective mode excitation. Light: Science & Applications 14, 254 (2025).
2. **Manuka Suriyage***, Hao Qin*, Xueqian Sun, Wenkai Yang, Shuyao Qiu, Qingyi Zhou, Zongfu Yu and Yuerui Lu. "Real-Space Imaging of Guided Exciton Polaritons in Free-standing Monolayer WSe2" (Under revision)
3. Xueqian Sun*, **Manuka Suriyage***, Ahmed Raza Khan, Mingyuan Gao, Jie Zhao, Boqing Liu, Md Mehedi Hasan, Sharidya Rahman, Ruo-Si Chen, Ping Koy Lam & Yuerui Lu. Twisted van der Waals quantum materials: fundamentals, tunability, and applications. Chemical Reviews 124, (2024).
4. **Manuka Suriyage**, Ruo-Si Chen & Yuerui Lu. Scalable heterostructures using photoresist-free patterning. Nature Electronics 8, 198–199 (2025).
5. **Manuka Suriyage**, Daniel Leyka, Yuerui Lu, Daria Smirnova. "Interaction-induced topological transitions in hybrid polaritonic metasurfaces" (Under revision – Nature Communications)
6. Sharidya Rahman*, Lakshmi Ullatil*, **Manuka Suriyage,** Anjalie Edirisooriya. "2D Materials: From Quantum Photonics to Biomedical Applications" - Invited Book chapter Springer Nature (Submitted)
7. **Manuka Suriyage***, Qingyi Zhou*, Hao Qin, Xueqian Sun, Zhuoyuan Lu, Stefan A. Maier, Zongfu Yu & Yuerui Lu. Selective excitation of long-propagating ghost phonon polaritons. In Proceedings of CLEO: Fundamental Science 2025 (Optica Publishing Group, 2025)
8. Zhuoyuan Lu, Jiri Janousek, Syed M. Assad, Shuyao Qiu, Mayank Joshi, Yecheng Hu, Alex Y. Song, Chuanyu Wang, **Manuka Suriyage**, Jie Zhao, Ping Koy Lam & Yuerui Lu. Counter-propagating entangled photon pairs from monolayer GaSe. *Nature Communications* **16**, 9616 (2025).
9. Anjalie Edirisooriya, **Manuka Suriyage**, Ning Lyu, Fiona Beck. "Wavelength-Guided Plasmonic Control of CO_2 Reduction: From Model Nanostructures to Gold Dendritic Electrodes" - Accepted for 16th META Conference on Metamaterials, Photonic Crystals and Plasmonics.

Abstract

Controlling light at the nanoscale underpins the advancement of next-generation photonic and optoelectronic technologies, with particular relevance for on-chip integration, optical communication, and quantum information processing. Traditional photonic systems face fundamental limitations, such as diffraction, weak light-matter interactions, and inefficient nonlinear effects at sub-wavelength scales. Overcoming these challenges requires new platforms that facilitate strong coupling between electromagnetic fields and material excitations, enabling light confinement, guidance, and control beyond the capabilities of conventional optics. Polaritonic excitations and nonlinear optical processes provide complementary strategies, supporting both efficient light propagation and enhanced light generation in compact systems.

Polaritons, arising from the strong coupling between photons and material excitations such as phonons and excitons, enable electromagnetic fields to be confined and guided far below the diffraction limit, offering a pathway toward highly directional energy transport. Nonlinear optical processes also play an important role in enabling functions such as frequency conversion and quantum light generation, both of which are essential for advanced photonic technologies. Although these effects occur in different operating regimes, together they provide a common basis for strengthening and exploiting light-matter interactions at the nanoscale. However, achieving deterministic control over excitation pathways, maintaining long-range and low-loss propagation, and translating these effects into practical photonic architectures remain fundamental challenges.

Low-dimensional and anisotropic materials provide a very promising way to overcome these limitations, although making full use of them requires careful design and control. Anisotropic polar dielectric crystals, for example, can support hyperbolic dispersion, which allows polaritons to propagate in naturally directional ways. Van der Waals materials, because of their reduced dimensionality enable strong optical confinement and tunable light-matter interaction. Among these materials, TMDCs stand out for their strong excitonic resonances and symmetry-dependent optical behavior, making them very appealing for both polaritonic and nonlinear optical studies. Still, having these favorable material properties is not enough on its own. To achieve selective mode excitation, low-loss propagation, and practical device integration, the surrounding environment and the photonic structure must be designed with great care.

To address these challenges, this thesis develops a systematic approach to engineering light-matter interactions by controlling guided polaritonic modes and nonlinear processes. The first part of this thesis focuses on the linear regime and the control of polariton direction and propagation. In anisotropic materials, polaritons behave in unusual ways because of hyperbolic dispersion, which allows light to travel in a highly directional manner while remaining confined far below the diffraction limit. A particularly interesting example is the ghost hyperbolic phonon polariton (g-HP), a special type of hybrid mode that travels along the surface while forming oblique wavefronts inside the material, giving rise to long-range, ray-like, and nearly diffraction-free propagation. Even though these modes are highly attractive for nanoscale light guiding, it has remained difficult to excite only the low-loss modes in a controlled way and to precisely steer the propagation direction. In this thesis, this challenge is addressed by developing a mode-selective excitation approach based on structural asymmetry, where carefully designed micro and nano-antennas act as momentum-selective sources that preferentially launch the desired polariton modes. This approach enables highly directional propagation and significantly extended propagation lengths, demonstrating that polariton transport can be actively controlled through excitation engineering. These results establish a new route for manipulating hyperbolic polaritons in natural anisotropic materials, opening opportunities for long-range energy transport and functional nanophotonic applications in the mid-infrared regime.

This idea is pushed even further in atomically thin materials, where exciton polaritons emerge, making TMDC monolayers stand out for their very strong excitonic response. At the same time, guiding light in a true monolayer is not straightforward, since such ultrathin systems suffer from weak confinement, mode cutoff, and a strong dependence on the surrounding dielectric environment. Through the second work discussed in this thesis, these limitations are addressed by using a suspended monolayer design, which makes it possible to observe guided exciton polaritons directly in real space for the first time. Near-field imaging and dispersion measurements clearly verify the fundamental guided mode and show pronounced light-matter coupling close to the excitonic resonance. Altogether, these findings open up a promising route toward ultracompact photonic devices with strong optical confinement based on monolayer materials.

Building on these advances, the thesis introduces an interaction-induced approach to generating topological polaritonic states. Unlike conventional systems in which non-trivial topology is encoded in the underlying photonic structure, the photonic and material subsystems considered

here are initially topologically trivial. Strong light-matter coupling induces band hybridisation and inversion, resulting in a topological transition and the emergence of an interface-localised hybrid polaritonic edge state. This mechanism is experimentally demonstrated through near-field imaging and frequency-dependent measurements, supported by theoretical band-structure calculations and control experiments on the uncoupled photonic system. The interaction-induced nature of the topological transition also provides opportunities for tuning the polaritonic response by modifying the light-matter coupling strength. While static control through hBN thickness is investigated, further theoretical analysis suggests the possibility of dynamic tuning using external stimuli such as mechanical strain or electrostatic gating. These findings establish a promising framework for developing reconfigurable topological polaritonic devices, with experimental realisation of dynamic switching remaining an important direction for future research.

The second part of the thesis focuses on nonlinear light-matter interactions in integrated photonic systems, where compact frequency conversion and controlled routing of optical signals remain significant challenges. To address these challenges, a nonlinear meta-waveguide platform based on non-centrosymmetric 3R-WS_2 is developed by integrating a patterned TMDC metasurface with a dielectric waveguide. The proposed structure exploits the strong second-order nonlinear response of 3R-WS_2 and metasurface-induced geometric phase control to investigate spin-selective optical coupling and directional routing. Experimental characterisation provides an initial demonstration of helicity-dependent directional coupling, while the relatively weak second-harmonic generation and guided-mode signals indicate that further optimisation is required to improve the nonlinear performance of the device. This exploratory demonstration establishes a foundation for developing integrated nonlinear photonic platforms, with potential future applications in more advanced frequency-conversion processes and quantum light generation.

In summary, this thesis develops strategies for controlling light-matter interactions across both linear and nonlinear regimes. Advances in guided polariton transport, interaction-driven topological states, and integrated nonlinear and quantum photonic platforms have helped connect fundamental studies of light-matter interaction with the development of practical device technologies. These results offer new approaches for nanoscale light manipulation and support the development of multifunctional photonic and optoelectronic systems based on low-dimensional material platforms.

Table of contents

Declaration iii

Acknowledgement v

Publications viii

Abstract ix

Table of Contents xii

List of Figures xv

List of Abbreviations and Acronyms xix

1. Introduction 1

1.1. Controlling light at the nano scale 1

1.2. Light-matter interaction beyond the diffraction limit 2

1.3. Polaritons as a platform for guided and directional light control 5

1.3.1. Phonon polaritons (PhPs) and Hyperbolic media 5

1.3.2. Exciton-polaritons (EPs) in low-dimensional materials 9

1.3.3. Topological polaritons 12

1.4. Nonlinear light-matter interactions in Nanophotonics 17

1.5. 2D materials and anisotropic platforms for nonlinear optics 17

1.6. Metasurfaces and waveguide integration 18

1.7. Thesis outline and scope 19

2. Experimental Techniques 31

2.1. Sample and Device fabrication 31

2.1.1. Mechanical Exfoliation, Dry transfer and physical stacking 31

2.1.2. Electron Beam Lithography 32

2.1.3. Electron Beam Evaporation 34

2.1.4. Inductive coupled Plasma-fluorine (ICP-F) etching 35

2.1.5. Chemical Vapor Deposition (CVD) 36

2.1.6. Focused Ion beam 38

2.2. Structural and Optical Characterization 40

2.2.1. Scanning electron microscope (SEM) 40

2.2.2. Phase Shift Interferometer (PSI) 42

2.2.3. Scattering field scanning near field optical microscope (s-SNOM) 43

2.2.4. Reflection and Transmission SHG. 47
2.2.5. Photoluminescence (PL) Spectroscopy. 48
3. Long Propagating Ghost polaritons Enabled by selective mode excitations. 50
3.1. Theoretical Framework of g-HPs inside the Anisotropic Media. 52
3.1.1. Anisotropic Dielectric Properties and Hyperbolic Dispersion in Calcite. 52
3.1.2. Ghost polariton formation at calcite-air interface. 55
3.1.3. Propagation length and decay mechanism. 56
3.1.4. Numerical simulation techniques. 61
3.2. Selective mode excitation via antenna engineering. 61
3.2.1. Conventional excitation. 61
3.2.2. Directional propagation tuning through excitation. 62
3.2.3. Engineering the nano antenna shape for tuning polariton excitation. 67
3.2.4. Directionality metric and observed directional propagation. 69
3.2.5. Edge assisted mode selection for directionality and long propagation. 70
3.3. Sample Fabrication. 74
3.4. Demonstration of edge assisted g-HPs through Near-Field Imaging. 76
3.4.1. Shape dependent Directional excitation. 76
3.4.2. Confirmation of edge assisted mode selection through near field imaging. . . 83
3.4.3. Confirmation of long propagation length of g-HPs. 90
4. Real space imaging of guided exciton polaritons in suspended monolayer TMDCs. 97
4.1. Challenges of realizing guided modes in Monolayer TMDCs. 98
4.2. Theory of guided Exciton Polaritons. 99
4.2.1. TE guided modes in monolayer WSe2. 99
4.2.2. Surface Susceptibility Model. 101
4.2.3. Dispersion Relations and key physical quantities. 102
4.3. Design strategy for Realizing guided modes in monolayers. 106
4.3.1. Concept of Suspended Monolayer. 106
4.3.2. Numerical simulation of guided mode exciton Polaritons. 107
4.4. Sample fabrication and Real-space observation of guided modes. 110
4.4.1. Device fabrication. 110
4.4.2. Near field imaging results for the suspended monolayer sample. 112
4.4.3. Physical origin of results. 113
4.5. Fringe formation mechanism and Analysis. 115
4.5.1. Boundary scattering model. 115

4.5.2. Phase interference model. 117
4.5.3. Simplified fringe condition. 119
4.6. Strong coupling and dispersion of guided exciton polaritons. 120
5. Induced Topological Phonon Polaritons. 127
5.1. Theoretical Background of Induced Topology. 128
5.1.1. Photonic system and trivial band structure. 128
5.1.2. Strong light-matter coupling with hBN and hybrid polaritons. 132
5.2. Experimental Design and Fabrication. 137
5.2.1. Proposed grating design and hybrid structure based on simulation results...137
5.2.2. Device Fabrication. 138
5.2.3. Final device. 140
5.3. Near-field characterization and experimental realization of induced topological polariton mode. 142
5.3.1. Characterization of the coupled hybrid system to investigate the induced topological polariton edge mode. 143
5.3.2. Trivial Photonic system characterization. 151
5.4. Discussion and future work. 155
6. Spin-Selective coupling of SHG using 3R-WS_2 metasurface. 159
6.1. Physical Principles of Valley-Selective Nonlinear Photonics. 160
6.1.1. Valley dependent Optical Selection Rules in TMDCs. 160
6.1.2. Geometric phase metasurfaces. 160
6.1.3. Spin-momentum locking and Directional coupling. 161
6.2. Device concept and design. 162
6.3. Fabrication of the Meta-waveguide platform and optical characterization. 164
6.3.1. Substrate and waveguide fabrication. 165
6.3.2. Metasurface fabrication (with 3R-WS2) 166
6.3.3. Fabricated results and final devices. 169
6.3.4. Optical characterization. 173
7. Conclusion and Future work. 176

List of Figures

1.1 Polaritons in vdW materials and other hybrid systems. 3
1.2 Polaritonic material platforms and respective dispersion characteristics. 5
1.3 Hyperbolic PhPs in uniaxial and biaxial material platforms. 6
1.4 Different types of Hyperbolic PhPs. **7**
1.5 Directional Propagation of Hyperbolic PhPs. 8
1.6 Cavity EPs. 10
1.7 Guided mode EPs in TMDCs. 11
1.8 Topological Photonics. 13
1.9 Topological exciton and phonon Polaritons. 14

2.1 Schematic of the mechanical exfoliation and dry transfer process. 32
2.2 Schematic of the electron beam lithography (EBL) process. 33
2.3 Schematic of the electron beam evaporation system. 34
2.4 Schematic of the inductively coupled plasma (ICP) etching system. 36
2.5 Schematic of the PECVD system used for thin film deposition. 37
2.6 Schematic of the dual-beam FIB-SEM system. 39
2.7 Schematic of the SEM system used for morphological characterisation. 41
2.8 Schematic of the phase-shifting interferometry (PSI) system. 42
2.9 Schematic of the s-SNOM setup used in this work. 44
2.10 Schematic of the s-SNOM interferometric optical setup. 45
2.11 Schematic of the optical setup used for reflection and transmission second-harmonic generation (SHG) measurements. 47

3.1 Permittivity tensor of calcite and its hyperbolic behaviour. 53
3.2 Effect of crystallographic orientation on the dispersion and propagation characteristics of phonon polaritons in calcite. 54
3.3 Momentum-space visualization of g-HP propagation lengths on the IFC. 60
3.4 Polariton parameters and asymmetric excitation scheme. 63
3.5 Asymmetric distribution of g-HPs under oblique excitation. 64
3.6 Asymmetric distribution based on the different polarization angle excitation. 66
3.7 Comparison of polariton propagation lengths for disk nanoantennas of different sizes.67
3.8 g-HPs excitation through different shapes. 68

3.9 Conceptual and theoretical description of the edge assisted mode selection mechanism……... 72
3.10 Nano / Micro antenna fabrication process. 75
3.11 Asymmetric g-HP excitation from shape dependent micro/nano antennas. 77
3.12 Directionality analysis of g-HPs excited by antennas of different shapes. 79
3.13 Fourier analysis of the s-SNOM images. 81
3.14 Effect of antenna curvature and edges on polariton excitation from disk to triangular geometries. 82
3.15 Effect of physical edge to enhance coupling of modes for selective excitation. 84
3.16 Edge assisted mode selection. 85
3.17 Edge assisted mode selection based on the rotational angle (σ) of the micro/nano antenna. 87
3.18 Determination of directionality of g-HPs and edge assisted mode selection for different rotational orientations of the triangle antenna. 89
3.19 Highly enhanced propagation length of g-HPs through different shaped micro/nano antennas. 92

4.1 Field configuration and parameters of a TE-guided exciton polariton in a free-standing monolayer WSe_2. 100
4.2 Physical Parameters of the guided mode EP. 103
4.3 Dispersion characteristics for bulk and monolayer WSe_2. 104
4.4 Suspended monolayer WSe_2 geometry. 107
4.5 COMSOL simulations of guided exciton polaritons under different cladding conditions…... 108
4.6 2D and 3D simulations of the conceptualized free-standing sample. 109
4.7 Fabrication process of the patterned substrate using photolithography, including resist coating, exposure, development, metal masking, and etching steps. 110
4.8 Optical microscopy and AFM characterization of the fabricated sample. 111
4.9 Experimental near-field images. 112
4.10 Exciton-polariton boundary scattering behaviour. 114
4.11 Fringe formation and numerical simulation results. 116
4.12 Dispersion analysis of the guided mode from a free standing monolayer WSe_2. 121

4.13 Experimentally reconstructed dispersion of guided exciton polaritons in a free-standing WSe_2 monolayer. 122

5.1 Si grating based photonic system. 130
5.2 Coupled topological polaritonic system. 134
5.3 Si grating design finalized parameters. 138
5.4 Fabrication process of the silicon photonic grating. 139
5.5 SEM images of the fabricated silicon grating. 141
5.6 Flake transferring onto the Si grating. 142
5.7 Topological edge mode realization in the coupled hybrid system. 143
5.8 Near-field measurements of a 70 × 5 μm regions across the interface, used to identify the topological band gap. 144
5.9 Edge mode identification using s-SNOM measurements at the centre of the band gap…... 145
5.10 Averaging method used to extract line profiles from experimental near-field images……. 147
5.11 Experimental near-field measurements within the topological band gap, with corresponding line-cut profile analysis. 148
5.12 Tunability of the interaction-induced topological phonon- polariton edge state through coupling strength.. 150
5.13 Control near-field characterization of the uncoupled trivial photonic system. 152
5.14 Near-field response of the uncoupled photonic system. 154

6.1 Schematic of the fabrication process flow for the Si_3N_4 waveguide on a quartz substrate.. 165
6.2 Fabrication process flow in creating the Cr protective layer for the Si3N4 waveguide…... 166
6.3 Fabrication process flow for the 3R-WS2 metasurface fabrication. 168
6.4 Fabrication flow diagram for the complete meta-waveguide device. 169
6.5 Waveguide fabrication and flake transfer. 170
6.6 Key EBL and etching steps used in the fabrication of the final device, highlighting the critical stages. 171
6.7 Microscopic images of the final fabricated device. 172
6.8 Spin-selective coupling and guiding in the meta-waveguide device. 173

List of Abbreviations and Acronyms

0D	zero-dimensional
1D	one-dimensional
2D	two-dimensional
2H	hexagonal phase
3D	three-dimensional
3R-phase	rhombohedral phase
α-MoO3	α-phase molybdenum trioxide
α-Si	amorphous silicon
AFM	atomic force microscopy
Ar	Argon
Au	Gold
BSE	backscattered electrons
C	Chern number
CCD	charge-coupled device
CdTe	cadmium telluride
CHF_3	trifluoromethane
CVD	chemical vapour deposition
DBR	distributed Bragg reflector
DI	deionized water
DOS	density of states
EBL	electron beam lithography
EM	electromagnetic
EP	Exciton-Polaritons
ETD	Everhart–Thornley detector
FIB	focused ion beam

Ga	gallium
GME	guided-mode expansion
g-HP	ghost hyperbolic phonon polariton
hBN	hexagonal boron nitride
He	helium
HgTe	mercury telluride
HOT	higher-order topology
ICP-F	fluorine-based inductively coupled plasma etching
IFC	isofrequency contour
InGaAs	indium gallium arsenide
IPA	isopropyl alcohol
IR	infrared
Laser	light amplification by stimulated emission of radiation
LED	light-emitting diode
LO	longitudinal optical
LPB	lower polariton branch
M	Dirac Mass
MoS_2	molybdenum disulfide
$MoSe_2$	molybdenum diselenide
MPB	middle polariton branch
N_2	nitrogen
N_2O	nitrous oxide
NH_3	ammonia
O_2	oxygen
O3A	third harmonic amplitude
O3P	third harmonic phase

OA	optic Axis
OPL	optical path length
OPO	optical parametric oscillator
PECVD	plasma-enhanced chemical vapour deposition
PB	Pancharatnam-Berry
PDMS	polydimethylsiloxane
PhP	phonon polariton
PL	photoluminescence
PSI	phase-shifting interferometry
Q	Q-factor
QCL	quantum cascade laser
RF	radio frequency
RPM	revolutions per minute
s-SNOM	scattering-type scanning near-field optical microscopy
sccm	standard cubic centimetres per minute
SE	secondary electrons
SEM	scanning electron microscopy
SF_6	sulfur hexafluoride
SHG	second-harmonic generation
Si	silicon
SiC	silicon carbide
SiH_4	silane
SiN_x	silicon nitride
SiO_2	silicon dioxide
SPDC	spontaneous parametric down-conversion
TE	transverse electric

TiO_2	titanium dioxide
TLD	through-the-lens detector
TM	transverse magnetic
TMDC	transition metal dichalcogenide
TO	transverse optical
UPB	upper polariton branch
UV	ultraviolet
vdW	van der Waals
VSI	vertical scanning interferometry
WSe_2	tungsten diselenide
WS_2	tungsten disulfide
Z_2	Z_2 topological invariant

1. Introduction

1.1 Controlling light at the nano scale

The ability to control light at the nanoscale represents one of the most fundamental challenges in modern photonics and optoelectronics. Integration of conventional optical systems in these devices and technologies is constrained by the diffraction limit. This limitation arises from the wave nature of light, which imposes fundamental constraints on the miniaturization and integration density of photonic devices. As a result, it hinders the development of compact, energy-efficient, and high-performance optical systems across a wide range of technological applications. In areas such as mid-infrared sensing, it reduces both the achievable spatial resolution and the strength of local field enhancement[1,2]. It also creates a serious challenge for emerging quantum technologies, where controlling light precisely at subwavelength scales is often essential[2]. Also, the conventional optical platforms often suffer from weak light-matter interaction because the optical field does not overlap strongly enough with the material, which in turn reduces the efficiency of light emission and nonlinear optical processes. Overcoming these limitations requires new platforms that can confine light much more tightly, strengthen its interaction with matter, and still remain practical for compact photonic integration[3,4].

Efforts to overcome the diffraction limit have led to the investigation of alternative light-control platforms. Plasmonic systems can confine light very strongly at the nanoscale, but their performance is often limited by high optical losses[5]. Photonic crystals and metamaterials offer greater control over dispersion through careful structural design, although they are still generally restricted by wavelength scale modes and can be challenging to fabricate[6]. Dielectric resonators and high-index waveguides help reduce these losses, but their performance is still tied to the refractive index contrast that can realistically be achieved in the material system[7,8].

A particularly promising way to overcome these limitations is through polaritons[9], which are hybrid quasiparticles formed by the strong coupling of light with material excitations. Because of this mixed light-matter nature, polaritons can support both deep subwavelength confinement and relatively long-range propagation. This makes them a powerful platform for controlling light at the nanoscale and allows them to bypass some of the key limitations associated with both conventional photonic systems and plasmonic structures[3,9,10]. Van der Waals materials are especially well suited for polaritons, offering smooth interfaces, tunable properties, and a wide range of excitations across the electromagnetic spectrum[9,10].

The applications enabled by nanoscale light control are vast and transformative. On-chip photonic communication could greatly benefit from ultracompact waveguides, modulators, and switches that use less space and consume less power, helping photonic circuits move closer to the integration density already achieved in electronics[11,12]. At the nanoscale, thermal management, which is crucial for high-power electronic devices and energy harvesting systems, could also be transformed by using polariton-mediated heat transfer pathways that go beyond the limits of conventional phonon-based conduction[13,14]. In the mid-infrared range, sensing and spectroscopy for applications such as environmental monitoring, medical diagnostics, and security could become far more sensitive and spatially precise by taking advantage of the strong field confinement and spectral selectivity offered by phonon polaritons[15-17]. In addition, quantum technologies such as single-photon sources, entangled photon-pair generators, and quantum repeaters depend on precise control over photon emission, polarization, and routing, all of which can be further improved through carefully engineered light-matter interactions in low-dimensional material systems[18,19].

The main aim of this thesis is to develop more effective methods for controlling guided polaritons and nonlinear light-matter interactions in van der Waals materials and hybrid photonic structures, with a clear focus on future on-chip photonic[20] and optoelectronic devices[21]. A major part of the work is focused on tackling some of the key obstacles that still stand in the way, such as how to selectively excite the right modes, control the direction of propagation, improve topological robustness, and achieve efficient nonlinear frequency conversion. By addressing these issues, the thesis tries to connect fundamental polariton physics with the kind of practical design strategies needed for device integration. It looks at both the linear regime, where strong coupling changes the dispersion and leads to unusual propagation behavior, and the nonlinear regime, where stronger light-matter interaction can be used for frequency conversion and quantum light generation in compact integrated structures.

1.2 Light-matter interaction beyond the diffraction limit

The transition from weak to strong light-matter coupling represents a fundamental change in how a photonic system behaves. In the weak coupling regime, light and matter still act largely as separate entities: a photon can be absorbed, or an excited state can emit a photon, but the two do not lose their individual character. In this case, the interaction is mainly described in terms of energy transfer and decay by Fermi's golden rule and the density of photonic and material states[22]. The situation changes fundamentally in the strong coupling regime. In this

case, the coherent exchange of energy between light and matter occurs at a rate that exceeds the dominant loss and dephasing processes. As a result, the system can no longer be described as independent photonic and material excitations; instead, they hybridize to form new eigenstates known as polaritons[9,10].

Polaritons are quasiparticles that embody the hybridization of electromagnetic fields with material excitations. This hybridization is not just a mathematical description. It is a real physical effect that can be directly observed through clear experimental signatures such as anticrossing in the dispersion, mode splitting in spectroscopy, and changes in decay behaviour that reveal the mixed light-matter nature of the states. Once polaritons are formed, the relationship between energy and momentum is fundamentally reshaped, giving rise to propagation behaviour that cannot be achieved in systems that are purely optical or material. Depending on the type of material excitation involved and the surrounding photonic structure, polaritons can display remarkable properties such as hyperbolic dispersion, flat bands, and topological edge states, all of which create new possibilities for controlling light at the nanoscale[9,10].

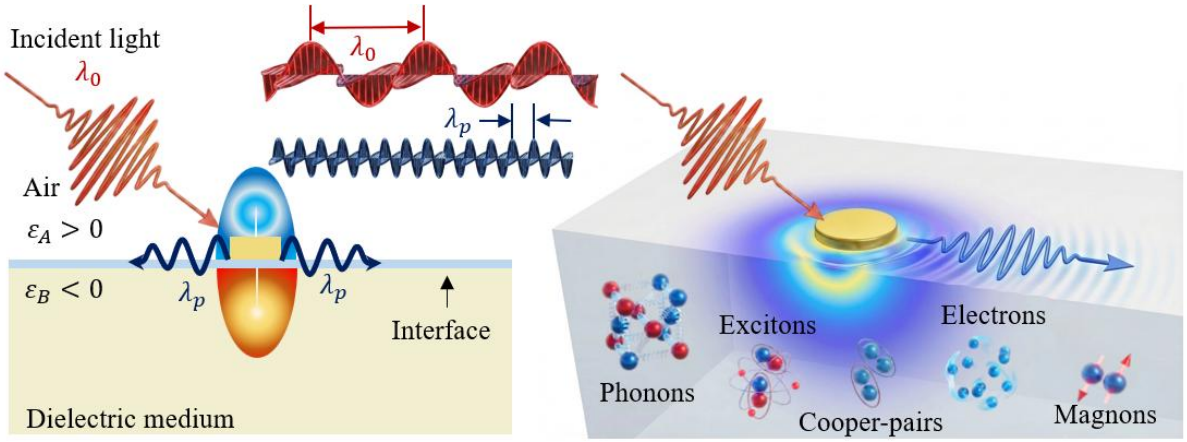


Figure 1.1 | Polaritons in vdW materials and other hybrid systems.

Van der Waals materials and other low-dimensional systems host a wide range of polaritons, each arising from the coupling of light to a distinct material excitation[9,10]. Plasmon polaritons, for example, arise when light couples to the collective motion of free carriers in metals or doped semiconductors[23,24]. In graphene and related two-dimensional conductors, these modes can confine light extremely strongly, with wavelengths compressed by well over two orders of magnitude, and can also be tuned electrically through gating, which makes them especially attractive for reconfigurable nanophotonic applications[24]. Phonon polaritons[10,25], in contrast, originate from the coupling of light to optical phonons, that is, lattice vibrations in polar

dielectric crystals where ionic motion produces oscillating dipoles. In materials such as hexagonal boron nitride (hBN)[26] and α-phase molybdenum trioxide (α-MoO_3)[27], these polaritonic modes can exhibit hyperbolic dispersion, allowing light to travel in highly directional ways, remain tightly confined far below the diffraction limit, and persist with relatively long lifetimes in the mid-infrared[28]. Another major class of polaritons is exciton polaritons[9], which are formed when photons strongly interact with excitons, that is, bound electron-hole pairs in semiconductors. In Transition metal dichalcogenides (TMDCs) such as WS_2[29], WSe_2[30], MoS_2[31], and $MoSe_2$[32], exciton polaritons inherit the valley-dependent optical properties of the underlying excitons, opening up exciting possibilities for valleytronic concepts and topologically protected photonic states.

Beyond these canonical examples, the polariton family extends to more exotic members. Cooper pair polaritons involve coupling between photons and the superconducting condensate in superconductors, potentially enabling ultra-low-loss quantum circuits and novel quantum phase transitions[33]. Magnon polaritons result from hybridization with spin waves in magnetic materials, offering routes to integrate spintronics with photonics and to explore magnetically tunable optical responses[34]. Although experimental studies of Cooper-pair polaritons and magnon polaritons in van der Waals materials are still quite limited, early theoretical ideas and initial proposals suggest that these systems could become an exciting direction for future research[9]. This wide variety of polariton types highlights just how rich the underlying material excitations are in van der Waals and other low-dimensional platforms. Each class of polariton appears in its own spectral range, has its own dispersion and loss behaviour, and responds differently to external controls such as electric fields, magnetic fields, strain, and temperature[9]. This diversity enables a modular approach to nanophotonic design. By selecting the appropriate material system and engineering the photonic environment, one can tailor polariton properties confinement, propagation length, group velocity, nonlinearity to match the requirements of specific applications[9,10].

This thesis looks at two closely connected aspects of light-matter interaction. The first, discussed in Sections 1.3 and 1.4, focuses on polaritons in the linear optical regime, where strong coupling changes the dispersion and allows electromagnetic energy to propagate in guided, directional, and even topologically protected ways at the nanoscale. Within this part of the work, three main polaritonic platforms are explored. Phonon polaritons in hyperbolic materials (Section 1.3.1), exciton polaritons in low-dimensional semiconductors (Section 1.3.2), and topological polaritons that emerge from interaction-driven band topology (Section

1.3.3). The second part of the thesis, covered in Sections 1.5 to 1.7, turns to nonlinear light-matter interactions, where strong field confinement and intrinsic material nonlinearities make it possible to achieve efficient frequency conversion, valley-selective photon generation, and compact on-chip quantum light sources. Taken together, these two regimes provide a broad framework for understanding and engineering light-matter interactions beyond the diffraction limit, with clear relevance for future integrated photonic and optoelectronic technologies.

1.3 Polaritons as a platform for guided and directional light control

1.3.1 Phonon polaritons (PhPs) and Hyperbolic media

Phonon polaritons in polar dielectric crystals arise from the resonant coupling between infrared photons and transverse optical (TO) phonons lattice vibrations that generate oscillating electric dipole moments[9,10]. The frequency-dependent dielectric response of such crystals exhibits characteristic Lorentzian resonances, with the real part of the permittivity becoming negative between the TO and longitudinal optical (LO) phonon frequencies, a spectral window known as the Reststrahlen band[9,10]. Within this band, electromagnetic waves cannot propagate in the bulk but instead couple to surface or guided modes, forming phonon polaritons with wavelengths far shorter than the free-space wavelength and lifetimes that can exceed hundreds of optical cycles.

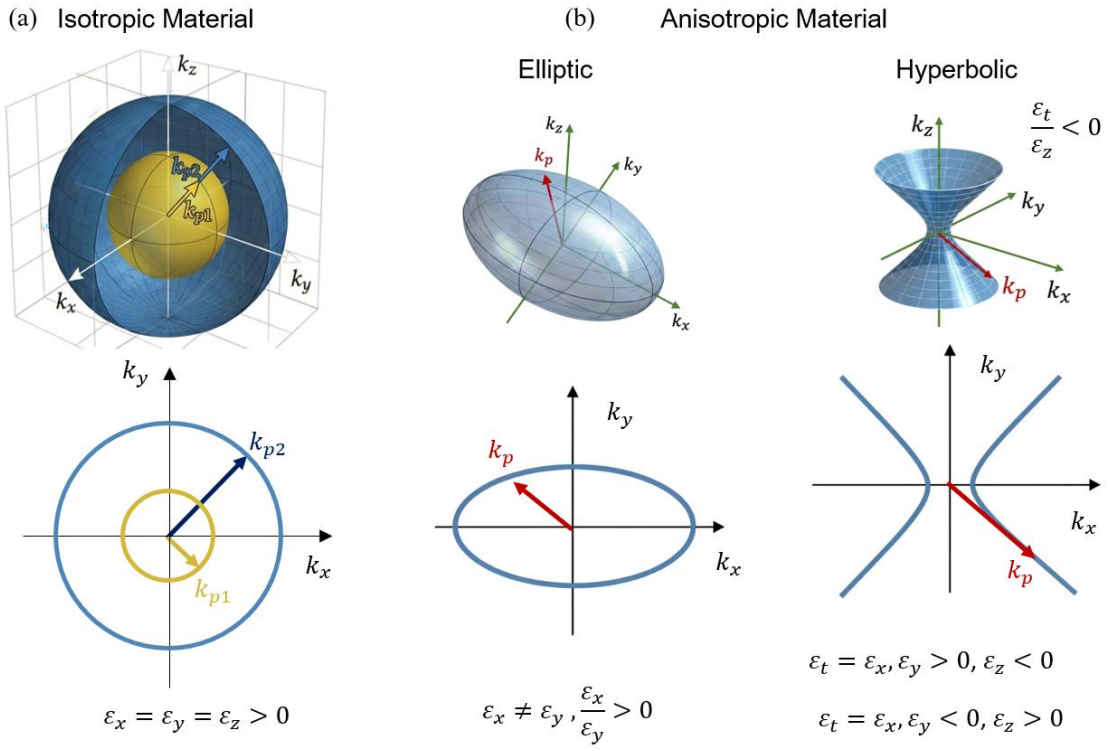


Figure 1.2 | Polaritonic material platforms and respective dispersion characteristics.

The dispersion and propagation characteristics of phonon polaritons are profoundly influenced by the anisotropy of the host crystal. In isotropic polar dielectrics, such as silicon carbide[35] (SiC), the dielectric tensor is scalar and the isofrequency contours surfaces of constant frequency in momentum space are circular, leading to isotropic propagation with no preferred direction (Figure 1.2a). In uniaxial crystals(Figure 1.3a), such as hexagonal boron nitride (hBN)[26,36], the dielectric tensor has two distinct principal values, One for the in-plane directions and one for the out-of-plane direction. When these two components have opposite signs within the Reststrahlen band, the isofrequency contour becomes a hyperboloid rather than an ellipsoid, a condition known as hyperbolic dispersion[9,10,26,27]. Hyperbolic dispersion enables highly directional propagation, with energy flowing along rays that can be steered by engineering the crystal orientation or the excitation geometry[9,10,27].

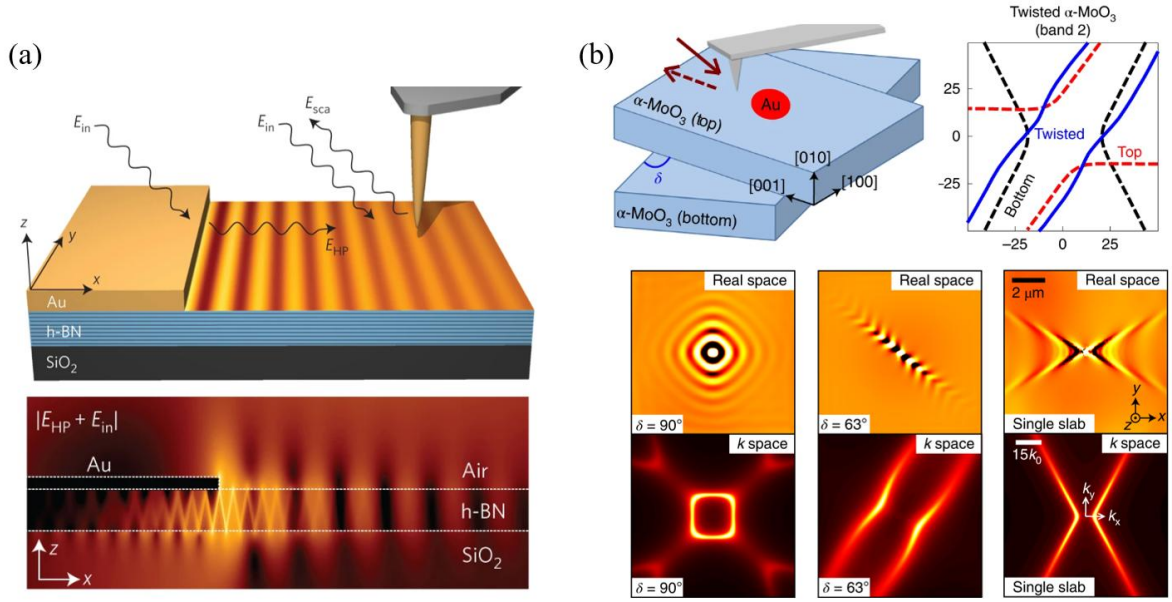


Figure 1.3 | Hyperbolic PhPs in uniaxial and biaxial material platforms. a, PhPs propagating in hBN[36]. **b,** PhPs propagating in α-MoO_3. Two slabs of α-MoO_3 are stacked to tune the twist angle to control the in-plane hyperbolic dispersion. Topological transition is achieved through the twist angle engineering and the elliptical, canalization and hyperbolic propagations are evident with the bottom near field images[27].

Hyperbolic dispersion in uniaxial materials is classified into two types based on the signs of the dielectric tensor components of the dielectric permittivity tensor. For uniaxial crystal with its optic axis along the z-direction Type I hyperbolic dispersion occurs when the in-plane permittivity components are positive while the out-of-plane permittivity is negative. This produces a two-sheet hyperboloid in three-dimensional momentum space, with the two sheets

separated along the optic-axis direction. In contrast, Type II hyperbolic dispersion arises when the in-plane permittivities are negative and the out-of-plane permittivity is positive, resulting in a one-sheet hyperboloid extending along the optic-axis directions[10,23,26,27]. hBN exhibits Type I and Type II hyperbolic behavior in two distinct Reststrahlen bands, enabling out-of-plane hyperbolic phonon polaritons that propagate with oblique wavefronts and extreme confinement. In contrast, biaxial crystals such as α-MoO_3[27] possess three distinct principal dielectric values, leading to in-plane hyperbolic dispersion where the hyperboloid opens within the plane of the crystal. This in-plane anisotropy (Figure 1.3b) enables directional propagation along specific crystallographic axes and subdiffractional focusing without the need for complex nano structuring.

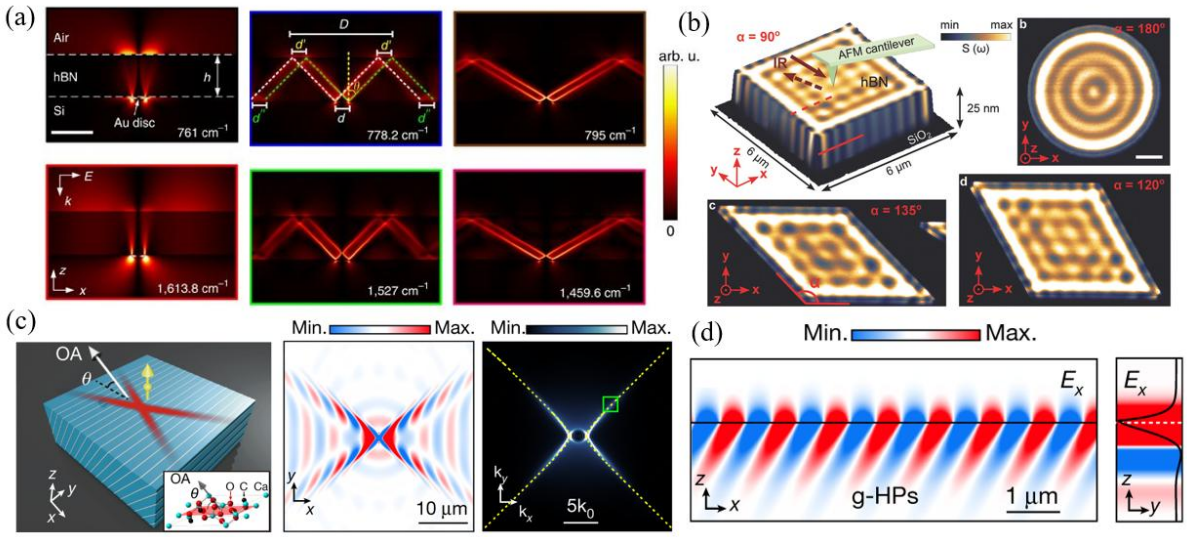


Figure 1.4 | Different types of Hyperbolic PhPs. a, Volume confined hyperbolic PhPs propagating inside hBN. Simulated electric-field distributions at various excitation frequencies showcasing the hyperbolic bulk propagation in both Type I and Type II regimes.[37] **b,** Surface PhPs in hBN nanodiamonds. Left top panel shows the experimental near field setup. The 3 near-field images demonstrate the surface polaritons for a 25nm thick hBN with different diamond corner angles.[38] **c,** Left panel: Schematic of a vertical dipole launching g-HPs on a calcite surface. Middle panel: Simulated near-field Re(Ez) at ω = 1470 cm^{-1}. Right panel : Fourier magnitude of the field distribution. **d,** cross section near-field distribution of g-HPs with surface mode coupled with oblique wavefronts in the bulk[39].

Phonon polaritons in hyperbolic media can be further classified based on their confinement and propagation characteristics (Figure 1.4). Volume confined hyperbolic (Bulk) phonon polaritons[37,40] propagate within anisotropic media (Figure 1.4a) with highly directional

wavevectors governed by hyperbolic dispersion[9,10]. Surface-confined phonon polaritons[38] are bound to interfaces between materials with different dielectric properties and decay evanescently into both media, with their dispersion and confinement determined by the permittivity contrast (Figure 1.4b). Most recently, g-HPs[39] have been reported (Figure 1.4c), showing in-plane hyperbolic dispersion at the surface of a polar uniaxial crystal and oblique wavefronts in the bulk (Figure 1.4d), similar to the ghost waves predicted earlier[41]. Owing to its oblique crystal lattice, and the ability to tune the orientation of the optical axis relative to the surface through mechanical cutting and polishing, calcite offers precise control over its polaritonic response.

The directionality of polaritons is important for many applications[3,42-44], especially where controlling electromagnetic energy flow at the nanoscale is required[45,46]. Previous studies have demonstrated directional propagation using several approaches, including grating diffraction, where polaritons are launched preferentially to one side of the grating[46], topological transitions in the surrounding medium, such as in photonic crystals[47], through layered structures with twist angles[48], hybrid plasmonic structures[49] and more recently, through polarized dipoles[50,51] and polaritonic crystals[52].

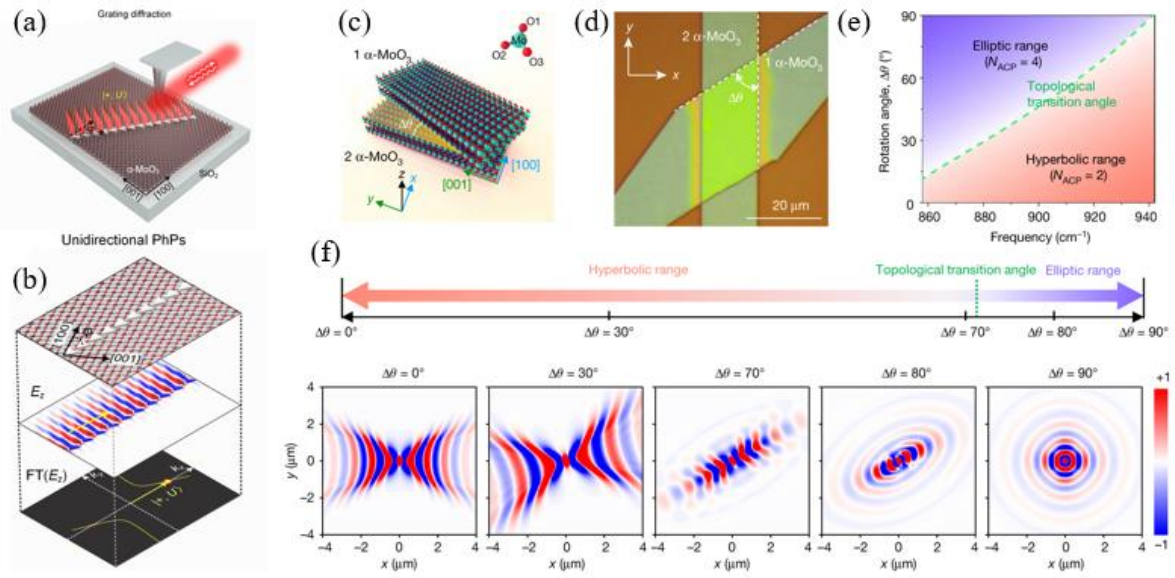


Figure 1.5 | Directional Propagation of Hyperbolic PhPs. a, The schematic representation of the grating assisted unidirectional PhPs in α-MoO_3[46]. **b,** Illustration of the grating (top panel) numerically simulated electric-field in the middle panel and the FT image in the lower panel[46]. **c,** Schematic of the two-slab twisted structure of α-MoO_3. **d,** Optical image of the actual twisted

heterostructure. **e,** Topological nature variation against the twist angle. **f,** Numerically simulated field distribution for different twist angles[48].

The applications of phonon polaritons[9,10,53,54], and particularly of engineered hyperbolic phonon polaritons, span multiple domains. In on-chip mid-infrared photonics, phonon polaritons offer a pathway to ultra-compact waveguides, modulators, and resonators that operate in the molecular fingerprint region, enabling integrated spectroscopic systems for chemical sensing and environmental monitoring. In thermal management[13,14], phonon polaritons mediate radiative heat transfer at the nanoscale, with hyperbolic dispersion enabling enhanced heat flux and quasi-ballistic thermal transport over distances far exceeding those accessible through phonon-phonon conduction. Experimental demonstrations have shown that surface phonon polaritons can carry heat over hundreds of micrometers in thin polar membranes, with apparent thermal conductivities that exceed bulk values and that can be tuned by engineering the polariton dispersion. Furthermore, hybrid plasmonic-phononic systems, where graphene or other two-dimensional conductors are integrated with polar dielectrics, exhibit coupled plasmon-phonon polaritons with tunable dispersion and enhanced near-field radiative transfer, offering additional degrees of freedom for thermal engineering[55].

1.3.2 Exciton-polaritons (EPs) in low-dimensional materials

Exciton polaritons arise from the strong coupling between photons and excitons Coulomb-bound electron-hole pairs in semiconductors[9]. TMDC layered semiconductors with the chemical formula MX_2, where M is a transition metal (Mo, W) and X is a chalcogen (S, Se) have emerged as a premier platform for exciton polaritonics in the 2D limit[30]. Monolayer TMDCs exhibit exceptionally strong excitonic resonances[56-58] due to reduced dielectric screening and enhanced Coulomb interactions in two dimensions, with exciton binding energies reaching hundreds of meV an order of magnitude larger than in conventional III-V quantum wells[59,60]. This strong binding ensures that excitons remain stable at room temperature, enabling robust exciton-polariton formation under ambient conditions[59,60].

EPs in TMDCs can be realized in two distinct operational modalities as cavity EPs (Figure 1.6) and guided EPs. Cavity EPs are formed by embedding TMDC monolayers or few-layers in Fabry-Pérot microcavities, where the excitons couple to discrete cavity photon modes[61-63]. Early theoretical work on quantum well EPs, based on distributed Bragg reflectors, paved the way for realizing cavity EPs with different optical resonances coupled to excitons[61]. More recent studies have explored a range of exciton complexes, including trions[62] (Figure 1.6a-c)

and defect-bound excitons[64], particularly in atomically thin TMDCs[63] (Figure 1.6d,e), revealing new cavity polariton behavior. However, cavity EPs are limited by fast radiative decay and low group velocity.

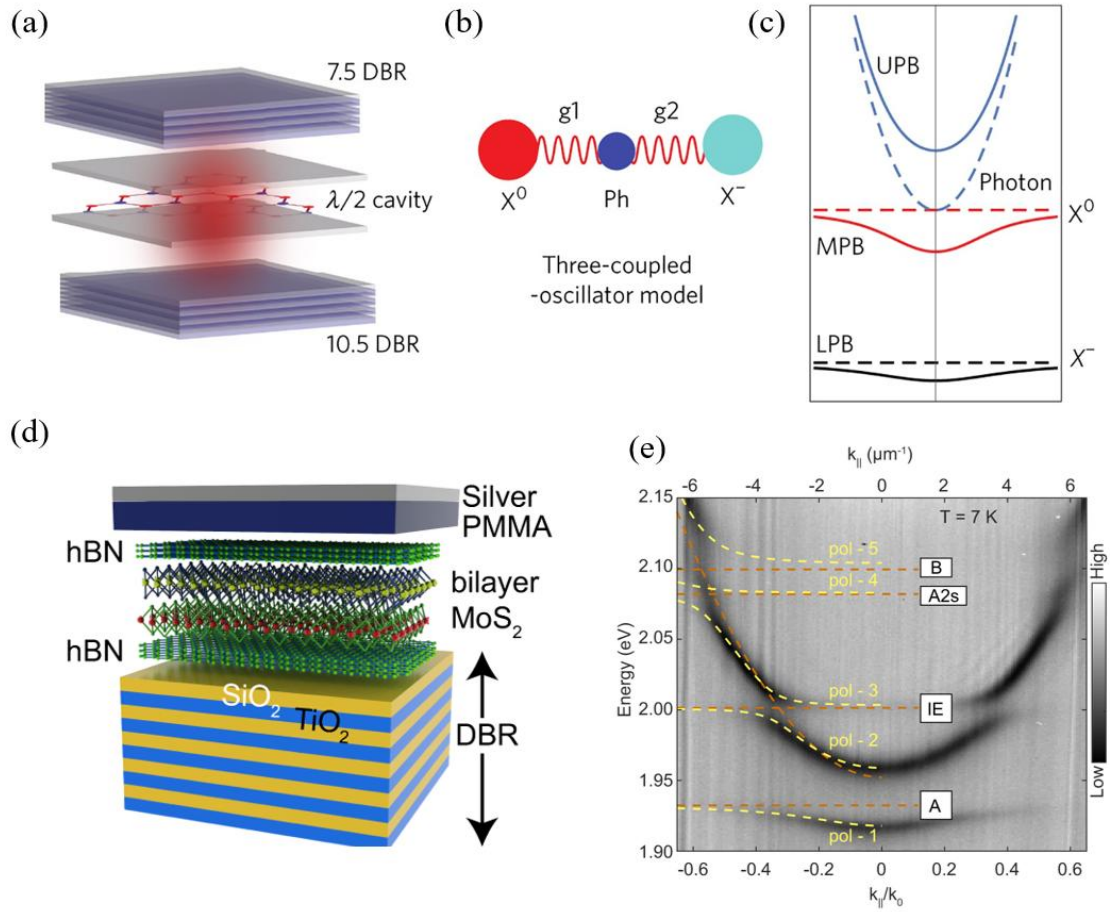


Figure 1.6 | Cavity EPs. **a,** Schematic of the optical cavity containing a monolayer $MoSe_2$ layer inside two Bragg mirrors. **b,** A coupled spring and mass oscillatory system representing the three coupled system in the cavity EP presented in a. **c,** Dispersion diagram for the uncoupled cavity and exciton and strongly coupled EP system. [62] **d,** Schematic of the cavity EP device where bilayer MoS_2 is sandwiched between two hBN layers and then placed in Bragg reflective mirrors. **e,** White light differential reflection measurement showcasing the dispersion relation of the strongly coupled cavity EP system[63].

To overcome this, excitons have been coupled to non-radiative waveguide modes in TMDCs, which offer higher group velocities and longer propagation lengths[32,65], making them more suitable for photonic applications in the near infrared[65] to visible range[66,67]. These guided EP modes (Figure 1.7) have been used to probe optical anisotropy in van der Waals materials and to develop waveguided polariton lasers. Experimental demonstrations of guided EPs have been reported in multilayer TMDCs such as WS_2[68,69], MoS_2[31,70], WSe_2[65], and $MoSe_2$[32]. Despite this

progress, achieving guided EPs in monolayers and very thin layers remains difficult. As thickness decreases, several limitations arise, including mode cut-off[70], reduced confinement, and strict boundary conditions. Still, monolayer TMDCs, with thicknesses of only a few angstroms, can sustain high current densities and show strong light-matter interaction, making them promising for nanoscale light control. While cavity EPs have been demonstrated in monolayers, experimental realization of guided EP modes in these systems is still lacking.

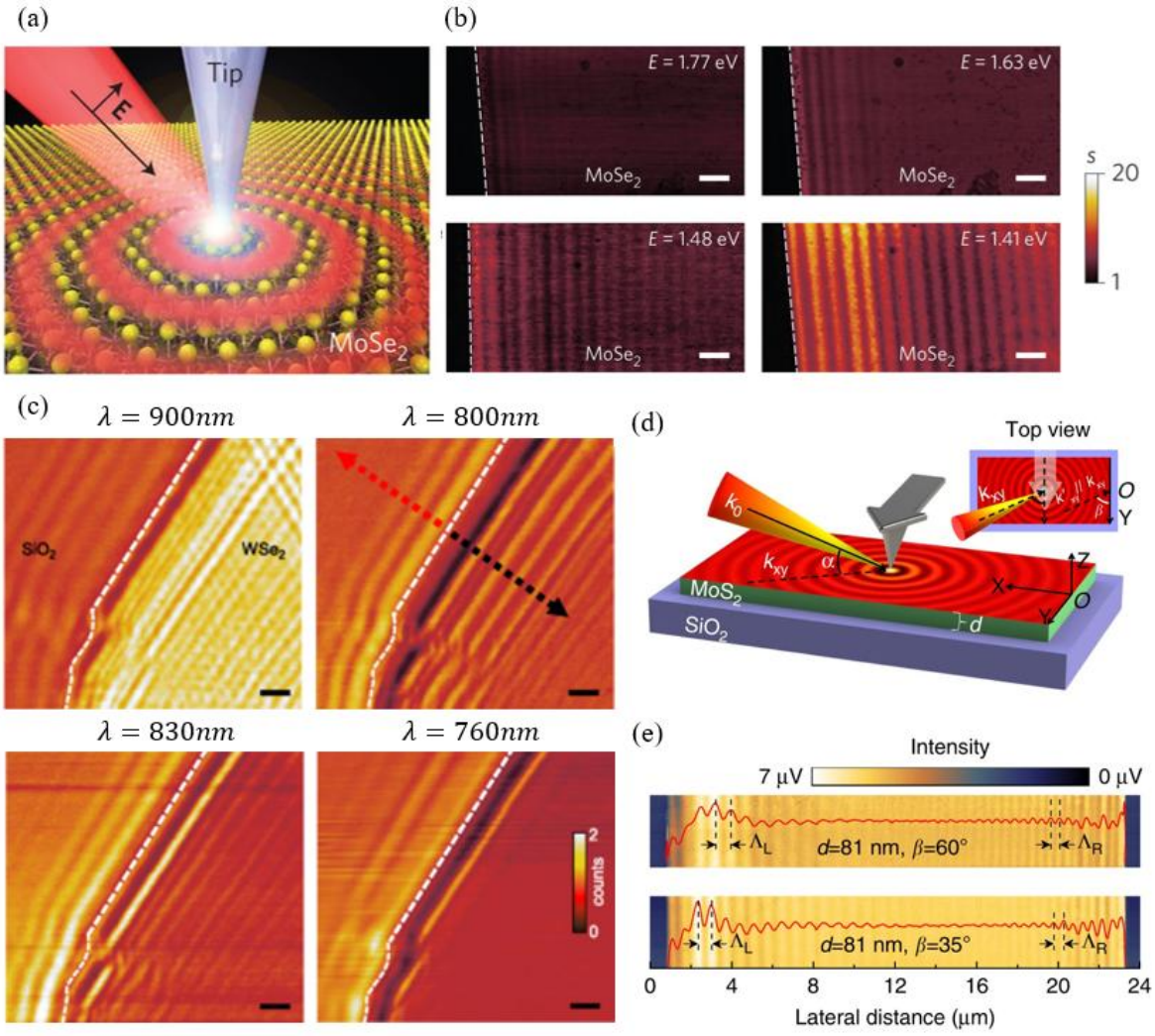


Figure 1.7 | Guided mode EPs in TMDCs. a, Schematic of concentric waveguide modes in $MoSe_2$ excited by a laser-illuminated s-SNOM tip. **b,** Corresponding s-SNOM images of a 156 nm thick $MoSe_2$ planar waveguide recorded at different excitation energies.[32]. **c,** Guided EPs in 260 nm thick WSe_2. Selected near-field images recorded at different excitation wavelengths.[65]. **d,** Schematic of the guided Eps on MoS_2 characterized by a s-SNOM setup. **e,** Near-field images and fringe profiles of an 81-nm-thick MoS2 sample. [70]

Surface related Polaritonic guided modes in plasmonic and phononic systems, such as SPPs and SPhPs, arise near resonances where the real part of the permittivity becomes negative[9]. These effects are well understood and widely observed across different materials[9,10]. In contrast, surface or guided EPs, although predicted theoretically[71], have not yet been experimentally demonstrated in natural materials. The idea of guided EPs in monolayer TMDCs originates from earlier studies on graphene, where Sergey Mikhailov and Karl Ziegler[72] showed that weakly confined TE modes can exist within a narrow spectral range where graphene's permittivity becomes positive. Building on this, Jacob Khurgin[73] proposed the possibility of a fundamental TE guided mode in monolayer TMDCs. While a few studies have discussed this concept in ultrathin layers, experimental realization of such guided modes remains elusive.

If guided exciton polaritons could be realized in monolayer TMDCs, they would open the door to a wide range of new device possibilities. For example, valley-selective polariton waveguides could make it possible to build on-chip valleytronic circuits, where information is carried not by charge alone but by the valley degree of freedom and directed using valley-dependent optical selection rules. In the same spirit, topologically protected polariton edge states formed by the coupling of valley excitons with topological photonic modes could provide robust optical pathways resistant to backscattering, which would be highly attractive for reliable on-chip light transport and communication. Furthermore, the strong nonlinearities inherent to monolayer TMDCs, including second-harmonic generation, four-wave mixing, and saturable absorption could be enhanced by the increased light-matter interaction in guided polariton geometries, enabling compact nonlinear optical devices and quantum light sources.

1.3.3 Topological polaritons

The concept of topology in condensed matter physics emerged from the discovery of the quantum Hall effect and was later generalized to time-reversal-invariant systems through the theoretical prediction of topological insulators[74,75]. Topological insulators are materials that are insulating in the bulk but host conducting edge or surface states protected by the nontrivial topology of the bulk band structure[75,76]. The seminal work of Kane and Mele in 2005 introduced the concept of the quantum spin Hall effect in graphene[77], where spin-orbit coupling opens a topological gap and gives rise to helical edge states. Shortly thereafter, Bernevig, Hughes, and Zhang predicted the quantum spin Hall effect in HgTe/CdTe quantum wells, a prediction that was experimentally confirmed and established the field of topological insulators[78]. The central idea is that the topology of the bulk bands, described by quantities such as the Chern number

or the Z_2 index, governs whether edge states can exist and what properties they will have[74-76]. These edge states are especially important because they can remain stable even in the presence of disorder or imperfections, as long as the relevant underlying symmetries are preserved.

The transfer of topological ideas from electronic systems into photonics began with the landmark work of Haldane and Raghu in 2008, who proposed a photonic version of the quantum Hall effect in a two-dimensional photonic crystal with broken time-reversal symmetry[79]. They showed that by introducing a periodic refractive index structure together with an effective magnetic field, photonic bands could acquire nontrivial topology and support one way edge states that are immune to backscattering. This prediction was soon followed by experimental demonstrations, most notably the observation of topological photonic edge states in a microwave photonic crystal (Figure 1.8a) containing gyromagnetic elements[80]. Together, these studies laid the foundation for topological photonics and showed that the ideas of topological band theory are not limited to electronic matter, but can also be applied to classical waves, opening up new possibilities for robust waveguiding, lasing, and quantum photonic functionalities.

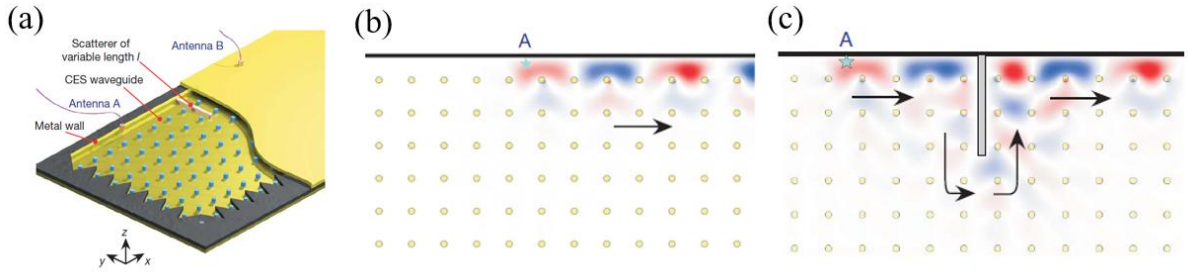


Figure 1.8 | Topological Photonics. a, Schematic of a gyromagnetic photonic-crystal waveguide. **b,** Simulated E_z field at 4.5 GHz shows unidirectional propagation. **c,** when a large obstacle is introduced, transmission remains unaffected, routing around the scatterer without backscattering[80].

The extension of topological concepts to polaritons hybrid light-matter quasiparticles introduces additional richness and complexity. Early theoretical work in this area mainly looked at creating topological polaritons by breaking time-reversal symmetry, usually through external magnetic fields or magneto-optical effects, so that nontrivial band topology could emerge. This opened up an entirely new setting in which topology and strong light-matter coupling could act together, making it possible to realize optical states that are not only robust but also highly tunable, and that would not normally appear in systems that are purely photonic or purely material. Karzig et al.[81] in 2015 proposed a scheme for realizing topological

polaritons in EP systems by applying a magnetic field to lift the spin degeneracy and to induce a synthetic gauge field, thereby opening a topological gap with nontrivial Chern number.

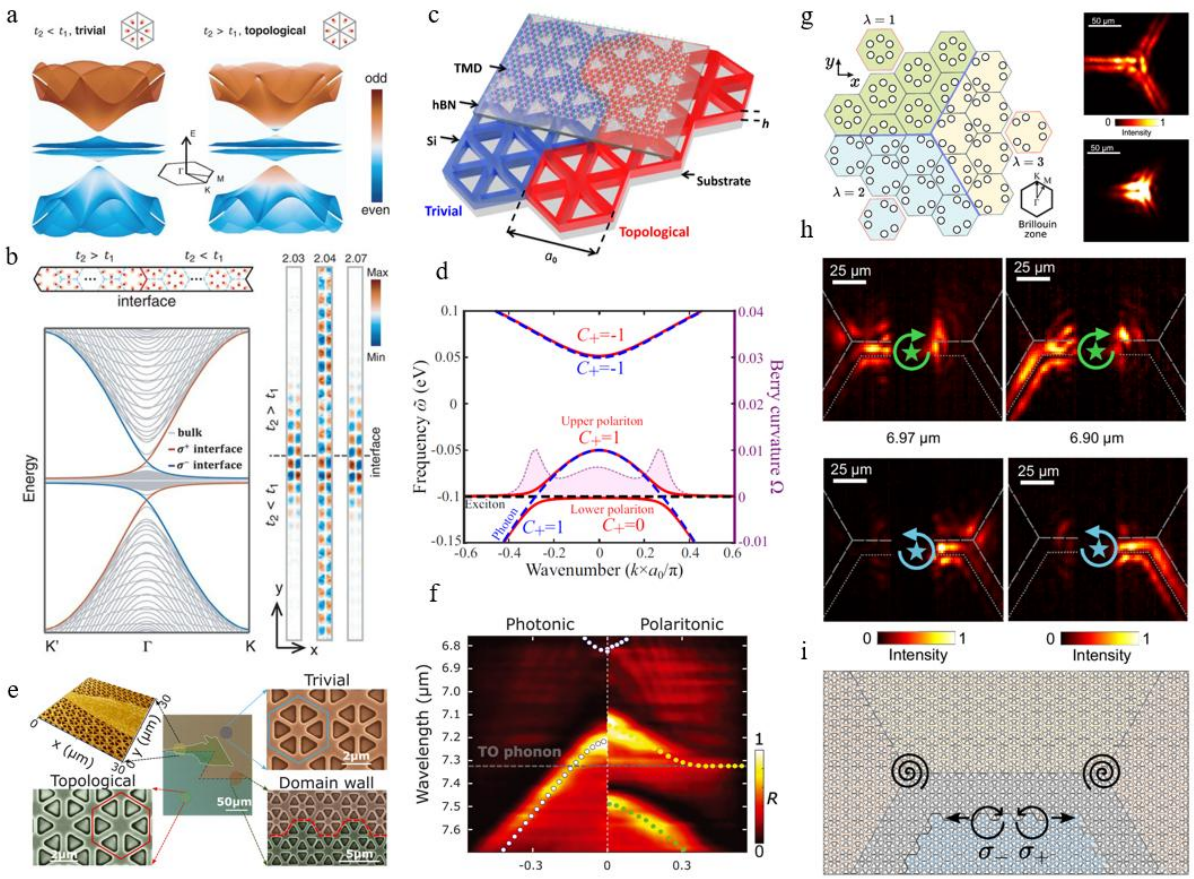


Figure 1.9 | Topological exciton and phonon Polaritons. a, calculated band structure for the helical topological polariton realized through coupling a monolayer WS_2 to a hexagonal photonic crystal. b, Helical topological interface polariton states at a zigzag domain wall between two polaritonic crystals with distinct topologies. [82] **c,** Schematic of the topological metasurface incorporating an hBN spacer with a $MoSe_2$ monolayer on top. **d,** alculated bulk band structure for a single (pseudo-)spin, shown without exciton–photon coupling (blue dashed) and with coupling q_d included (red solid).[83] e, SEM image of the metasurface showing trivial (orange) and topological (green) domains separated by an armchair-shaped domain wall. Insets display AFM images of hBN-covered regions, highlighting the domains and interface. f, Fourier tomogram slices reveal frequency bands along the x direction, comparing photonic (no hBN) and polaritonic (with hBN) responses. [84] g, Schematic of a topological point defect formed by stitching domains with three distinct unit cell configurations, with corresponding real-space field images showing confinement along line and point defects. h, Experimental real-space intensity distributions at on- and off-resonance wavelengths of the higher-order

topological (HOT) point defect under right- and left-circularly polarized excitation. i, Top view of the trapezoidal structure composed of interconnected line defects and zigzag domain walls[85].

Subsequent developments found a more practical way forward by removing the need for external magnetic fields altogether. Instead, nontrivial topological behaviour can emerge simply through the way the photonic structure is designed. By deliberately breaking certain spatial symmetries and carefully controlling the geometry, coupling, and material composition, systems such as photonic crystals and metasurfaces can develop topological band structures without relying on external magnetic fields. In this sense, the topology is built directly into the structure itself through design (Figure 1.9).

A landmark experimental demonstration Liu et al.[82] demonstrated that coupling a monolayer WS_2 to a hexagonal photonic crystal can realize a quantum spin Hall-like system, supporting helical topological polaritons observable up to 200 K (Figure 1.9 a, b). Importantly, these states can be tuned via temperature and external fields, offering a highly flexible platform for exploring tunable topological phases beyond conventional condensed matter systems. In a similar direction Li et al. in 2021, realized Z_2 topological exciton polaritons in a TMDC coupled photonic metasurface[83]. By combining monolayer WSe_2 with a photonic metasurface engineered to support a topological band structure, they were able to observe spin-polarized polariton edge states forming at the interface between two topologically different regions of the metasurface (Figure 1.9 c,d). These edge states travelled in only one direction and remained stable even when disorder was present, providing clear evidence of their topological protection.

A similar strategy has also been extended to phonon polaritonic systems using engineered photonic and metasurface platforms. Sriram Guddala et al.[84] demonstrated topological phonon polaritons in structured van der Waals materials, where tailored nano-resonator arrays enable robust, directional propagation of phonon polariton modes (Figure 1.9 e,f). More recently, this concept has been extended beyond propagating edge states to the realization of strongly localized topological modes. In particular, the study by Daria et.al[85] demonstrates the emergence of zero-dimensional (0D) topological defect states in phonon polaritonic systems, where the polaritonic energy is confined to spatially localized regions rather than propagating along one-dimensional interfaces (Figure 1.9 g-i). Together, these studies highlight that the combination of metasurfaces and photonic crystals provides a versatile route to extend topological protection beyond exciton polaritons to phonon-based platforms, opening new opportunities for low-loss, nanoscale light-matter control.

A common feature of these demonstrations is that the photonic structure is pre-designed to have nontrivial topology, and the material excitations (excitons, phonons) are then coupled to this topological photonic environment. The photonic system whether a metasurface, photonic crystal, or waveguide array possesses a trivial region and a nontrivial region, with an interface that generates topological edge states. The role of the material excitation is to hybridize with the photonic modes, thereby transferring the topological character to the polariton bands[82-84]. While this approach has proven highly successful, it requires precise nanofabrication of the photonic structure and offers limited tunability once the device is fabricated.

This thesis introduces a fundamentally different paradigm which is interaction-driven topological polaritons in a completely trivial photonic system. In this approach, the photonic structure itself is topologically trivial it consists of two domains with trivial photonic band structures and no intrinsic topological invariants. However, when the photonic system is coupled to a material excitation (e.g., excitons in a TMDC monolayer) the strong light-matter interaction converting the trivial photonic bands into nontrivial polariton bands in one domain as designed. The interface between the trivial and nontrivial domains in the coupled system then hosts topological edge states, not because of pre-engineered photonic topology, but because the interaction itself induces the topology.

The advantages of interaction-driven topological polaritons are manifold. First, topology is not pre-engineered but emerges from the coupling, meaning that the same photonic structure can be reconfigured to exhibit different topological phases by tuning the material properties or the coupling strength. Second, dynamic tunability becomes possible whereby applying external stimuli such as strain, electrostatic gating, or optical pumping, one can modulate the exciton resonance energy, oscillator strength, or spatial distribution, thereby controlling the topological phase in real time.

The realization of interaction-driven topological polaritons in van der Waals materials represent an exciting new direction in topological photonics, with strong potential for applications such as robust on-chip optical communication, topologically protected lasing, and quantum information processing. By showing that topological behaviour can emerge purely from light-matter interactions, even in photonic systems that are otherwise topologically trivial, this thesis points to a new way of designing tunable and reconfigurable topological devices. In doing so, it highlights how the unique properties of two-dimensional materials and hybrid photonic platforms can be used to create new opportunities for future photonic technologies.

1.4 Nonlinear light-matter interactions in Nanophotonics

Nonlinear optical processes, in which the optical response of a material depends nonlinearly on the intensity of the incident light, are central to modern photonics, enabling functionalities that are impossible in the linear regime. Among the most important nonlinear processes are second-harmonic generation[86,87] (SHG), in which two photons at a fundamental frequency are converted into a single photon at twice the frequency, and spontaneous parametric down-conversion[88,89] (SPDC), in which a single pump photon spontaneously splits into a pair of lower-energy photons (signal and idler). SHG is widely used to convert light into new frequency ranges that are difficult to reach directly with conventional lasers[90], and it also plays an important role in the characterization of ultrafast optical pulses[91]. SPDC, on the other hand, is a central process in quantum optics and is commonly used to produce entangled photon pairs[92,93] for applications in quantum communication, quantum computing, and fundamental quantum studies.

Despite their importance, nonlinear optical processes are difficult to implement in compact photonic systems. A key limitation is the weak nonlinear response of most materials[94]. Since the efficiency of second-order processes depends on $\chi^{(2)}$ and the square of the optical intensity, significant conversion typically requires long interaction lengths[87] (millimetres to centimetres), which is incompatible with chip-scale devices operating at micrometre scales. In addition, materials with strong nonlinearities, such as lithium niobate[95] and KTP, are challenging to integrate with platforms like silicon due to material and fabrication mismatches[96].

A second major challenge is phase matching, where the interacting waves must remain in phase as they propagate. In dispersive materials, different refractive indices at different frequencies cause phase mismatch, limiting conversion efficiency over short coherence lengths[97]. In bulk systems, phase matching can often be achieved through well-established methods such as birefringence[98], temperature tuning, or periodic poling[99]. In nanophotonic structures, however, this becomes much more challenging because strong optical confinement and geometry-dependent dispersion make the phase-matching condition highly sensitive to the device design. As a result, the waveguide geometry and material platform must be engineered with great precision

1.5 2D materials and anisotropic platforms for nonlinear optics

Monolayer TMDCs possess a unique combination of properties that make them exceptionally attractive for nonlinear optics and valleytronics[100-102]. The broken inversion symmetry in

monolayer TMDCs, combined with strong spin-orbit coupling, leads to the formation of two inequivalent valleys in the Brillouin zone labeled K and K′ where the conduction and valence band extrema are located. These valleys are related by time-reversal symmetry but are not equivalent under spatial inversion, resulting in valley-contrasting physical properties such as Berry curvature, orbital magnetic moment, and optical selection rules[103]. The valley-selective optical selection rules in monolayer TMDCs are among their most remarkable features. Due to the combination of broken inversion symmetry and strong spin-orbit coupling, excitons in the K valley couple selectively to right-circularly polarized (σ^+) light, while excitons in the K′ valley couple to left-circularly polarized (σ^-) light.

While monolayer TMDCs exhibit strong excitonic resonances and valley-selective optical properties, their second-order nonlinear susceptibility $\chi^{(2)}$ is limited by the atomic-scale thickness and the relatively weak oscillator strength of the exciton transition. To overcome this limitation, researchers have turned to 3R-phase (rhombohedral) TMDCs[104], where non-centrosymmetric stacking of multiple layers breaks inversion symmetry across the entire multilayer structure, enabling a bulk-like second-order nonlinearity. In 3R-stacked TMDCs[87,105], each layer contributes coherently to the nonlinear response, resulting in a $\chi^{(2)}$ that scales with the number of layers and can exceed that of monolayers by several orders of magnitude. Additionally stacking these materials with twist angles can boost the nonlinear response due to the quasi-phase matching[106].

1.6 Metasurfaces and waveguide integration

Metasurfaces, composed of subwavelength resonators, enable compact control of light's amplitude, phase, and polarization by introducing abrupt phase shifts at the nanoscale. This allows a wide range of planar optical functionalities, including beam shaping[107], focusing, and nonlinear frequency conversion. In nonlinear optics[108], they offer key advantages such as precise control of emission direction through phase engineering, enhancement of second-order nonlinear processes via symmetry breaking in otherwise centrosymmetric systems and strong local field enhancement that significantly boosts nonlinear conversion efficiency.

Meta-waveguides combine metasurfaces and waveguides into a single platform, enabling simultaneous control of phase, polarization, and emission direction while preserving strong confinement and long interaction lengths. This approach addresses a key challenge in nonlinear photonics by allowing both generation and routing of chiral or valley-polarized photons within one integrated system. Recent approaches using 3R-TMDC waveguides combine counter-

propagating pumping ensuring momentum conservation and photonic band-edge enhancement to increase interaction time and improve conversion efficiency. However, realizing such meta-waveguide platforms requires overcoming challenges in fabrication, including precise alignment, low-damage patterning, and high-quality interfaces to reduce losses. Despite these challenges, meta-waveguides offer a promising route toward compact and efficient nonlinear photonic devices by combining metasurface-based phase control and field enhancement with waveguide-based confinement and routing, enabling integrated light sources, frequency converters, and quantum photon-pair generators

1.7 Thesis outline and scope

This thesis centres on developing new methods to engineer guided polaritons and nonlinear light-matter interactions in van der Waals materials and hybrid photonic structures, with the broader goal of supporting future on-chip photonic and optoelectronic technologies. To address this aim in a clear and structured way, the thesis is organized into seven chapters that move progressively from fundamental concepts and theoretical understanding to experimental realization and device-oriented demonstrations. In doing so, it covers both the linear polaritonic and nonlinear optical regimes, while throughout focusing on the key challenges and opportunities associated with nanoscale light control.

Chapter 2 presents the experimental methods and describes the fabrication techniques used to prepare the samples and device structures, as well as the optical characterization tools used to probe their behaviour. Particular emphasis is placed on scattering-type scanning near-field optical microscopy (s-SNOM), which enables real-space imaging of polaritons at the nanoscale. In addition, the chapter introduces the spectroscopic methods employed to investigate excitonic resonances, polariton dispersion, and nonlinear optical responses.

Chapter 3 focuses on how g-HPs can be excited selectively and steered in chosen directions through antenna design. By using asymmetric triangular gold antennas with carefully tuned apex angles and orientations, the study shows that both the propagation direction and the modal content of g-HPs in calcite can be controlled through engineering the nano/microstructure used to excite the PhPs. Near-field optical microscopy and infrared spectroscopy are then used to directly visualize the launched polariton fields. These experimental results are further supported by numerical simulations, which help explain the observed behaviour and provide practical design rules for controlled g-HP excitation.

Chapter 4 presents the first direct real-space experimental observation of guided exciton-polariton propagation in a free-standing single-monolayer WSe_2 waveguide, extending earlier studies of propagating exciton polaritons in multilayer and few-layer TMDC structures. By suspending monolayer WSe_2 on a pre patterned substrate realized guided mode EPs, thereby overcoming the modal cutoff that normally prevents guided modes in the monolayer limit. Near-field optical microscopy directly reveals the guided modes, including the characteristic anticrossing between the excitonic resonance and the waveguide dispersion. The study also examines the confinement, propagation behaviour, and loss mechanisms of these modes in detail, with numerical simulations supporting and clarifying the experimental observations.

Chapter 5 explores interaction-induced topological polaritons, demonstrating how non-trivial topology can emerge through strong light-matter coupling between initially trivial photonic and material subsystems. Theoretical analysis shows that sufficiently strong coupling can induce band inversion and open a topological band gap, supporting an interface-localised hybrid polaritonic edge state. Near-field optical microscopy and frequency-dependent measurements experimentally reveal pronounced field localisation at the interface, supported by spatial-decay analysis and control measurements on the uncoupled silicon grating. Theoretical investigations further examine the effects of dissipation and suggest potential routes for dynamically tuning the topological phase through mechanical strain or electrostatic gating. These findings establish an interaction-driven approach to engineering topological polaritonic states and provide a foundation for future reconfigurable photonic devices.

Chapter 6 introduces a meta-waveguide platform designed for valley-selective second-harmonic generation (SHG) and chiral photon routing in TMDC-based systems. In this approach, a non-centrosymmetric 3R-phase TMDC metasurface is integrated directly with a dielectric waveguide, forming a unified structure in which nonlinear light generation and optical routing occur simultaneously. In this system, circularly polarized excitation selectively excites valley states in the TMDC, leading to helicity-dependent second-harmonic generation mediated by the material's nonlinear response. The generated signal is then directionally coupled into guided modes of the waveguide through a metasurface-imposed geometric phase gradient. This demonstrates an integrated platform for generating and guiding chiral photons, with potential for compact valley-multiplexed photonic circuits. The chapter also covers device design, fabrication, and experimental characterization.

References

1. Wang, T., Li, P., Chigrin, D. N., Giles, A. J., Bezares, F. J., Glembocki, O. J., Caldwell, J. D., & Taubner, T.(s). Phonon-polaritonic bowtie nanoantennas: controlling infrared thermal radiation at the nanoscale. Acs Photonics 2017, 4 (7), 1753-1760.

2. Gubbin, C. R., De Liberato, S., & Folland, T. G.(s). Surface phonon polaritons for infrared optoelectronics. Journal of applied physics 2022, 131 (3),

3. Wu, Y., Duan, J., Ma, W., Ou, Q., Li, P., Alonso-González, P., Caldwell, J. D., & Bao, Q.(s). Manipulating polaritons at the extreme scale in van der Waals materials. Nature Reviews Physics 2022, 4 (9), 578-594.

4. Ling, H., Nourbakhsh, M., Whiteside, V. R., Tischler, J. G., & Davoyan, A. R.(s). Near-unity light–matter interaction in mid-infrared van der waals metasurfaces. Nano Letters 2024, 24 (11), 3315-3322.

5. Derrien, T. J., Krüger, J., & Bonse, J.(s). Properties of surface plasmon polaritons on lossy materials: Lifetimes, periods and excitation conditions. Journal of Optics 2016, 18 (11), 115007.

6. Ibbotson, L. A., Demetriadou, A., Croxall, S., Hess, O., & Baumberg, J. J.(s). Optical nano-woodpiles: large-area metallic photonic crystals and metamaterials. Scientific Reports 2015, 5 (1), 8313.

7. Urbonas, D., Mahrt, R. F., & Stöferle, T.(s). Low-loss optical waveguides made with a high-loss material. Light: science & applications 2021, 10 (1), 15.

8. Wang, Z., Yang, Z., Wang, H., Zhang, W., Wang, R., & Xu, P.(s). High-Q chalcogenide racetrack resonators based on the multimode waveguide. Applied Optics 2023, 62 (9), 2278-2282.

9. Basov, D., Fogler, M., & García de Abajo, F.(s). Polaritons in van der Waals materials. Science 2016, 354 (6309), aag1992.

10. Galiffi, E., Carini, G., Ni, X., Álvarez-Pérez, G., Yves, S., Renzi, E. M., Nolen, R., Wasserroth, S., Wolf, M., & Alonso-Gonzalez, P.(s). Extreme light confinement and control in low-symmetry phonon-polaritonic crystals. Nature Reviews Materials 2024, 9 (1), 9-28.

11. Xiong, C., Pernice, W. H., Li, M., & Tang, H. X.(s). High performance nanophotonic circuits based on partially buried horizontal slot waveguides. Optics Express 2010, 18 (20), 20690-20698.

12. Zhuang, L., Marpaung, D., Burla, M., Beeker, W., Leinse, A., & Roeloffzen, C.(s). Low-loss, high-index-contrast Si3N4/SiO2 optical waveguides for optical delay lines in microwave photonics signal processing. Optics Express 2011, 19 (23), 23162-23170.

13. Chen, S., Fu, C., & Hu, G.(s). Phonon-polariton-mediated configurable radiative thermal router. Acs Photonics 2024, 12 (1), 271-281.

14. Li, D., Pan, Z., & Caldwell, J. D.(s). Phonon polariton-mediated heat conduction: Perspectives from recent progress. Journal of Materials Research 2024, 1-9.

15. Butt, M. A., Juchniewicz, M., Słowikowski, M., Kozłowski, Ł., & Piramidowicz, R.(s). Mid-infrared photonic sensors: exploring fundamentals, advanced materials, and cutting-edge applications. Sensors 2025, 25 (4), 1102.

16. Zhou, H., Li, D., & Lee, C.(s). Technology landscape review of in-sensor photonic intelligence: from optical sensors to smart devices. AI Sensors 2025, 1 (1), 5.

17. Xia, L., Liu, Y., Chen, R. T., Weng, B., & Zou, Y.(s). Advancements in miniaturized infrared spectroscopic-based volatile organic compound sensors: A systematic review. Applied Physics Reviews 2024, 11 (3),

18. Esmann, M., Wein, S. C., & Antón-Solanas, C.(s). Solid-state single-photon sources: recent advances for novel quantum materials. Advanced Functional Materials 2024, 34 (30), 2315936.

19. Gupta, S., Wu, W., Huang, S., & Yakobson, B. I.(s). Single-photon emission from two-dimensional materials, to a brighter future. The journal of physical chemistry letters 2023, 14 (13), 3274-3284.

20. Karabchevsky, A., Katiyi, A., Ang, A. S., & Hazan, A.(s). On-chip nanophotonics and future challenges. Nanophotonics 2020, 9 (12), 3733-3753.

21. Li, Z., Xu, B., Liang, D., & Pan, A.(s). Polarization-dependent optical properties and optoelectronic devices of 2D materials. Research 2020,

22. Hertzog, M., Wang, M., Mony, J., & Börjesson, K.(s). Strong light–matter interactions: a new direction within chemistry. Chemical Society Reviews 2019, 48 (3), 937-961.

23. Guo, X., Lyu, W., Chen, T., Luo, Y., Wu, C., Yang, B., Sun, Z., García de Abajo, F. J., Yang, X., & Dai, Q.(s). Polaritons in van der Waals heterostructures. Advanced Materials 2023, 35 (17), 2201856.

24. In, C., Kim, U. J., & Choi, H.(s). Two-dimensional Dirac plasmon-polaritons in graphene, 3D topological insulator and hybrid systems. Light: science & applications 2022, 11 (1), 313.

25. Hu, G., Shen, J., Qiu, C. W., Alù, A., & Dai, S.(s). Phonon polaritons and hyperbolic response in van der Waals materials. Advanced Optical Materials 2020, 8 (5), 1901393.

26. Dai, S., Fei, Z., Ma, Q., Rodin, A., Wagner, M., McLeod, A., Liu, M., Gannett, W., Regan, W., & Watanabe, K.(s). Tunable phonon polaritons in atomically thin van der Waals crystals of boron nitride. Science 2014, 343 (6175), 1125-1129.

27. Chen, M., Lin, X., Dinh, T. H., Zheng, Z., Shen, J., Ma, Q., Chen, H., Jarillo-Herrero, P., & Dai, S.(s). Configurable phonon polaritons in twisted α-MoO3. Nature materials 2020, 19 (12), 1307-1311.

28. Ni, G., McLeod, A. S., Sun, Z., Matson, J. R., Lo, C. F. B., Rhodes, D. A., Ruta, F. L., Moore, S. L., Vitalone, R. A., & Cusco, R.(s). Long-lived phonon polaritons in hyperbolic materials. Nano Letters 2021, 21 (13), 5767-5773.

29. Flatten, L. C., He, Z., Coles, D. M., Trichet, A. A., Powell, A. W., Taylor, R. A., Warner, J. H., & Smith, J. M.(s). Room-temperature exciton-polaritons with two-dimensional WS2. Scientific Reports 2016, 6 (1), 33134.

30. Hu, F., Luan, Y., Speltz, J., Zhong, D., Liu, C., Yan, J., Mandrus, D., Xu, X., & Fei, Z.(s). Imaging propagative exciton polaritons in atomically thin WSe 2 waveguides. Physical Review B 2019, 100 (12), 121301.

31. Kusch, P., Mueller, N. S., Hartmann, M. T., & Reich, S.(s). Strong light-matter coupling in MoS 2. Physical Review B 2021, 103 (23), 235409.

32. Hu, F., Luan, Y., Scott, M., Yan, J., Mandrus, D., Xu, X., & Fei, Z.(s). Imaging exciton–polariton transport in MoSe2 waveguides. Nature Photonics 2017, 11 (6), 356-360.

33. Berkowitz, M. E., Kim, B. S., Ni, G., McLeod, A. S., Lo, C. F. B., Sun, Z., Gu, G., Watanabe, K., Taniguchi, T., & Millis, A. J.(s). Hyperbolic cooper-pair polaritons in planar graphene/cuprate plasmonic cavities. Nano Letters 2020, 21 (1), 308-316.

34. Zhang, D., Luo, X.-Q., Wang, Y.-P., Li, T.-F., & You, J.(s). Observation of the exceptional point in cavity magnon-polaritons. Nature communications 2017, 8 (1), 1368.

35. Kazantsev, D. V.(s). Phonon-polariton waves on the surface of SiC crystal. Journal of Experimental and Theoretical Physics Letters 2006, 83 (8), 323-326.

36. Yoxall, E., Schnell, M., Nikitin, A. Y., Txoperena, O., Woessner, A., Lundeberg, M. B., Casanova, F., Hueso, L. E., Koppens, F. H., & Hillenbrand, R.(s). Direct observation of ultraslow hyperbolic polariton propagation with negative phase velocity. Nature Photonics 2015, 9 (10), 674-678.

37. Li, P., Lewin, M., Kretinin, A. V., Caldwell, J. D., Novoselov, K. S., Taniguchi, T., Watanabe, K., Gaussmann, F., & Taubner, T.(s). Hyperbolic phonon-polaritons in boron nitride for near-field optical imaging and focusing. Nature communications 2015, 6 (1), 7507.

38. Dai, S., Tymchenko, M., Yang, Y., Ma, Q., Pita-Vidal, M., Watanabe, K., Taniguchi, T., Jarillo-Herrero, P., Fogler, M. M., & Alù, A.(s). Manipulation and steering of hyperbolic surface polaritons in hexagonal boron nitride. Advanced Materials 2018, 30 (16), 1706358.

39. Ma, W., Hu, G., Hu, D., Chen, R., Sun, T., Zhang, X., Dai, Q., Zeng, Y., Alù, A., & Qiu, C.-W.(s). Ghost hyperbolic surface polaritons in bulk anisotropic crystals. Nature 2021, 596 (7872), 362-366.

40. Caldwell, J. D., Kretinin, A. V., Chen, Y., Giannini, V., Fogler, M. M., Francescato, Y., Ellis, C. T., Tischler, J. G., Woods, C. R., & Giles, A. J.(s). Sub-diffractional volume-confined polaritons in the natural hyperbolic material hexagonal boron nitride. Nature communications 2014, 5 (1), 5221.

41. Narimanov, E.(s). Ghost resonance in anisotropic materials: negative refractive index and evanescent field enhancement in lossless media. Advanced Photonics 2019, 1 (4), 046003-046003.

42. Dai, S., Ma, Q., Andersen, T., Mcleod, A., Fei, Z., Liu, M., Wagner, M., Watanabe, K., Taniguchi, T., & Thiemens, M.(s). Subdiffractional focusing and guiding of polaritonic rays in a natural hyperbolic material. Nature communications 2015, 6 (1), 6963.

43. Bylinkin, A., Schnell, M., Autore, M., Calavalle, F., Li, P., Taboada-Gutièrrez, J., Liu, S., Edgar, J. H., Casanova, F., & Hueso, L. E.(s). Real-space observation of vibrational strong coupling between propagating phonon polaritons and organic molecules. Nature Photonics 2021, 15 (3), 197-202.

44. Alfaro-Mozaz, F., Alonso-González, P., Vélez, S., Dolado, I., Autore, M., Mastel, S., Casanova, F., Hueso, L., Li, P., & Nikitin, A. Y.(s). Nanoimaging of resonating hyperbolic polaritons in linear boron nitride antennas. Nature communications 2017, 8 (1), 15624.

45. Liu, J. F., Wu, J. W., Fu, X., Zhang, H. C., Tang, W., & Cui, T. J.(s). Spin-controlled reconfigurable excitations of spoof surface plasmon polaritons by a compact structure. Laser & Photonics Reviews 2023, 17 (1), 2200257.

46. Zhang, Q., Ou, Q., Si, G., Hu, G., Dong, S., Chen, Y., Ni, J., Zhao, C., Fuhrer, M. S., & Yang, Y.(s). Unidirectionally excited phonon polaritons in high-symmetry orthorhombic crystals. Science advances 2022, 8 (30), eabn9774.

47. Duan, J., Álvarez-Pérez, G., Voronin, K. V., Prieto, I., Taboada-Gutiérrez, J., Volkov, V. S., Martín-Sánchez, J., Nikitin, A. Y., & Alonso-González, P.(s). Enabling propagation of anisotropic polaritons along forbidden directions via a topological transition. Science advances 2021, 7 (14), eabf2690.

48. Hu, G., Ou, Q., Si, G., Wu, Y., Wu, J., Dai, Z., Krasnok, A., Mazor, Y., Zhang, Q., & Bao, Q.(s). Topological polaritons and photonic magic angles in twisted α-MoO3 bilayers. Nature 2020, 582 (7811), 209-213.

49. Passler, N. C., Ni, X., Hu, G., Matson, J. R., Carini, G., Wolf, M., Schubert, M., Alù, A., Caldwell, J. D., & Folland, T. G.(s). Hyperbolic shear polaritons in low-symmetry crystals. Nature 2022, 602 (7898), 595-600.

50. Hu, C., Sun, T., Zeng, Y., Ma, W., Dai, Z., Yang, X., Zhang, X., & Li, P.(s). Source-configured symmetry-broken hyperbolic polaritons. Elight 2023, 3 (1), 14.

51. Matson, J., Wasserroth, S., Ni, X., Obst, M., Diaz-Granados, K., Carini, G., Renzi, E. M., Galiffi, E., Folland, T. G., & Eng, L. M.(s). Controlling the propagation asymmetry of hyperbolic shear polaritons in beta-gallium oxide. Nature communications 2023, 14 (1), 5240.

52. Lv, J., Wu, Y., Liu, J., Gong, Y., Si, G., Hu, G., Zhang, Q., Zhang, Y., Tang, J.-X., & Fuhrer, M. S.(s). Hyperbolic polaritonic crystals with configurable low-symmetry Bloch modes. Nature communications 2023, 14 (1), 3894.

53. Jia, G., Luo, J., Wang, H., Ma, Q., Liu, Q., Dai, H., & Asgari, R.(s). Two-dimensional natural hyperbolic materials: from polaritons modulation to applications. Nanoscale 2022, 14 (46), 17096-17118.

54. Chen, S., Wu, X., & Fu, C.(s). Active tuning of anisotropic phonon polaritons in natural van der Waals crystals with negative permittivity substrates and its application in energy transport. Opto-Electronic Science 2024, 3 (6), 240002-240001-240002-240019.

55. Zhou, H., Ren, Z., Li, D., Xu, C., Mu, X., & Lee, C.(s). Dynamic construction of refractive index-dependent vibrations using surface plasmon-phonon polaritons. Nature communications 2023, 14 (1), 7316.

56. Datta, S., & Marie, X.(s). Excitons and excitonic materials. MRS Bulletin 2024, 49 (9), 852-861.

57. Chen, X., Lian, Z., Meng, Y., Ma, L., & Shi, S.-F.(s). Excitonic complexes in two-dimensional transition metal dichalcogenides. Nature communications 2023, 14 (1), 8233.

58. Sun, X., Zhu, Y., Qin, H., Liu, B., Tang, Y., Lü, T., Rahman, S., Yildirim, T., & Lu, Y.(s). Enhanced interactions of interlayer excitons in free-standing heterobilayers. Nature 2022, 610 (7932), 478-484.

59. Zhu, B., Chen, X., & Cui, X.(s). Exciton binding energy of monolayer WS2. Scientific Reports 2015, 5 (1), 9218.

60. Hansen, K. R., Colton, J. S., & Whittaker-Brooks, L.(s). Measuring the exciton binding energy: learning from a decade of measurements on halide perovskites and transition metal dichalcogenides. Advanced Optical Materials 2024, 12 (3), 2301659.

61. Weisbuch, C., Nishioka, M., Ishikawa, A., & Arakawa, Y.(s). Observation of the coupled exciton-photon mode splitting in a semiconductor quantum microcavity. Physical review letters 1992, 69 (23), 3314.

62. Dhara, S., Chakraborty, C., Goodfellow, K., Qiu, L., O'Loughlin, T., Wicks, G., Bhattacharjee, S., & Vamivakas, A.(s). Anomalous dispersion of microcavity trion-polaritons. Nature Physics 2018, 14 (2), 130-133.

63. Datta, B., Khatoniar, M., Deshmukh, P., Thouin, F., Bushati, R., De Liberato, S., Cohen, S. K., & Menon, V. M.(s). Highly nonlinear dipolar exciton-polaritons in bilayer MoS2. Nature communications 2022, 13 (1), 6341.

64. Chakraborty, C., Kinnischtzke, L., Goodfellow, K. M., Beams, R., & Vamivakas, A. N.(s). Voltage-controlled quantum light from an atomically thin semiconductor. Nature nanotechnology 2015, 10 (6), 507-511.

65. Fei, Z., Scott, M., Gosztola, D., Foley IV, J., Yan, J., Mandrus, D., Wen, H., Zhou, P., Zhang, D., & Sun, Y.(s). Nano-optical imaging of WS e 2 waveguide modes revealing light-exciton interactions. Physical Review B 2016, 94 (8), 081402.

66. Cho, H., Shin, D.-J., Sung, J., & Gong, S.-H.(s). Ultra-thin grating coupler for guided exciton-polaritons in WS2 multilayers. Nanophotonics 2023, 12 (13), 2563-2571.

67. Zhou, J., Huang, D., Wang, Y., Chen, Y., Xia, M., & Zhang, X.(s). Chiral absorption enhancement via critically coupled resonances in atomically thin photonic crystal exciton-polaritons. Optics Letters 2024, 49 (14), 3990-3993.

68. Lee, S. W., Lee, J. S., Choi, W. H., & Gong, S. H.(s). Ultrathin WS2 polariton waveguide for efficient light guiding. Advanced Optical Materials 2023, 11 (16), 2300069.

69. Kondratyev, V. I., Permyakov, D. V., Ivanova, T. V., Iorsh, I. V., Krizhanovskii, D. N., Skolnick, M. S., Kravtsov, V., & Samusev, A. K.(s). Probing and control of guided exciton–polaritons in a 2D semiconductor-integrated slab waveguide. Nano Letters 2023, 23 (17), 7876-7882.

70. Hu, D., Yang, X., Li, C., Liu, R., Yao, Z., Hu, H., Corder, S. N. G., Chen, J., Sun, Z., & Liu, M.(s). Probing optical anisotropy of nanometer-thin van der waals microcrystals by near-field imaging. Nature communications 2017, 8 (1), 1471.

71. Hu, F., & Fei, Z.(s). Recent progress on exciton polaritons in layered transition-metal dichalcogenides. Advanced Optical Materials 2020, 8 (5), 1901003.

72. Mikhailov, S. A., & Ziegler, K.(s). New electromagnetic mode in graphene. Physical review letters 2007, 99 (1), 016803.

73. Khurgin, J. B.(s). Two-dimensional exciton–polariton—light guiding by transition metal dichalcogenide monolayers. Optica 2015, 2 (8), 740-742.

74. Ozawa, T., Price, H. M., Amo, A., Goldman, N., Hafezi, M., Lu, L., Rechtsman, M. C., Schuster, D., Simon, J., & Zilberberg, O.(s). Topological photonics. Reviews of Modern Physics 2019, 91 (1), 015006.

75. Lu, L., Joannopoulos, J. D., & Soljačić, M.(s). Topological photonics. Nature Photonics 2014, 8 (11), 821-829.

76. Khanikaev, A. B., & Shvets, G.(s). Two-dimensional topological photonics. Nature Photonics 2017, 11 (12), 763-773.

77. Kane, C. L., & Mele, E. J.(s). Quantum spin Hall effect in graphene. Physical review letters 2005, 95 (22), 226801.

78. Bernevig, B. A., Hughes, T. L., & Zhang, S.-C.(s). Quantum spin Hall effect and topological phase transition in HgTe quantum wells. Science 2006, 314 (5806), 1757-1761.

79. Raghu, S., & Haldane, F. D. M.(s). Analogs of quantum-Hall-effect edge states in photonic crystals. Physical Review A—Atomic, Molecular, and Optical Physics 2008, 78 (3), 033834.

80. Wang, Z., Chong, Y., Joannopoulos, J. D., & Soljačić, M.(s). Observation of unidirectional backscattering-immune topological electromagnetic states. Nature 2009, 461 (7265), 772-775.

81. Karzig, T., Bardyn, C.-E., Lindner, N. H., & Refael, G.(s). Topological polaritons. Physical Review X 2015, 5 (3), 031001.

82. Liu, W., Ji, Z., Wang, Y., Modi, G., Hwang, M., Zheng, B., Sorger, V. J., Pan, A., & Agarwal, R.(s). Generation of helical topological exciton-polaritons. Science 2020, 370 (6516), 600-604.

83. Li, M., Sinev, I., Benimetskiy, F., Ivanova, T., Khestanova, E., Kiriushechkina, S., Vakulenko, A., Guddala, S., Skolnick, M., & Menon, V. M.(s). Experimental observation of topological Z2 exciton-polaritons in transition metal dichalcogenide monolayers. Nature communications 2021, 12 (1), 4425.

84. Guddala, S., Komissarenko, F., Kiriushechkina, S., Vakulenko, A., Li, M., Menon, V. M., Alù, A., & Khanikaev, A. B.(s). Topological phonon-polariton funneling in midinfrared metasurfaces. Science 2021, 374 (6564), 225-227.

85. Smirnova, D., Komissarenko, F., Vakulenko, A., Kiriushechkina, S., Smolina, E., Guddala, S., Allen, M., Allen, J., Alù, A., & Khanikaev, A. B.(s). Polaritonic states trapped by topological defects. Nature communications 2024, 15 (1), 6355.

86. Fu, Y., Liu, Z., Yue, S., Zhang, K., Wang, R., & Zhang, Z.(s). Optical second harmonic generation of low-dimensional semiconductor materials. Nanomaterials 2024, 14 (8), 662.

87. Huang, W., Xiao, Y., Xia, F., Chen, X., & Zhai, T.(s). Second harmonic generation control in 2D layered materials: status and outlook. Advanced Functional Materials 2024, 34 (16), 2310726.

88. Xuan, F., Lai, M., Wu, Y., & Quek, S. Y.(s). Exciton-enhanced spontaneous parametric down-conversion in two-dimensional crystals. Physical review letters 2024, 132 (24), 246902.

89. Kellner, J., Sabatti, A., Kuttner, T., Chapman, R. J., & Grange, R.(s). Counter-propagating spontaneous parametric down-conversion source in lithium niobate on insulator. Optica Quantum 2026, 4 (2), 100-107.

90. Liu, X., Hao, W., Yang, Z., Mao, M., & Tang, Y.(s). Ultra-broadband visible random laser generation via hybrid SHG and SFG processes. Journal of Lightwave Technology 2023, 42 (6), 2131-2136.

91. Dong, T., Zhang, S. J., & Wang, N. L.(s). Recent development of ultrafast optical characterizations for quantum materials. Advanced Materials 2023, 35 (27), 2110068.

92. Eshun, A., Varnavski, O., Villabona-Monsalve, J. P., Burdick, R. K., & Goodson III, T.(s). Entangled photon spectroscopy. Accounts of Chemical Research 2022, 55 (7), 991-1003.

93. Lu, Z., Janousek, J., Assad, S. M., Qiu, S., Joshi, M., Hu, Y., Song, A. Y., Wang, C., Suriyage, M., & Zhao, J.(s). Counter-propagating entangled photon pairs from monolayer GaSe. Nature communications 2025, 16 (1), 9616.

94. Xie, Z., Zhao, T., Yu, X., & Wang, J.(s). Nonlinear optical properties of 2D materials and their applications. Small 2024, 20 (34), 2311621.

95. Liu, X., Wu, Q., Lv, S., Sun, K., Song, Q., & Li, L.(s). Recent advances in lithium niobate photonics: processing, applications and perspective. Journal of Physics D: Applied Physics 2026, 59 (2), 023007.

96. Palici, A. M., Lu, X., Srinivasan, K., Lu, X., Labbe, F., Ding, Y., Laroque, H., Hamerly, R., Errando-Herranz, C., & Pu, M. (2024). Heterogeneous integration of lithium niobate and silicon photonics for nonlinear optics. CLEO: Applications and Technology,

97. Xu, X., Trovatello, C., Mooshammer, F., Shao, Y., Zhang, S., Yao, K., Basov, D. N., Cerullo, G., & Schuck, P. J.(s). Towards compact phase-matched and waveguided nonlinear optics in atomically layered semiconductors. Nature Photonics 2022, 16 (10), 698-706.

98. Song, X., Tang, Y., Ding, T., Ding, W., Qiu, J., Li, Z., Dai, J., Li, H., Liu, S., & Chen, X.(s). Broadband birefringence phase-matched second-harmonic generation in a slightly curved lithium niobate-on-insulator waveguide. Applied Optics 2026, 65 (5), 1511-1515.

99. Singh, U., Kumar, A., Dwivedi, P. P., Mishra, A., & Dixit, N.(s). Different phase matching schemes of terahertz wave generation using periodic poled lithium niobate for real-world applications. Physics Open 2025, 100357.

100. Wang, S.(s). Valley-dependent Berry phase effects and related valleytronic applications in two-dimensional materials. Modern Physics Letters B 2025, 39 (35), 2530002.

101. Soni, A., & Pal, S. K.(s). Valley degree of freedom in two-dimensional van der Waals materials. Journal of Physics D: Applied Physics 2022, 55 (30), 303003.

102. Li, C., Xing, K., Zhai, W., Sortino, L., Tittl, A., Aharonovich, I., Fuhrer, M. S., Watanabe, K., Taniguchi, T., & Ou, Q.(s). Valley optoelectronics based on meta-waveguide photodetectors. arXiv preprint arXiv:2503.19565 2025,

103. Herrmann, P., Klimmer, S., Lettau, T., Weickhardt, T., Papavasileiou, A., Mosina, K., Sofer, Z., Paradisanos, I., Kartashov, D., & Wilhelm, J.(s). Nonlinear valley selection rules and all-optical probe of broken time-reversal symmetry in monolayer WSe2. Nature Photonics 2025, 19 (3), 300-306.

104. Rajarapu, R., Barman, P. K., Biswal, B., Poudyal, S., Yadav, R., Deka, M., Rahman, W., Nayak, P. K., & Misra, A.(s). Robust valley quantum coherence in synthetic 3R-phase MoS2: A material for future valley based devices. Applied Physics Letters 2024, 124 (3),

105. Thomas, S., Moolayadukkam, S., & Priyanka, K. (2024). Structural, mechanical, and electronic properties of in-plane 1T/2H-MoS2, 2H-MoS2, and 3R-MoS2. In *Science and Technology of 2D MoS2* (pp. 55-64). Springer.

106. Tang, Y., Sripathy, K., Qin, H., Lu, Z., Guccione, G., Janousek, J., Zhu, Y., Hasan, M. M., Iwasa, Y., & Lam, P. K.(s). Quasi-phase-matching enabled by van der Waals stacking. Nature communications 2024, 15 (1), 9979.

107. Nielsen, K. E., Carlsen, M. A., Zambrana-Puyalto, X., & Raza, S.(s). Non-imaging metasurface design for collimated beam shaping. Optics Express 2023, 31 (23), 37861-37870.

108. Hu, G., Hong, X., Wang, K., Wu, J., Xu, H.-X., Zhao, W., Liu, W., Zhang, S., Garcia-Vidal, F., & Wang, B.(s). Coherent steering of nonlinear chiral valley photons with a synthetic Au–WS2 metasurface. Nature Photonics 2019, 13 (7), 467-472.

2. Experimental Techniques

2.1 Sample and Device fabrication

2.1.1 Mechanical Exfoliation, Dry transfer and physical stacking

Mechanical exfoliation is a widely used technique for obtaining thin and bulk TMDC flakes. This process is typically performed using either dry or wet exfoliating techniques. Dry exfoliation with Scotch tape yields high-quality flakes but provides limited control over flake size, thickness, and uniformity, and may leave adhesive residues[1]. Initially, this method was used to isolate graphene layers and later played a key role in advancing the field of 2D materials by enabling the study of monolayer and thin layer properties[2]. But still, this technique is difficult to scale and generally requires significant manual effort.

Because of the limitations of dry exfoliation, researchers have developed several wet exfoliation techniques, such as liquid phase exfoliation via intercalation or sonication[3]. While these techniques allow processing larger volumes of material, they also have drawbacks. Mostly, the chemical solvents leave residues or cause partial delamination. Then steps like sonication may break the flakes into smaller fragments. In addition, these methods often require controlled environments, higher temperatures, and longer processing times[4].

In this thesis, the dry exfoliation technique was employed throughout to obtain materials of varying thicknesses for transfer onto substrates and waveguides. The mechanical exfoliation and transfer process is illustrated in Figure 2.1. The procedure consists of repeatedly peeling adhesive tape from a bulk crystal to thin the material using scotch tape. Then the tape with the thinnest flakes is attached to a PDMS (Gel film) layer, and using a cotton bud, pressure is applied to transfer it to the PDMS layer. These flakes may be monolayers, thin layers or bulk flakes of the TMDC material. Suitable flakes on the gel film are identified using an optical microscope when we observe clear optical contrast and colour profiles. Then the thickness will be confirmed with optical measurement techniques such as phase-shifting interferometry (PSI), vertical scanning interferometry (VSI), Raman spectroscopy, and photoluminescence (PL). The selected flakes with the desired thickness are then transferred onto substrates and waveguides using a transfer stage. The PDMS layer is attached to a glass slide, which is then mounted to an x,y,z-controlled stage to properly align the flake with the markers on the substrate or sample. Then the flake will come into contact with the sample / substrate. Depending on the flake thickness and the substrate, based on experience, different heating temperatures and pressures

will be applied to assist the transferring process. Following transfer, the flakes are re-examined to confirm thickness using optical and topographical characterization methods, including atomic force microscopy (AFM) and a surface profiler.

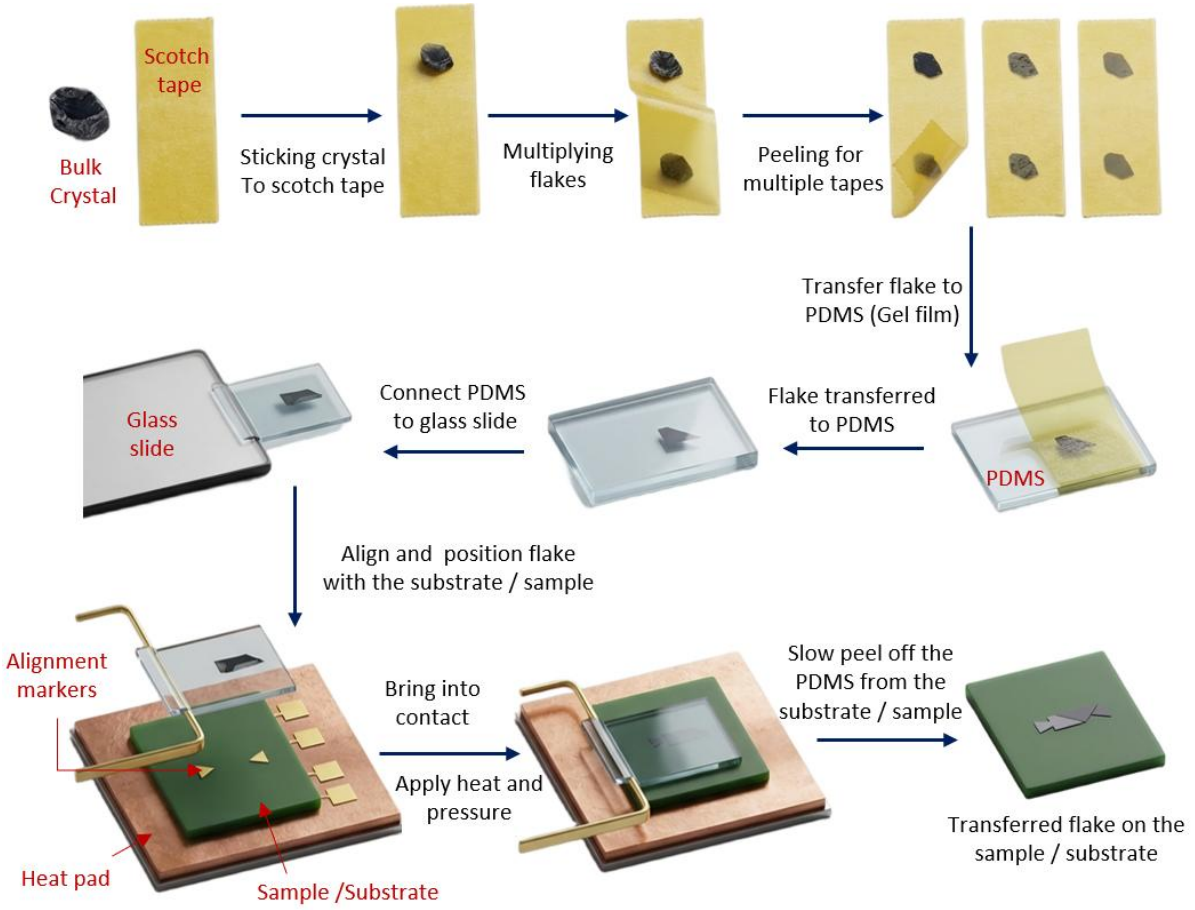


Figure 2.1 | Schematic of the mechanical exfoliation and dry transfer process. Thin flakes are exfoliated from a bulk crystal using Scotch tape, transferred onto a PDMS stamp, aligned with the target substrate, and then deposited onto the sample by controlled contact, heating, and slow PDMS peeling.

2.1.2 Electron Beam Lithography

In almost all project fabrication processes, photolithography or electron beam lithography (EBL) was used multiple times to fabricate different nano/microstructures. These processes were used to pattern nanostructures, metasurfaces, alignment marks, and metal masks for etching[5]. These are similar processes which only differ based on the exposing mechanism of the photoresist. As illustrated in Figure 2.2, samples will first be spin-coated with a suitable photoresist. For the works discussed in this thesis, multiple photoresists were used due to different requirements at different stages of fabrication. Mainly AZ MIR 701 and LOR 3A

photoresists were used for photolithography. ZEP and ARP photoresists were used for EBL processes. After spin coating the electron beam resist, with different spinning recipes to achieve different thicknesses the sample will be baked at 180 degrees Celsius for ZEP and at 150 degrees Celsius for ARP.

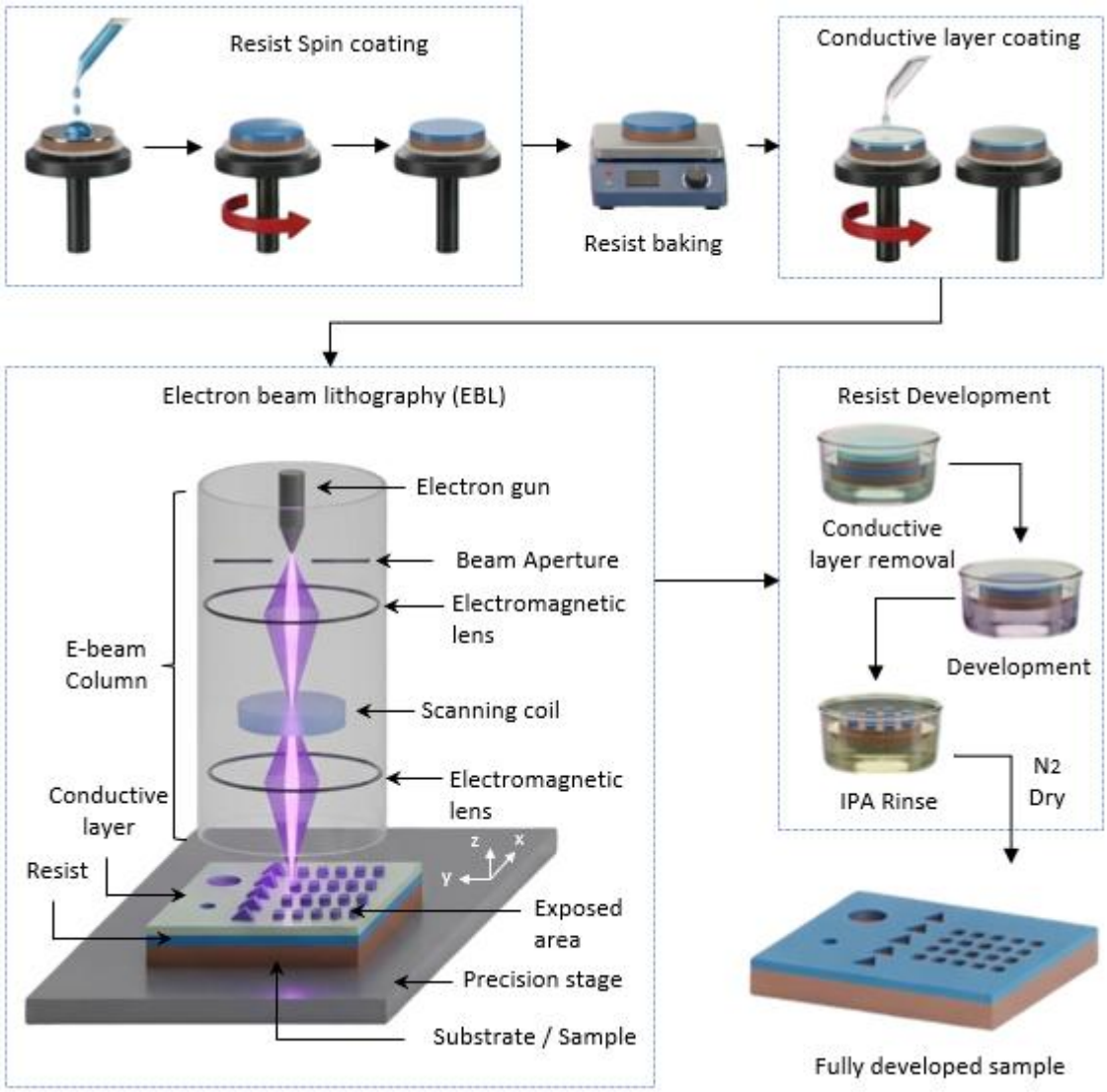


Figure 2.2 | Schematic of the electron beam lithography (EBL) process. The substrate is spin coated with resist, baked, and coated with a conductive layer before electron beam exposure. After pattern writing, the conductive layer is removed and the resist is developed, rinsed, and dried to produce the final patterned sample.

Then the sample will be coated with a thin conductive layer (typically 10nm Au layer) with a thermal evaporator, or a conductive polymer layer is spin coated on to the resist. Then the sample will be exposed with an electron beam (in EBL) to pattern the resist (UV light is used in photolithography to expose and a conductive layer is not needed for this). After exposing the

conductive layer was removed using an etchant or DI water. Then the Resist is developed in the developer solution followed by an IPA bath to clean the sample. In most of these works, positive photoresists were used, with the exposed area developed and etched thoroughly. After that, in most works, a metal mask is deposited on the patterned areas using electron-beam evaporation, and then the remaining unexposed area is lifted off. In one work, since the metal mask is not suitable, the photoresist itself was used as the mask. Once the mask is deposited and patterned, the samples will be etched using Inductive coupled plasma-Fluorine (ICP-F) based etching to fabricate the patterns and the metasurfaces.

2.1.3 Electron Beam Evaporation

Electron beam (E-beam) evaporation is a high vacuum physical vapor deposition (PVD) technique in which a focused, high energy electron beam is used to heat a solid source material until it melts and evaporates, forming a vapor that condenses as a thin film on cooler substrates. In a typical system as illustrated in Figure 2.3, electrons are emitted from a heated filament, accelerated to several kilovolts, and magnetically focused onto a small area of the target (ingot or pellets) held in a water-cooled hearth.

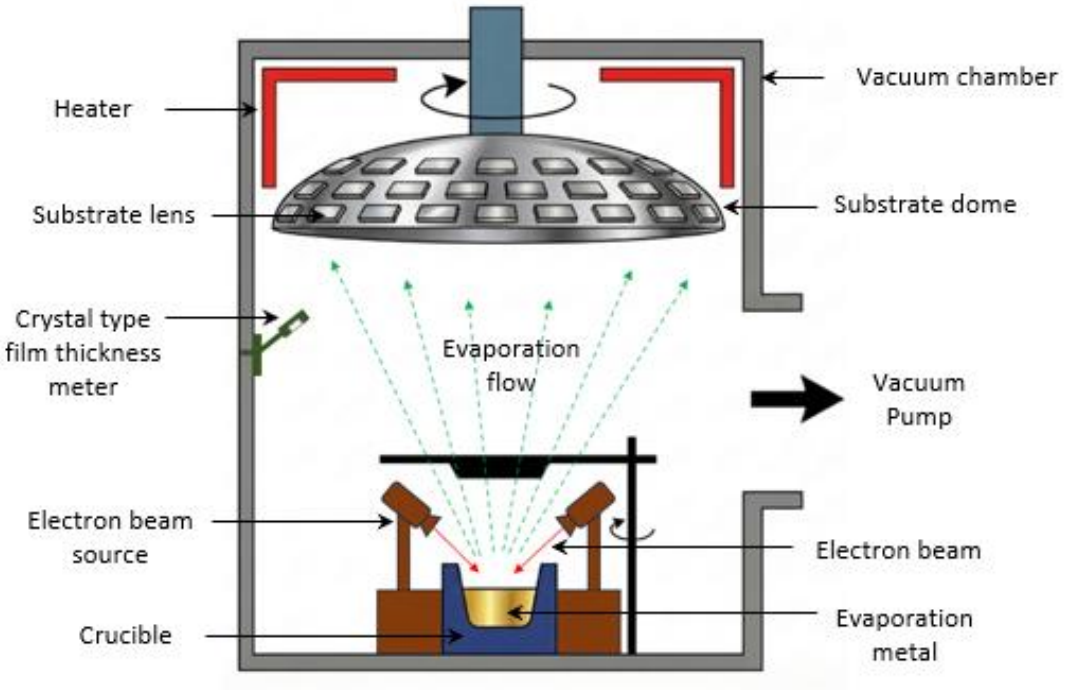


Figure 2.3 | Schematic of the electron beam evaporation system. An electron beam heats the source material in a crucible under vacuum, causing it to evaporate and deposit onto the rotating substrate, while the film thickness is monitored during deposition.

The very high-power density in this localized region heats the material well above its melting point, while the bulk of the source and crucible remain comparatively cool, enabling efficient evaporation of even high melting point metals and ceramics with minimal contamination from the crucible. Under high vacuum, the evaporated atoms travel predominantly in straight lines (line of sight) to the substrates, where they nucleate and grow into a thin film and the thickness and microstructure are controlled by parameters such as beam power, deposition rate, chamber pressure, and substrate temperature. Because the beam power can be adjusted over a wide range, electron beam evaporation can achieve both very low and very high deposition rates and is widely used for depositing metals, oxides, and nitrides in microelectronics, optics, and plasmonic devices.

2.1.4 Inductive coupled Plasma-fluorine (ICP-F) etching

In almost all projects, employing a top-down fabrication approach, the samples were etched using ICP-F etching. Silicon, silicon nitride (Si_3N_4), and various TMDC materials were etched using ICP-F. CHF_3, SF_6, and Ar were used as process gases in different ratios, flow rates, and ICP parameters to realize the required etch depths and profiles for metasurfaces, gratings, and waveguides. The specific process recipes and gas compositions used for each device are described in the corresponding chapters, together with a detailed discussion of the rationale behind the chosen parameters.

ICP F etching uses a high-density plasma generated by inductive coupling to provide a large flux of reactive fluorine species to the surface, and controls ion energy independently via the RF bias at the substrate as shown in Figure 2.4. This decoupled control over ion flux and ion energy enables highly anisotropic, high selectivity etching, enabling the formation of high aspect ratio nanostructures with well-defined sidewalls. In an ICP reactor, RF power applied to an inductive coil generates a high-density plasma consisting of ions, electrons, and reactive radicals. A separate RF bias on the substrate accelerates ions toward the surface, enabling directional (anisotropic) etching. The overall etching behavior is determined by a combination of chemical reactions, ion assisted sputtering, and surface passivation. SF_6 works as the main source of fluorine radicals, which react chemically with Si, Si_3N_4, and TMDCs during the etching process. Etch rate can be increased by increasing SF_6 flow, but this results in isotropic etching. CHF_3, while providing fluorine for etching, produces C-based species that attach to the sidewalls, and this stops lateral etching and leads to vertical sidewall profiles. As an inert gas, Ar promotes physical sputtering. Ar^+ ions mainly help remove reaction by-products while

cleaning the surface. These Ions break the passivation layer at the bottom of the features, enhancing anisotropy.

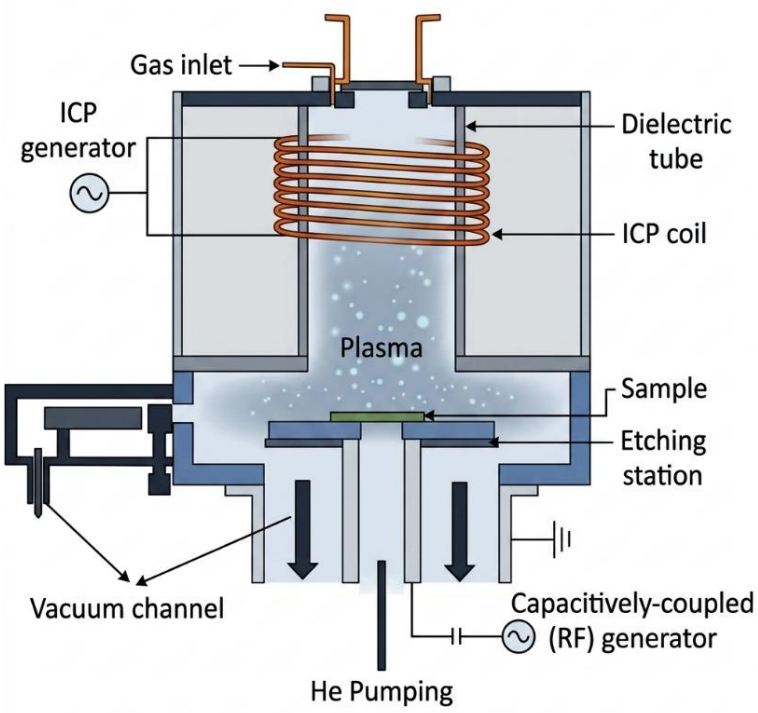


Figure 2.4 | Schematic of the inductively coupled plasma (ICP) etching system. Process gases are introduced into the chamber and ionised by the ICP coil to generate a high-density plasma, while RF bias at the sample stage drives directional ion bombardment for substrate etching under vacuum.

Throughout this thesis, the ICP F parameters (gas ratios, pressures, ICP power, and RF bias) are tailored to each material system and device geometry. The corresponding chapters provide detailed recipes and discuss how these parameters were optimized to achieve the target etch profiles for Si, Si_3N_4, and TMDC based nanophotonic structures.

2.1.5 Chemical Vapor Deposition (CVD)

Chemical Vapour Deposition or CVD is a widely used technology, characterized by its ability to produce high purity and quality deposition of thin films from a vapour phase onto the substrate through a series of chemical reactions[6]. In a typical CVD process, the precursor gases are delivered through a controlled gas delivery system into a heated chamber containing the substrate, and the supplied thermal energy promotes the decomposition or chemical transformation of the gaseous species into reactive intermediates. These species then adsorb onto the substrate surface, where surface diffusion, nucleation, and subsequent growth take

place, leading to the formation of the desired thin film. The overall deposition behavior and film quality are strongly influenced by process parameters such as temperature, pressure, and gas flow rate, as these govern both the gas phase reactions and the surface reaction kinetics[7]. A conventional CVD system therefore generally consists of a reaction chamber, gas delivery system, heating arrangement, and substrate holder, all of which must be carefully controlled to achieve uniform film thickness, composition, and material quality[8]. Depending on the material system, deposition requirements, and desired film characteristics, several CVD variants can be employed.

A well-established CVD technique is Plasma Enhanced Chemical Vapor Deposition (PECVD) which is widely used to deposit films like SiOx, SiNx, α-Si, with high uniformity at relatively lower temperatures compared to the traditional thermal CVD technique. The PECVD process chamber (Figure 2.5) consists of two parallel electrodes, where the upper electrode is connected to plasma generators operating at high and low radio frequencies, while the lower electrode is grounded and functions as the substrate holder. The use of mixed frequency plasma excitation provides improved control over important film properties, particularly the residual stress within the deposited layer. To enhance the density and overall quality of the deposited films, the substrate holder can be heated during the process, while the chamber pressure is maintained at 650mTorr for SiO_x, SiN_x and at 1500mTorr for α-Si deposition ensuring stable plasma generation.

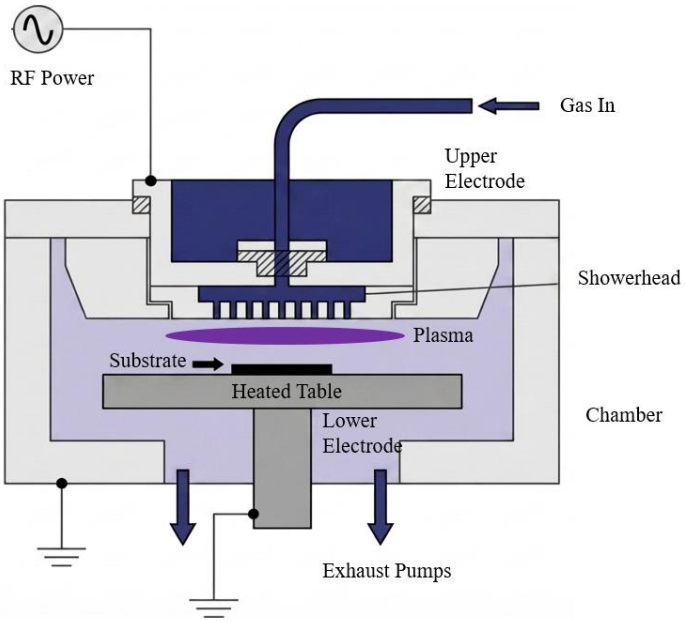


Figure 2.5 | Schematic of the PECVD system used for thin film deposition. The chamber consists of parallel electrodes, where RF plasma is generated at the upper electrode and the

grounded lower electrode acts as the heated substrate holder for uniform deposition of SiO_x, SiN_x and α-Si films.

Different precursor gas combinations are introduced depending on the thin film to be deposited. For silicon oxide (SiO_x) deposition, silane (SiH_4), nitrous oxide (N_2O), and nitrogen (N_2) are introduced into the chamber at flow rates of 9.7 sccm, 710 sccm, and 161 sccm, respectively. The deposition is carried out at a substrate temperature of 300 °C with an RF power of 40 W. For silicon nitride (SiN_x) deposition, silane (SiH_4), ammonia (NH_3), and nitrogen (N_2) are used at flow rates of 16 sccm, 14 sccm, and 980 sccm, respectively, with the substrate maintained at 300 °C and an RF power of 20 W. For amorphous silicon (a-Si) deposition, silane (SiH_4) and helium (He) are supplied at flow rates of 25 sccm and 475 sccm, respectively, while the substrate temperature is maintained at 150 °C and the RF power is set to 40 W. Under radio frequency plasma excitation, these reactant gases are dissociated through capacitive coupling discharge between the electrodes, generating reactive species that undergo a series of chemical reactions and subsequently deposit as thin films on the substrate surface.

2.1.6 Focused Ion beam

Focused ion beam (FIB) is a micro and nanoscale processing technique in which a beam of high energy ions which are typically produced from a liquid metal ion source, most commonly using gallium ions and are generated, focused, and scanned across a specimen surface for both imaging and direct material modification. Unlike electron beams, ions are much more massive, and this greater mass gives them a much stronger ability to alter the sample surface during irradiation. As a result, FIB is not only an imaging tool but also a machining platform capable of performing highly localized surface processing. There are mainly four basic FIB functions: milling, deposition, implantation, and imaging.

FIB Milling occurs when energetic ions strike the surface and, through predominantly elastic collisions, eject surface atoms from the material in a sputtering process. Because this removal can be confined to a selected region, FIB milling is particularly useful for site specific machining, allowing the user to excavate material with high positional accuracy. This capability can be used for relatively simple operations, such as drilling probe holes, as well as more advanced procedures, including the preparation of precise 3D cross sections. A major strength of FIB milling is that it can isolate and modify only the region of interest while preserving the integrity of the surrounding sample. This makes the technique highly suitable for localized structural analysis and sample preparation[9].

FIB can also be operated in deposition mode, which significantly broadens its fabrication capability. In this process, a gas delivery system introduces a precursor gas, often an organometallic species, into the path of the ion beam just above the sample surface. The interaction of the beam with this gaseous layer promotes localized deposition of material exactly where the beam is directed, commonly enabling the growth of metallic features. The source emphasizes that when deposition is combined with milling, the FIB can fabricate highly complex microstructures and perform both additive and subtractive processing within the same instrument. Another important process is ion implantation, in which incident ions become incorporated into the near surface region of the specimen and thereby modify the surface. Consequently, FIB is not limited to material removal alone but can also be used as a flexible platform for surface engineering and localized fabrication[9].

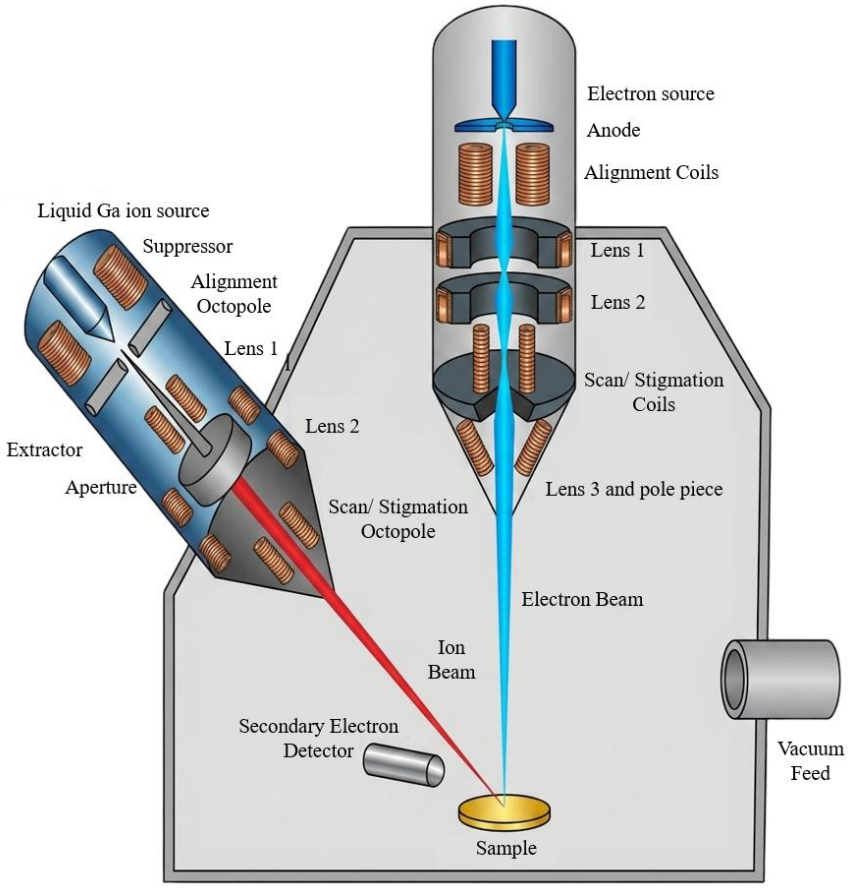


Figure 2.6 | Schematic of the dual-beam FIB-SEM system. The instrument combines a focused gallium ion beam for site specific milling, deposition, implantation, and ion beam imaging with an electron beam column for high resolution, less destructive SEM imaging of the same sample region.

Imaging is the fourth major FIB function and is closely linked to the same ion-solid interactions that enable processing. When the ion beam strikes the sample, it generates secondary electrons and secondary ions that can be collected to form an image, allowing the specimen to be observed before, during, and after modification. This real time imaging capability is particularly useful because it enables direct monitoring of milling, deposition, and implantation processes at the target site. However, the FIB system can introduce unwanted damage to the specimen, which is one limitation of ion beam processing. To address this, dual beam systems were developed by integrating FIB with scanning electron microscopy in a single instrument. In such systems, the FIB provides precise machining and site-specific processing, while the SEM contributes high resolution and less destructive imaging. This combination is especially powerful for structural, chemical, and geometrical analysis of cross sections in complex materials, making dual beam FIB-SEM platforms particularly valuable for advanced characterization and nanoscale fabrication[9].

2.2 Structural and Optical Characterization

2.2.1 Scanning electron microscope (SEM)

Scanning electron microscopy (SEM), shown in Figure 2.7 is a powerful imaging technique in which a focused beam of high energy electrons is directed onto a sample surface to generate signals that can be used to reveal the topography, morphology, composition and the crystallographic information of the material. In SEM technology, the study of the material is based on mainly two different types of signals, namely, secondary and backscattered electrons. Secondary electrons (SEs) are mainly produced through inelastic interactions and scattering between the incident primary electrons and the atoms in the sample. Because these electrons have relatively low kinetic energy (less than 50eV), only those generated very close to the sample surface can escape and be collected by the detector. As a result, SE imaging is highly sensitive to surface and is particularly useful for examining fine topographical details and surface morphology[10,11].

Back scattered electrons(BSEs), in contrast retain a much larger fraction of the energy of the incident beam. They originate from primary electrons that are scattered back out of the sample, either after elastic scattering or after limited energy loss. Owing to their higher energy, BSEs can escape from deeper within the interaction volume compared to SEs. The intensity of the BSE signal depends strongly on the atomic number of the material, with regions containing heavier elements appearing brighter than those composed of lighter elements. For this reason,

BSE imaging is especially valuable for distinguishing material contrast and identifying compositional variations across the sample[10,11].

In this thesis, an FEI Verios 460 SEM system was used for the morphological characterization of waveguides and metasurfaces. In this instrument, a monochromatic electron beam is generated using a Schottky field emission gun and accelerated at voltages typically ranging from 1 to 30 kV. The beam is then shaped and focused onto the sample surface by a series of electromagnetic lenses, including the condenser and objective lenses, to produce a probe of the desired size. An aperture is used to restrict the electron beam and reduce spherical aberration, thereby improving image quality. Raster scanning of the beam across the sample surface is achieved using scanning coils. For conventional surface imaging, the microscope collects emitted electrons using detectors such as the Everhart Thornley detector (ETD) and the through the lens detector (TLD), which are primarily used for SE and general surface sensitive imaging. In addition, a mirror detector (MD) positioned within the objective lens is employed in atomic number contrast or Z contrast imaging mode to detect high energy BSEs.

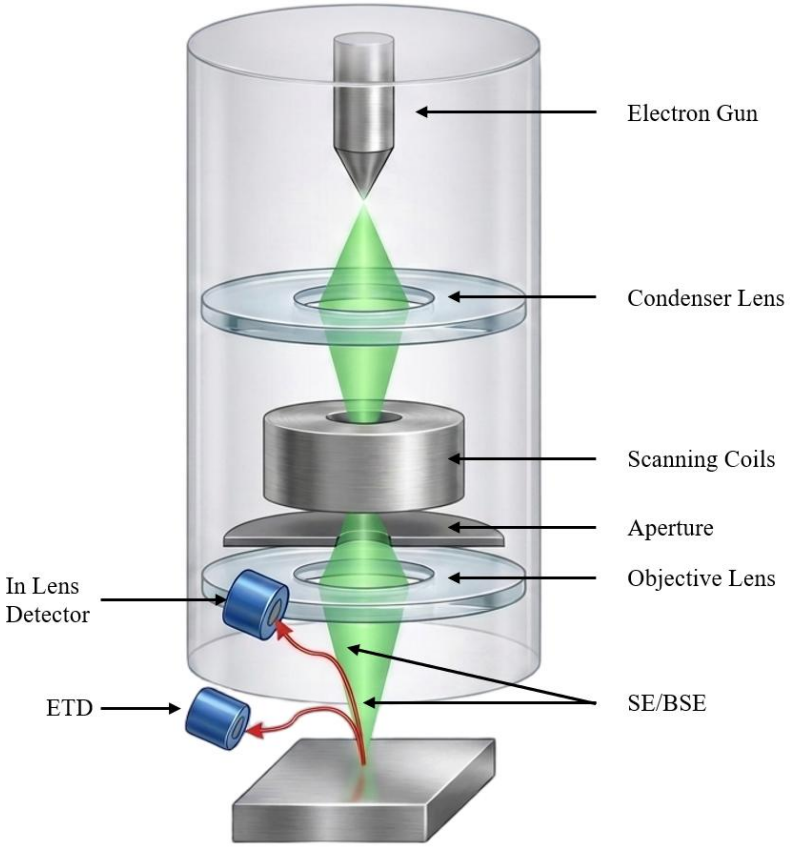


Figure 2.7 | Schematic of the SEM system used for morphological characterisation. A focused accelerated electron beam scans the sample, while secondary electrons (SEs) and BSEs are collected to obtain surface morphology and Z contrast images.

2.2.2 Phase Shift Interferometer (PSI)

PSI is a rapid, non-invasive optical technique used to characterize the surface topography and layer number of two-dimensional materials. For atomically thin systems such as MoS_2, WS_2, graphene, hBN and black phosphorus, thickness strongly influences the electronic and optical response, making accurate layer identification essential. Compared with conventional techniques such as AFM, TEM and STM, PSI offers a simpler and faster route to thickness determination because it does not require slow scanning or invasive tip-based probing. Instead, it measures the optical response of the flake relative to the substrate and converts this into a surface height related optical path length (OPL), making it particularly attractive for routine characterization of fragile and ultrathin 2D materials.

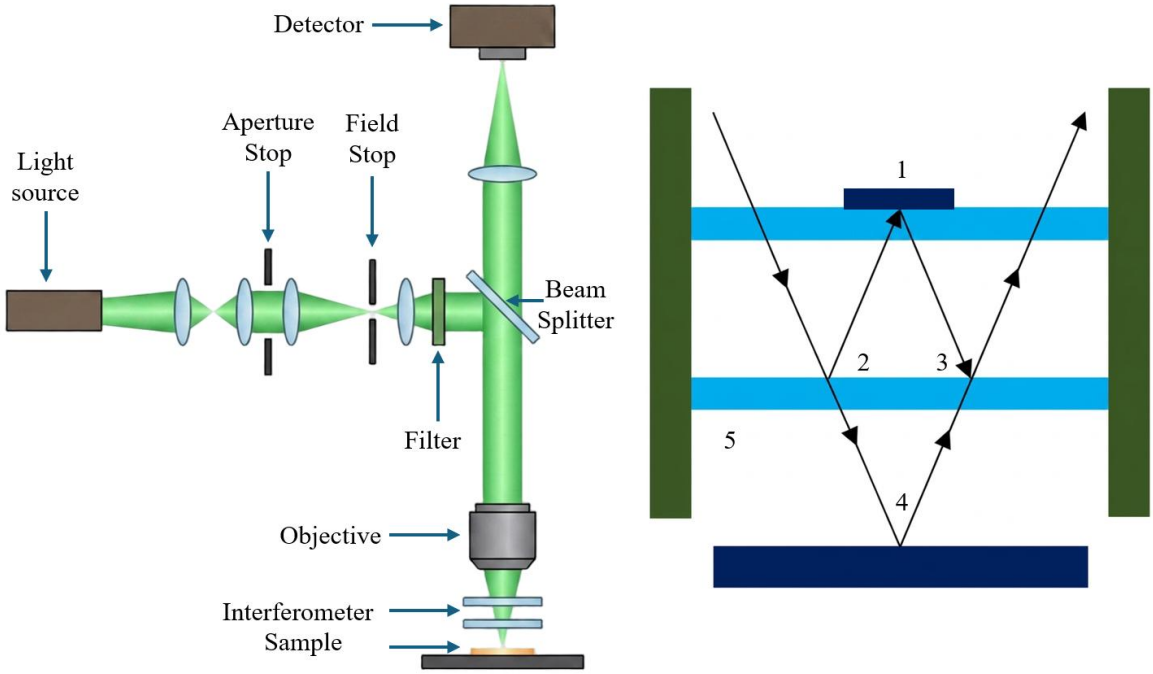


Figure 2.8 | Schematic of the phase-shifting interferometry (PSI) system. The inset shows the Mirau interferometer, where the reference and sample beams are split and recombined to generate the interference signal used for measurement. 1. Reference mirror; 2. First reflection of the reference beam; 3. Third reflection of the reference beam; 4. Reflection of the test/objective beam; 5. Semi-transparent mirror. 2-1-3 represents the reference beam and 2---3 represents the test/objective beam.

The working principle of PSI is based on optical interference. In a typical PSI system as shown in Figure 2.8, light from a filtered source is divided into a reference beam and a sample beam through a Mirau interferometer integrated into the microscope objective. The sample beam

reflects from the 2D material and the underlying substrate, while the reference beam follows a known optical path, which is the two beams recombining at the detector to generate an interference signal. By introducing a controlled phase shift between the beams and analyzing the resulting interferograms, the system calculates the phase difference and hence the optical path difference. For 2D material measurements, the quantity of interest is the OPL contrast between the flake and the substrate, which is then correlated with layer thickness. In this way, PSI provides a quantitative optical map of the sample without physically contacting or damaging the surface.

A major strength of PSI for 2D material characterization is its combination of speed, simplicity and high sensitivity. The method has been shown to provide OPL values that scale linearly with layer number for materials such as MoS_2, phosphorene, hBN and graphene, with good agreement between experiment and simulation. Importantly, the optical contrast can be much larger than the true physical thickness; for example, a monolayer MoS_2 thickness of about 0.7 nm can produce an OPL signal amplified by more than fifty times, greatly improving layer discrimination. PSI is also especially valuable for air sensitive materials because it uses a low density, non-focused LED source and enables one step measurement with minimal sample handling. Although the measured OPL depends on parameters such as substrate, refractive index and illumination wavelength, this sensitivity can be advantageous, since it allows PSI to serve as a robust and versatile platform for rapid thickness identification and surface topography analysis of a wide range of 2D materials. The Vecco NT9100 PSI system is used in this thesis with a green LED light source at 535 nm and a 10 nm bandpass filter.

2.2.3 Scattering field scanning near field optical microscope (s-SNOM)

s-SNOM has opened up the pathway for nanoscale optical imaging. In these systems, the localized interaction between a sharp metallic probe and the sample is used to probe the near field E field distributions. Compared to diffraction limited far field techniques, s-SNOM can access the evanescent near field and convert it into propagating radiation via tip scattering, which is then detected to image the near field interaction. This is essential for exploring near field light matter interactions, especially in this thesis, to investigate propagating polaritonic modes in materials.

As illustrated in Figure 2.9, a metal coated atomic AFM tip is illuminated by a focused laser beam, acting as an optical nanoantenna. In this dissertation, we have used the s-SNOM system in both the visible and mid-IR regimes. So, a Mir cat mid-IR laser (5.5um to 7.7um) and a

Maitai laser (690nm - 1040nm), coupled with an OPO (345nm - 2.5um), are used to excite the samples.

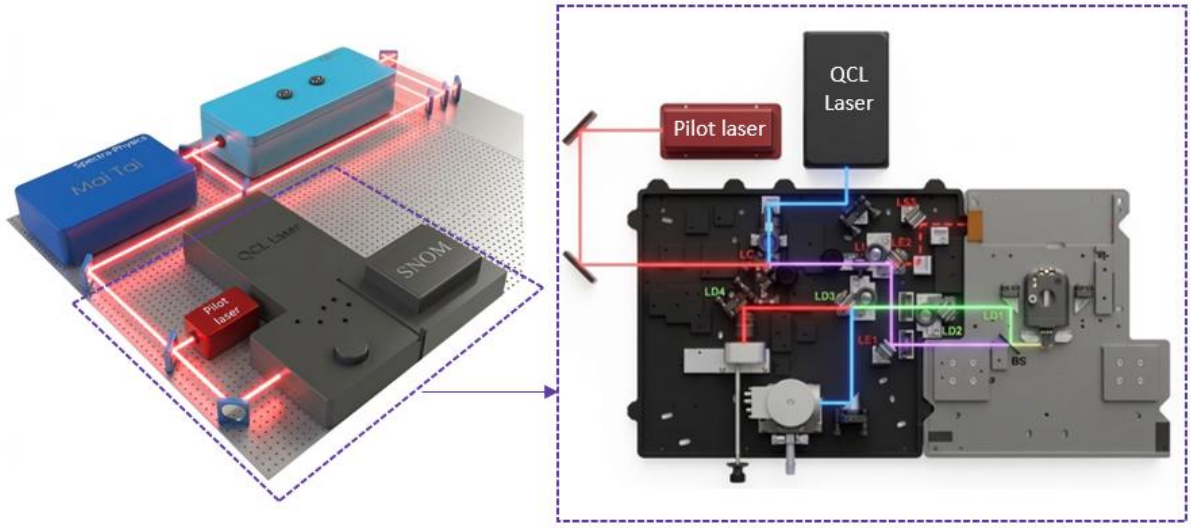


Figure 2.9 | Schematic of the s-SNOM setup used in this work. The system employs a metal coated AFM tip illuminated as an optical nanoantenna, with excitation provided by a Mai Tai laser/OPO for the visible-NIR range and a Mircat QCL laser for mid-IR measurements.

The lasers are guided using the optical path towards the Michelson interferometer. As illustrated in Figure 2.10, the incoming beam is split into two paths to the sample stage, and the oscillating mirror defines the two optical paths in the interferometer. The beam that goes towards the sample stage and the AFM is then focused onto the AFM tip by a parabolic mirror, where the focus beam spot is around 20nm in size. The incident field is strongly confined at the tip apex, generating a highly localized electromagnetic field that interacts with the sample. This interaction induces a dipolar response that depends on the local dielectric environment beneath the tip. The scattered field from the tip contains both near-field and background contributions. The other beam will be modulated by the oscillating mirror at a frequency M in our setup, which is 3 MHz.

A key challenge in s-SNOM is the separation of the weak near field signal from the much stronger background scattering. This is achieved by operating the AFM in tapping mode, where the tip oscillates vertically at a frequency Ω, periodically modulating the tip-sample distance. Because the near field interaction decays rapidly with distance, it is strongly modulated by this oscillation. In contrast, the background scattering varies only weakly with the tip position. By demodulating the detected signal at higher harmonics of the tapping frequency (typically $n\Omega$, with $n \geq 2$), the near field contribution can be selectively extracted.

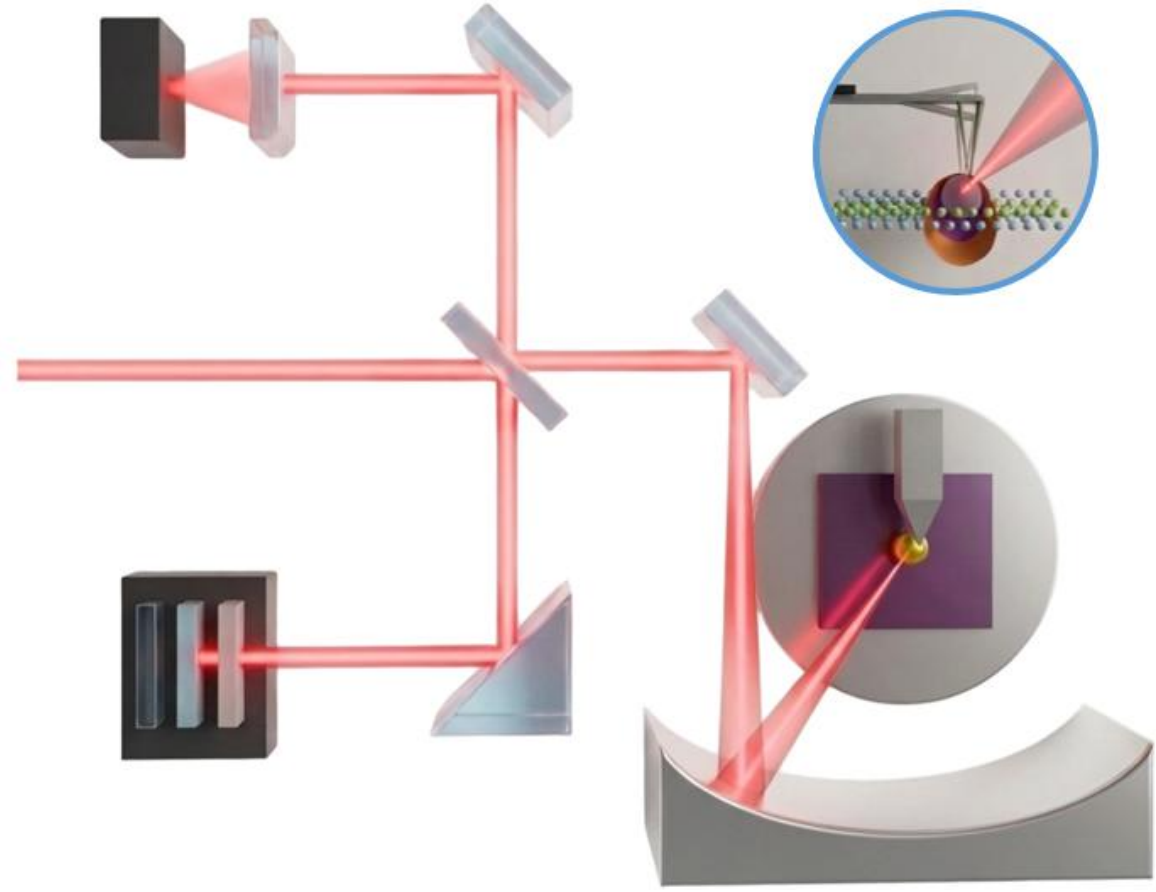


Figure 2.10 | Schematic of the s-SNOM interferometric optical setup. The incident beam is split into reference and sample arms, with the sample beam focused onto the AFM tip by a parabolic mirror to generate a localized near field signal.

Higher-order harmonics provide enhanced near field sensitivity and effective suppression of background signals. In this dissertation, the near field amplitude and phase are primarily obtained from the 2nd harmonic and 3rd harmonic demodulated signals, ensuring that the measured response is dominated by localized tip-sample interactions. Both the amplitude and phase of the scattered near field is accessed through the interferometric detection scheme. The scattered light from the tip is combined with a reference beam in a Michelson-type interferometer, enabling coherent detection of the optical signal.

A pseudo-heterodyne detection method is used, in which the reference mirror is periodically modulated to introduce a controlled phase shift. This modulation allows simultaneous extraction of the amplitude and phase of the near field signal through lock-in detection. The resulting complex signal can be expressed as a complex quantity,

- The amplitude, which is sensitive to local field enhancement and absorption
- The phase, which reflects the local dielectric response and resonant behaviour

This phase-resolved detection is particularly important for studying polaritonic systems, where both amplitude and phase carry essential information about mode propagation and interference. All measurements in this thesis were performed using a commercial s-SNOM system (Neaspec GmbH) integrated with a tapping-mode AFM. A tunable mid-infrared laser source (MIRcat) was used to illuminate the tip-sample region.

The incident beam is focused onto the metallic AFM tip at an oblique angle, enabling efficient excitation of the tip dipole and coupling to in-plane momentum components. The scattered light is collected in the far field and directed to the interferometric detection unit for amplitude and phase retrieval.

The main components of the setup include:

- A metal coated AFM tip acting as a nanoscale optical antenna
- Tapping-mode operation for distance modulation
- A tunable laser source for spectral and resonant excitation
- An interferometric detection system for phase-resolved measurements
- Lock-in detection for harmonic demodulation

The spatial resolution is determined by the tip apex radius (~10–30 nm), allowing optical imaging well below the diffraction limit. In addition to probing the local optical response, the s-SNOM tip also acts as a nanoscale source of high momentum fields capable of launching polaritons in the sample. Upon illumination, the tip provides the necessary momentum to couple incident photons into confined polaritonic modes. This tip or metallic nano structures launched polaritons propagate along the material surface. The interference of these polaritons with the incident beam or the interference between the excited polariton and edge reflected polaritons generate the interference fringes. The spatial periodicity of these fringes has a relation to the polariton wavelength, enabling direct extraction of dispersion relations. Furthermore, the decay of fringe amplitude provides insight into propagation losses and mode confinement.

2.2.4 Reflection and Transmission SHG

SHG is a nonlinear optical response where two photons with angular frequency ω interact with a nonlinear material to generate a single photon with angular frequency 2ω. A home built optical setup was used for all the SHG measurements carried out in this thesis as shown in Figure 2.11. The Mai tai laser (690nm -1040nm) coupled with an OPO (345nm - 2.5um) was used to excite the samples. The measurements were carried out with linear and circular polarized light, so the beam excitation side contains a half wave plate and a quarter wave plate to control the polarization.

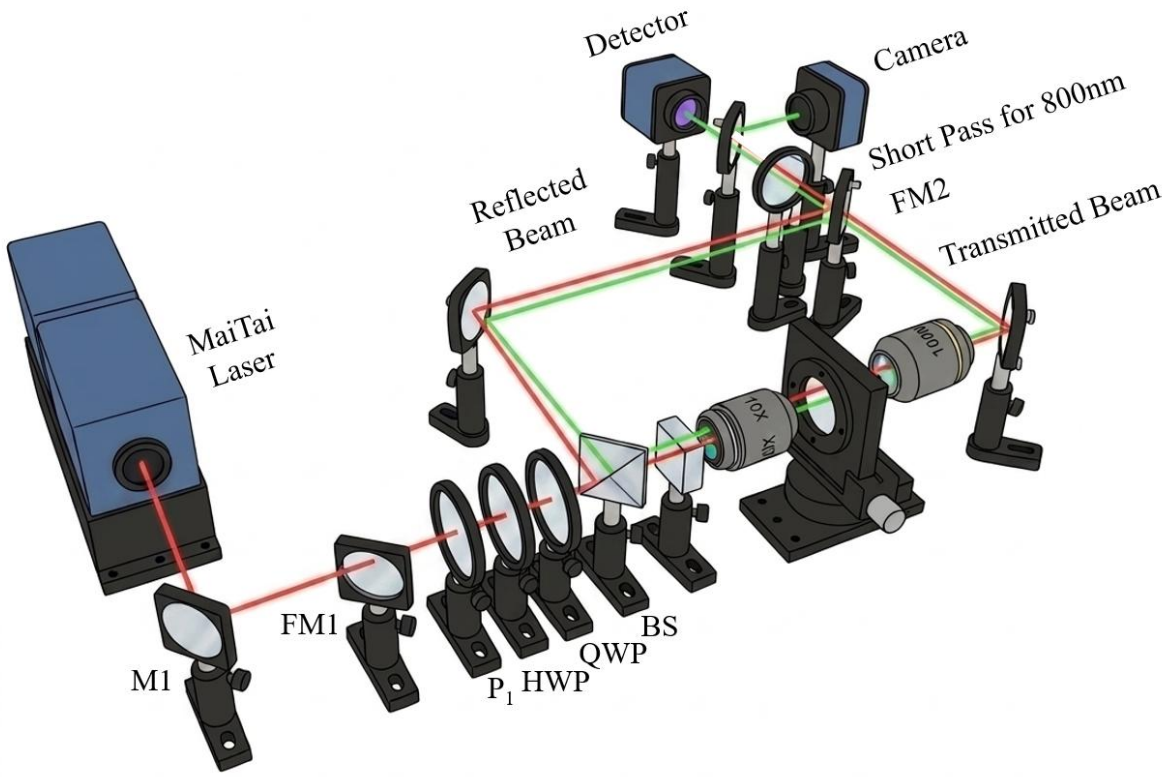


Figure 2.11 | Schematic of the optical setup used for reflection and transmission second-harmonic generation (SHG) measurements. The fundamental laser beam is directed onto the sample, and the generated SH signal is collected in both the reflected and transmitted directions for nonlinear optical characterisation

For reflection SHG, the second harmonic light is collected on the same side as the incident beam (Figure 2.11), and this is the most common geometry for exfoliated, or CVD grown 2D flakes on SiO2/Si substrates. SHG measurements were carried out both in reflection and transmission modes. Depending on the wavelength range being measured, the signal was recorded with either a silicon CCD detector or a liquid-nitrogen-cooled InGaAs detector.

2.2.5 Photoluminescence (PL) Spectroscopy

PL spectroscopy is a widely used optical characterization technique for studying how a material emits light upon optical excitation. Because it is a non-contact, non-invasive, and versatile method, it is particularly useful for investigating delicate samples without changing their properties. In semiconductor and materials research, PL is commonly used to examine electronic structure, optical transitions, defect states, and impurity-related effects, all of which strongly influence device performance. By analyzing the emitted light in terms of wavelength, intensity, spatial distribution, and temporal behavior, valuable information can be obtained about a material's band structure and overall optical quality. For this reason, PL spectroscopy is especially important in the study of light-emitting materials used in devices such as LEDs and lasers.

In this thesis, PL measurements were carried out using a commercial Horiba LabRAM micro-PL spectroscopy system equipped with confocal optics, giving an excitation spot size of about 0.5 μm on the sample surface. The samples were excited using either a 532 nm diode-pumped solid-state laser or a SuperK EXTREME supercontinuum laser, which allows wavelength-tunable excitation. The light emitted by the sample was collected and guided through a focusing mirror, then sent into a double monochromator, and the desired spectral components are selected. Depending on the wavelength range being measured, the signal was recorded with either a silicon CCD detector or a liquid-nitrogen-cooled InGaAs detector. To improve sensitivity and achieve a cleaner signal, a standard lock-in detection method was used.

This setup makes it possible to record luminescence from materials such as silicon over a very wide dynamic range, reaching up to five orders of magnitude. However, despite its high sensitivity, the relatively large excitation spot limits the spatial resolution of the system. As a result, when the sample contains features smaller than about one micrometer, it becomes difficult to isolate their optical response from that of the surrounding region. Even so, the system remains a powerful and reliable tool for obtaining detailed optical information from a broad range of semiconductors and photonic materials.

References

1. Gao, E., Lin, S.-Z., Qin, Z., Buehler, M. J., Feng, X.-Q., & Xu, Z.(s). Mechanical exfoliation of two-dimensional materials. Journal of the Mechanics and Physics of Solids 2018, 115 248-262.

2. Novoselov, K. S., Geim, A. K., Morozov, S. V., Jiang, D., Katsnelson, M. I., Grigorieva, I. V., Dubonos, S. V., & Firsov, A. A.(s). Two-dimensional gas of massless Dirac fermions in graphene. nature 2005, 438 (7065), 197-200.

3. Chavalekvirat, P., Hirunpinyopas, W., Deshsorn, K., Jitapunkul, K., & Iamprasertkun, P.(s). Liquid phase exfoliation of 2D materials and its electrochemical applications in the data-driven future. Precision Chemistry 2024, 2 (7), 300-329.

4. Huo, C., Yan, Z., Song, X., & Zeng, H.(s). 2D materials via liquid exfoliation: a review on fabrication and applications. Science bulletin 2015, 60 (23), 1994-2008.

5. Chen, Y.(s). Nanofabrication by electron beam lithography and its applications: A review. Microelectronic Engineering 2015, 135 57-72.

6. Awan, T. I., Afsheen, S., & Kausar, S. (2025). Chemical vapor deposition technique. In *Thin Film Deposition Techniques: Thin Film Deposition Techniques and Its Applications in Different Fields* (pp. 65-96). Springer.

7. Sun, L., Yuan, G., Gao, L., Yang, J., Chhowalla, M., Gharahcheshmeh, M. H., Gleason, K. K., Choi, Y. S., Hong, B. H., & Liu, Z.(s). Chemical vapour deposition. Nature Reviews Methods Primers 2021, 1 (1), 5.

8. Dobkin, D., & Zuraw, M. K. (2003). *Principles of chemical vapor deposition*. Springer Science & Business Media.

9. Nan, Y. (2007). Introduction to the focused ion beam system. In *Focused Ion Beam Systems: Basics and Applications* (pp. 1-30). Cambridge University Press.

10. Goodhew, P. J., & Humphreys, J. (2000). *Electron microscopy and analysis*. CRC press.

11. Egerton, R. F. (2005). *Physical principles of electron microscopy* (Vol. 56). Springer.

3. Long Propagating Ghost polaritons Enabled by selective mode excitations

Controlling light at the nanoscale using strong light-matter interactions has opened new opportunities in nanophotonics applications ranging from on-chip optical communication[1-4] to quantum information computation[5,6]. Among these, PhPs have attracted significant attention for their ability to confine light well below the diffraction limit with relatively low losses[7,8]. One important class of polaritonic systems arises in anisotropic materials[9], which exhibit different dielectric permittivities along different crystal lattice axes. In such systems, when the permittivity tensor has principal components with opposite signs, the dispersion of these PhPs becomes hyperbolic[7,9,10]. This results in highly directional energy propagation, enabling phenomena such as sub-diffraction focusing and canalization[11,12]. These hyperbolic PhPs can propagate either on the surface or within the bulk of the material resulting in two different forms of propagating polaritons[7] named surface[13,14] and bulk PhPs[15].

Most recently, g-HPs were discovered[16], which exhibits in-plane hyperbolic dispersion on the surface of a polar uniaxial crystal as well as oblique wave fronts in the bulk, similar to recently predicted ghost waves[17]. This hybrid nature of long-range, ray-like propagation, making g-HPs highly attractive for applications requiring low-loss and directional energy transport. However, obtaining greater control over directionality and propagation length remained a challenge, and in this work, we showcase how this can be achieved by selectively exciting specific polariton modes to achieve controlled directionality and long propagation lengths. We explored the behaviour of conventional excitation approaches, such as dipole-like nanoantennas and AFM tips, and found that these techniques excite a broad spectrum of polariton modes simultaneously, resulting in an energy distribution across multiple modes. This excitation generates polaritons with weak directionality and shorter propagation lengths, mainly limited by the presence of high-loss modes or by mode accumulation.

The experimental observation of g-HPs in calcite was first established by Ma et al. [16], who demonstrated their distinctive dispersion characteristics, long-range directional propagation, and dependence on excitation conditions, including illumination and antenna dimensions. Building on this foundation, Hu et al. [18] subsequently demonstrated that the excitation-source configuration could be used to control the asymmetry of hyperbolic polariton propagation by adjusting the effective in-plane polarization of the source. These studies established that both the intrinsic anisotropic dispersion of calcite and the configuration of the excitation source play important roles in determining the observed polariton propagation characteristics.

The present work builds upon these advances by investigating a complementary aspect of polariton excitation, where the selective coupling of incident light into a restricted range of polariton wavevectors

through finite antenna geometry. Rather than focusing primarily on controlling the relative intensity of different propagation directions, this approach explores how the physical edges and vertices of an asymmetric triangular antenna influence the momentum distribution of the excited polaritons. In particular, the inclined antenna edges preferentially enhance coupling to wavevectors oriented approximately normal to the corresponding edge, while the vertices contribute to the initial excitation of a broader range of modes. By adjusting the triangle geometry, the relative excitation strengths of different modes along the isofrequency contour can be controlled.

This edge-assisted momentum-selection mechanism is investigated through theoretical analysis, numerical simulations, Fourier-space analysis, and experimental s-SNOM measurements. The resulting selective excitation favours particular propagating components, including long-lived modes, providing a means of engineering the observed directionality and propagation characteristics without modifying the intrinsic dispersion of calcite. Specifically, we demonstrate that structural asymmetry can be used as a mechanism for mode-selective excitation. By tailoring the geometry of a micro/nano antenna, particularly using an asymmetric triangular design, it is possible to:

- selectively excite specific g-HP modes,
- achieve highly directional propagation,
- and greatly improve propagation length.

This approach is based on a newly identified mechanism, termed edge-assisted mode selection[19], in which the physical edges of the antenna act as momentum filters, preferentially coupling light into polariton modes with specific wavevectors. In this framework, the antenna geometry does not merely act as a passive scatterer but actively defines the momentum distribution of the excited modes.

The results obtained through theoretical analysis and numerical simulations are further validated experimentally through near-field optical measurements of fabricated samples. We demonstrate that this approach enables efficient excitation of long-propagating g-HP modes with significantly extended propagation distances[19]. These results establish that long-range polariton propagation is not solely determined by intrinsic material losses but can be actively engineered through selective excitation of low-loss modes. This chapter therefore introduces a unique and novel framework for controlling polariton excitation, demonstrating that mode selectivity enabled by structural engineering, combined with material properties is key to achieving both high directionality and long-range propagation in polaritonic systems.

3.1 Theoretical Framework of g-HPs inside the Anisotropic Media

3.1.1 Anisotropic Dielectric Properties and Hyperbolic Dispersion in Calcite

The optical response of an anisotropic crystal is governed by a tensorial permittivity which leads to fundamentally different behaviour of light propagation compared isotropic materials. Calcite, a uniaxial crystal, has a dielectric tensor in its principal coordinate system that is expressed as follows:

$$\bar{\bar{\varepsilon}} = \begin{pmatrix} \varepsilon_{\perp} & 0 & 0 \\ 0 & \varepsilon_{\parallel} & 0 \\ 0 & 0 & \varepsilon_{\perp} \end{pmatrix}$$

Where $\varepsilon_{\parallel}$ and $\varepsilon_{\perp}$ denote the permittivity components parallel and perpendicular to the optic axis. In calcite, the optical axis is inclined[16] with respect to the surface, and therefore the tensor must be rotated accordingly to introduce the coupling between field components. Under specific frequency ranges, the principal components of the permittivity tensor can take opposite signs[16,19], satisfying:

$$\varepsilon_{\perp} \cdot \varepsilon_{\parallel} < 0$$

This condition defines a hyperbolic medium, (Figure 3.1a). Based on the real part of the permittivity extracted from IR reflectance measurements calcite exhibit two spectral regions; Lower and upper Reststrahlen bands where the $\varepsilon_{\parallel}$ and $\varepsilon_{\perp}$ have opposite signs. These regions give rise to hyperbolic dispersion, where the isofrequency surface becomes an open hyperbola in momentum space, enabling highly anisotropic propagation. These regions correspond to Type I and Type II Hyperbolicity. In this work, we focus on the Type II region, and the corresponding permittivity for calcite (100) calculated using the Lorentz oscillator model is presented in Figure 3.1c,d[19]. In hyperbolic media, the direction of energy flow (group velocity) is not aligned with the wavevector, leading to highly directional, ray-like propagation. This property is central to the behaviour of ghost polaritons explored in this chapter.

Even though many anisotropic crystals support hyperbolic PhPs, calcite offers a unique advantage. Here the propagation behaviour can be tuned through crystallographic orientation without requiring complex heterostructures. By rotating the optic axis (OA), the polariton dispersion can be modified in all spatial dimensions (Figure 3.2). This can be achieved by mechanically cutting the calcite substrate in a specific crystalline orientation, as shown in Figure 3.2 b. For example, if cut in a plane where $\theta = 23.3^{\circ}$ we can get a sample with a surface along the (100) crystal orientation and if $\theta = 90^{\circ}$ the surface crystal orientation would be

(001). This provides a direct experimental handle to control the isofrequency contour (IFC) shape and therefore the polariton propagation behaviour

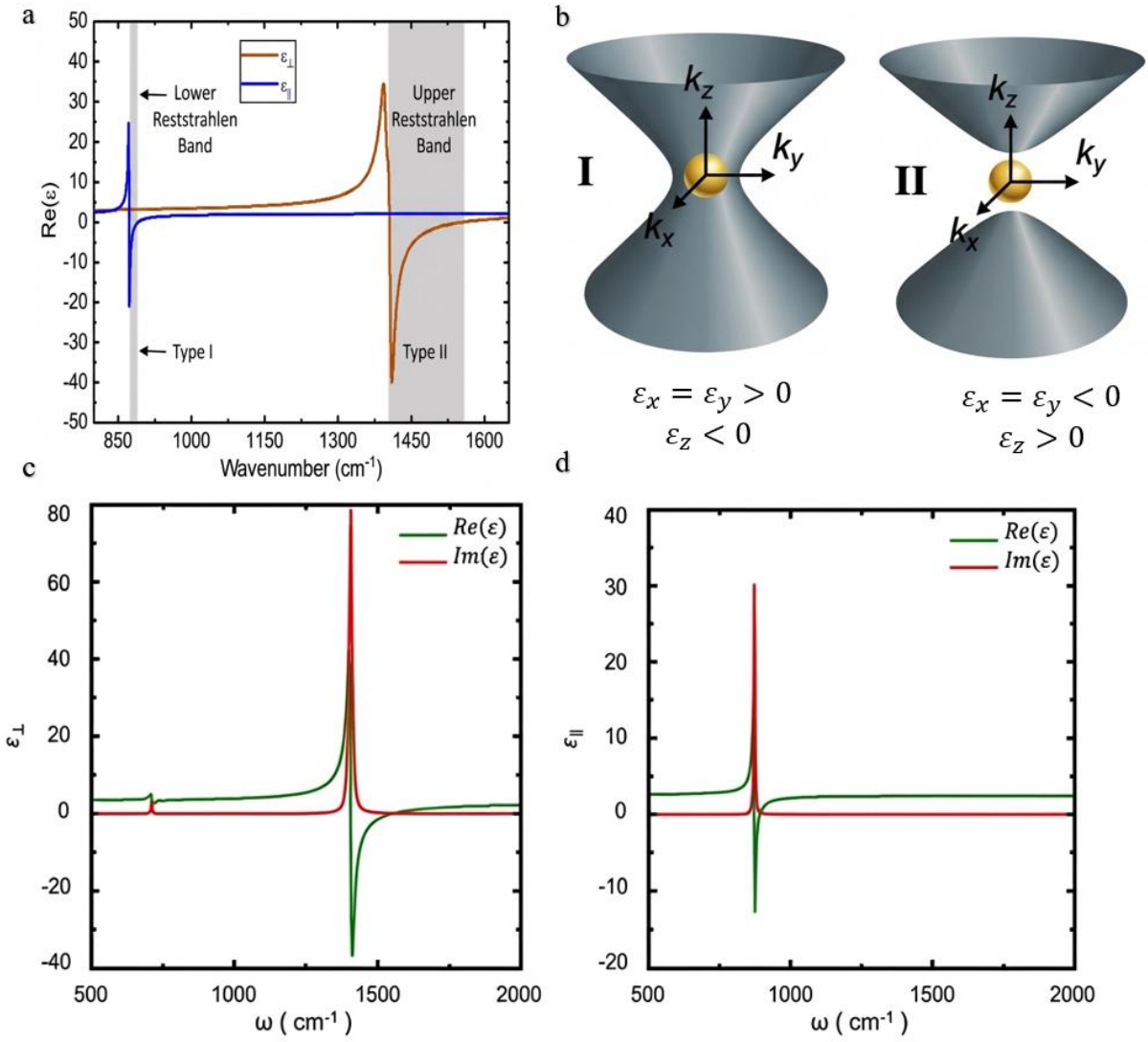


Figure 3.1 | Permittivity tensor of calcite and its hyperbolic behavior. a, Real part of the permittivity tensor of calcite. **b,** Schematic illustration of the three-dimensional Type I and Type II hyperbolic dispersion of calcite within the lower and upper Reststrahlen bands. **c,** Real and imaginary parts of calcite's permittivity tensor component $\epsilon_\perp$. **d,** Real and imaginary parts of calcite's permittivity tensor component $\epsilon_\parallel$.

The orientation of the optic axis relative to the calcite-air interface plays a critical role in determining the dispersion and propagation characteristics of hyperbolic phonon polaritons. Varying the crystallographic orientation modifies the projected in-plane isofrequency contours and can produce transitions between different polaritonic regimes. For tilted optic-axis configurations, such as the (100)-oriented calcite surface with $\theta = 23.3^{\circ}$, the anisotropic

dispersion and electromagnetic boundary conditions can support ghost hyperbolic surface polaritons, characterized by hyperbolic in-plane propagation and simultaneous phase progression and evanescent decay within the crystal.

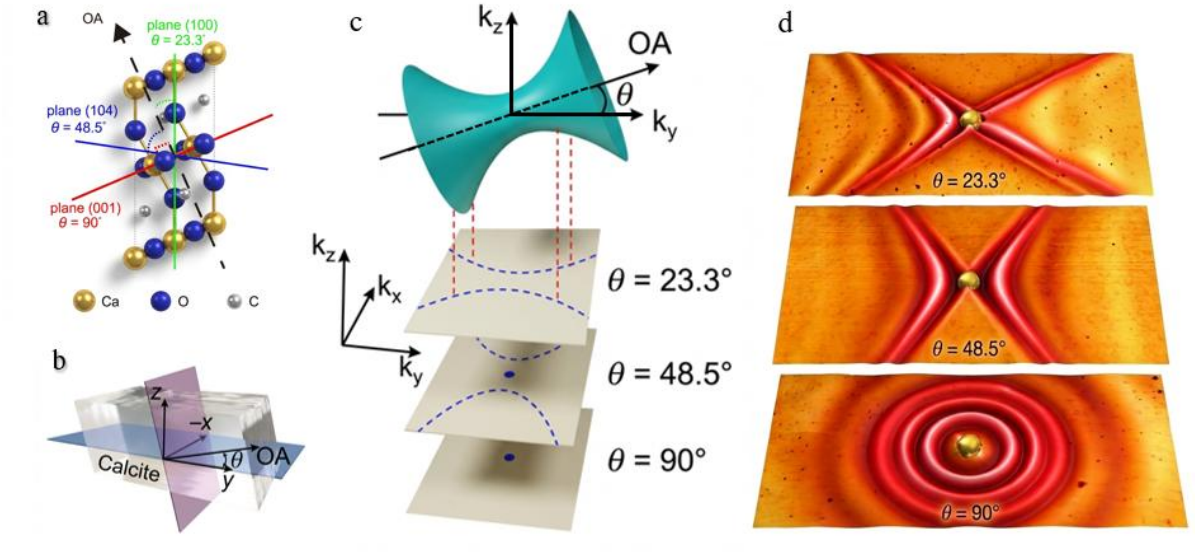


Figure 3.2 | Effect of crystallographic orientation on the dispersion and propagation characteristics of phonon polaritons in calcite. a, Schematic illustrating the crystallographic planes of calcite and the corresponding angle (θ) defined relative to the optic axis (black dashed arrow). The characteristic (100), (001), and (104) planes are marked by green, red, and blue lines, respectively. **b,** Geometry of a selected crystallographic plane in calcite, where the optic axis lies in the y-z plane and the interface is defined in the x-y plane. θ is measured between the optic axis and the y axis. The blue and purple surfaces denote the (100) plane at $\theta = 23.3^{\circ}$ and the (001) plane at $\theta = 90^{\circ}$, respectively. **c,** Projected in-plane isofrequency contours (IFCs) at $\theta = 23.3^{\circ}$, $\theta = 48.5^{\circ}$, $\theta = 90^{\circ}$ illustrating the transition from anisotropic hyperbolic to rotationally symmetric dispersion. **d,** Schematic representations of the corresponding polariton propagation patterns for the three characteristic planes when $\theta = 23.3^{\circ}$, $\theta = 48.5^{\circ}$, $\theta = 90^{\circ}$.

In contrast, when $\theta = 90^{\circ}$, the optic axis is perpendicular to the interface, resulting in rotationally symmetric in-plane dispersion. This configuration is associated with a different polaritonic regime and should not be identified as a ghost hyperbolic surface mode. The experimental investigations in this chapter primarily focus on (100)-oriented calcite with $\theta = 23.3^{\circ}$, where the ghost-polariton mode is supported and its excitation can be engineered using appropriately designed micro- and nanoantennas.

3.1.2 Ghost polariton formation at calcite-air interface.

We verify the existence of ghost polariton modes at the interface between calcite and vacuum. Consider the interface between anisotropic calcite crystal ($z < 0$) and vacuum ($z \geq 0$). The optic axis (OA) of the calcite crystal is initially aligned with the y-axis and then rotated by an angle θabout the x-axis. The permittivity tensor in the rotated coordinate system is therefore given by:

$$\bar{\bar{\varepsilon}} = R_x(-\theta) \cdot \begin{pmatrix} \varepsilon_\perp & 0 & 0 \\ 0 & \varepsilon_\parallel & 0 \\ 0 & 0 & \varepsilon_\perp \end{pmatrix} \cdot R_x(\theta),$$

where $R_x(\theta)$ represents the rotation matrix with respect to x-axis. The permittivity tensor can be derived as:

$$\bar{\bar{\varepsilon}} = \begin{pmatrix} \varepsilon_\perp & 0 & 0 \\ 0 & \varepsilon_\parallel \cos^2\theta + \varepsilon_\perp \sin^2\theta & (\varepsilon_\parallel - \varepsilon_\perp)\sin\theta\cos\theta \\ 0 & (\varepsilon_\parallel - \varepsilon_\perp)\sin\theta\cos\theta & \varepsilon_\perp \cos^2\theta + \varepsilon_\parallel \sin^2\theta \end{pmatrix}$$

Wave propagation inside the anisotropic media is described using Maxwell's equations in the frequency domain:

$$\nabla \times \nabla \times \mathbf{E} - k_0^2 \bar{\bar{\varepsilon}} \cdot \mathbf{E} = 0$$

where k_0 denotes the wave vector inside vacuum. By focusing on eigenmodes with $e^{i\vec{k}\cdot\vec{r}}$ dependence. The above Maxwell's equation is thus simplified:

$$\vec{k} \times \vec{k} \times \vec{E} + k_0^2 \bar{\bar{\varepsilon}} \cdot \vec{E} = 0.$$

Denote the components of $\vec{k}$ as $\vec{k} = [k_x, k_y, k_{2z}]$. The fact that this equation has non-zero solution for $\vec{E}$ indicates that the following determinant equals zero:

$$\begin{vmatrix} -k_{2z}^2 - k_y^2 + \varepsilon_\perp k_0^2 & k_x k_y & k_{2z} k_x \\ k_x k_y & -k_{2z}^2 - k_x^2 + k_0^2(\varepsilon_\parallel \cos^2\theta + \varepsilon_\perp \sin^2\theta) & k_{2z} k_y + k_0^2(\varepsilon_\parallel - \varepsilon_\perp)\sin\theta\cos\theta \\ k_{2z} k_x & k_{2z} k_y + k_0^2(\varepsilon_\parallel - \varepsilon_\perp)\sin\theta\cos\theta & -k_x^2 - k_y^2 + k_0^2(\varepsilon_\perp \cos^2\theta + \varepsilon_\parallel \sin^2\theta) \end{vmatrix}$$

After factorization, this yields two equations.

$$k_x^2 + k_y^2 + k_z^2 = \varepsilon_\perp k_0^2,$$

$$\frac{(k_y \cos\theta + k_{2z} \sin\theta)^2}{\varepsilon_\perp} + \frac{k_x^2 + (k_y \sin\theta - k_{2z} \cos\theta)^2}{\varepsilon_\parallel} = k_0^2.$$

The first equation corresponds to ordinary wave (o-wave), while the second equation corresponds to extraordinary wave (e-wave). The ordinary wave exhibits isotropic behaviour, while the extraordinary wave shows anisotropic dispersion. The extraordinary wave is responsible for hyperbolic dispersion under appropriate conditions. These two eigenmodes form the basis for constructing polaritonic solutions at solid material interfaces. For arbitrary given k_x and k_y, the value of k_{2z} can be derived by solving the quadratic equation:

$$k_{2z} = \frac{-k_y(\varepsilon_{\parallel} - \varepsilon_{\perp}) \sin\theta \cos\theta \pm \sqrt{\Delta}}{\varepsilon_{\perp} \cos^2\theta + \varepsilon_{\parallel} \sin^2\theta}$$

where $\Delta = \varepsilon_{\perp}[\varepsilon_{\parallel} k_y^2 + (\varepsilon_{\perp} \cos^2\theta + \varepsilon_{\parallel} \sin^2\theta)(k_x^2 - \varepsilon_{\parallel} k_0^2)]$. When $\Delta < 0$, k_{2z} under the appropriate hyperbolic and optic-axis orientation conditions, the normal wavevector component of the extraordinary wave becomes complex, possessing both nonzero real and imaginary parts. Consequently, the electromagnetic field exhibits simultaneous phase progression and exponential decay along the direction normal to the calcite-air interface. This produces oblique wavefronts within the crystal while maintaining surface confinement. Importantly, this complex normal wavevector is an intrinsic consequence of the anisotropic electromagnetic dispersion and can exist even in the ideal lossless limit, where the permittivity tensor components are purely real. Therefore, the ghost-wave character is fundamentally different from the complex wavevectors that arise solely due to material absorption. The resulting surface-bound solutions, satisfying the electromagnetic boundary conditions at the calcite-air interface, are referred to as ghost hyperbolic surface polaritons because they combine propagating and evanescent field characteristics within the crystal bulk. The corresponding IFC can be approximated as:

$$\frac{k_x^2}{c_x} - \frac{k_y^2}{c_y} = 1$$

3.1.3 Propagation length and decay mechanism

The electric field of a polaritonic mode propagating along the calcite-air interface can be written as,

$$E(\mathbf{r}) \propto e^{i(k_x x + k_y y)}$$

Here, the in-plane wavevector components are complex and can be expressed as:

$$k_x = \mathrm{Re}(k_x) + i\,\mathrm{Im}(k_x), k_y = \mathrm{Re}(k_y) + i\,\mathrm{Im}(k_y)$$

It is important to distinguish the complex in-plane wavevector components, which describe the attenuation of the polariton during propagation along the interface in the presence of losses, from the complex normal wavevector component responsible for the characteristic ghost-wave behaviour inside calcite. The latter can possess both real and imaginary parts even in the lossless limit, arising from the anisotropic dispersion and the inclination of the optic axis rather than material absorption. Substituting these into the field expression separates the solution into oscillatory (propagating) and exponentially decaying components:

$$E(\mathbf{r}) \propto e^{i(\mathrm{Re}(k_x)x+\mathrm{Re}(k_y)y)}\, e^{-\mathrm{Im}(k_x)x}\, e^{-\mathrm{Im}(k_y)y}$$

The real part of the in-plane wavevector determines the phase propagation of an individual polariton eigenmode, whereas its imaginary part governs the spatial attenuation of the field. Since g-HP propagation is highly anisotropic, the attenuation length depends on the direction along which the field is evaluated. Consequently, the field-amplitude propagation length L_p of an individual polariton mode, defined as the length at which the electric field's magnitude decays to $1/e$ can be expressed as:

$$L_p = \frac{1}{\sqrt{\mathrm{Im}(k_x)^2 + \mathrm{Im}(k_y)^2}}$$

Here, the denominator represents the magnitude of the imaginary in-plane wavevector. This expression gives the field-amplitude attenuation length when the measurement direction is parallel to the imaginary in-plane wavevector. For an arbitrary direction defined by $\hat{S} = (\cos\emptyset\,, \sin\emptyset)$, where $\emptyset$ is the angle measured relative to the positive x-axis, the propagation length is instead determined by the projection of the imaginary wavevector onto that direction given by the following expression:

$$L_p(\emptyset) = \frac{1}{\mathrm{Im}(k_x)\cos\emptyset + \mathrm{Im}(k_y)\sin\emptyset}$$

The projected attenuation coefficient is assumed to be positive along the selected measurement direction. Importantly, the intrinsic propagation length of an individual polariton eigenmode is determined by the electromagnetic properties of the calcite–air interface at a given frequency and propagation direction. Changing the excitation antenna does not modify the intrinsic attenuation of the same eigenmode in an otherwise unchanged, uniform structure. Instead, antenna geometry controls the relative excitation amplitudes of the available modes, thereby influencing the spatial decay, interference, and visibility of their measured superposition.

The finite propagation length of g-HP modes arises due to intrinsic material losses and modal dispersion. Inside anisotropic polar crystals such as calcite, the permittivity is frequency-dependent and exhibits dispersive behaviour due to phonon damping. This behaviour can be described using a Lorentz oscillator model.

$$\varepsilon(\omega) = \varepsilon_\infty \left(1 + \frac{\omega_{LO}^2 - \omega_{TO}^2}{\omega_{TO}^2 - \omega^2 - i\omega\Gamma}\right)$$

Where, Γ represents phonon damping, ω_{TO}, ω_{LO} are transverse and longitudinal optical phonon frequencies. The imaginary component of the permittivity introduces absorption, resulting in complex-valued wavevectors and therefore finite propagation lengths for all polariton modes. To quantitatively determine the dispersion and propagation characteristics of g-HP modes, the full electromagnetic boundary problem at the calcite-air interface must be solved. For a given in-plane wavevector (k_x, k_y), the eigenmodes in both media are first obtained.

In air ($z > 0$), the wavevector is given by:

$$\vec{k}_1 = [k_x, k_y, k_{1z}]$$

$$k_{1z} = i\sqrt{k_x^2 + k_y^2 - k_0^2}$$

The eigenmodes can be decomposed into two independent solutions, corresponding to the plane wave solutions with TM and TE polarizations:

$$\vec{E}^{\mathrm{TM}} \sim \left[-k_x k_{1z}, -k_y k_{1z}, k_x^2 + k_y^2\right]$$

$$\vec{E}^{\mathrm{TE}} \sim [-k_y, k_x, 0]$$

For eigenmodes inside calcite, denote the wave vector as:

$$\vec{k}_2 = [k_x, k_y, k_{2z}]$$

Two solutions exist and for the ordinary wave ($\vec{E}^o$) we use

$$\vec{E}^o = k_{2z} = -i\sqrt{k_x^2 + k_y^2 - \epsilon_\perp k_0^2}$$

to make sure that the electric field decays to zero when $z \to -\infty$. For the extraordinary wave ($\vec{E}^e$) two k_{2z} solutions are obtained by solving the quadratic equation. Note that only the solution which satisfies $\mathrm{Im}[k_{2z}] < 0$ will be used Once the valid k_{2z} values are obtained, the

corresponding electric field $\vec{E}^o$ (o-wave) and $\vec{E}^e$ (e-wave) can be derived by solving the source-free Maxwell's equation:

$$\vec{E}^e = \vec{k}_2 \times \vec{k}_2 \times \vec{E} + k_0^2 \bar{\bar{\epsilon}} \cdot \vec{E} = 0.$$

which is a linear equation with respect to E_x, E_y, E_z components. The g-HP mode is constructed as a superposition of eigenmodes in both regions (calcite and vacuum). Specifically, in $z > 0$ region the electric field distribution can be written as:

$$\vec{E}(z > 0) = a^{\mathrm{TE}}\vec{E}^{\mathrm{TE}} + a^{\mathrm{TM}}\vec{E}^{\mathrm{TM}}$$

while in $z < 0$ region the electric field distribution can be written as:

$$\vec{E}(z < 0) = a^o\vec{E}^o + a^e\vec{E}^e$$

where $a^{\mathrm{TM}}/a^{\mathrm{TE}}$ and a^o/a^e are the coefficients of eigenmodes inside air and calcite, respectively. Applying the continuity of tangential field components (E_x, E_y, H_x, H_y)at the interface (at $z = 0$) leads to a system of linear equations:

$$A \cdot \mathbf{a} = 0$$

$$\begin{pmatrix} E_x^o & E_x^e & -E_x^{\mathrm{TM}} & -E_x^{\mathrm{TE}} \\ E_y^o & E_y^e & -E_y^{\mathrm{TM}} & -E_y^{\mathrm{TE}} \\ H_x^o & H_x^e & -H_x^{\mathrm{TM}} & -H_x^{\mathrm{TE}} \\ H_y^o & H_y^e & -H_y^{\mathrm{TM}} & -H_y^{\mathrm{TE}} \end{pmatrix} \begin{pmatrix} a^o \\ a^e \\ a^{\mathrm{TM}} \\ a^{\mathrm{TE}} \end{pmatrix} = \vec{0}$$

A non-trivial solution exists only when the determinant of this system vanishes:

$$\det(A) = 0$$

$$\det(A) = \begin{vmatrix} E_x^o & E_x^e & -E_x^{\mathrm{TM}} & -E_x^{\mathrm{TE}} \\ E_y^o & E_y^e & -E_y^{\mathrm{TM}} & -E_y^{\mathrm{TE}} \\ H_x^o & H_x^e & -H_x^{\mathrm{TM}} & -H_x^{\mathrm{TE}} \\ H_y^o & H_y^e & -H_y^{\mathrm{TM}} & -H_y^{\mathrm{TE}} \end{vmatrix} = 0$$

This condition defines the dispersion relation of the g-HP modes. For any given g-HP mode lying on the IFC, both the real and imaginary components of the in-plane k_x, k_y can be calculated numerically. The corresponding coefficients a^{TM}, a^{TE}, a^o, a^e, and electromagnetic field distributions, can then be obtained numerically.

To investigate the variation in intrinsic modal attenuation across the isofrequency contour, the field-amplitude propagation lengths of the numerically calculated g-HP eigenmodes were evaluated using the magnitude of the imaginary in-plane wavevector, as defined previously.

The resulting propagation lengths, normalised to the free-space wavelength λ_0, are presented in Figure 3.3.

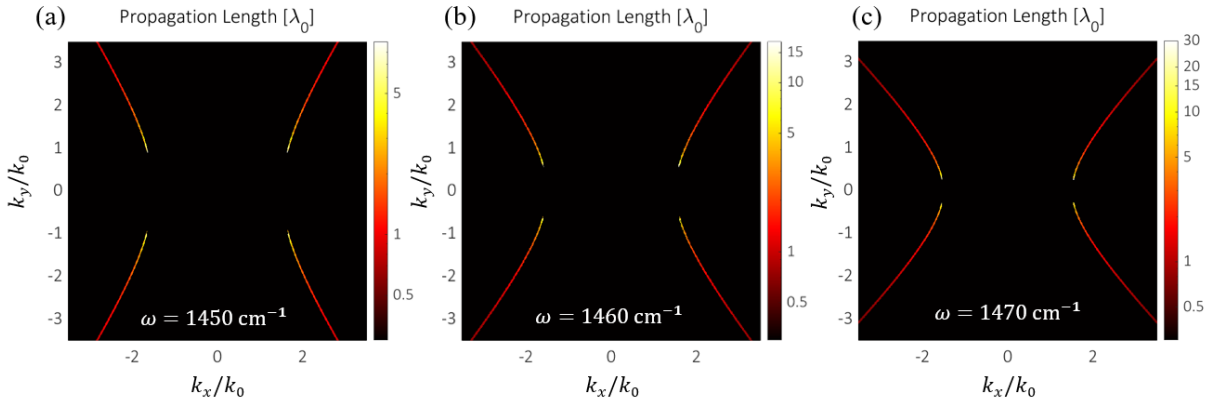


Figure 3.3 | Momentum-space visualization of g-HP propagation lengths on the IFC. a – c, Numerically calculated propagation lengths normalized to the vacuum wavelength λ_0 for excitation at $\omega = 1450\ cm^{-1}, 1460\ cm^{-1}\ and\ 1470\ cm^{-1}$.

These results illustrate the variation in intrinsic propagation characteristics between different polariton modes, independently of the antenna geometry used for excitation. There are several points that we observed through this numerical analysis.

- While high-k g-HP modes cannot propagate long, the propagation length L_p can be large ($> 10\lambda_0$) for certain low-k g-HP modes.

For example, at 1470 cm^{-1} the predicted L_p of the g-HP mode located at $(\mathrm{Re}k_x, \mathrm{Re}k_y) = (-1.544k_0, -0.295k_0)$ can exceed $162.7\ \mu$m, which is remarkable and justifies the improvement in this work.

- For small $|k_y|$, no valid g-HP solution can be found numerically, meaning that g-HP mode does not exist if the angle is too small.

We've verified that this behaviour comes from the fact that neither of the two k_{2z} solutions for e-wave can satisfy the $\mathrm{Im}(k_{2z}) < 0$ condition. Without a valid e-wave mode, the g-HP mode cannot be constructed by imposing the boundary conditions, leading to a large $|\det(A)|$ value. The directionality angle increases with increasing frequency, consistent with the literature and our experimental results[16,19].

3.1.4 Numerical simulation techniques

The simulations for this work were primarily carried out by my collaborator, Qingyi Zhou, at the University of Wisconsin-Madison. COMSOL Multiphysics 5.1 was used to simulate the electric-field distribution of g-HPs excited by a gold antenna. The simulations were designed to replicate experimental conditions. Since the s-SNOM system that we use has an oblique incident, the simulations were with a p-polarized plane wave, with a defined incident angle ($\varphi = 60^{\circ}$) was used to excite the nano/micro antennas. This configuration ensures efficient field confinement at the antenna, enabling the launch of polariton waves along the calcite surface. The scattered electric field was computed using the finite-element method, and the near-field intensity was evaluated at a plane located 100 nm above the calcite surface to enable direct comparison with experimental s-SNOM measurements The frequency-dependent permittivity of calcite was modelled using a Lorentz oscillator model:

$$\varepsilon_{\perp} = \varepsilon_{\infty,1}\left(1 + \frac{\omega_{LO,1}^2 - \omega_{TO,1}^2}{\omega_{TO,1}^2 - \omega^2 - i\omega\Gamma_1} + \frac{\omega_{LO,2}^2 - \omega_{TO,2}^2}{\omega_{TO,2}^2 - \omega^2 - i\omega\Gamma_2}\right)$$

$$\varepsilon_{\parallel} = \varepsilon_{\infty,3}\left(1 + \frac{\omega_{LO,3}^2 - \omega_{TO,3}^2}{\omega_{TO,3}^2 - \omega^2 - i\omega\Gamma_3}\right)$$

The optic axis is initially aligned along the y-axis and subsequently rotated about the x-axis by $\theta = 23.3^{\circ}$ consistent with the experimental geometry.

The permittivity of gold (Au) was taken from experimentally measured data[20]. Within the wavelength range of interest, gold exhibits a large negative permittivity. As a result, the gold antenna behaves similarly to a perfect electric conductor (PEC): with negligible electric field inside the metal. Solving Maxwell's equations in the frequency domain for anisotropic materials such as calcite can lead to poor convergence when iterative solvers are used. Therefore, the direct solver "PARDISO" is used in all our COMSOL simulations.

3.2 Selective mode excitation via antenna engineering

3.2.1 Conventional excitation

As discussed in the previous section, calcite can generate a broad range of modes across the IFC. These modes exhibit significantly different propagation lengths depending on their loss characteristics. Low-k modes exhibit long propagation distances, whereas high-k modes decay more readily while being tightly confined. This variation in propagation length across the IFC

highlights the importance of selectively exciting low-loss modes to achieve long-range propagation.

In most experimental studies in literature, PhPs are excited using localized sources such as AFM tips or symmetric metallic nanoantennas (e.g., disks), which strongly confine the incident electromagnetic field and enable efficient coupling to phonons. These excitation sources can be approximated as dipole emitters, generating highly localized fields in real spaces. As a consequence, they produce a broad Fourier spectrum containing a broader range of in-plane momenta. These sources efficiently excite polaritons but can introduce limitations for controlled excitations of PhPs or in this case g-HPs.

While this enables efficient excitation, it also introduces several limitations. First, multiple polariton modes across the IFC are excited simultaneously, rather than selectively. As a result, the injected energy is distributed across modes with different propagation characteristics. These modes can also interfere with each other as they propagate leading to complex wavefronts and reduced control over directionality. While localized dipole-like sources enable efficient polariton excitation, they generally couple to a broad range of wavevectors along the IFC. Consequently, multiple g-HP modes with different intrinsic attenuation characteristics can be excited simultaneously. The resulting near-field distribution represents a superposition of these modes, whose relative amplitudes, propagation directions, and interference determine the observed spatial envelope. Although long-lived, low-loss modes may also be excited, their contribution to the measured field can be less prominent when other momentum components are strongly excited. Therefore, broadband excitation can produce a spatially complex near-field response with a relatively short effective decay length along a selected observation direction. This motivates excitation strategies that preferentially couple energy into a restricted range of long-lived modes, improving the directionality and spatial extent of the observed polariton field without modifying the intrinsic attenuation of the individual modes.

3.2.2 Directional propagation tuning through excitation

A key requirement for achieving selective excitation of polariton modes is the breaking of spatial symmetry in the excitation process. In symmetric excitation geometries, such as disk antennas, the structure is rotationally invariant, and all directions in momentum space are equivalently accessible. As a result, polariton modes are excited symmetrically across the IFC leading to nearly identical excitation of the four polaritonic branches defined as (U+, U−, L+, L−) (Figure 3.4a) and producing symmetric hyperbolic propagation patterns.

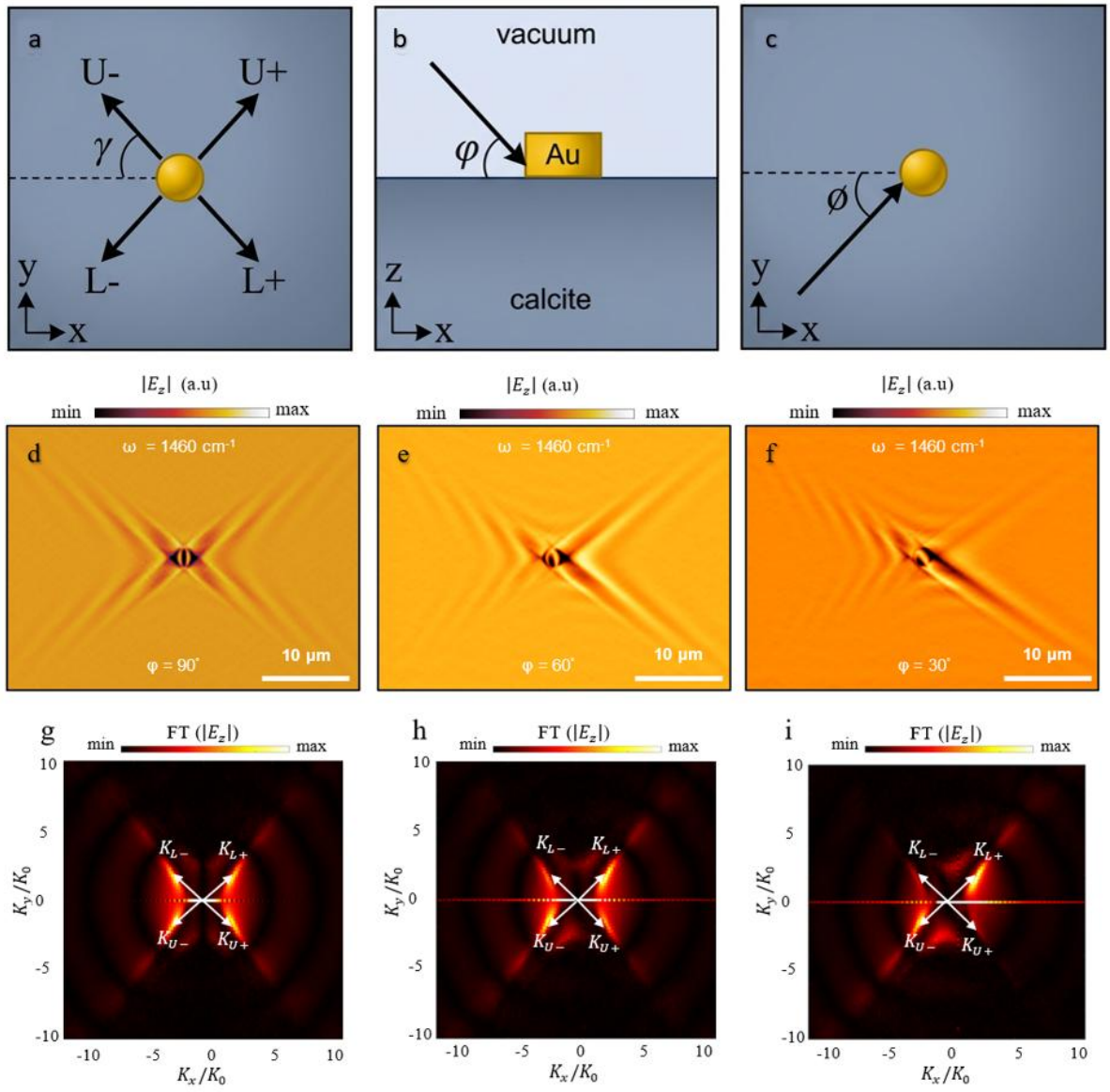


Figure 3.4 | Polariton parameters and asymmetric excitation scheme. a, Schematic of the four polariton branches of polaritons U+ (upper positive), U- (upper negative), L+ (lower positive), L- (lower negative) together with the propagation direction angle γ. **b,** Schematic of the illumination geometry, where the incident angle $\boldsymbol{\varphi}$ is measured relative to the sample surface (x-y plane). **c,** Schematic of the polarization angle, corresponding to the incident angle of the photon in the x-y plane. **d-f**, Simulated near-field images of antenna-excited g-HPs. **g-i**, Fourier transformed $|\boldsymbol{E_z}|$, corresponding to the disk-antenna excitations shown in (d–f). The white arrows indicate the wave vectors of the modes excited by the antenna.

To introduce directionality, several approaches can be explored, including variation of the incident angle, polarization control, and geometrical asymmetry. First, we examine the effect of the incident angle φ, as illustrated in Figure 3.4(b).We observe a change in the intensities

propagating through the 4 different polariton branches. When it is a normal incident ($\varphi = 90^{\circ}$) the propagation is symmetric in all directions as evident from the simulation results shown in Figure 3.4d. If we further analyse the data in Fourier space, we can see that the gold antenna, when coupled to normal incident light, excites modes across all four branches simultaneously (Figure 3.4g), as indicated by the 4 bright, symmetrical regions in the FT image. As the incident angle deviates from normal incidence, we observe a slight asymmetry in the propagation of the four polaritonic branches.

The formation of these symmetric g-HPs on the right and left sides of the disk antenna can be explained by the localized electric fields on either side of the nanometallic disk. As illustrated in Figure 3.5a and b, if the Au antenna is excited with a normal incident, the two ends of the Au antenna will have a symmetric E field distribution, resulting in a symmetric polariton mode excitation. If the Au antenna is excited with an oblique incident as illustrated in Figure 3.5 panel c, a larger E field, which indicates a higher local photonic DOS, is confined at the right side of the Au antenna. This allows the right side to excite more polaritons, leading to preferential excitation of polaritons on that side. At the same time, in both cases, the excited polaritons will propagate away from the metal disk, and therefore the interference fringes that we observe will have equal distributions in the normal incident case but will showcase different gaps between fringes in the oblique incident case.

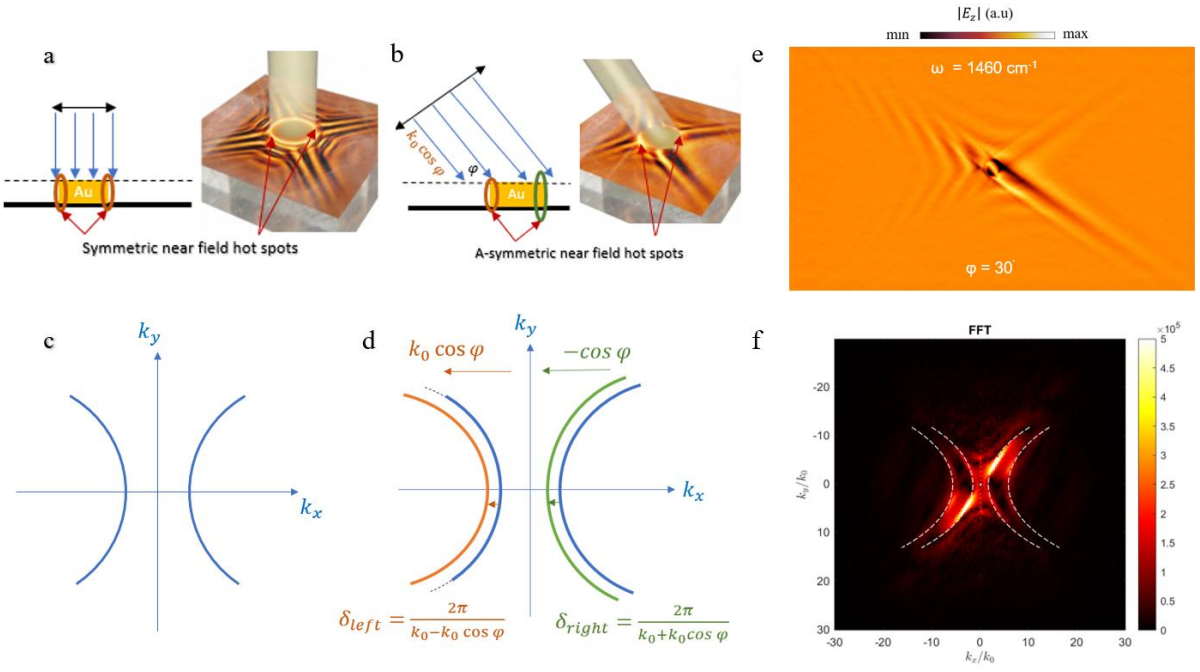


Figure 3.5 | Asymmetric distribution of g-HPs under oblique excitation. a, b, Schematic illustrations of the excitation conditions for (a) normal and [16] oblique incidence, showing the

corresponding symmetric and asymmetric field confinement (hot spots) at the two edges of the nanoantenna. **c, d,** Isofrequency contours (IFCs) for the normal and oblique excitation cases in a and b, respectively, highlighting the shift in the IFC under oblique incidence due to asymmetric excitation. **e,** simulated electric field distribution of a disk nanoantenna under oblique incidence, demonstrating the asymmetric field profile. **f,** Corresponding FFT of e, revealing the presence of two IFC branches and their relative shift.

The spacings of the illumination fringes on the left side are $\delta_{left} = \frac{2\pi}{k_p - k_0 \cos\varphi}$. This explains the larger gap between the fringes that is observe on the left side in the oblique incident compared to the normal inside as evident by comparing Figure 3.4 panel d and e. Similarly, the illumination fringe spacing on the right side is $\delta_{right} = \frac{2\pi}{k_p + k_0 \cos\varphi}$ which explains why the right-side fringes look merged together to form a ray like propagation. This asymmetric distribution occurred due to the difference in energy confinement at the two ends of the antenna (Figure 3.5 e).

As illustrated in Figure 3.5f, oblique illumination produces an apparent displacement and asymmetry of the Fourier-space features associated with the excited polariton interference patterns (two different hyperbolic IFCs in k-space with a shift of $\pm k_0 \cos\varphi$). This displacement arises from the contribution of the in-plane illumination wavevector and the interference between the polariton and reference fields, rather than a modification of the intrinsic g-HP dispersion. Such illumination-dependent shifts in the apparent Fourier contours were also discussed by Ma et.al[16]. Therefore, the observed Fourier-space response reflects both the underlying polariton modes and their excitation and interference conditions.

In addition to the excitation angle, the polarization angle $\emptyset$ can be controlled to tune the directional excitation of polaritons, as observed in the simulation results. This effectively introduces an additional degree of freedom in the excitation technique for such polaritons to achieve directional propagation. As illustrated in Figure 3.6, the light is excited with the oblique incident angle $\varphi = 60^{\circ}$, but for each simulation a-e, the excitation angle in the x-y plane (polarization angle $\emptyset$) has changed. This clearly affects the symmetry of the polariton excitation at the surface, and when the polarization of the light is aligned along a principal axis ($\emptyset = 0^{\circ}$), the induced field distribution is symmetric (the slight asymmetry we observe is due to the incident angle in the x-z plane $\varphi = 60^{\circ}$). But as shown in panels b and c, when the polarization angle is changed from $\emptyset = 0^{\circ}$ to $\emptyset = 30^{\circ}$ till $\emptyset = 60^{\circ}$ the polariton-propagating directions U-

and L+ become more dominant, making the propagation directional. Here, when the polarization angle is rotated, the projection of the E field onto the metal disk antenna becomes asymmetric, leading to an uneven local field confinement and intensity.

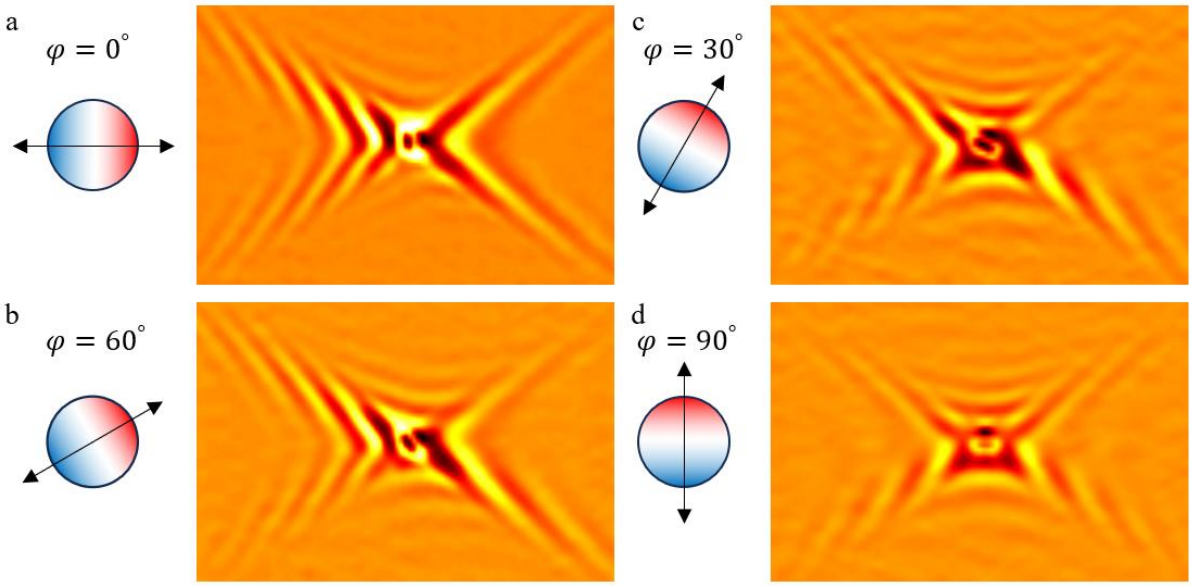


Figure 3.6 | Asymmetric distribution based on the different polarization angle excitation. a-d, left panel: polarization angle and the dipolar electric field of the disk nano antenna. right panel: Simulated near-field g-HPs distribution at the illumination frequency of ω = 1460 cm^{-1} with an incident angle of $\varphi = 60^{\circ}$.

This asymmetry in the local field modifies the local photonic DOS across different regions of the antenna, enhancing propagation of g-HPs in specific directions. This is the ability to alter the coupling efficiency between the incident wave and the polaritonic modes on the IFC in the Fourier space. While we observed these effects of incident light on the directionality of polariton mode propagation, another work also reported this in detail[18]. These results explain how a-symmetric g-HPs can be excited using metallic nano- and micro-antennas. However, from an application perspective, this approach alone is not sufficient. Therefore, in this chapter, we explore other techniques to control the directionality and excitation of these polariton modes, not only by controlling excitation via the light source or intrinsic material properties, but also by introducing engineering solutions for mode selection and polariton excitation with greater tunability.

3.2.3 Engineering the nano antenna shape for tuning polariton excitation

This section details how different shapes of the nano antenna affect the excitation of the g-HPs. The antenna geometries were chosen to balance fabrication simplicity with sufficient structural complexity to enable tunable polariton excitation. We first consider the simplest structure, a disk antenna, and investigate how varying its diameter influences polariton excitation (Figure 3.7).

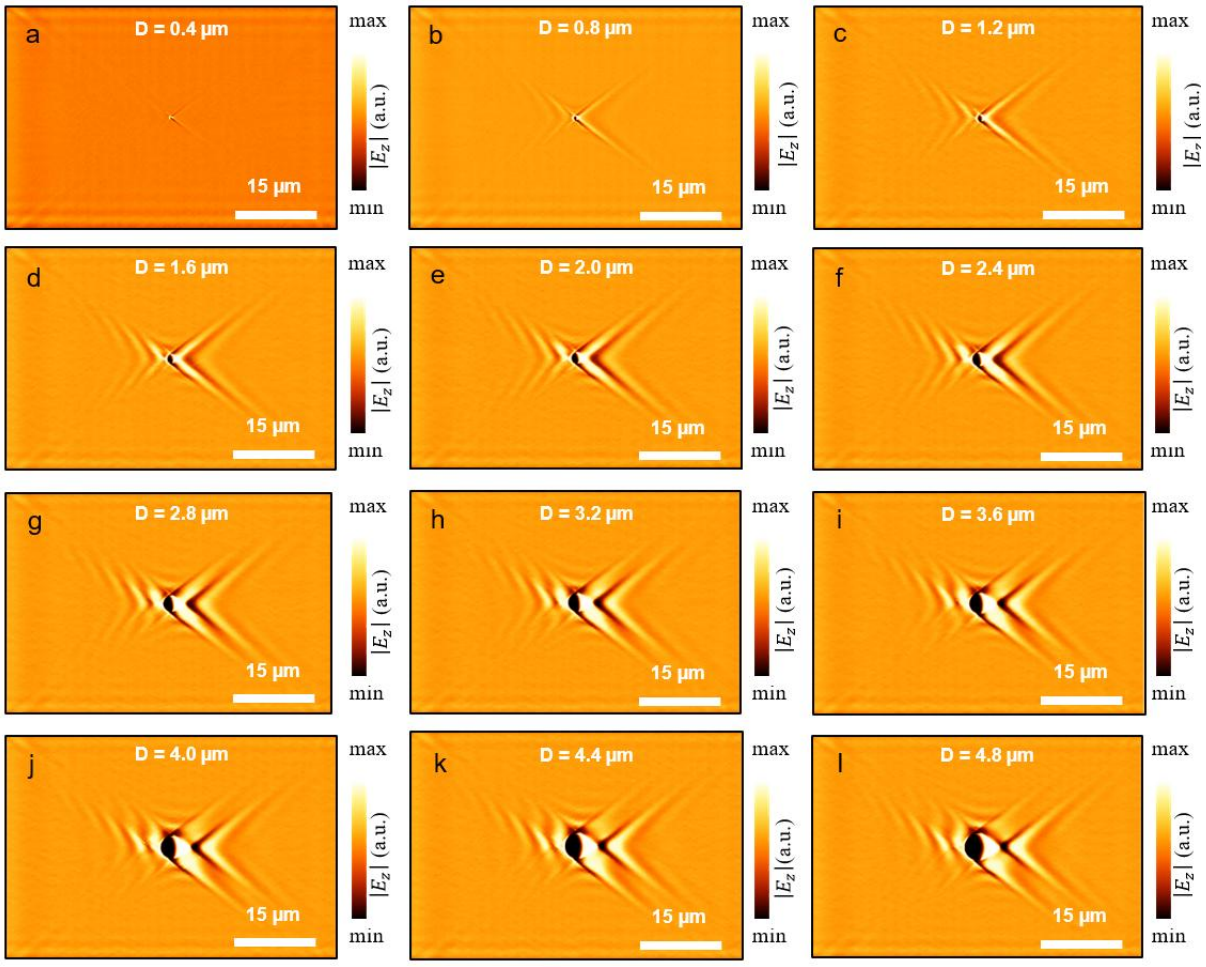


Figure 3.7 | Comparison of polariton propagation lengths for disk nanoantennas of different sizes. a-l, Simulated near-field images of disk-launched hyperbolic polaritons for a range of disk antenna sizes at an illumination frequency of 1460 cm^{-1}.

When the disk diameter is reduced, the disk becomes smaller and confines light strongly, coupling it to high-k modes, resulting in ray-like propagation. Notably, even these high-k modes in calcite can propagate over ~16 µm, which is relatively long compared to other phonon polariton systems. When the disk gets bigger, the excitation becomes more complicated, instead of behaving as a single dipole, multiple excitation points emerge along the antenna perimeter

leading to more complex fringe patterns. But increasing the diameter does not tune the directionality or the propagation length, it primarily modifies the distribution of excited modes without enabling selective excitation. When the diameter is larger, it confines more energy, but rather than having a high-intensity local field, it has a complex E field that couples the energy to many modes, including low- and high-k propagation modes. This indicates that simply modifying the antenna size does not provide sufficient control over the momentum distribution of excited modes and therefore cannot achieve true mode selectivity.

Instead of limiting to a disk structure, we explored a few other shapes, including an ellipse, a square, a rectangle, and a triangle with different sizes and geometrical conditions. First, Numerical simulations were performed for these geometries under varying size parameters and excitation conditions, as shown in Figure 3.8. The simulations reveal that polariton excitation is predominantly localized at the edges of the structures, with multiple excitation points becoming more prominent as the antenna size increases. These results indicate that the curvature of the antenna vertices plays a key role in determining which momentum components are excited on the IFC. Sharper features tend to excite higher-k components, while smoother or more extended features allow coupling to a broader range of modes. To analyse all these in actual fabricated samples, we fabricated these structures and explored the s-SNOM images as discussed in section 3.3.

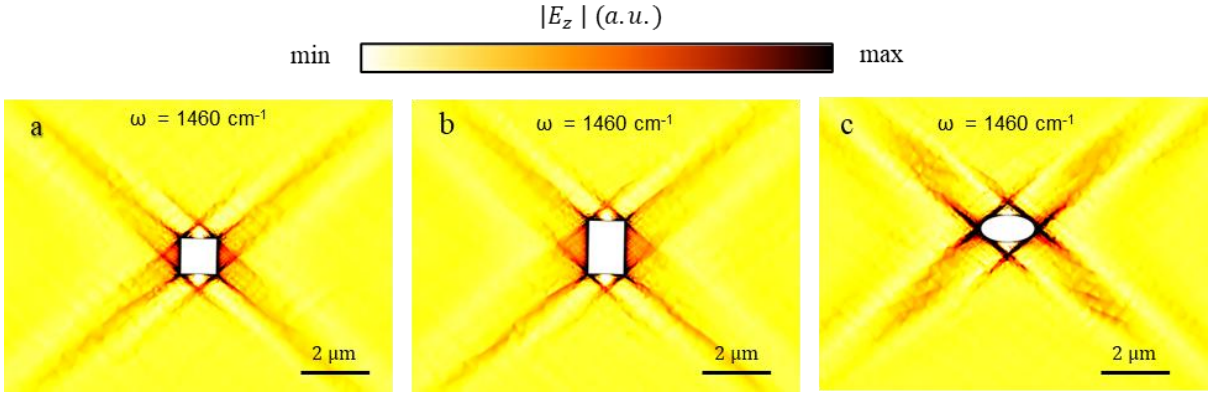


Figure 3.8 | g-HPs excitation through different shapes. a-c, simulated near-field images for different shaped, square 1x1 μm (a), rectangle 1x2 μm(b) and an ellipse micro antenna launched hyperbolic polaritons for the illumination frequency 1460 cm^{-1}.

3.2.4 Directionality metric and observed directional propagation

To quantitatively evaluate the degree of directional excitation, a directionality parameter is introduced based on the relative near field amplitudes of the upper and lower polariton branches. The directionality factor β is defined as:

$$\beta = \left| \frac{\text{Amplitude of the upper polariton branch}}{\text{Amplitude of the lower polariton branch}} \right|$$

The directionality parameter was evaluated using the experimental s-SNOM line-cut profiles extracted from the U- and L- polariton branches. The line cuts were selected to provide maximum fringe contrast, and the corresponding branch amplitudes were determined from the difference between the maximum and minimum near-field signal values. The ratio of these amplitudes was used to calculate β values, as discussed in section 3.4.1. This analysis quantifies the relative excitation strength of the two branches rather than the selectivity of individual wavevectors along the isofrequency contour. This parameter provides a direct measure of the imbalance between different propagation channels (i.e., polariton propagating branches).

- $\beta \approx 1$: symmetric excitation (no preferred direction)
- $\beta > 1$: preferential excitation of one branch
- $\beta \gg 1$: strong directional propagation

For dipole-like or symmetric antennas, the excitation of polariton branches is nearly equal, resulting in $\beta \approx 1$. As asymmetry is introduced into the antenna geometry, the excitation becomes increasingly biased toward specific branches, and the value of βincreases, leading to more pronounced directional propagation. This directional behaviour is observed in real-space polariton patterns as the suppression of certain propagation directions, enhancement of others, and the formation of anisotropic, ray-like wavefronts. However, this parameter alone is not sufficient to fully characterize mode excitation and tunability. Therefore, Fourier-transformed (FT) images of both numerical and experimental data are used to analyse the distribution of excited modes on the IFC. While directional propagation can be achieved through antenna geometry, this does not necessarily imply selective excitation of a single mode. Directional bias can still arise from multi-mode excitation with unequal intensities, rather than true mode selectivity. In the next section, we introduce edge-assisted mode selection, which enables true mode selectivity and is validated through both simulations and experiments.

3.2.5 Edge assisted mode selection for directionality and long propagation

The ability to selectively excite specific ghost hyperbolic phonon polariton (g-HP) modes is governed by the interaction between the excitation source and the anisotropic dispersion of the material. As discussed in Section 3.2, previous studies have established that the directional propagation and excitation asymmetry of g-HPs can be controlled through the illumination conditions, source configuration, and antenna dimensions. The present analysis focuses more specifically on the distribution of excited polariton wavevectors along the isofrequency contour. While a localized dipole-like excitation can couple to multiple available polariton modes, introducing an extended antenna edge modifies the relative coupling strengths of these momentum components. In particular, the finite edge preferentially enhances wavevectors oriented approximately perpendicular to its direction, thereby restricting the dominant excited momentum range. This mechanism, referred to here as edge-assisted mode selection, provides an additional degree of control over the excited modal distribution through antenna geometry. By adjusting the edge orientation, vertex curvature, and overall antenna dimensions, the momentum-space excitation profile can be engineered to favour selected propagating modes, including components associated with longer propagation lengths.

The edge-normal momentum-selection rule provides an approximate description of the dominant excitation mechanism, assuming that the antenna edge can be treated as a locally straight and coherently excited source. For an ideal infinitely extended edge with uniform excitation, momentum selection would be strongly constrained by the translational symmetry along the edge. However, the finite length of the physical antenna edge introduces a finite momentum acceptance range, while nonuniform excitation, vertex curvature, and contributions from neighbouring edges can further broaden the excited momentum distribution. Therefore, the edge-normal construction identifies the preferentially excited momentum components rather than enforcing coupling to one exact wavevector. The experimentally observed mode distribution is consequently determined by the overlap between the antenna-induced momentum spectrum and the available polariton states along the isofrequency contour.

In this mechanism, the vertices of the antenna geometry excite polaritonic modes, and the sharpness of the vertex determines the range of momentum components that can be excited. Sharper vertices preferentially excite higher-k modes, while smoother or more curved vertices generate a broader distribution of momentum components. The key principle in this mechanism is that antennas with straight physical edges (e.g., square, rectangular, or triangular geometries)

can act as momentum-selective boundaries. Specifically, the antenna edges preferentially enhance coupling to polariton modes whose wavevectors are oriented perpendicular to the edge. Based on simulations of various geometries (Figure 3.8 and Figure 3.9), triangular antennas were selected due to their ability to independently control vertex curvature and edge orientation, providing greater flexibility in tuning momentum selectivity. The interplay between vertex-driven excitation and edge-induced momentum filtering enables selective coupling into a limited set of g-HP modes, and in some cases near single-mode excitation.

As shown in Figure 3.9a, the interaction between the IFC and the triangular antenna geometry determines which modes are excited. The momentum-space schematic shows the IFC for three different excitation frequencies $1430\ cm^{-1}$ (blue), $1460\ cm^{-1}$ (black), $1490\ cm^{-1}$ (red). The three vertices of the triangle antenna (A,B,C) are allowed to excite a set of modes on the IFC with respect to the excitation wavelength. As demonstrated, the angle δ can be tuned to change the position and angle of the AC physical edge. As shown in panel a, when the triangle vertex A excites a certain set of modes, the physical edge can selectively enhance the coupling efficiency of the mode on the IFC with momentum perpendicular to the physical edge. Thus, the edge acts as a momentum filter, selecting modes at the intersection between the IFC and the edge-normal direction. So, if we use the green triangle shape, the vector K_{e1} is a momentum vector corresponding to a mode on the IFC for excitation at $1430\ cm^{-1}$, and it is normal to the AC edge. Therefore, the triangle can effectively couple the mode M_{e1}, and the polariton will then propagate on the surface with a group velocity V_{ge1}. But if we use an excitation frequency like $1490\ cm^{-1}$, the triangle edge is not perpendicular to any of the modes on the respective IFC, so the AC edge cannot enhance the coupling of any modes for this excitation frequency.

Instead of using a single triangle and relying on the excitation frequency, if a specific mode or a set of modes needs to be excited selectively for a specific excitation frequency, the AC edge of the triangle can be tuned accordingly. As illustrated in the schematic in Figure 3.9b, the black IFC (for an excitation frequency of $1460\ cm^{-1}$) can excite any of the modes on the IFC. However, due to the confining limitations, only a limited region of the IFC can be excited, as highlighted in the yellow region. Within this range of the IFC, the A vertex of the triangle can excite a collection of modes, and the confinement ability (curvature of the vertex) determines how many and which k modes are excited, and how the coupling energy is distributed among them. But if the AC edge is perpendicular to any momentum vector of a mode allowed by the calcite substrate for $1460\ cm^{-1}$, the edge can strengthen the coupling and excite the mode selectively. As demonstrated in panel b, three different angles of δ generate three separate

triangles with different AC edge orientations. The smallest triangle with the smallest δ angle has an AC physical edge where the perpendicular direction to the AC edge (l_1 dotted line) does not intersect with any points on the IFC. Therefore, the smallest green-coloured triangular shape can't excite a single mode or assist efficient strong coupling to a single mode via the AC edge. As the angle δ increases, as demonstrated with the red and blue triangles, the perpendicular lines to those two respective triangles (l_2 and l_3 dotted lines) intersect with the IFC at two different points with momentum vectors k_{e2} and k_{e3}, so those two triangles can selectively excite too separate modes with different momenta. As evident by increasing the δ angle, lower-k modes can be selectively excited, and by tuning the δ properly, it is possible to excite any k mode allowed by the material at the excitation frequency. Therefore, by tuning the antenna geometry, it is possible to select specific regions of the IFC and target modes with desired propagation characteristics.

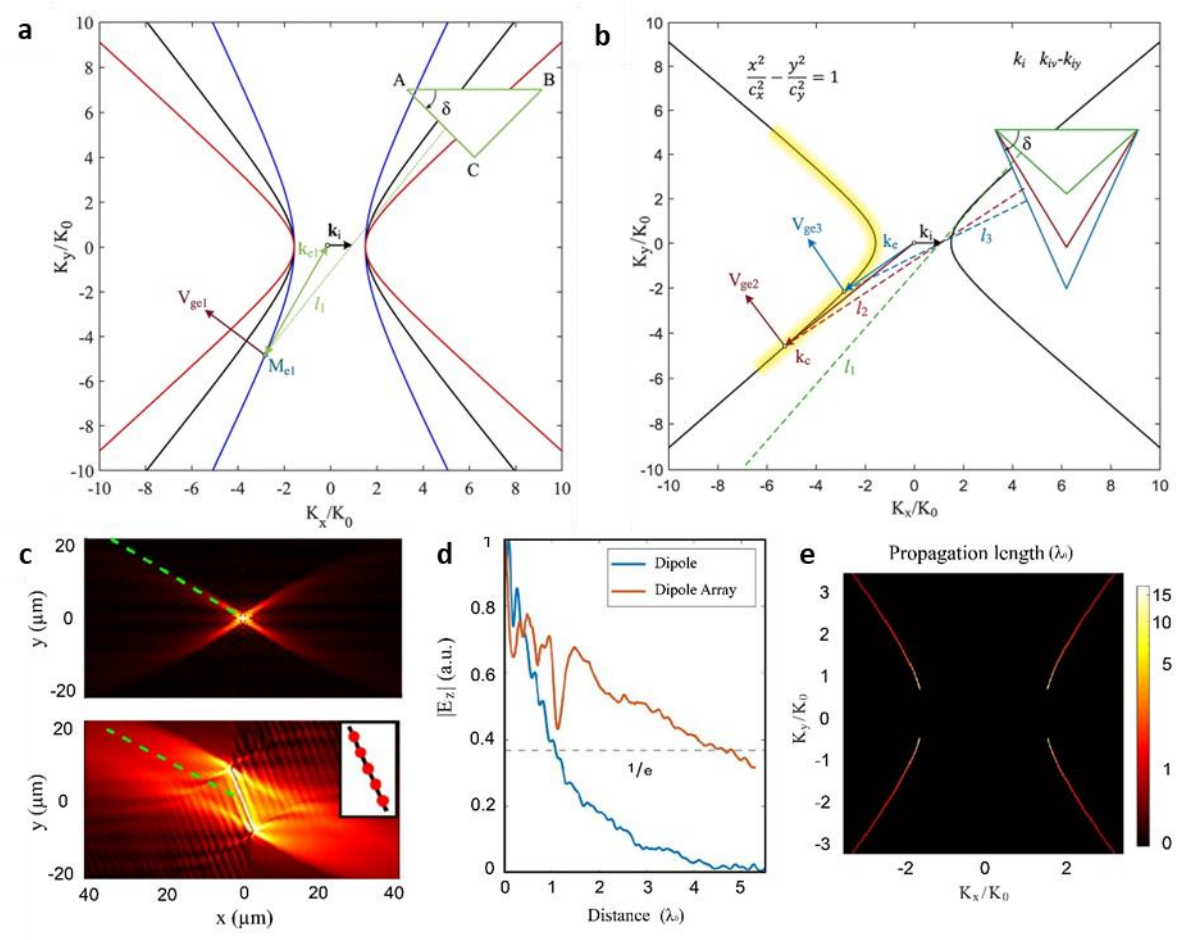


Figure 3.9 | Conceptual and theoretical description of the edge assisted mode selection mechanism. a, Schematic of frequency-dependent mode selection by a triangular antenna. The blue, black, and red solid curves show the IFCs of calcite at $1430\,cm^{-1}$,

$1460\ cm^{-1}, 1490\ cm^{-1}$ respectively. l_1 is the line normal to the AC edge, M_{e1} is the selected mode at the IFC and l_1 intersection. K_{e1} is the wave vectors and k_i is the incident wave vector. **b,** Schematic showing mode selection controlled by the triangle size. The black solid curve is the IFC at $1490\ cm^{-1}$. Green, red, and blue triangles correspond to $\delta = \delta_1, \delta_2, \delta_3$ with l_1, l_2, l_3 normal to the AC edge. M_{e2} , M_{e3} denote the selected modes and K_{e2} and K_{e3}, their corresponding wave vectors. **c,** Simulated g-HP excitation by a single dipole and by a dipole array with $N = 51$ dipoles and $d = 0.04\lambda_0$, matched to the mode at $k_x = -1.604k_0$, $k_y = -0.648k_0$ calculated at frequency $1460\ \text{cm}^{-1}$. **d,** $|E_z|$ linecuts taken along the green dashed lines in (a). (e) Momentum-space map of g-HP propagation lengths on the IFC at $1460\ \text{cm}^{-1}$, normalized to λ_0.

This selective excitation mechanism not only enables directional propagation but also plays a critical role in achieving long propagation lengths. As discussed in Section 3.1.3, the intrinsic propagation length of a given g-HP mode is determined by the imaginary part of its in-plane wavevector components and varies significantly across the IFC. Low-k modes exhibit substantially longer propagation lengths compared to high-k modes, as illustrated in Figure 3.3. Therefore, long-range propagation is not solely determined by material properties but is strongly dependent on how efficiently energy is coupled into low-loss modes. The intrinsic propagation length of an individual g-HP mode is determined by its complex wavevector and the associated material and electromagnetic properties of the calcite-air interface. As illustrated in Figure 3.3, different modes along the IFC can exhibit substantially different attenuation lengths. The antenna geometry does not modify these intrinsic modal properties in the uniform region away from the excitation source. Instead, it determines the relative excitation strengths of the available modes. By preferentially coupling incident light into a restricted momentum range containing long-lived polariton components, the antenna can produce a near-field distribution with a longer effective decay length and improved directional visibility. Thus, the observed enhancement in propagation distance arises from selective excitation of inherently low-attenuation modes, rather than a reduction in the material absorption or intrinsic damping of individual polariton modes.

To further understand this, we analyse the excitation behaviour using simplified models, as shown in Figure 3.9 (c-e). In the case of a conventional dipole-like excitation source, such as a small disk antenna or AFM tip, the excitation is highly localized in real space. This results in a broad distribution of momentum components in Fourier space, allowing simultaneous coupling to a wide range of g-HP modes across the IFC. Therefore, both low-k (long-lived) and high-k

(rapidly decaying) modes are excited. Since the injected energy is distributed among multiple modes with different propagation characteristics, the overall observed propagation is dominated by the faster decaying components, leading to a relatively short effective propagation length, as demonstrated in Figure 3.9c (top panel).

In contrast, when the excitation is extended spatially in a controlled manner, such as using a dipole array with a defined orientation, the coupling becomes highly selective. As shown in Figure 3.9c (bottom panel), a dipole array aligned along a specific direction preferentially excites modes with wavevectors matching this orientation. This effectively suppresses coupling to unwanted high-k modes and concentrates the energy into a narrow region of the IFC. The corresponding line profiles in Figure 3.9d clearly show a significantly slower decay for the dipole-array excitation compared to the single dipole case, indicating a substantial enhancement in propagation length. This behaviour can be directly correlated with the propagation length distribution shown in Figure 3.9e, where the selectively excited modes lie in the low-k region associated with long propagation distances.

Importantly, the triangular nanoantenna operates under a similar physical principle. While it is not explicitly a dipole array, its extended edges act as a distributed excitation source, effectively mimicking a collection of closely spaced dipoles. The vertices of the triangle provide the initial broad excitation, while the edges impose momentum-selective constraints, filtering out unwanted modes and enhancing coupling into specific low-k branches of the IFC. This combined effect enables efficient loading of energy into long-lived g-HP modes, thereby significantly increasing the observed propagation length.

Therefore, the long propagation demonstrated in this work does not arise from a reduction in intrinsic material losses, but rather from the ability to selectively excite modes with inherently low attenuation. This highlights the importance of excitation engineering in polaritonic systems, where controlling the distribution of energy in momentum space is key to accessing the full potential of long-propagating modes.

3.3 Sample Fabrication

To demonstrate the proposed concepts, a set of samples were fabricated as discussed in this section. Since hyperbolic dispersion is observed for the (100) crystal orientation, all results discussed here are based on samples fabricated on (100) calcite substrates. Micro- and nano-antennas were fabricated on the calcite surface using EBL. The fabrication process is illustrated in Figure 3.10.

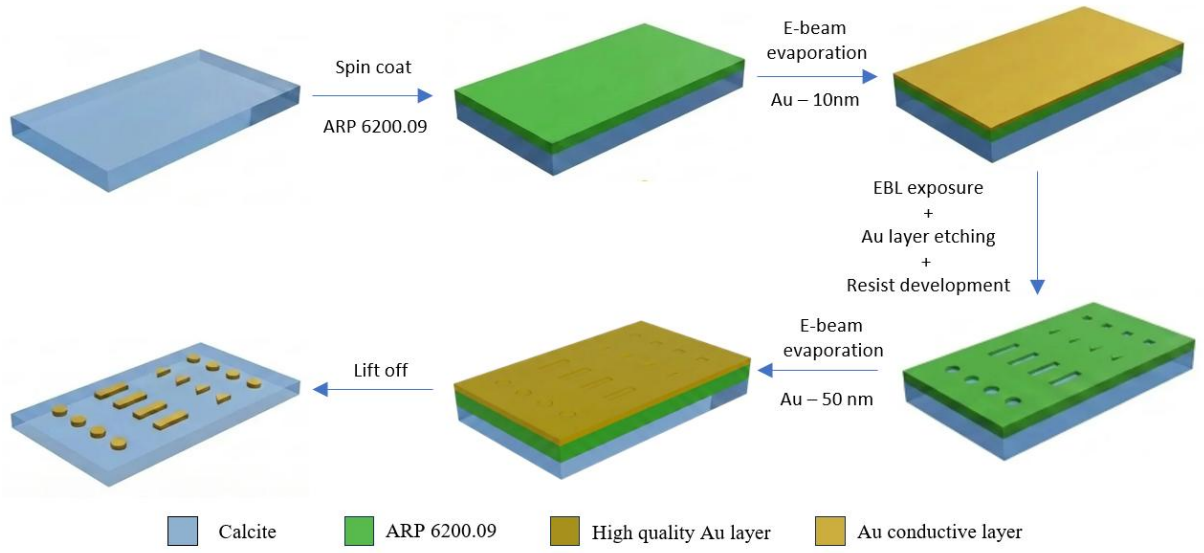


Figure 3.10 | Nano / Micro antenna fabrication process.

The fabrication process begins with spin-coating a high-resolution electron beam resist onto the calcite substrate (calcite substrate is 1x1cm with a thickness of 0.5mm). ARP 6200.09 resist was chosen after testing ZEP and different types of ARP resists. Although ZEP provides high-resolution patterning, its post-bake temperature (~180 °C) caused cracking of the calcite substrate, making it unsuitable for this process. The ARP 6200.09 resist was spin-coated in a two-step process: the sample was ramped to 3000 rpm over 5 seconds and maintained at this speed for 55 seconds. The one-minute spin-coating process deposited an ARP 6200.09 resist layer of 150–200nm. Then, a 10nm gold layer was deposited using a thermal evaporator to provide a conductive layer that minimizes charging effects during electron beam exposure. Then the sample was patterned using EBL (20 kV acceleration voltage, ~50 pA beam current, 10 nm step size, and ~100 μC/cm² dose). A dose factor of 0.6 was used for the exposure. After electron beam exposure, the sample was treated with an Au etchant to remove the Au layer, followed by cleaning with DI water. Then the sample was developed in the ARP developer solution for 1 minute, followed by a 1-minute dip in IPA solution for rinsing, then N_2 gas drying. Subsequently, a thin metallic Cr/Au (5nm/45nm) layer is deposited by E-beam evaporation. The Cr layer serves as the adhesion layer between the calcite substrate and the 45nm gold layer. The Au 45 nm layer is deposited under high vacuum pressure at $9e^{-6}\ Torr$. Then the sample was left in the ARP remover solution overnight to perform the lift-off, and the final antenna structures were obtained.

Three distinct antenna geometries, disks, rectangles, and triangles were fabricated using the same lithographic process on multiple calcite substrates that were mechanically cut along two different crystalline orientations (001) and (100) The antennas were patterned with varying sizes and orientations, and in some cases arranged as arrays to investigate collective excitation effects.

To systematically study the role of geometry, each antenna shape was designed to introduce a different level of symmetry. Disk antennas, being fully symmetric, act as reference dipole-like sources with no preferential directionality. Rectangular antennas introduce partial asymmetry, enabling a degree of directional bias in the excitation. In contrast, triangular antennas exhibit strong geometric asymmetry and are central to enabling mode-selective excitation in this work. These behaviours are validated through near-field imaging and numerical simulations, as discussed in the following sections.

3.4 Demonstration of edge assisted g-HPs through Near-Field Imaging

The excitation and imaging of g-HP modes were performed using an SNOM system as discussed in chapter 2.2.2. The mid-IR laser and the wavelengths within the Reststrahlen band of calcite are used for the characterization.

3.4.1 Shape dependent Directional excitation

Using disk, rectangle, triangle, and a few other antenna geometries, the g-HPs' excitation and propagation are demonstrated. This analysis highlights the role of antenna geometry in controlling g-HP excitation and propagation on the calcite substrate. The near-field experimental images, the corresponding numerical simulation results, and the FT images are presented in Figures 3.11-3.14. Figure 3.11(a-c) shows the experimentally measured s-SNOM near-field amplitude distributions of g-HPs launched by disk, rectangular, and triangular antennas respectively, at an excitation frequency of $\omega = 1460\ \mathrm{cm}^{-1}$. The corresponding numerical simulations shown in Figure 3.11(d–f) reproduce the observed propagation patterns with excellent agreement. Importantly, the simulations were performed without including the AFM tip, confirming that the observed interference fringes originate from the nanoantenna rather than tip-induced effects. This confirms that the nanoantenna acts as the primary excitation source for the g-HP modes.

As observed, a clear transition from symmetric to highly directional propagation occurs when the antenna shape is modulated from a disk to a triangle. As shown in Figure 3.11a, the disk

antenna excites polariton wavefronts symmetrically in both upper and lower branches. Minor asymmetry in fringe spacing arises from oblique illumination, as discussed previously. The symmetric distribution arises from the dipole-like nature of the disk antenna. The disk confines the incident field, generating a localized excitation with a broad momentum distribution across all four branches (U+, U−, L+, L−), as evident in Figure 3.11a. As a result, multiple modes across the IFC are simultaneously excited, leading to weak directionality (Figure 3.11g).

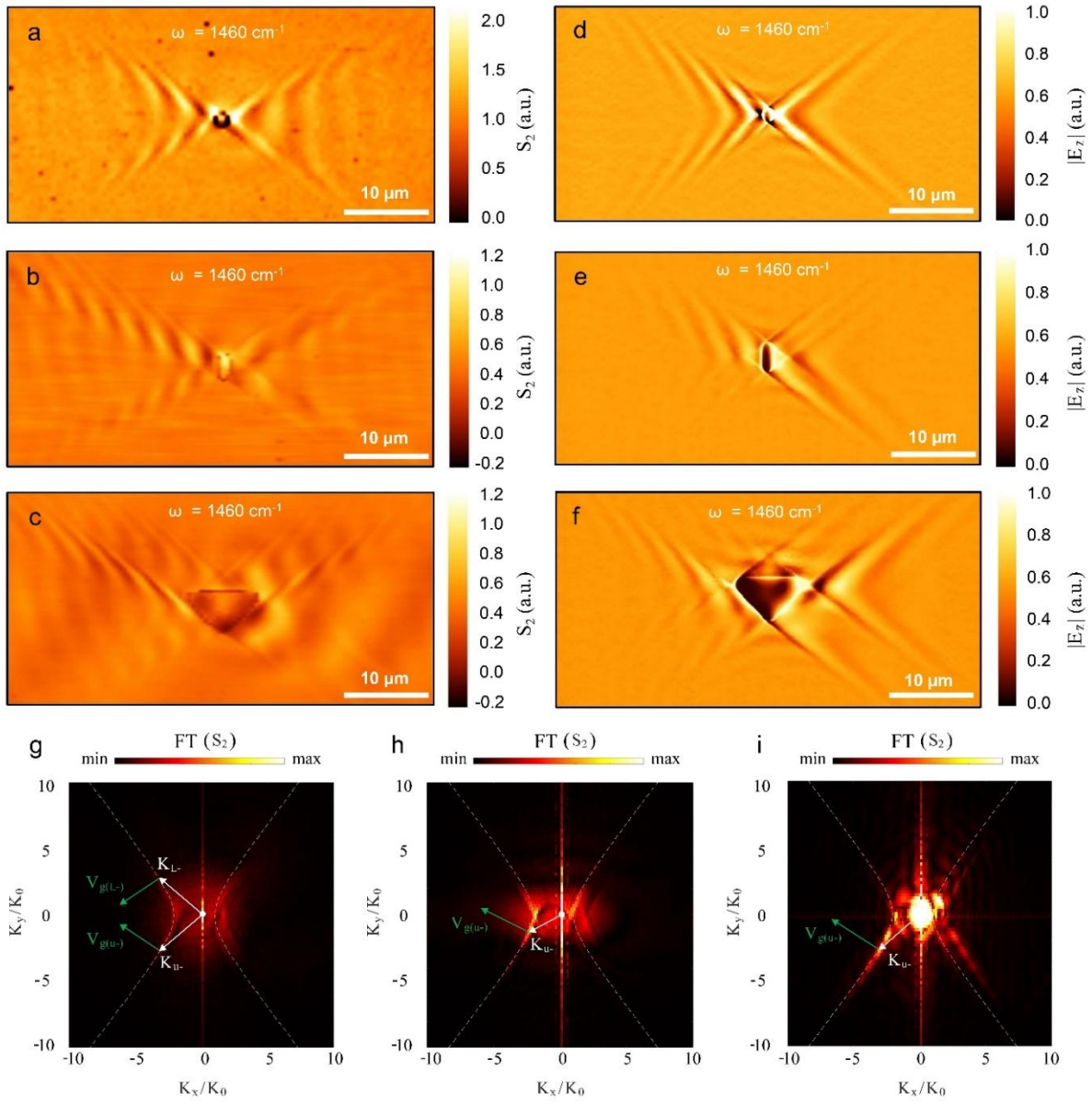


Figure 3.11 | Asymmetric g-HP excitation from shape dependent micro/nano antennas. a-c, Experimental near-field images of g-HPs launched by disk, rectangular, and triangular antennas at $\omega = 1460\ \mathrm{cm}^{-1}$. **d-f**, Corresponding simulated near-field images. **g-i,** Magnitude of the Fourier transforms of (a-c), where the bright features indicate the excited modes. White

arrows mark the wave vectors of the antenna-launched g-HPs, green arrows indicate the group velocity$V_{g(i)}$ and the white dotted curves show the left and right IFCs.

The directional propagation is quantified using two techniques. The first uses the directionality parameter β, defined as the ratio between the amplitudes of the upper and lower polariton branches. For the polaritons generated by the three shapes we calculated the amplitude profile of the upper and lower branches of the polariton by considering a line cut profile for the obtained results (Figure 3.12a, d and g). The line cuts were produced such that the polariton intensity contrast (ratio between the highest and the lowest values) is the maximum. For the three main nano antenna shapes the directionality constant results are as follows (amplitude values shown in Figure 3.12 c, f and i).

$$\beta_{disk} = \left|\frac{0.113}{0.108}\right| = 1.046$$

$$\beta_{rectangle} = \left|\frac{0.446}{0.149}\right| = 2.99$$

$$\beta_{triangle} = \left|\frac{0.474}{0.109}\right| = 4.348$$

The calculated value $\beta \approx 1$ for the disk shape antenna indicates nearly equal excitation of both branches, consistent with symmetric propagation. This is further confirmed by the FT images (Figures 3.11g and 3.12j). When the antenna geometry is modified to a rectangle (Figure 3.11b) and a triangle (Figure 3.11c), the polariton excitation and distribution becomes increasingly asymmetric. This is evident in the directionality parameter calculations, which show an increase in the directionality parameter ($\beta_{rectangle} = 2.99$ and $\beta_{triangle} = 4.348$), confirming preferential excitation of one polariton branch over the other. In momentum space, the FT images (Figure 3.11h,i) show reduced mode distribution, with intensity concentrated in fewer regions of the IFC. This indicates partial momentum selectivity, where certain modes are suppressed while others are enhanced. The most pronounced directional behaviour is observed for the triangular antenna. As shown in Figure 3.11c, the near-field image exhibits highly asymmetric, ray-like propagation predominantly along a single branch. The corresponding line-cut analysis (Figure 3.12g-i) results in a calculation of $\beta = 4.348 \gg 1$, demonstrating a pronounced imbalance between the upper and lower polariton branches and confirming the strongly directional excitation achieved using the triangular antenna.

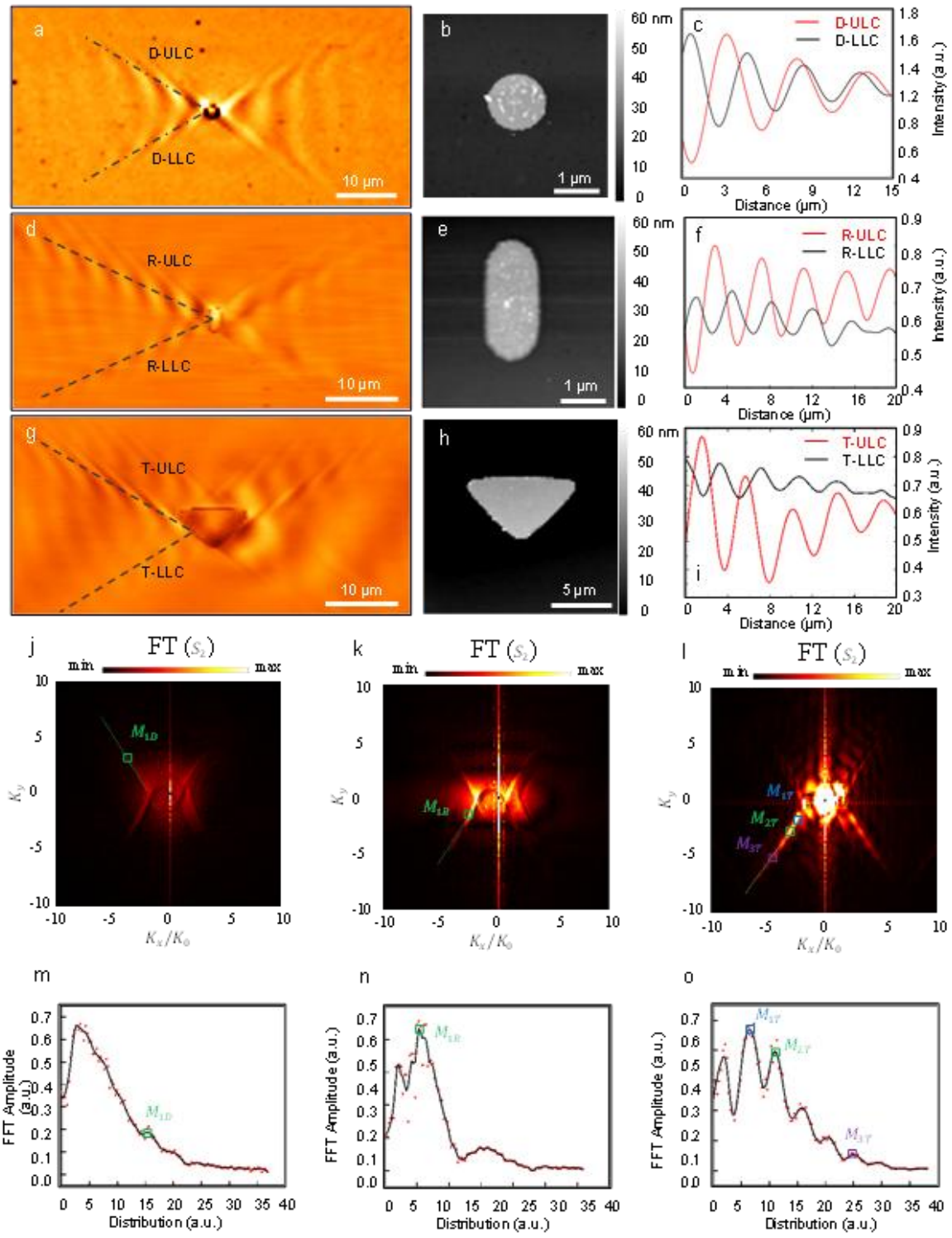


Figure 3.12 | Directionality analysis of g-HPs excited by antennas of different shapes. a, d, g, 50 μm × 25 μm s-SNOM images of disk, rectangular, and triangular antennas, respectively, with the upper- and lower-line cuts marked as D-ULC/D-LLC, R-ULC/R-LLC, and T-ULC/T-LLC. **b, e, h,** AFM images of the corresponding antennas: disk antenna (diameter = 1.5 μm), rectangle antenna (W × H = 1.2 μm × 3.2 μm), and triangle antenna (L × H = 8.8

μm × 4.9 μm). **c, f, i,** Upper and lower line-cut intensity profiles extracted from (a), (d), and (g). **j-l,** Absolute value of the Fourier transforms of the images shown in (a), (d), and (g). **m-o** FFT amplitude profiles taken along the green dotted lines in (j-l), showing the excited modes M_{1T} , M_{2T} , M_{3T}.

To further evaluate the momentum selectivity of the different antenna geometries, one-dimensional Fourier amplitude profiles were extracted along the selected momentum-space directions, as shown in Figures 3.12m-o. These profiles provide a consistent representation of the relative excitation strengths of different polariton wavevector components. While the disk antenna produces a relatively broad momentum distribution, the rectangular antenna exhibits a more pronounced dominant spectral feature. In contrast, the triangular antenna produces several distinguishable peaks corresponding to preferentially excited polariton modes M_{1T}, M_{2T} and M_{3T}. The FFT analysis further clarifies this behaviour. The FT image (Figure 3.12l) show discrete, localized bright spots corresponding to a limited number of excited polariton modes (M_{1T} , M_{2T} , M_{3T}). Unlike disk and rectangular antennas, the triangular antenna concentrates energy into specific regions of the IFC. This indicates strong momentum selectivity introduced by the antenna geometry. This demonstrates that momentum-space selectivity directly translates into directional propagation in real space.

As discussed above Fourier analysis was performed on the simulated and experimental near-field distributions to investigate the momentum-space characteristics of the excited g-HP modes. The numerical simulations provide the electromagnetic field distribution, from which the relevant field component or amplitude can be selected for Fourier analysis. For the experimental s-SNOM measurements, both the second-harmonic-demodulated near-field amplitude and phase were recorded, as shown in Figures 3.13a and 3.13b, respectively.

These measurements were combined to reconstruct the complex near-field signal according to,

$$E = A \times e^{i\emptyset}$$

where A and ∅ represent the measured near-field amplitude and phase. The Fourier transform of this reconstructed complex signal was then used to obtain the momentum-space distribution presented in Figure 3.13c. This complex-field reconstruction preserves the phase information that would otherwise be lost when Fourier transforming the amplitude alone. This Fourier analysis provides a direct link between real-space propagation patterns and the underlying modal distribution on the IFC.

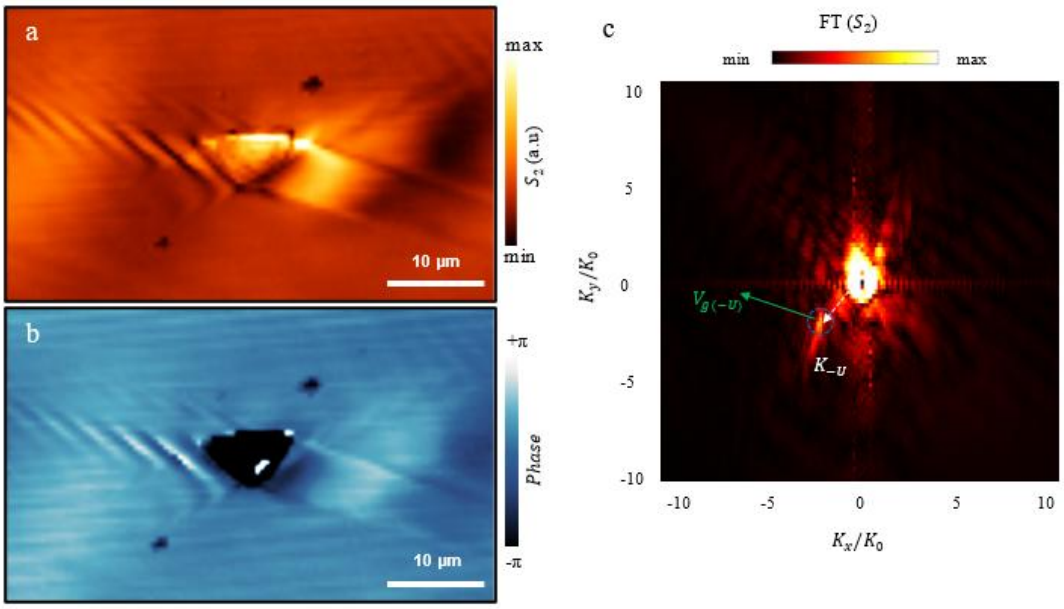


Figure 3.13 | Fourier analysis of the s-SNOM images. a, Experimental near-field amplitude image of g-HPs launched by a triangular antenna at the illumination frequency $\omega = 1440\ cm^{-1}$. **b,** Corresponding near-field phase image. **c,** Magnitude of the Fourier transform of the reconstructed complex near-field signal, obtained from the experimental s-SNOM amplitude and phase measurements in panels (a) and (b). The dotted blue circle marks the excited mode, the white arrow shows its wave vector, and the green arrow denotes the polariton group velocity.

To further understand the role of antenna geometry, the evolution of polariton excitation from symmetric to asymmetric structures is illustrated in Figure 3.14. We investigated polariton excitation behaviour through the experimental near-field results for a few different disk antennas with increasing diameters (see Figure 3.14a-c). As the diameter increases, the electric field distribution becomes more complex, allowing multiple curved points along the antenna edge to excite polaritons. As illustrated in Figure 3.14c, the disk antenna (radius = 2 µm) showcases four curved points (A-D) where polariton rays are excited. When the diameter decreases, these points come closer together, resulting in highly confined polariton excitations. If the disk structure is extended along the y or x axis to generate an elliptical shape, we observed that two curved points dominate the excitation of polariton modes. As illustrated in Figure 3.14d, the vertical ellipse with a major axis in the y direction (major axis = 8 µm, minor axis = 4 µm) excites two portions at curved points C and D. The interference fringes of both those excited polaritons (at points C and D) towards the left side (- branch) can be observed clearly.

So overall, disk and elliptical antennas exhibit smooth curvature, leading to multiple excitation points distributed along their edges and broad momentum excitation.

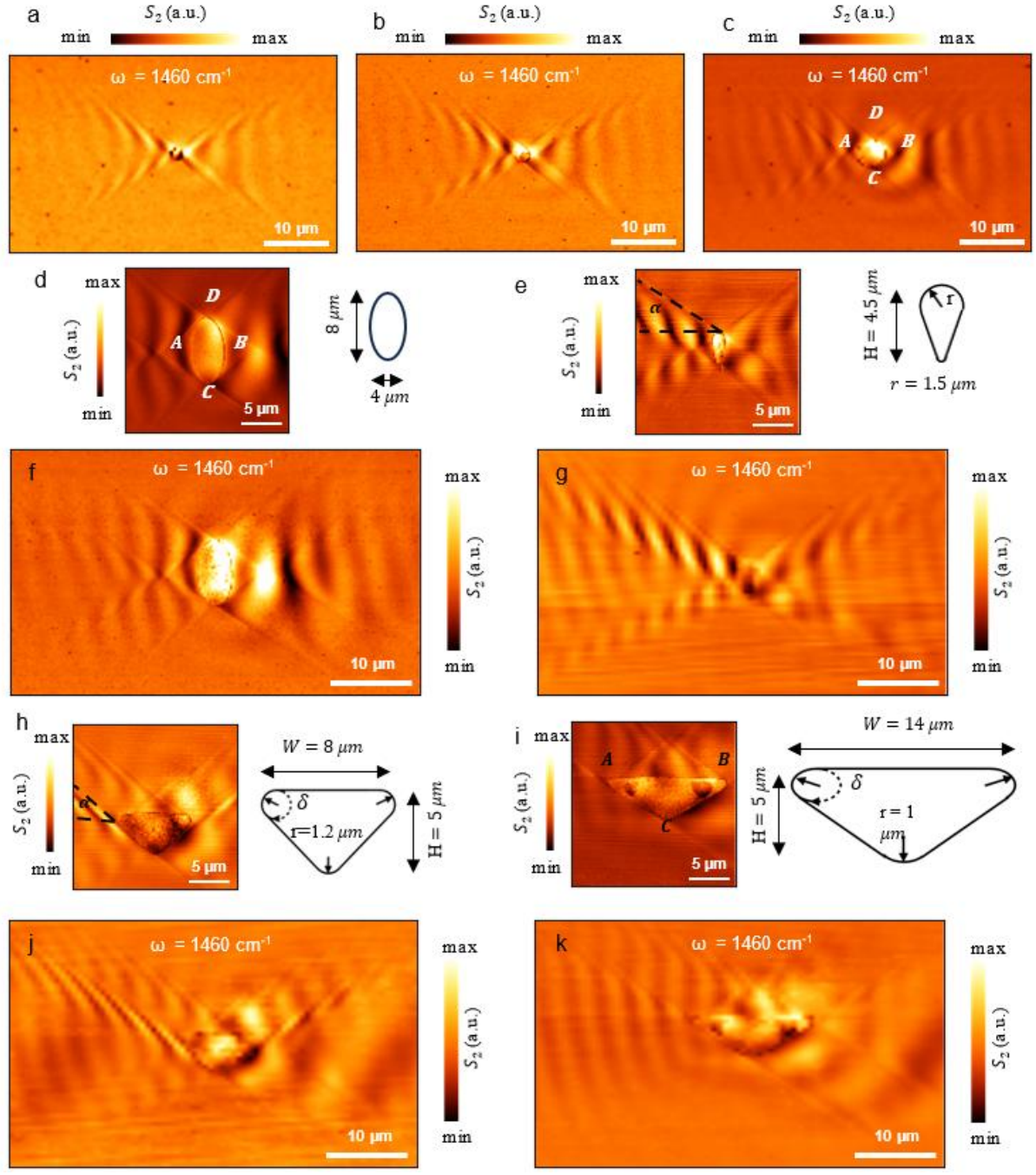


Figure 3.14 | Effect of antenna curvature and edges on polariton excitation from disk to triangular geometries. a-c, 50 × 30 μm s-SNOM images of disk antennas with radii of 0.75 μm, 1 μm, and 2 μm; A–D denote the four curved edge points. **d,** 20 × 20 μm near-field image and schematic of an ellipse antenna with minor and major axis diameters of 4 μm and 8 μm, respectively; A–D mark the curved edge points. **e,** 20 × 20 μm near-field image and schematic of a small triangular antenna with curved point D of radius of curvature 1.5 μm and height 4.5

μm; α is the open angle between the two dotted lines. **f, g,** 50 × 30 μm s-SNOM images of the ellipse and triangle antennas shown in (d) and (e). **h, i,** 20 × 20 μm near-field images and schematics of triangular antennas with curved points at A, B, and C having radii of curvature 1.2 μm and 1 μm, respectively, and a height of 5 μm; α is indicated by the two dotted lines in (i). **j, k,** 50 × 30 μm s-SNOM images of the triangular antennas shown in (h) and (i). δ denotes the internal angle of the triangle and describes the inclination of its side.

Then we extended the design to a triangle with three curved points (vertices) named A, B, and C (see Figure 13.4i, left panel; near-field image). These three vertices will act as polariton excitation points, and the curvature will determine which modes are most efficiently excited by the curved points of the triangle micro antenna. For a triangle-shaped antenna, the left side polariton branches (- branch) are assisted by the collective excitation of the two vertices A and C of the triangle. By changing the curvature of the curved points A and C, the excited mode can be altered. Then the inclined edge AC of the triangle can either enhance or suppress the excited polariton modes. This behaviour is further discussed in Section 3.4.2, where the edge-assisted mode-selection mechanism determines the excitation of modes in a triangle where only modes with wavevectors aligned perpendicular to the antenna edges are efficiently coupled.

Therefore, the observed increase in directionality from disk to rectangle to triangle can be understood as a transition from broadband excitation to selective mode excitation. The disk antenna excites a wide range of modes with no directional preference, the rectangular antenna introduces partial filtering of modes, and the triangular antenna enables strong momentum selectivity through its edges, resulting in highly directional propagation. Overall, the excellent agreement between experimental near-field measurements and numerical simulations, combined with the consistent trends observed in the directionality parameter β and FFT analysis, confirms that the directional propagation of g-HPs is governed by antenna geometry. By engineering the shape of the excitation source, it is possible to control the distribution of energy in momentum space, selectively excite specific polariton modes, and achieve highly directional and long-range propagation.

3.4.2 Confirmation of edge assisted mode selection through near field imaging

Following the demonstration of shape-dependent directional excitation, here we experimentally and numerically confirm the mechanism responsible for the observed tunability, referred to as edge-assisted mode selection. This mechanism predicts that the physical edges

of the nanoantenna act as momentum-selective boundaries, preferentially enhancing coupling to modes whose wavevectors are perpendicular to the edge.

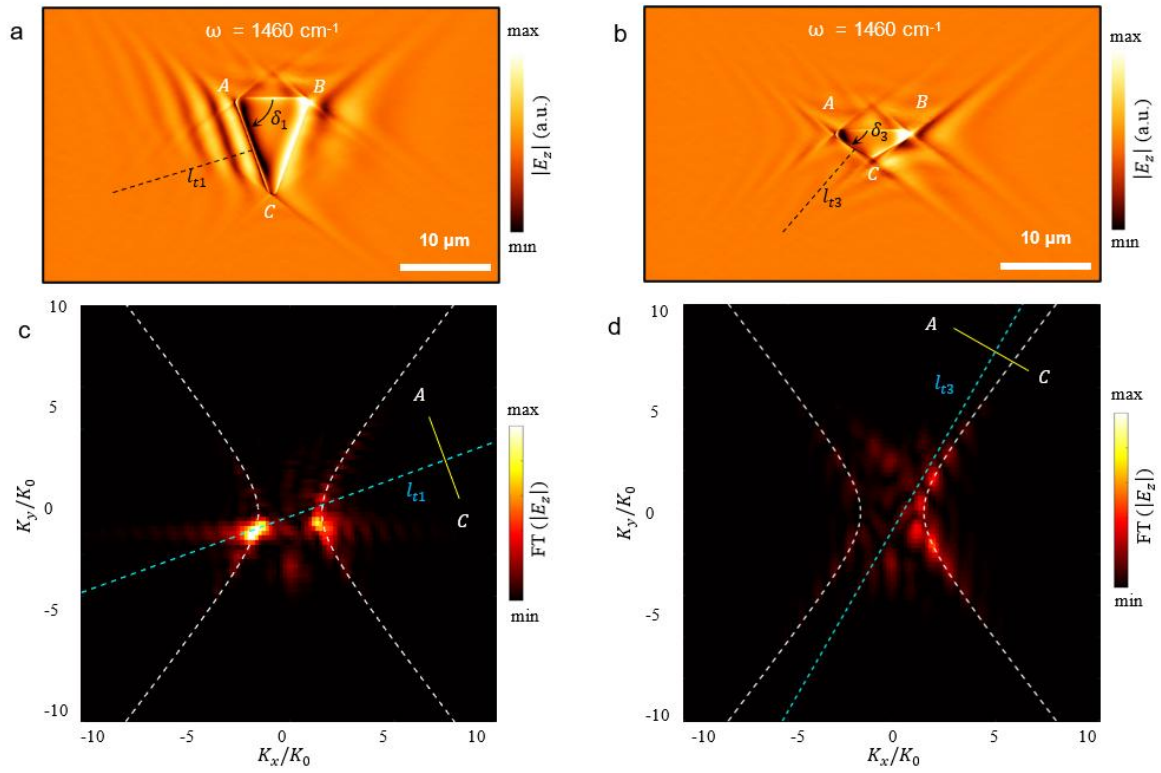


Figure 3.15 | Effect of physical edge to enhance coupling of modes for selective excitation. (**a, b**) Simulated near-field images of antenna-launched g-HPs for triangles with two distinct internal angles (δ). $\delta_1 = 70^{\circ}$ and $\delta_2 = 30^{\circ}$. (**c, d**) Absolute value of the Fourier transform of the images a and b. l_{t1} and l_{t2} are the perpendicular axis to the AC physical edge of the triangles with internal angles δ_1 and δ_2.

First, this mechanism is confirmed through numerical simulations (Figure 3.15). Two triangular antennas with different internal angles ($\delta_1 = 70°$ and $\delta_2 = 30°$) are simulated to demonstrate how edge orientation influences momentum coupling. The simulated near-field distributions (Figure 3.15a,b) show distinct propagation patterns despite identical excitation conditions. The corresponding FT images (Figure 3.15c,d) clearly show differences in mode excitation. For each triangle, the direction perpendicular to the AC edge (denoted as $l_{t1}$and l_{t2}) is defined.

The FT results (Figure 3.15c,d) show that the excited modes are strongly influenced by the AC edge orientation. When the edge-normal direction intersects the IFC, a dominant mode is excited along this direction. This results in parallel fringes in real space, confirming that momentum selection is governed by the edge orientation. Conversely, when the edge-normal

direction does not intersect the IFC, excitation becomes less selective , as observed for the second triangle where l_{t2} does not intersect the IFC. This provides direct numerical evidence that the edge acts as a momentum filter, confirming the edge-assisted mode-selection mechanism observed in simulation.

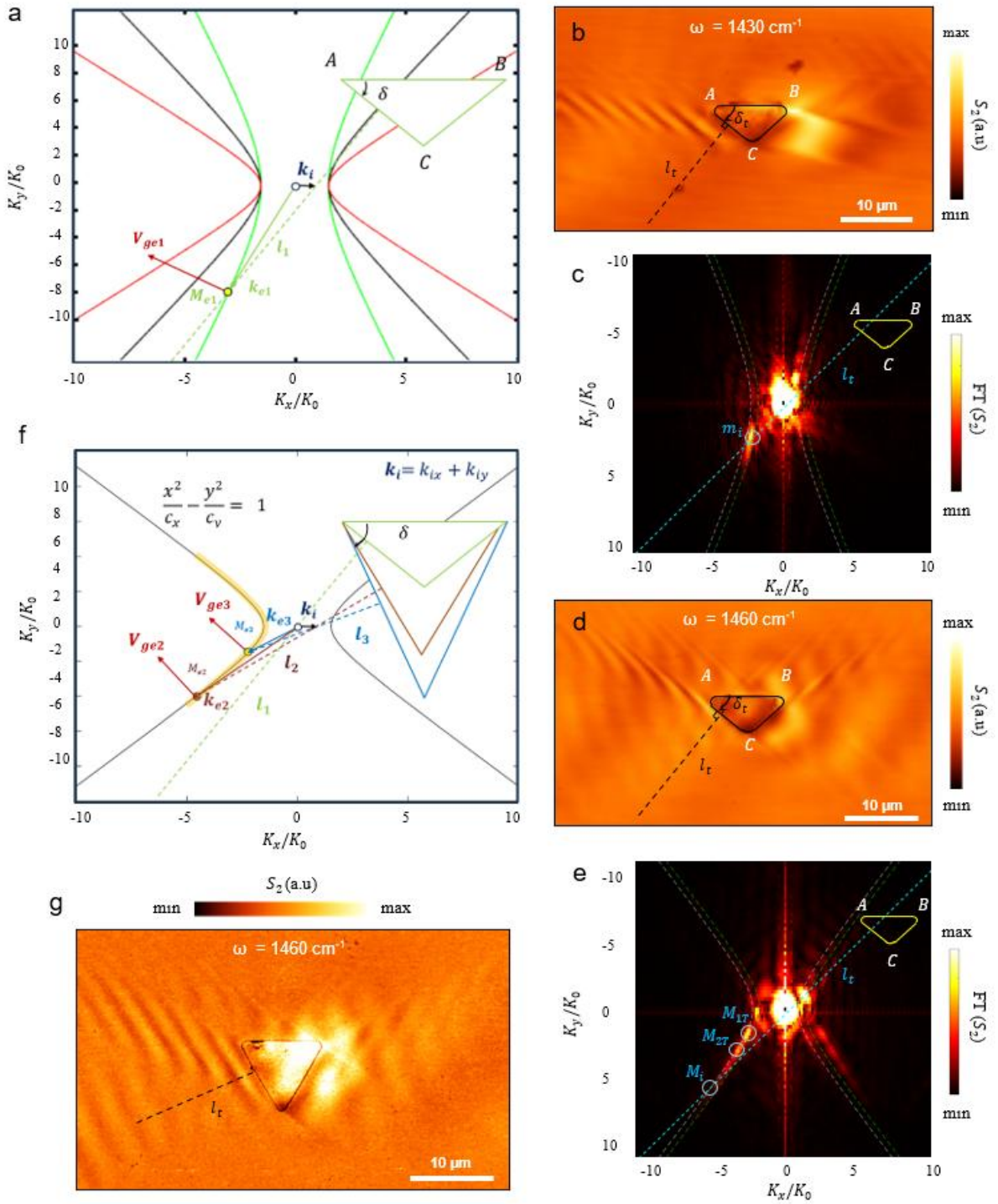


Figure 3.16 | Edge assisted mode selection. a, Schematic illustration of the edge assisted mode selection by a triangular antenna for different excitation frequencies. The green, black,

red solid line represents the IFC for calcite at 1430 cm^{-1}, 1460 cm^{-1}, 1490 cm^{-1}. l_1 is the line normal to the AC edge of the triangle. M_{e1} is the mode at the intersection of IFC and l_1 lines. K_{e1} represent the corresponding wave vectors for mode M_{e1}. k_i represent the wave vector for the incident wave. **b,** Near-field amplitude images of a triangular antenna-launched g-HPs at the illumination frequency $\omega = 1430\ \mathrm{cm}^{-1}$. **c,** Absolute value of the Fourier transforms of the images shown in b. m_i is the intersection point of line l_t and the IFC at $\omega = 1430\ \mathrm{cm}^{-1}$. **d,** Near-field amplitude images of a triangular antenna-launched g-HPs at the illumination frequency $\omega = 1460\ \mathrm{cm}^{-1}$. Triangle inner angle $\delta_t = 43^{\circ}$ and l_t is the normal axis to the AC edge of the triangle. **e**, Absolute value of the Fourier transforms of the images shown in d. M_{1t} and M_{2t} are the antenna excited modes at $\omega = 1460\ \mathrm{cm}^{-1}$. M_i is the intersection point of line l_t and the IFC at $\omega = 1460\ \mathrm{cm}^{-1}$. **f,** Schematic illustration of the edge assisted mode selection at the boundary by tuning the size of the triangle antenna. Black solid line represents the IFC for calcite at 1490 cm^{-1}. Green, red, and blue triangles represent three separate triangles with three distinct angles $\delta = \delta_1, \delta_2, \delta_3$. l_1, l_2, l_3 are the three lines normal to the AC edge of each triangle. M_{e2} , M_{e3} are the two modes at the intersection of IFC and l_2, l_3 lines. K_{e2} and K_{e3} represent the corresponding wave vectors for modes M_{e2} and M_{e3}. **g,** Near-field amplitude image antenna-launched g-HPs at the illumination frequency $\omega = 1460\ \mathrm{cm}^{-1}$ for a triangular antenna with a larger internal angle $\delta_t = 60^{\circ}$.

This behaviour is further confirmed experimentally through near-field imaging (Figure 3.16). As discussed in section 3.2.5. Figure 3.16a presents the conceptual framework, where the IFCs at different excitation frequencies are overlaid with a line (l_1) perpendicular to the AC edge of the triangular antenna. The intersection between this direction and the IFC determines the allowed excited mode , Me_1 with the corresponding wavevector defining the propagation direction. This is experimentally confirmed in Figure 3.16b for a triangle-shaped antenna with a small δ angle At a given excitation frequency of $1430cm^{-1}$ (Figure 3.16b), the FFT (Figure 3.16c) shows a dominant bright spot located precisely at the intersection point between the IFC and the perpendicular line l_t. This indicates predominantly single-mode excitation (M_i), with the measured Fourier response concentrated near the expected intersection between the edge-normal direction and the isofrequency contour, consistent with the proposed momentum-selection mechanism. For the same triangle at $1460cm^{-1}$ (Figure 3.16d,e two modes (M_{1T} and M_{2T}) are excited, corresponding to complex excitation behaviour within the allowed excitation region.

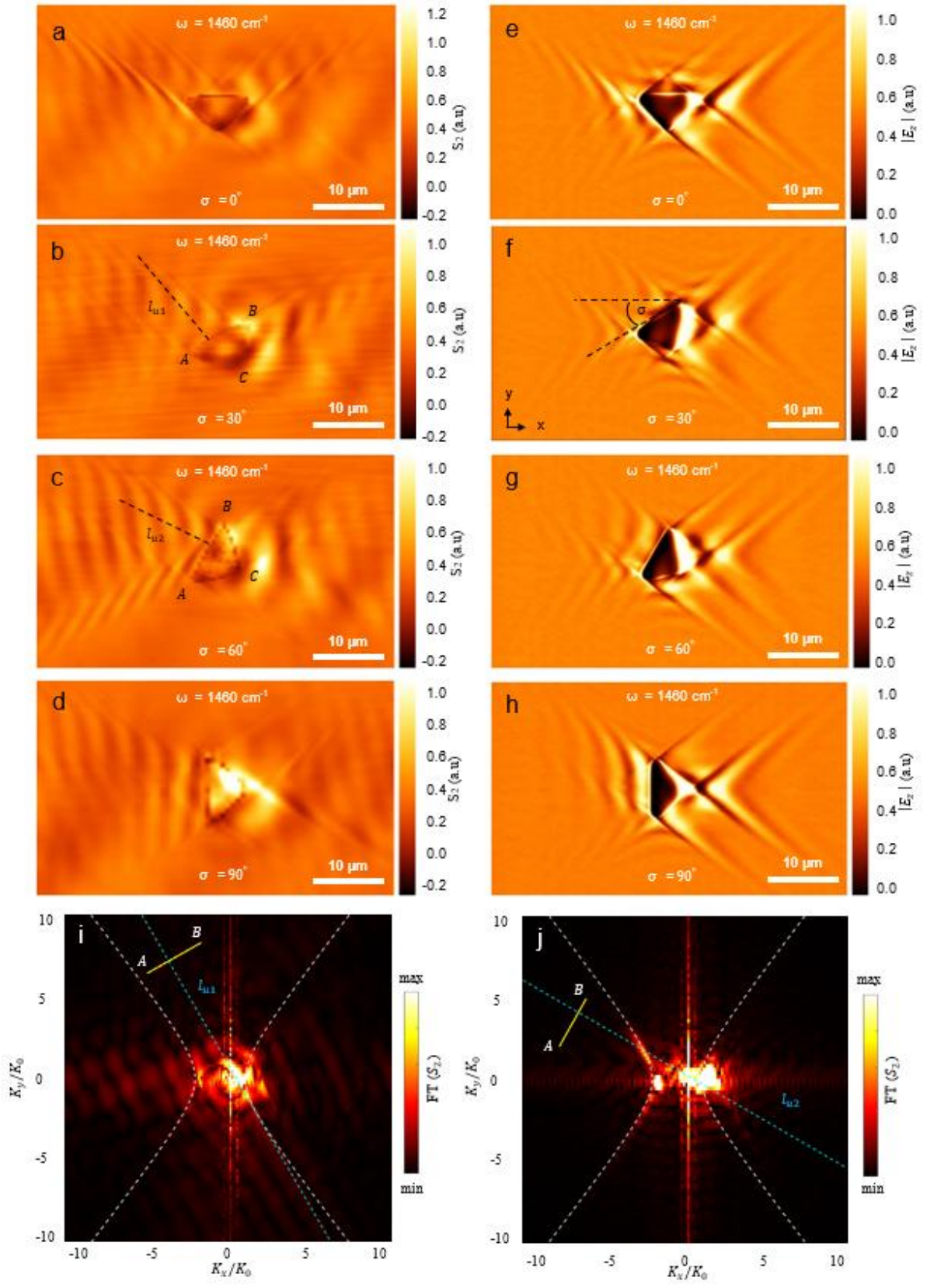


Figure 3.17 | Edge assisted mode selection based on the rotational angle (σ) of the micro/nano antenna. a-d, Experimental near-field images of antenna-launched g-HPs for the rotational angles σ = 0˚, 30˚, 60˚, 90˚ . l_{u1} and l_{u2} are the perpendicular axis to the BA physical

edge of the triangles with rotational angles σ = 30°, 60°. **e-h,** Simulated near-field images of antenna-launched g-HPs, for the rotational angles σ = 0°, 30°, 60°, 90°. **i, j,** Absolute value of the Fourier transforms of the images b and c. Yellow AB line represents the AB physical edge of the triangle.

In this case, although an intersection exists between l_t and the IFC where the mode on the IFC is M_T, the vertex curvature limits efficient excitation of high-k modes to couple effectively by the edge. Therefore, the triangle antenna excites multiple modes depending on the complexity of the vertex A and the AC edge. But in this case, the angle delta is not large enough to excite a single k mode on the IFC. This highlights that both edge orientation and vertex curvature jointly determine mode selectivity.

By modifying the triangle geometry (internal angle δ), the edge orientation and therefore, the direction of its perpendicular momentum selection can be tuned. This enables controllable selection of different modes across the IFC. As illustrated in Figure 3.16f,g, different triangle geometries excite different modes on the IFC. This behaviour can be understood by considering that each triangle vertex initially excites a broad distribution of polariton modes due to strong local-field confinement. However, only a subset of these modes is efficiently coupled and propagated, determined by the boundary condition imposed by the antenna edge.

Specifically, the straight edge acts as a momentum-selective boundary, favouring modes with wavevectors perpendicular to the edge. This arises because efficient coupling occurs when the spatial phase variation of the polariton field matches the translational symmetry along the edge, leading to constructive interference and enhanced field buildup for those modes. As a result, the dominant excited modes correspond to the intersection points between the isofrequency contour (IFC) and the edge-normal direction. When the internal angle δ is varied, the orientation of the AC edge changes, thereby rotating the perpendicular direction in momentum space. Consequently, the intersection points between this direction and the IFC shift, leading to selective excitation of different polariton modes.

In cases where the perpendicular direction does not intersect the IFC within the accessible momentum range, efficient coupling is suppressed, resulting in weaker or multi-mode excitation. Therefore, mode selectivity is not solely determined by the excitation frequency but can be engineered through the antenna's geometry by controlling the orientation of its edges relative to the IFC. To further demonstrate the controllability of this mechanism, we investigate the effect of rotating the triangular antenna in the x-y plane, as shown in Figure 3.17. By

rotating the triangle, the orientation of its edges and therefore the direction of the perpendicular momentum selection changes relative to the IFC.

As shown in Figure 3.17(a), when the triangle is oriented at $\sigma = 0^{\circ}$, the AC edge is aligned such that its perpendicular direction intersects the IFC along the U- branch. This results in highly directional propagation along this branch, as observed in the near-field image. When the triangle is rotated (Figure 3.17c), the relevant edge (now effectively the AB edge) becomes aligned such that its perpendicular direction intersects the IFC along the L- branch.

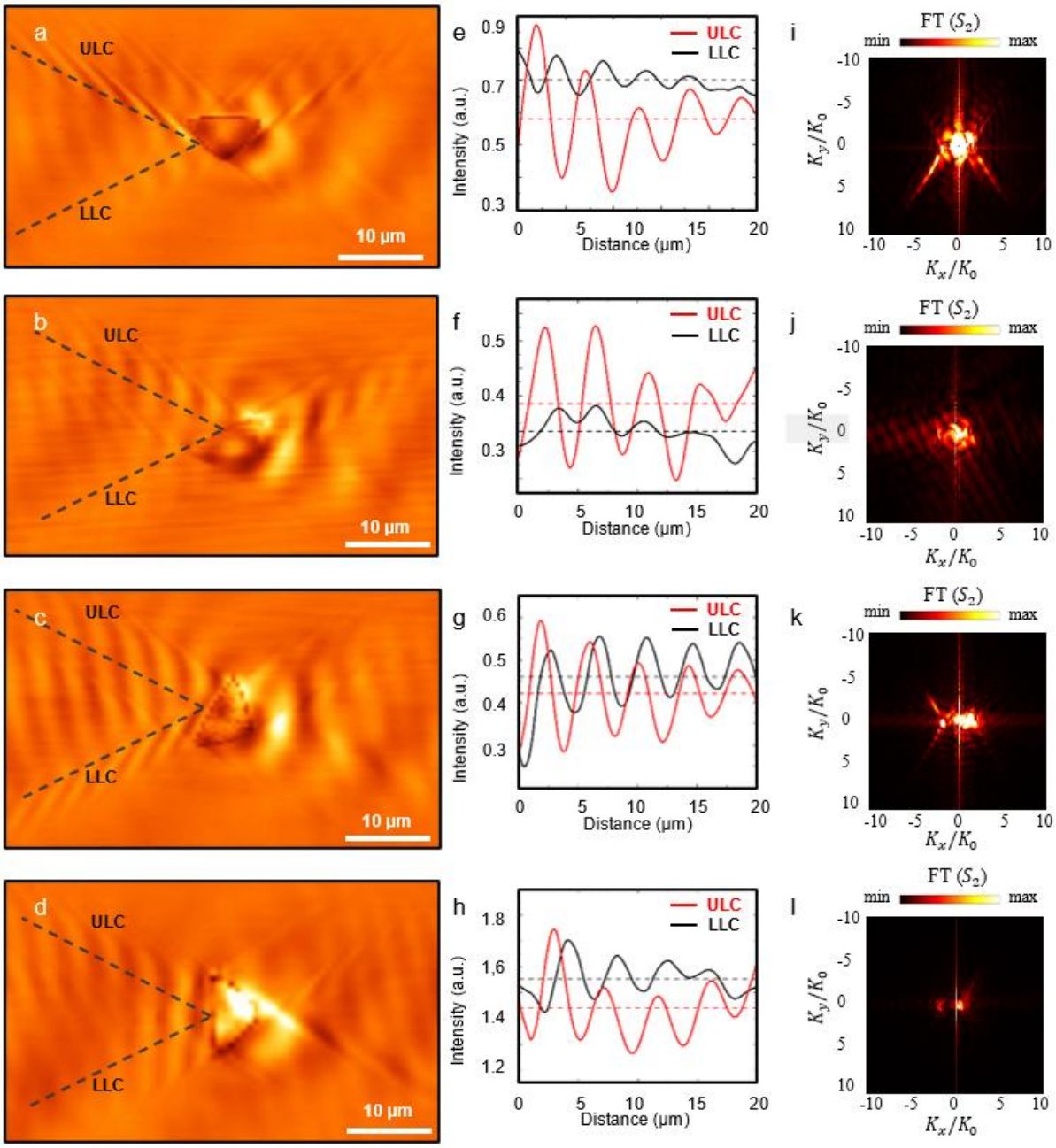


Figure 3.18 | Determination of directionality of g-HPs and edge assisted mode selection for different rotational orientations of the triangle antenna. a-d, 50μm × 30μm s-SNOM

scan of a triangle-shaped nano antenna marked with the upper line cut (ULC) and lower line cut (LLC) profiles for the rotational angles β = 0˚, 30˚, 60˚, 90˚. **e-h**, Upper and lower line cut intensity profiles of s-SNOM images presented in a-d. **i-l,** Absolute value of the Fourier transform of the images shown in a-d.

Consequently, the excitation shifts to this branch resulting in directional propagation along the L- branch. The corresponding FFT images (Figure 3.17i,j) clearly show that the excited modes shift position in momentum space in accordance with the rotation, providing direct evidence that the excited polariton branch is determined by the orientation of the antenna edge relative to the IFC.

Finally, this behaviour is quantitatively confirmed using the directionality analysis presented in Figure 3.18. The s-SNOM images for different rotational angles (σ = 0°, 30°, 60°, 90°) are analysed using upper- and lower-line cuts to extract the directionality parameter β. As shown in Figure 3.18(e-h), the relative amplitudes of the polariton branches vary significantly with rotation, indicating a clear redistribution of energy between different propagation channels. The corresponding FFT images Figure 3.18(i-l) further confirm that the dominant excited modes shift across the IFC as the triangle is rotated. For orientations where the edge normal aligns with a specific branch, the β parameter becomes significantly larger ($\beta \gg 1$), indicating strong suppression of other branches and efficient single-branch excitation. In contrast, when alignment is less optimal, multiple modes are excited, reducing directionality. This establishes edge-assisted mode selection as the fundamental mechanism enabling both directional propagation and selective excitation of long-lived g-HP modes, providing a powerful and tunable approach for controlling polariton behavior in anisotropic materials.

3.4.3 Confirmation of long propagation length of g-HPs

As demonstrated in the previous sections, antenna geometry controls the relative excitation strengths of different g-HP modes and therefore influences the measured spatial extent of the resulting polariton field. To investigate this effect, the propagation characteristics of different antenna-launched fields were compared using numerical simulations and experimental near-field measurements in this section. As discussed in Section 3.1.3, the intrinsic attenuation length of an individual polariton mode is determined by its complex in-plane wavevector along a specified propagation direction. However, when several modes are excited simultaneously, the measured near-field signal represents their superposition, and its spatial decay cannot necessarily be attributed to a single modal attenuation constant.

For a localized dipole-like source, the broad momentum distribution allows the simultaneous excitation of modes with different propagation directions and attenuation rates. Their combined contributions produce a spatial envelope whose effective decay length depends on the relative modal amplitudes and interference. In contrast, when the excitation is spatially extended, the coupling becomes highly selective. This was demonstrated using a dipole array consisting of $N = 51$dipoles with a spacing of $d = 0.05\lambda_0$, as shown in Figure 3.9c (bottom panel). In this case, the excitation is effectively restricted to a narrow range of wavevectors that match the orientation of the array. The corresponding field distributions along the dotted lines are presented in Figure 3.9d, where a clear difference in the decay behaviour is observed. By limiting excitation to fewer modes, the propagation length increases significantly (approximately fourfold. Importantly, the photonic environment, defined by the calcite-air interface, remains unchanged in both cases Therefore, the intrinsic modal properties remain the same the observed difference in decay behaviour arises solely from the way in which energy is distributed among the available modes. In the dipole case, the incident energy is shared among multiple modes, many of which decay rapidly, resulting in a short effective propagation length. In contrast, selective excitation concentrates energy into long-lived modes, enabling extended propagation.

To quantitatively compare the experimentally observed propagation characteristics, near-field line profiles were extracted along a fixed direction relative to the crystallographic axes and fitted using a damped sinusoidal function. The corresponding fitted decay constants represent effective attenuation parameters of the measured near-field response. Since the signal may contain contributions from several excited polariton modes, these values should not automatically be interpreted as the intrinsic attenuation coefficients of individual eigenmodes. Instead, they quantify the spatial extent of the antenna-dependent field distribution along the selected measurement direction.

This principle directly explains why long-propagating g-HP modes have not been observed in earlier works using disk antennas up to the level that we observe here in this work. Although such antennas can excite most of the available modes, including long-lived ones, the contribution of these modes is suppressed due to the simultaneous excitation of rapidly decaying high-k components. As a result, the overall propagation appears short.

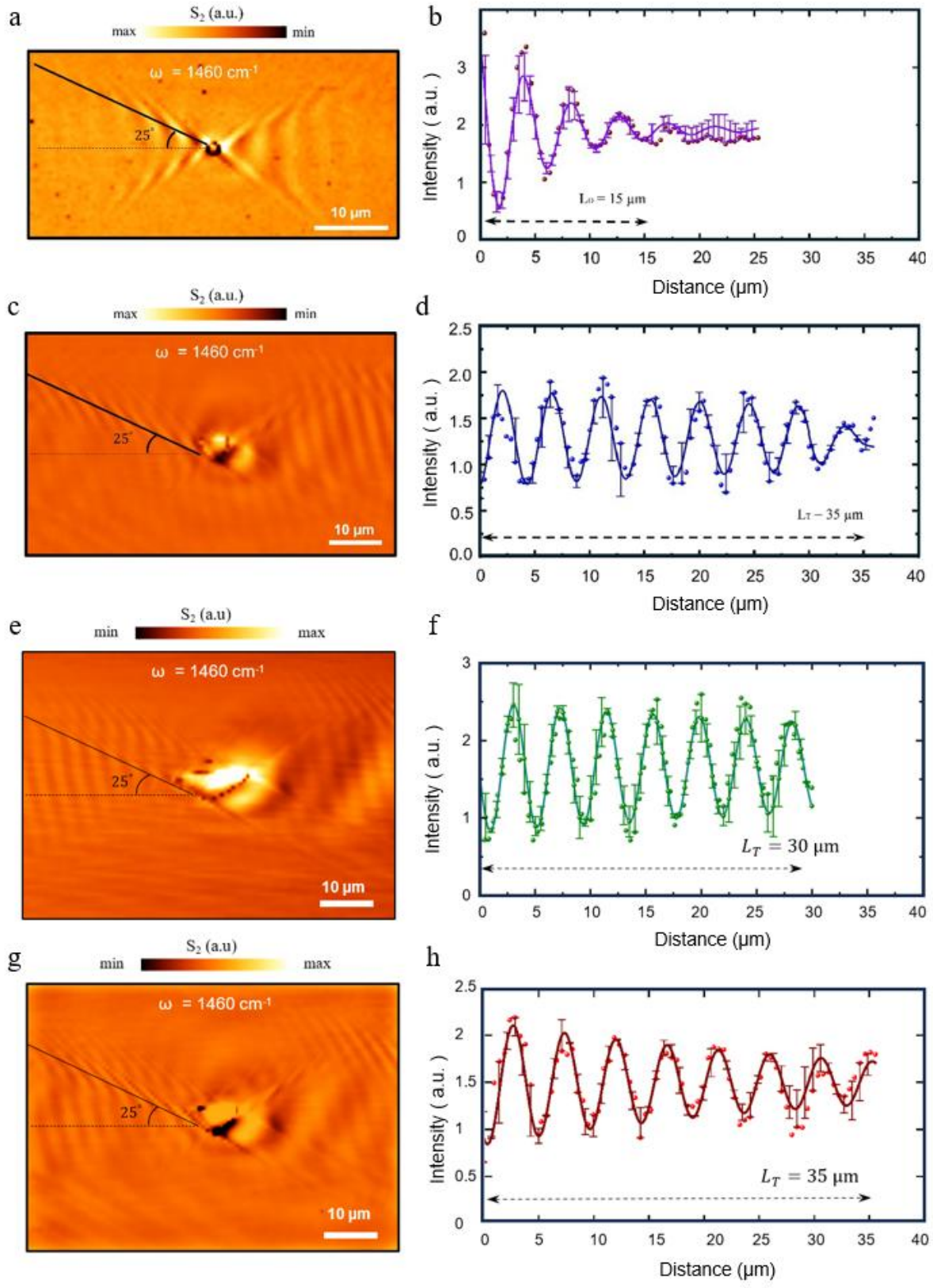


Figure 3.19 | Highly enhanced propagation length of g-HPs through different shaped micro/nano antennas. a, Experimental near-field result of a disk-shaped nano antenna with a larger scanning area of 50 × 25 μm. **b,** Line cut profile data for the disk-shaped nano antennas

with an angle of 25° w.r.t the x axis. Dark red balls represent the actual line cut profile data and the purple line is the sine damp fitted function explained in supplementary note 5 with a decay constant of $1.579 \times 10^{5}\, m^{-1}$ **c,** Experimental near-field result of a triangular-shaped micro antenna with an inner angle $\delta = 55^{\circ}$ and a scanning area of 70 × 50 μm. **d,** Line cut profile with an angle of 25° w.r.t the x axis for the triangle-shaped micro antenna in c. Blue balls represent the actual line cut profile data and the dark blue line is the sine damp fitted function with a decay constant of $1.44 \times 10^{4}\, m^{-1}$. The error bars in e and g represent the fitting uncertainty. **e,** Experimental near-field result of a triangular-shaped micro antenna with an inner angle $\delta < 43^{\circ}$ and a scanning area of 70 × 50 μm. **f,** Line cut profile with an angle of 25° w.r.t the x axis for the triangle-shaped micro antenna in c. green balls represent the actual line cut profile data and the dark green line is the sine damp fitted function with a decay constant of $1.22 \times 10^{4}\, m^{-1}$. **g,** Experimental near-field result of a triangular-shaped micro antenna with an inner angle $\delta = 43^{\circ}$ and a scanning area of 70 × 50 μm. **h,** Line cut profile with an angle of 25° w.r.t the x axis for the triangle-shaped micro antenna in g. red balls represent the actual line cut profile data and the Brown is the sine damp fitted function with a decay constant of $3.0341 \times 10^{4}\, m^{-1}$.

In practice, implementing an ideal dipole array is challenging. As discussed in Sections 3.2.5 and 3.4.2, the antenna edge acts as a distributed excitation source, effectively mimicking a closely spaced dipole array. The vertices provide broadband excitation, while the edges impose momentum-selective constraints, favouring modes with wavevectors perpendicular to the edge. This enables selective coupling into long-lived, low-loss modes. By aligning the edge orientation with the wavefront of a desired g-HP mode, the incident field is strongly coupled into a long-lived polariton branch.

The experimental confirmation of long propagation is presented in Figure 3.19. The near-field images show highly collimated, directional polariton wavefronts extending over tens of micrometres from the excitation region, with minimal spreading and reduced attenuation. This behaviour is in strong contrast to the rapidly decaying patterns observed for symmetric antennas. To quantitatively extract the propagation length, line-cut profiles are taken along the propagation direction and fitted using a decaying sinusoidal function:

$$y(x) = y_0 + A \times e^{-dx} \times \sin\left(\frac{\pi(x - x_c)}{w}\right)$$

where y_0 = offset, A = amplitude, d = decay constant, x_c = phase shift, w = fringe period. The propagation length is given by $L_p = 1/d$.

The fitted results show that the propagation length of the selectively excited g-HP modes exceeds 82 μm. For comparison, Ma et al.[16] previously demonstrated ghost hyperbolic surface polariton propagation over distances around 20 μm using near-field imaging. However, this reported observation distance does not represent a maximum propagation limit or an independently extracted 1/e decay length. The significance of the present results lies in demonstrating that geometry-controlled, edge-assisted excitation can preferentially couple incident light into a restricted momentum range containing long-lived polariton components. This produces an extended near-field response without modifying the intrinsic material attenuation. The Fourier-space analysis in Figures 3.16 and 3.17 further supports this interpretation by demonstrating that appropriately designed triangular antennas concentrate the excited polariton response within selected regions of the isofrequency contour, in contrast to the broader momentum distributions produced by symmetric excitation sources.

Overall, these results demonstrate that the long propagation of g-HPs can be achieved by controlling the excitation mechanism. By transitioning from multi-mode excitation (dipole-like sources) to selective excitation (dipole array or edge-assisted excitation), it is possible to concentrate energy into long-lived modes and significantly extend the observable propagation length. This establishes excitation engineering as a powerful approach for accessing and controlling long-range polaritonic transport in anisotropic materials.

References

1. Tao, L., Chen, Z., Li, Z., Wang, J., Xu, X., & Xu, J. B.(s). Enhancing light-matter interaction in 2D materials by optical micro/nano architectures for high-performance optoelectronic devices. InfoMat 2021, 3 (1), 36-60.

2. He, M., Matson, J. R., Yu, M., Cleri, A., Sunku, S. S., Janzen, E., Mastel, S., Folland, T. G., Edgar, J. H., & Basov, D.(s). Polariton design and modulation via van der Waals/doped semiconductor heterostructures. Nature communications 2023, 14 (1), 7965.

3. Jin, W., Li, Z., Shan, Y., Liang, Y., Yang, K., & Lian, L. (2024). Dual-channel chip-to-chip communication employing field enhancement spoof surface plasmon polaritons transmission line. 2024 Photonics & Electromagnetics Research Symposium (PIERS),

4. Shang, Q., Dini, K., Jiang, H., Seet, N. W. E., Cai, X., Ru, S., Lu, X., Yu, W. C., Zhao, J., & Xiong, Q.(s). On-chip photonic crystal dressed Rydberg exciton polaritons with enhanced nonlinearity in monolayer WS2. Nature communications 2025, 16 (1), 10352.

5. González-Tudela, A., Reiserer, A., García-Ripoll, J. J., & García-Vidal, F. J.(s). Light–matter interactions in quantum nanophotonic devices. Nature Reviews Physics 2024, 6 (3), 166-179.

6. Kavokin, A., Liew, T. C., Schneider, C., Lagoudakis, P. G., Klembt, S., & Hoefling, S.(s). Polariton condensates for classical and quantum computing. Nature Reviews Physics 2022, 4 (7), 435-451.

7. Basov, D., Fogler, M., & García de Abajo, F.(s). Polaritons in van der Waals materials. Science 2016, 354 (6309), aag1992.

8. Guo, X., Lyu, W., Chen, T., Luo, Y., Wu, C., Yang, B., Sun, Z., García de Abajo, F. J., Yang, X., & Dai, Q.(s). Polaritons in van der Waals heterostructures. Advanced Materials 2023, 35 (17), 2201856.

9. Ma, W., Shabbir, B., Ou, Q., Dong, Y., Chen, H., Li, P., Zhang, X., Lu, Y., & Bao, Q.(s). Anisotropic polaritons in van der Waals materials. InfoMat 2020, 2 (5), 777-790.

10. Hu, G., Shen, J., Qiu, C. W., Alù, A., & Dai, S.(s). Phonon polaritons and hyperbolic response in van der Waals materials. Advanced Optical Materials 2020, 8 (5), 1901393.

11. Chen, M., Lin, X., Dinh, T. H., Zheng, Z., Shen, J., Ma, Q., Chen, H., Jarillo-Herrero, P., & Dai, S.(s). Configurable phonon polaritons in twisted α-MoO3. Nature materials 2020, 19 (12), 1307-1311.

12. Hu, G., Ou, Q., Si, G., Wu, Y., Wu, J., Dai, Z., Krasnok, A., Mazor, Y., Zhang, Q., & Bao, Q.(s). Topological polaritons and photonic magic angles in twisted α-MoO3 bilayers. Nature 2020, 582 (7811), 209-213.

13. Xu, X. G., Ghamsari, B. G., Jiang, J.-H., Gilburd, L., Andreev, G. O., Zhi, C., Bando, Y., Golberg, D., Berini, P., & Walker, G. C.(s). One-dimensional surface phonon polaritons in boron nitride nanotubes. Nature communications 2014, 5 (1), 4782.

14. Ocelic, N., & Hillenbrand, R.(s). Subwavelength-scale tailoring of surface phonon polaritons by focused ion-beam implantation. Nature materials 2004, 3 (9), 606-609.

15. Galiffi, E., Carini, G., Ni, X., Álvarez-Pérez, G., Yves, S., Renzi, E. M., Nolen, R., Wasserroth, S., Wolf, M., & Alonso-Gonzalez, P.(s). Extreme light confinement and control in low-symmetry phonon-polaritonic crystals. Nature Reviews Materials 2024, 9 (1), 9-28.

16. Ma, W., Hu, G., Hu, D., Chen, R., Sun, T., Zhang, X., Dai, Q., Zeng, Y., Alù, A., & Qiu, C.-W.(s). Ghost hyperbolic surface polaritons in bulk anisotropic crystals. Nature 2021, 596 (7872), 362-366.

17. Narimanov, E.(s). Ghost resonance in anisotropic materials: negative refractive index and evanescent field enhancement in lossless media. Advanced Photonics 2019, 1 (4), 046003-046003.

18. Hu, C., Sun, T., Zeng, Y., Ma, W., Dai, Z., Yang, X., Zhang, X., & Li, P.(s). Source-configured symmetry-broken hyperbolic polaritons. Elight 2023, 3 (1), 14.

19. Suriyage, M., Zhou, Q., Qin, H., Sun, X., Lu, Z., Maier, S. A., Yu, Z., & Lu, Y.(s). Long-propagating ghost phonon polaritons enabled by selective mode excitation. Light: Science & Applications 2025, 14 (1), 254.

20. Babar, S., & Weaver, J.(s). Optical constants of Cu, Ag, and Au revisited. Applied Optics 2015, 54 (3), 477-481.

4. Real space imaging of guided exciton polaritons in suspended monolayer TMDCs

In chapter 3, PhPs specifically, hyperbolic PhPs was explored by highlighting the tunability of PhPs to achieve selective mode excitation and long propagation lengths. PhPs mostly operate in the mid-IR regime and are governed by lattice vibrations. In this chapter, we explore a different class, EPs[1,2] in which the coupling between excitons and photons is examined. These EPs enable light-matter interactions at higher energies, extending into the visible and near-IR spectral regimes, and offer new opportunities for nanoscale photonic manipulation.

As discussed in the introduction chapter, the TMDCs have attracted significant attention in exciton physics[1], and among these materials 2D, and in particular monolayer TMDCs, are especially attractive due to the exceptionally strong exciton resonances[3] they exhibit, driven by large binding energies[4,5] and reduced dielectric screening in 2D. These properties provide ideal conditions to observe EPs with highly enhanced light-matter interactions. Research has been carried out to realize these EPs in TMDCs, and several works have established the basis of realizing cavity EPs[2,6] in ultra-thin and monolayer TMDCs[7]. However, as discussed in detail in chapter 1, these are bound to the cavity and cannot propagate in-plane, unlike guided-mode EPs. These guided modes in thin and bulk TMDCs have been investigated by several groups up to the thickness limit of 7-10nn corresponding to several atomic layers[8-13], but it remains fundamentally challenging to realize these guided-mode EPs in ultrathin or monolayer materials. There are certain limiting and dependent factors, such as cutoff conditions[14], weak mode confinement in ultrathin TMDCs[15], and the critical dependence on the dielectric environment surrounding the monolayer[15,16]. Although theoretical studies have proposed the existence of these EPs in monolayers and ultrathin samples[16], their experimental realization has remained elusive.

In this chapter, we present an experimental approach to overcome these challenges and demonstrate the real-space observation of guided EPs in a suspended monolayer TMDC using near-field imaging with a s-SNOM. The cutoff limitation is addressed through a suspended structure, and several sample-preparation modifications, and a proper understanding of s-SNOM interference fringe formation in suspended samples enabled the realization of guided modes in monolayer TMDCs. Through combined theoretical and numerical analysis, we establish the physical origin of these fringes and develop a robust framework to extract the intrinsic polariton wavelength and dispersion directly from experimental data. Most

importantly, by extracting guided-mode propagation from near-field images over a broad excitation energy range near the A exciton of WSe_2, we experimentally map the dispersion characteristics of guided EPs in a monolayer TMDC. We observe pronounced back-bending in the dispersion, confirming the existence of guided-mode Eps in monolayer TMDC. This behaviour is further supported by theoretical modelling based on the TMDC's surface susceptibility, which confirms the formation of a fundamental TE-guided EP mode.

Overall, this chapter presents the first direct real-space experimental observation of guided EP propagation in a free-standing single-monolayer WSe_2 waveguide, extending previous demonstrations in thicker and few-layer TMDC structures to the suspended monolayer limit. The results not only deepen the understanding of light-matter interactions in 2D systems but also establish a foundation for integrating monolayer TMDCs into future nanoscale photonic and polaritonic devices.

4.1. Challenges of realizing guided modes in Monolayer TMDCs

As discussed in Chapter 1, EPs have been observed in bulk and multilayer TMDCs[8-10]. Extending these concepts to the monolayer or thin-layer limit presents several fundamental challenges. First, compared to thicker systems, monolayer TMDCs are in an extreme regime where the material thickness is multiple orders of magnitude smaller than the wavelength of the excitation light, which renders conventional waveguide-based descriptions of optical confinement and mode propagation in bulk materials inapplicable. Therefore, the existence of these modes strongly influenced by both intrinsic material properties and extrinsic boundary conditions[16].

In conventional dielectric waveguides, the mode confinement is achieved through total internal reflection[15], and this requires a sufficiently large refractive index contrast and a considerable finite thickness to support the standing waves. This mechanism is not applicable to monolayers, as their atomically thin nature prevents the formation of such standing-wave confinement. The absence of thickness limits the confinement, leading to rapid leakage of the electric field into the surrounding medium[9,15] and driving the system toward cutoff conditions, preventing stable mode propagation.

In addition to confinement limitations, the strong dependence of exciton polaritons on the dielectric environment introduces another critical challenge. In monolayer TMDCs, the optical response is governed by a surface susceptibility[16] rather than a bulk dielectric function[15], meaning that the interaction between light and the material is highly influenced by the

refractive indices of the surrounding media. Even small asymmetries between the substrate and superstrate can significantly alter the electromagnetic boundary conditions, disrupting the balance required for guided mode formation. Consequently, achieving the appropriate dielectric environment is essential for sustaining EP propagation in ultrathin systems. Furthermore, the presence of strong excitonic absorption near resonance, while beneficial for enhancing light–matter coupling, can also contribute to increased optical losses. Near the exciton transition energy, the absorption reaches a maximum, thereby suppressing the propagation of guided modes and reducing their effective propagation length. This introduces a trade-off between strong coupling and efficient transport, requiring careful consideration of the excitation energy and material parameters when probing these modes. Overcoming these limitations requires a design strategy that simultaneously enhances field confinement, minimizes radiative leakage, and maintains dielectric symmetry around the monolayer. These challenges collectively define the extreme limit of guided mode formation in 2D systems, distinguishing monolayer TMDCs from conventional photonic waveguides. In this chapter, we demonstrate how these challenges can be overcome and confirm the existence of guided mode EPs in monolayer TMDCs.

4.2. Theory of guided Exciton Polaritons

A surface-response frame is used to describe guided EPs in monolayers rather than relying on bulk-optic principles. In this section, the theoretical framework for the existence of guided modes in monolayer WSe_2 is discussed by detailing the conditions for electromagnetic fields, the excitonic surface susceptibility, the dispersion relation, and the key parameters governing propagation and confinement.

4.2.1. TE guided modes in monolayer WSe_2

As shown in Figure 4.1 a monolayer WSe_2 embedded between two dielectric media with refractive indices n_1(superstrate) and n_2(substrate), forming a three-layer system is considered. For the case of s-polarized excitation in the s-SNOM configuration, the electric field is oriented along the y-direction, and the guided mode propagates along the x-axis.

The electric field associated with the guided mode can be expressed as

$$E_y = E_0 e^{\mp qz} e^{i(\beta x - \omega t)} \tag{4.1}$$

Here, β is the generally complex in-plane propagation constant, q is the complex out-of-plane decay constant, and ω is the angular frequency. The upper and lower signs $\mp$ apply to the

regions z > 0 and z < 0, respectively. For a physically confined guided mode, the selected solution must satisfy $Re[q(\omega)] > 0$, ensuring that the electromagnetic field decays away from the monolayer into the surrounding dielectric media. This condition determines the physically acceptable guided-mode branch and must be satisfied together with the electromagnetic boundary conditions at the monolayer interface.

For a TE mode in a dielectric medium by applying the Maxwell-Faraday equation:

$$\nabla \times \boldsymbol{E} = -\mu_0 \frac{\partial \boldsymbol{H}}{\partial t}$$

Since $E_z = E_x = 0$ and considering **i** and **k** as unit vectors in x and z directions the Faraday law can be written as,

$$-\frac{\partial E_y}{\partial z}\boldsymbol{i} + \frac{\partial E_y}{\partial x}\boldsymbol{k} = -\mu_0 \frac{\partial \boldsymbol{H}}{\partial t}$$

$$-qE_0 e^{\mp qz} e^{i(\beta x - \omega t)}\boldsymbol{i} + i\beta E_0 e^{\mp qz} e^{i(\beta x - \omega t)}\boldsymbol{k} = -\mu_0 \frac{\partial \boldsymbol{H}}{\partial t}$$

Therefore, the relative magnetic field components of the system can be described as,

$$H_x = \mp \frac{iq}{\omega \mu_0} E_0 e^{\mp qz} e^{i(\beta x - \omega t)} \tag{4.2}$$

$$H_z = \frac{\beta}{\omega \mu_0} E_0 e^{\mp qz} e^{i(\beta x - \omega t)} \tag{4.3}$$

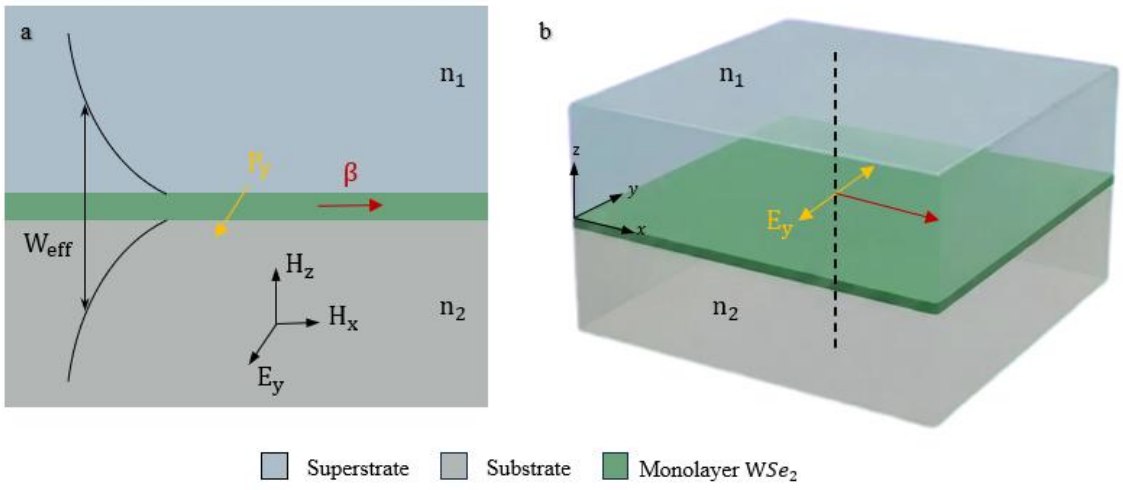


Figure 4.1 | Field configuration and parameters of a TE-guided exciton polariton in a free-standing monolayer WSe_2. a, 2D schematic of the structure showing the monolayer embedded between two dielectric media with refractive indices n_1 and n_2. **b,** Corresponding 3D representation of the electric field distribution and cladding environment. β is the in-plane propagation constant, and q represents the out-of-plane decay constant.

By considering the wave equation in the dielectric for the applied s polarized electric field we can calculate the relationship between β, and q as follows:

$$\nabla^2 E - \frac{n^2}{c^2}\frac{\partial^2 E}{\partial t^2} = 0$$

$$\beta^2 - q^2 = \frac{n^2\omega^2}{c^2} \tag{4.4}$$

This expression describes the balance between in-plane propagation and out-of-plane confinement of the guided mode.

4.2.2. Surface Susceptibility Model

The electromagnetic field-material interaction in a monolayer system is governed by a surface polarization rather than a bulk dielectric response. The induced surface polarization along the y-direction can be written as,

$$P_y^{(s)} = \varepsilon_0 \chi^{(s)} E_y \tag{4.5}$$

Where $\chi^{(s)}$ is the complex surface susceptibility of the monolayer. This quantity captures the excitonic response and is generally frequency-dependent:

$$\chi^{(s)}(\omega) = \chi_r^{(s)}(\omega) + \chi_i^{(s)}(\omega) \tag{4.6}$$

The presence of this surface polarization modifies the electromagnetic boundary conditions at the monolayer interface. By applying Maxwell's equations across the interface and integrating over an infinitesimal thickness, the discontinuity in the magnetic field can be expressed as

$$H_x(+0) - H_x(-0) = i\omega P_y^{(s)}$$

Substituting the expressions for the magnetic field leads to a relation between the decay constant and the surface susceptibility:

$$\frac{2q}{\omega\mu_0} = \omega\varepsilon_0\chi^{(s)}$$

which can be rearranged to give

$$q(\omega) = \frac{\omega^2\chi^{(s)}}{2c^2} \tag{4.7}$$

This expression highlights the direct role of the excitonic response in determining the confinement of the guided mode. To model the excitonic resonance, the surface susceptibility is described using a Lorentzian form:

$$\chi^{(s)}(\omega) = \frac{\alpha_{\max} cn}{\omega} \cdot \frac{\gamma/2}{\omega_0 - \omega - i\gamma/2} \tag{4.8}$$

where $\alpha_{\max}$ is the peak absorption coefficient, γ is the linewidth, and ω_0 is the exciton resonance frequency. The surface susceptibility in Eq. (4.8) represents the resonant excitonic contribution, without including a separate non-resonant background susceptibility. For the assumed field dependence in Eq. (4.1), the physical guided-mode solution must satisfy $Re[q(\omega)] > 0$, ensuring exponential decay of the electromagnetic field away from the monolayer. According to Eq. (4.7), this condition is governed by the real part of the surface susceptibility. Within the present Lorentzian model, the required positive real part occurs on the lower-frequency side of the exciton resonance $\omega < \omega_0$. At resonance, the real part approaches zero, while on the higher-frequency side it becomes negative. Consequently, the dispersion obtained from the squared susceptibility should be interpreted together with the normal-decay condition, rather than regarding every mathematical branch as a physically confined guided mode. The inclusion of a non-resonant susceptibility contribution could modify the spectral interval over which this condition is satisfied.

4.2.3. Dispersion Relations and key physical quantities

By combining the field relations and the surface susceptibility model, the dispersion relation of the guided exciton polariton can be obtained. Substituting the expression for $q(\omega)$into the wave equation yields the propagation constant as,

$$\beta(\omega) \approx \frac{n\omega}{c}\left[1 + \left(\frac{\omega\chi^{(s)}}{2nc}\right)^2\right]$$

This expression describes how the propagation constant deviates from the free-space dispersion due to the excitonic response of the monolayer. Near the exciton resonance, the surface susceptibility becomes large, leading to a strong modification of the dispersion. This results in a nonlinear behavior of $\beta(\omega)$, which is characteristic of strong light-matter coupling. In particular, the dispersion exhibits a back-bending feature near resonance, where the propagation constant increases sharply as the frequency approaches ω_0. This behaviour distinguishes guided exciton polaritons from conventional photonic modes and provides a direct signature of hybridization between light and excitons in the monolayer system.

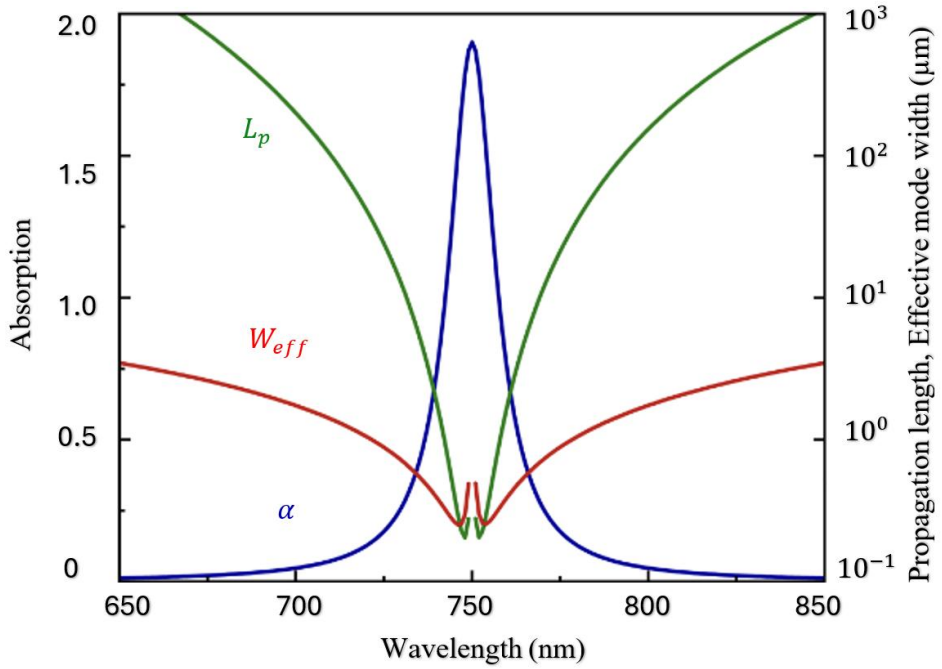


Figure 4.2 | Physical parameters of the guided mode EP. Absorption profile (α), Propagation length (L_p) and effective mode width (W_{eff}) of and EP of monolayer suspended WSe_2 sample.

The surface susceptibility is directly related to the absorption by the monolayer WSe_2 according to the boundary conditions defined in[16] and therefore according to the excitonic absorption (Lorentzian shape with peak absorption at the exciton resonance α_{max} and FWHM linewidth γ) of WSe_2 monolayer presented in Figure 4.2 the 2D susceptibility can be written as,

$$\chi^{(s)}(\omega) = \frac{\alpha_{max} cn}{\omega} \frac{\frac{\gamma}{2}}{\omega_0 - \omega - i\frac{\gamma}{2}}$$

Through combining above equations, the decay coefficient and the dispersion relations can be obtained in terms of the absorption parameters α_{max} and γ as below.

$$q(\omega) = \frac{n\omega}{c} \frac{\alpha_{max}\gamma}{4} \frac{1}{\omega_0 - \omega - i\frac{\gamma}{2}} \tag{4.9}$$

$$\beta = \frac{n\omega}{c}\left[1 + \frac{\alpha_{max}^2 \cdot \gamma^2}{32}\left(\frac{(\omega_A - \omega) + i\gamma/2}{(\omega_A - \omega)^2 + \gamma^2/4}\right)^2\right] \tag{4.10}$$

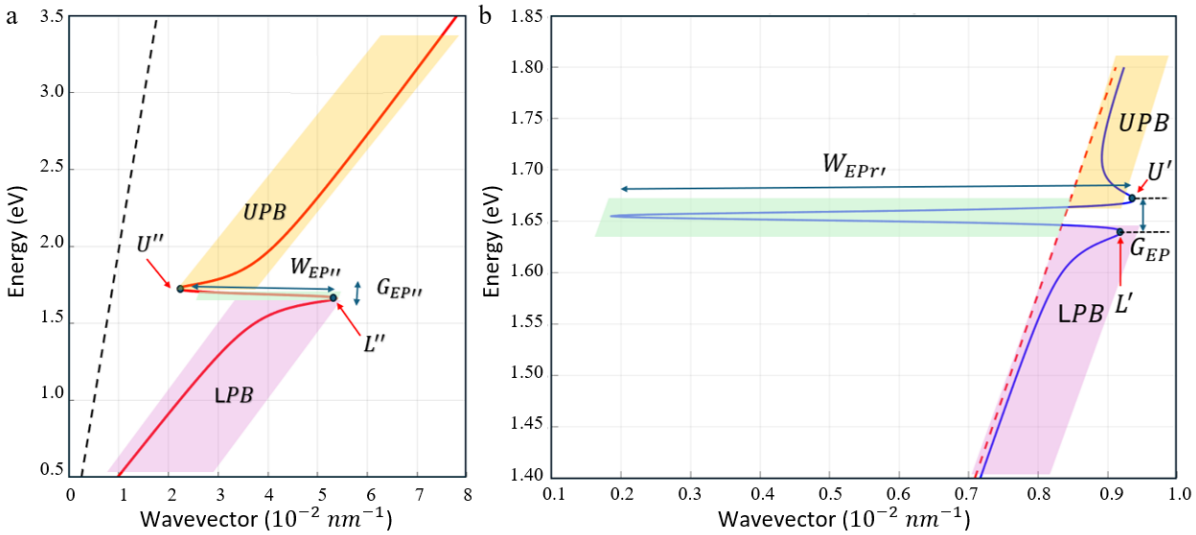


Figure 4.3 | Dispersion characteristics for bulk and monolayer WSe2. a, Dispersion diagram for a WSe_2 50nm flake on SiO2 substrate and air as the superstrate modelled based on a dielectric constant as in[8]. **b,** Dispersion diagram for a monolayer WSe2 with symmetrical cladding with Air as the substrate and the superstrate based on the derived equation. UPB – upper polariton branch, LPB – Lower portion branch. U'', U' - the UPB starting point and L'', L' - the LPB starting point, W''_{EP}, W'_{EP} - width of the resonance, G''_{EP}, G'_{EP} - Band gap for 50 nm flake and monolayer WSe_2.

This propagation constant relation is used to model the dispersion behavior shown in Figure 4.3. The dispersion of a 50 nm thick WSe_2 layer was modelled following the approach outlined in ref[8], where a similar framework was applied to multilayer MoS_2. As shown in Figure 4.3a, the resulting dispersion is characteristic of a slab-guided exciton polariton, where the finite thickness supports a waveguide mode. In this case, the TE-guided mode is governed by conventional waveguide dispersion, with the excitonic resonance incorporated through a dispersive dielectric function, capturing the hybrid light-matter nature of the mode. In contrast, the dispersion of a monolayer WSe_2 with symmetric air cladding, shown in Figure 4.3b, is described within a surface-susceptibility framework. Here, the propagation constant depends on the frequency-dependent surface susceptibility $\chi^{(s)}(\omega)$, which modifies the dispersion through the excitonic response of the atomically thin layer.

As the excitation energy approaches the exciton resonance from below, the real part of the surface susceptibility increases, leading to an increase in the propagation constant β and hence a larger in-plane wavevector along the lower polariton branch (LPB). This reflects enhanced light-matter coupling and increased field confinement, rather than purely photonic behavior. Near resonance, the strong dispersive and absorptive response of the exciton causes a rapid

variation in $\chi^{(s)}(\omega)$ resulting in the characteristic back-bending of the dispersion. Importantly, although the wavevector exceeds that of free-space photons in the vicinity of the resonance, the mode remains only weakly bound compared to conventional surface polaritons, with confinement determined by the decay constant $q(\omega)$ This indicates that the mode is not a bulk exciton polariton, but rather a monolayer-guided 2D exciton polariton, supported by the excitonic response of the sheet.

From the derived dispersion relation, several important physical quantities can be extracted to characterize the guided 2D exciton polariton (Figure 4.2). The propagation length L_p, which describes how far the mode can travel before decaying, is given by,

$$L_p = \frac{1}{2\,\mathrm{Im}(\beta)} \tag{4.11}$$

Here, L_p is defined as the intensity propagation length, corresponding to the distance over which the guided-mode intensity decreases to 1/e of its initial value. For a complex propagation constant β, the intensity decays as $I(x)\mathrm{e}^{-2\mathrm{Im}(\beta)\mathrm{x}}$, whereas the corresponding electric-field amplitude decays as $E(x)\mathrm{e}^{-\mathrm{x}/(2L_p)}$. This propagation length is strongly influenced by excitonic absorption and generally decreases near the exciton resonance due to increased optical losses.

The effective mode width W_{eff}, which characterizes the spatial confinement of the mode perpendicular to the monolayer, is defined as

$$W_{\mathrm{eff}} = \frac{1}{\mathrm{Re}(q)} \tag{4.12}$$

Near the exciton resonance, the increase in surface susceptibility leads to larger decay constants, resulting in stronger confinement and reduced mode width. It is important to distinguish the atomic-scale physical thickness of the WSe_2 monolayer from the spatial extent of the guided electromagnetic mode. Although the material consists of a single atomic layer, the associated electromagnetic field extends into the surrounding dielectric environment. The effective mode width defined in Eq. (4.12) characterises the exponential decay length of the field amplitude normal to the monolayer rather than the physical thickness of the material. Consequently, the guided mode can remain relatively weakly confined in the out-of-plane direction despite being supported by an atomically thin semiconductor.

In addition to these quantities, the existence of a guided mode in a monolayer system imposes a constraint on the dielectric environment. Specifically, the difference in refractive indices

between the superstrate and substrate must remain within a certain limit to ensure sufficient confinement:

$$\Delta n = n_1 - n_2 < \frac{\alpha_{\max}}{2n} \cdot \frac{\gamma^2}{(\omega_0 - \omega)^2 + \gamma^2/4} \tag{4.13}$$

This condition highlights the critical role of cladding symmetry in sustaining guided modes. As demonstrated by Khurgin[16] The presence of a guided mode EP in ultrathin WSe_2 is highly dependent on the refractive index condition in Equation 4.13. A significant mismatch in refractive indices between the n_1 and n_2 can greatly impact the electric field's interaction with the monolayer, potentially creating a cutoff condition that disrupts the formation of a confined mode. However, when Δn is within the acceptable range this cutoff is avoided, allowing the mode to remain confined even in extremely thin layers.

4.3. Design strategy for Realizing guided modes in monolayers

As discussed in the previous section, based on the theoretical framework, the existence of the guided-mode EP in a monolayer WSe_2 is governed by the perfect balance between EM confinement, the cladding condition, and the excitonic response. In particular, the requirement for refractive index symmetry in the cladding and the suppression of cutoff conditions impose strict constraints on sample design observe these guided modes. The design strategy used to overcome these limitations and enable the observation of guided-mode EPs in a monolayer WSe_2 is outlined below. .

4.3.1. Concept of Suspended Monolayer

In most conventional designs, a TMDC monolayer is simply placed on top of a substrate such as SiO_2 or sapphire. In these cases, the surrounding environment is clearly not symmetric, since the refractive index of the substrate is much higher than that of air. This leads to an uneven EM field distribution, causing leakage of the guided mode into the higher-index region. As discussed in Section 4.2, this effect is more pronounced for ultrathin materials, where the field is already weakly confined and extends significantly outside the layer.

To solve this problem, a suspended WSe_2 monolayer configuration is employed, as illustrated in Figure 4.4, where the monolayer is transferred onto a pre-patterned hole in the substrate. In this configuration, the monolayer is surrounded by air on both sides, creating a symmetric dielectric environment. As a result, the EM field spreads more evenly across the superstrate and the substrate, leading to reduced leakage into the cladding material and allowing a well-

confined guided mode to form. Removing the high-refractive-index substrate further reduces optical losses, by reducing unwanted losses, enabling longer-distance propagation. This can facilitate near-field observation of guided modes, as the long propagation length allows interference fringes to be observed in s-SNOM measurements.

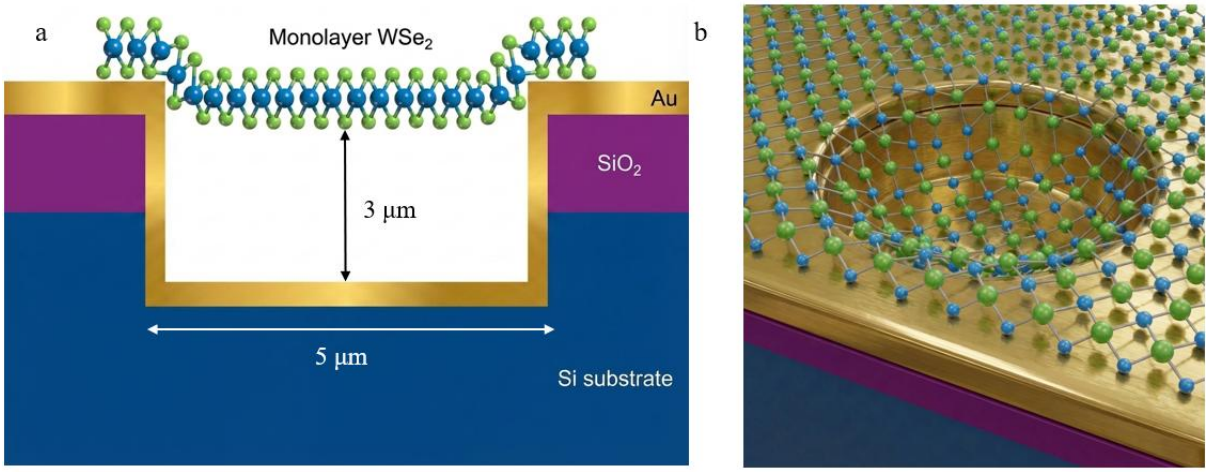


Figure 4.4 | Suspended monolayer WSe_2 geometry. a, 2D schematic of a free-standing monolayer suspended over a pre-patterned $Si/SiO_2/Au$ substrate. **b,** 3D cross-sectional view illustrating the symmetric air cladding surrounding the monolayer.

4.3.2. Numerical simulation of guided mode exciton Polaritons

To validate the proposed design strategy, numerical simulations were performed to investigate the existence and behaviour of guided modes under different cladding conditions. The simulations were carried out using 2D and 3D models that capture the essential physics of the system while maintaining computational efficiency for an atomically thin structure.

In the 2D simulation, the monolayer WSe_2 is represented as a thin sheet characterized by its surface susceptibility, and the guided mode is excited as a propagating electromagnetic wave along the in-plane direction. The electric field distribution is evaluated in the x-z plane, allowing visualization of both the in-plane propagation and out-of-plane confinement of the modeThese 2D simulations are used to calculate the EP wavelength and propagation length, while systematically exploring different cladding conditions and to assess the leakage of those modes into the asymmetric superstrate and substrate. As discussed in section 4.2, the cladding condition affects the existence of the EP within the monolayers. While asymmetric cladding can still support guided modes in multilayer TMDCs. First to validate this, simulations were performed, as shown in Figure 4.5. As clearly observed in Figure 4.5 panel a and b when a multilayer WSE_2 in this case a 30nm thick layer is considered even with symmetric or a-

symmetric cladding conditions the EP guided modes are confined within the TMDC layer. In contrast when a monolayer WSe_2 is considered as shown in panel c and d the leakage into the superstrate and the substrate is high as discussed in the previous sections. Even with different cladding conditions with Au, Silicon dioxide the a-symmetry of the substrate and the superstrate is affecting the existence and the guided modes of the EPs in monolayer WSe_2 as evident by the simulation results inn Figure 4.4 panels d-f.

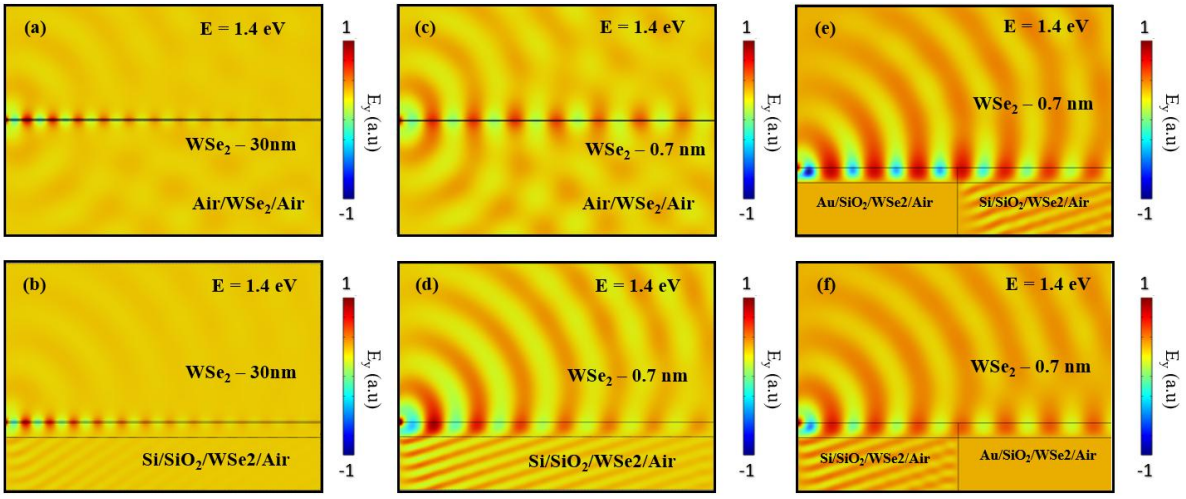


Figure 4.5 | COMSOL simulations of guided exciton polaritons under different cladding conditions. a, b, 30 nm multilayer showing confined modes under symmetric and asymmetric cladding. **c–f,** Monolayer WSe_2 showing significant field leakage and suppression of guided modes under asymmetric environments.

Then a 2D simulation was carried out to mimic the experimental device geometry to observe how the EP propagation and mode confinement behaves as illustrated in Figure 4.6a. Additionally a 3D simulation was carried out with the regions shown in Figure 4.6 b-d. In Figure 4.6a, two representative configurations were considered: a suspended WSe_2 monolayer surrounded by air on the left, and a substrate-supported monolayer on a Si/SiO2/Au substrate. This represents a simplified cross-section of the experimental geometry in 3D (Figure 4.6 b-c), assuming the AFM tip is positioned at the centre and the EP is coupled in the middle, the guided mode is excited from the left side edge in the 2D simulation layout, as shown by the yellow colour arrow in Figure 4.6a. In the suspended configuration, a well-defined guided mode is observed, with the electric field confined near the monolayer and propagating along the in-plane direction. In contrast, for the substrate-supported case (Si/SiO2/Au/WSe2) , the guided mode is significantly suppressed. Instead of Au, if the WSe_2 layer is transferred onto SiO_2, the field is still expected to leak into the substrate, as shown in Figure 4.5, resulting in a

failure to maintain a confined propagation profile. The 3D simulation, performed with the geometry shown in Figure 4.6b, c, with a dipole along the y-axis to mimic the AFM tip, further confirmed the existence of the TE-guided mode in monolayer WSe_2 within the suspended layer.

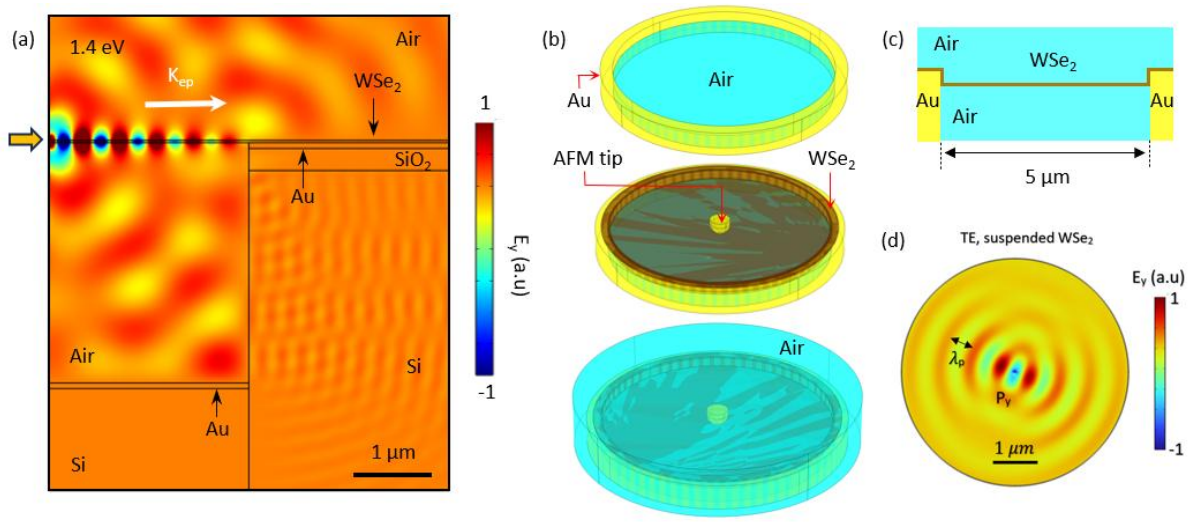


Figure 4.6 | 2D and 3D simulations of the conceptualized free-standing sample. a, Simulated 2D guided mode in half of the free-standing monolayer sample, illustrating the tip-generated mode confinement and propagation when the tip is positioned at the centre of the free-standing monolayer region. **b,** exploded view of the OCMSOL 3D simulation model to showcase the simulated geometry. **c,** The corresponding cross section 2D image of b to highlight the substrate, superstrate and the Au suspended layers and the WSe_2 monolayer placement. **d,** COMSOL simulation of TE modes on the sample surface (X-Y plane cut profile of the 3D simulation shown in (b)). Dipole P_y was used to excite the polariton on the surface mimicking an AFM tip confinement. λ_p marks the TE mode wavelength.

The XY plane E_y profile at the surface of the suspended WSe_2 monolayer shown in Figure 4.6d confirms the presence of a propagating field under the symmetric cladding condition. In comparison, if the air layer underneath is a different material, like SiO_2, the TE modes no longer exist. These results confirm that the presence of a symmetric dielectric environment is critical for sustaining guided EPs in a monolayer system. The simulations also provide insight into the propagation characteristics of the mode, including its effective width and decay behaviour, which are consistent with the theoretical predictions presented in Section 4.2.3. These simulations demonstrate that a sufficiently symmetric dielectric environment is important for sustaining guided exciton polaritons in monolayer WSe_2 for the material and geometric parameters considered here. Although perfect dielectric symmetry is not strictly necessary, as indicated by the finite refractive-index mismatch tolerance in Eq. (4.13), the free-standing

configuration provides nearly symmetric air cladding on both sides of the monolayer. This minimises substrate-induced asymmetry and supports the formation and propagation of the weakly confined guided mode.

4.4. Sample fabrication and Real-space observation of guided modes

Following the design strategy outlined in the previous section, a suspended monolayer WSe_2 structure was fabricated to realize the conditions necessary for supporting guided exciton polaritons. near-field optical measurements were performed to directly visualize the propagation of these modes in real space.

4.4.1. Device fabrication

The patterned substrate was first fabricated by photolithography using a designed photomask with different shapes, as shown in Figure 4.7. A Si/SiO2 substrate was first spin-coated with a photoresist (AZ MIR 701 and LOR 3A). LOR 3A is applied by spin-coating the clean substrate at 500 rpm for 5 s and 4000 rpm for 45 s, followed by a 2-minute bake at 180°C. Subsequently, AZ MIR 701 positive resist is spin-coated at 500 rpm for 5 s, then at 6000 rpm for 1 minute, followed by a 2-minute bake at 85°C.

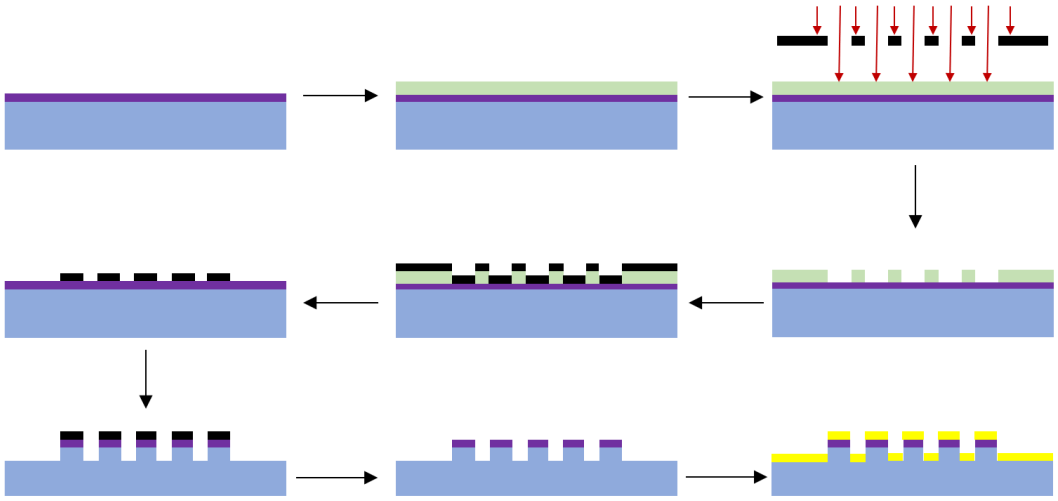


Figure 4.7 | Fabrication process of the patterned substrate using photolithography, including resist coating, exposure, development, metal masking, and etching steps.

Once the photoresist is applied, the next step is to align the photolithography mask with the substrate, which is performed using a Karl Suss MA6/BA6 mask aligner. The photolithography mask is designed with Raith 150 e-beam lithography software. Following this alignment, the substrate is exposed for 35 seconds in soft-contact mode using UV light with a wavelength range of 280-350 nm. The sample is then developed using AZ 726 MIF developer for 45-60

seconds. Following the photolithography process, SiO_2/Si substrates bearing photoresist patterns will be deposited with an Al mask using E-beam evaporation. Then the resist will be lifted off using Acetone overnight. After that, the patterns will be etched into the substrate using ICP-F etching. Finally, the Al mask will be etched, and the etched substrate with holes is cleaned using IPA and O_2 plasma. To enhance the near-field signal and improve fringe visibility, a thin Au layer is deposited on the patterned substrate once again using e-beam evaporation.

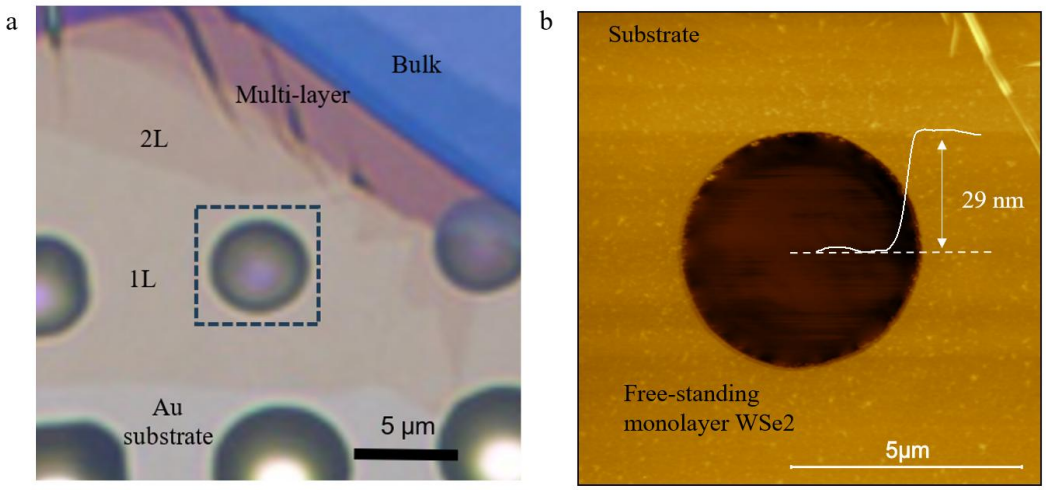


Figure 4.8 | Optical microscopy and AFM characterization of the fabricated sample. a, Optical image showing monolayer, bilayer, and bulk regions on the patterned substrate. **b,** AFM image of the suspended monolayer region.

The suspended monolayer WSe_2 sample is then prepared using mechanical exfoliation and dry transfer. High-quality bulk WSe_2 crystals were first exfoliated to obtain monolayer flakes, which were subsequently identified through optical contrast and photoluminescence measurements. The monolayer was then transferred onto the pre-patterned substrate consisting of a Si/SiO_2/Au stack, with circular and rectangular holes defined prior to transfer. Both circular and rectangular cavity geometries were fabricated to investigate the influence of the suspension boundary on guided exciton-polariton propagation and interference fringe formation. Multiple monolayer transfer attempts were carried out to obtain intact suspended regions suitable for near-field characterization, as the transfer process is sensitive to flake integrity, alignment and handling conditions. The selected circular holes typically had a diameter of approximately 5 μm and a depth of around 3 μm, providing a sufficiently large, suspended region for optical measurements. By positioning the monolayer over these holes, a free-standing configuration was achieved (Figure 4.8) where the WSe_2 layer is surrounded by air on both sides. This geometry satisfies the symmetric cladding condition discussed in Section 4.2 and is essential

for supporting guided modes in the ultrathin limit. The fabricated samples contain regions of monolayer, multilayer, and bulk WSe_2, allowing direct comparison of their optical responses within the same device. The suspended monolayer region, located above the circular hole, serves as the primary area of interest for investigating guided exciton polaritons.

4.4.2. Near field imaging results for the suspended monolayer sample

To probe the guided modes, real-space imaging was performed using a s-SNOM system similar to how the g-HPs were observed in chapter 3. In this case, a Mai Tai laser was externally coupled to the system instead of the mid-IR source. The incident laser was tuned across an energy range (1.37 eV to 1.8 eV) spanning the A-exciton resonance of WSe_2, and only s-polarized light was used to selectively excite TE modes. The near-field signal was detected using a pseudo-heterodyne interferometric scheme, allowing both amplitude and phase information to be extracted. To suppress background contributions, the signal was demodulated at higher harmonics of the tip tapping frequency. For visible-range measurements, the third harmonic amplitude (O3A) and phase (O3P) signals were used. The resulting near-field images of the suspended monolayer region reveal clear interference fringe patterns. The appearance of such well-defined fringes indicates the presence of propagating modes within the monolayer and provides evidence of guided exciton polaritons (Figure 4.9a).

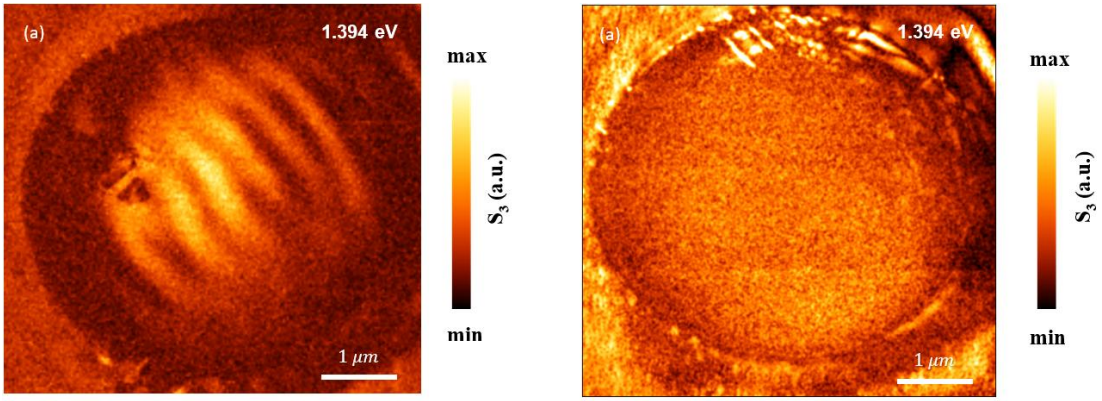


Figure 4.9 | Experimental near-field images. a, suspended monolayer WSe_2 showing clear interference fringes. **b,** Control measurement on an empty hole without WSe_2, showing absence of guided mode fringes.

In contrast, measurements on substrate-supported regions (Figure 4.9a, surrounding the suspended area) and on the empty hole without a transferred flake (Figure 4.9b) do not show comparable fringe patterns, underscoring the essential role of the suspended geometry in enabling guided mode propagation. These fringes are predominantly parallel or slightly curved, even though the guided modes are launched radially from the AFM tip. This arises from

boundary scattering at the circular edge and the s-SNOM detection mechanism, which is analysed in detail in the following section to extract the dispersion relations of the guided exciton polaritons.

The fabrication of suspended monolayer WSe_2 devices involves a technically challenging dry-transfer process, as successfully positioning atomically thin flakes over patterned cavities requires careful handling and depends significantly on the operator's experience. Consequently, the fabrication yield can vary depending on the transfer conditions and operator expertise. To evaluate the reproducibility of guided exciton-polariton propagation, approximately five to six independently fabricated samples incorporating both circular and rectangular cavities were investigated using s-SNOM near-field imaging. The consistency of the guided-mode response was evaluated by comparing interference fringe periods at selected excitation wavelengths above and below the A-exciton resonance across different samples. Although the fringe patterns were influenced by the cavity geometry and boundary-scattering conditions, the characteristic guided-mode behaviour was consistently observed across the investigated samples. These measurements also helped identify circular cavities as a more suitable geometry for obtaining well-defined interference fringes and performing reliable quantitative analysis. Subsequently, two independently fabricated suspended monolayer samples (with circular holes) were selected for detailed wavelength-dependent near-field characterization and dispersion analysis.

4.4.3. Physical origin of results

The observed fringe patterns arise from the interference between different optical pathways in the s-SNOM measurement. When the AFM tip is illuminated, it generates a localized electromagnetic field that excites guided exciton polaritons in the monolayer. These polaritons propagate radially away from the tip until they reach the boundary of the suspended region. At the circular edge, a portion of the guided mode is scattered back into free space as photons (Figure 4.10). These scattered photons travel towards the detector and interfere with the photons directly scattered from the AFM tip. As a result, the detected signal contains contributions from both the tip-scattered field (P_1) and the edge-scattered field (P_2). A third pathway (P3) may arise when polaritons reflected from the boundary are re-scattered by the AFM tip. Away from resonance, where the propagation length is larger, this pathway can contribute to the detected signal. However, its contribution is significantly weaker than that of P_2 Near the exciton resonance, where the propagation length is strongly reduced, the contribution of P_3 becomes negligible (Figure 4.2). Therefore, the fringe formation is assumed

to arise predominantly from the interference between P_1 and P_2. There are two main types of EP emission, scattering configurations that must be considered (Figure 4.10 b and c). The first corresponds to tip-emission and edge-scattering, where the AFM tip launches polaritons that propagate toward the boundary. When the tip is positioned near the centre of the suspended region, the interference patterns are dominated by this mechanism. As the tip approaches the boundary, the incident field can also directly excite the edge. Therefore, both tip-launched and edge-excited contributions are present, leading to additional scattering pathways. Additionally, since the tip is closer to the boundary now the reflected EPs can also scatter back through the P_3 scattering path. This explains why the fringe pattern becomes distorted or disappears near the boundary.

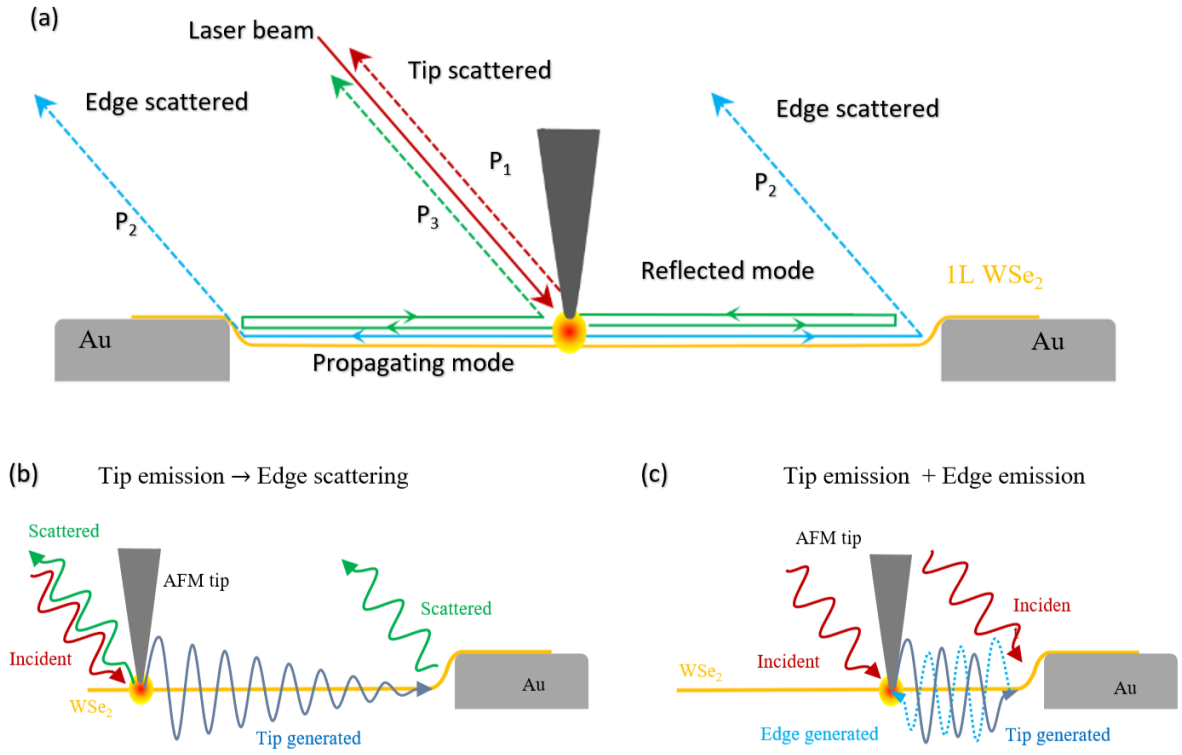


Figure 4.10 | Exciton-polariton boundary scattering behaviour. a, Illustration of various photon collection paths by the s-SNOM detector. The red solid arrow indicates the incident beam, while the red dotted line shows the path of tip-scattered photons along P_1. The blue solid and dotted lines represent the guided mode EP and edge-scattered photons, which are collected along path P_2. Green solid and dotted arrows illustrate the edge-reflected guided mode and tip-scattered photons moving along path P_3. **b,** Schematic illustrations of polariton generation and scattering conditions when the AFM tip is positioned near the centre of the circular boundary. **c,** Schematic illustrations of polariton generation and scattering conditions when the tip is closer to the boundary edge.

Therefore, the EP interference fringes observed in these experiments arise from the interference between the two propagation pathways, P_1 and P_2. The superposition of these contributions produces a spatial modulation in the detected signal, giving rise to the observed fringe patterns. The fringe periodicity is determined by the phase difference between these pathways, which is determined by the propagation characteristics of the guided mode within the monolayer. This interference mechanism forms the basis for quantitatively extracting the polariton wavelength from the observed fringe periodicity.

An important feature of the experimental observations is that the fringes remain largely parallel over a wide region, even though the underlying polariton propagation is radial. This behaviour indicates that the interference is dominated by specific scattering pathways at the boundary, rather than by the full radial distribution of the mode. A detailed theoretical analysis of this phenomenon, including the role of boundary scattering and phase accumulation, that is presented in the following section.

4.5. Fringe formation mechanism and Analysis

The real-space near-field images presented in the previous section exhibit well-defined interference fringe patterns across the suspended monolayer region. While these fringes provide clear evidence of guided mode propagation, their nearly parallel appearance, despite radial excitation requires a detailed physical explanation. In this section, we develop a theoretical framework to describe the origin of these fringes, based on the interference between different scattering pathways (P_1, P_2 P_3) in the s-SNOM measurement.

4.5.1. Boundary scattering model

To analyse the fringe formation, we consider the geometry of the suspended monolayer, where the AFM tip is located at a position defined in a coordinate system aligned with the incident beam (Figure 4.11a). As the guided EPs propagate radially from the tip, they reach the circular boundary and can be scattered back into free space. Due to momentum conservation at the boundary, only specific points on the circular edge contribute significantly to the detected signal. For a given tip position A (d, d'), two dominant scattering points can be identified on the boundary, denoted as E_1 and E_2. These boundary points can scatter these polaritons toward the detector while conserving the momentum along the scattering boundary directions labelled BE_1 and BE_2. At these points the in-plane momentum of the guided mode is partially converted into free-space photon momentum directed towards the detector. Practically, in the s-SNOM

setup there is a small region of the boundary cantered at E_1 and E_2 that can scatter the light towards the detector since there is collection angle (for scattered photons) that depends on the physical placement of the parabolic mirror in the system as discussed in ref[10].

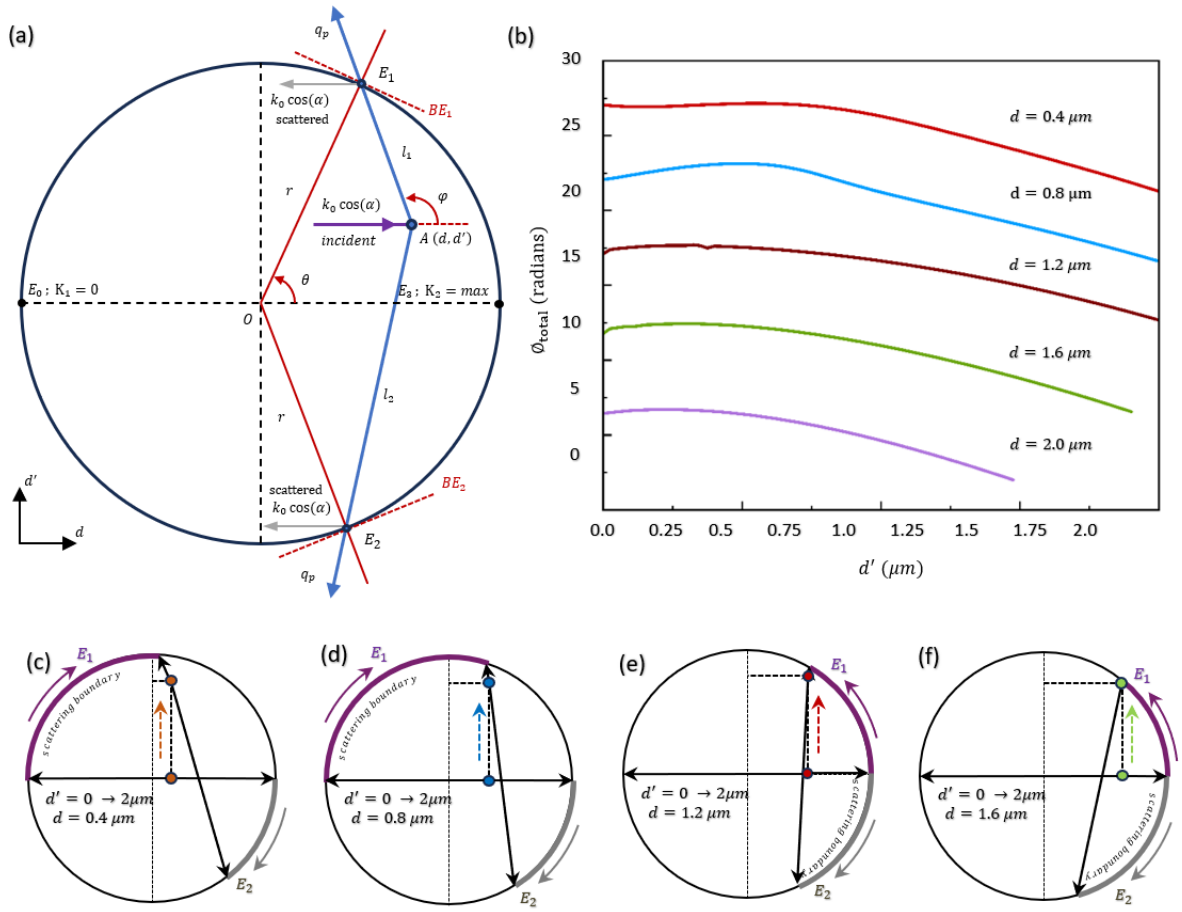


Figure 4.11 | Fringe formation and numerical simulation results. a, 2D Schematic of the guided mode with a wave vector q_p scattering at boundary points E_1 and E_2 along the circular edge, producing free-space photons (k_0) directed towards the detector. $r = 2.5\mu m$, where r is the radius of the hole. l_1 and l_2 are the propagation distances of the guided modes propagating from the AFM tip position to E_1 and E_2 scattering points. K_1 and K_2 are the guided mode edge scattering efficiencies for the two scattering points. E_0 and E_3 are the two points in the boundary with minimum and maximum boundary scattering efficiency. θ is the angle between OE_1 and the d axis. φ represents the angle of q_p w.r.t the d axis. d-d' coordinate frame is 45° rotated relative to the x-y sample coordinate frame to align the actual incident laser direction along the d axis. BE_1 and BE_2 are the scattering boundary edge directions at scattering points E_1 and E_2. **b,** Numerical simulation result of the total phase difference in the SNOM-detected signal for various AFM tip positions at fixed d coordinates: $d = 0.4, 0.8, 1.2, 1.6$ and $2\ \mu m$. **c-f,** Schematic of boundary scattering points for specific AFM tip positions within the circular

boundary. The dotted vertical arrows indicate AFM tip movement in each panel, with the *d* axis coordinate held constant at *d* = 0.4, 0.8,1.2, and 1.6 μm. E_1 and E_2 mark the scattering points for each AFM tip position. The purple boundary region and arrow depict changes in the E_1 scattering point, while the green boundary region and arrow represent changes in the E_2 scattering point as the AFM tip moves, shown by the dotted vertical arrows in each panel.

But here for simplicity of the calculation, we assume that the collection angle is zero and only considers the edge scattered photons that moves directly towards the detector in the same path that the incident beam approached the AFM tip. The propagation distances from the AFM tip to these scattering points, denoted as $l_1$and l_2, determine the phase accumulated by the guided mode before scattering. The resulting scattered photons then interfere with the directly scattered photons from the tip, forming the detected signal. This boundary scattering mechanism is fundamentally different from conventional straight-edge systems, where the scattering geometry is simpler. In the present case, the circular boundary introduces a position-dependent scattering condition, which plays a key role in shaping the fringe patterns.

4.5.2. Phase interference model

The interference pattern observed in the s-SNOM signal arises from the phase difference between photons collected through two main pathways P_1 and P_2 followed by propagation to the detector. The phase difference associated with the scattering at a given boundary point can be expressed as the sum of two contributions. The phase accumulated by the guided exciton polariton during propagation, and the phase associated with the free-space photon propagation after scattering. For the two dominant scattering points $E_1$and E_2, the phase differences of the photons scattered from path P_1 and P_2 can be written as,

$$\Phi_1 = q_p l_1 + k_0 \cos(\alpha)\, l_1 \cos(\phi) \tag{4.14}$$

$$\Phi_2 = q_p l_2 + k_0 \cos(\alpha)\, l_2 \cos(\phi) \tag{4.15}$$

where q_p is the in-plane momentum of the guided mode, $k_0$is the free-space wavevector of the incident light, α is the incident angle, and ϕ is the propagation direction of the guided mode relative to the coordinate system.

For the guided mode EPs scattered at boundary points E_1 and E_2, momentum conservation along the scattering boundary must be maintained as follows:

$$q_p \sin(\theta - \varphi) = k_0 \sin(\theta) \cos(\alpha) \tag{4.16}$$

Here, θ represents the angle between OE (the line connecting the centre to the scattering point) and the d-axis, which defines the direction of the scattering boundary. For a given AFM tip position, the guided exciton polaritons scattered from the two dominant boundary points, E_1 and E_2, contribute complex optical fields with amplitudes A_1 and A_2 and relative phases Φ_1 and Φ_2, respectively. Taking the directly tip-scattered field as the phase reference, the combined edge-scattered field is obtained through coherent superposition of these two contributions. Therefore, the effective phase of the combined edge-scattered field relative to the tip-scattered reference is given by:

$$\Phi_{edge} = arg(A_1 e^{i\Phi_1} + A_2 e^{i\Phi_2}) \tag{4.17}$$

The amplitudes of the scattered signals (A_1 and A_2) from the two boundary points depend on factors such as propagation loss and scattering efficiency at the boundary.

$$A_1 = \mathrm{K}_1 e^{-\kappa l_1}$$

$$A_2 = \mathrm{K}_2 e^{-\kappa l_2}$$

Here, K_1 and K_2 represent the effective scattering coefficients at the corresponding boundary points, while l_1 and l_2 denote the guided-mode propagation distances from the AFM tip to these points. Since the propagation length $L_p(\omega)$ defined in Eq. (4.11) corresponds to the (1/e) intensity decay length, the electric-field amplitude decreases as $e^{-l/(2L_p)}$. Accordingly, the amplitude attenuation coefficient is defined as:

$$\kappa = \frac{1}{2L_p(\omega)}$$

Then the scattering boundary point has a scattering efficiency which is dependent on the angle of the direction of the propagating polariton and the respective boundary. Additionally, since our suspended layer is curved into the hole at the edges one half of the boundary is reducing the scattering efficiency much more. Therefore K_1 and K_2 introduce the scattering efficiencies at the respective boundaries. The scattering efficiency K_1 is smaller when the scattering point is in the second or third quadrant (Figure 4.11c-f) due to the curved in nature of the suspended sample into the hole. We used a zero-scattering efficiency for K_1 if it is scattered at the boundary point E_0 (Figure 4.11a) and it gradually increased with the scattering angle up until point E_3 (Figure 4.11a) where K (K_1 *and* K_2) is maximum.

Using the equations above, we numerically simulated the total phase change (Φ_{total}) of the detected signal in the s-SNOM system, mapping it within the d-d' coordinate frame based on

the AFM tip's position. According to the dispersion relation discussed in section 4.2.3 for guided mode EPs in monolayer WSe_2, we simulated fringe formation across different excitation energies. As demonstrated by Khurgin[16] the confinement of these guided mode EPs are closer to 1. We therefore selected multiple excitation energies where the EP confinement was close to this value and conducted numerical simulations. For the numerical phase calculation, the incident photon energy was set to 1.61 eV. The guided polariton and incident optical field share the same excitation frequency, while the polariton in-plane wavevector is determined by the dispersion relation evaluated at that frequency. The result obtained for this is shown in Figure 4.11b. Even with variations in the assumed EP energy, the fringe patterns remained largely parallel, with phase values slightly adjusted for different $\langle d, d' \rangle$ coordinates making the fringe period different. These results indicate that the fringes are nearly parallel, as illustrated in Figure 4.11b, enabling the AFM tip to travel along a line parallel to d axis to measure fringe periodicity and accurately determine guided mode parameters. This formulation captures the essential physics of fringe formation, showing that the observed interference pattern is governed by the interplay between guided mode propagation and boundary scattering.

4.5.3. Simplified fringe condition

While the full interference model involves contributions from multiple scattering points, the fringe pattern can be significantly simplified under certain conditions. When the AFM tip is positioned along the central axis of the circular boundary, the symmetry of the system leads to a dominant contribution from a single effective scattering point. In this case, boundary scattering efficiency is minimum at E_0 and maximum at E_3, allowing only the edge point E_3 to scatter photons along path P_2 towards the detector. Under this condition, the total phase difference can be approximated as

$$\Phi_{\text{total}} \approx (r - d)\big(q_p + k_0 \cos(\alpha)\big) \tag{4.18}$$

where r is the radius of the circular boundary and d is the distance of the AFM tip from the centre. The fringe pattern corresponds to locations where the phase difference changes by 2π. Therefore, the experimentally observed fringe period ρ is given by

$$\rho = \frac{\lambda_p}{1 + \frac{\lambda_p}{\lambda_0}\cos(\alpha)}$$

which can be rearranged to express the polariton wavelength as

$$\lambda_p = \frac{\rho\,\lambda_0}{\lambda_0 - \rho\cos(\alpha)} \tag{4.19}$$

where λ_0 is the free-space wavelength of the excitation laser. This result provides a direct relationship between the experimentally measurable fringe period and the intrinsic wavelength of the guided exciton polariton.

4.6. Strong coupling and dispersion of guided exciton polaritons.

The theoretical framework and analysis developed in the previous sections enable the extraction of the dispersion relation of guided EPs from real-space near-field measurements. The simplified fringe condition enables a practical method for extracting the dispersion of guided exciton polaritons from near-field imaging data. By measuring the fringe period ρ from line profiles taken across the s-SNOM images, the polariton wavelength λ_p can be calculated using the relation derived (equation 4.18). The line cuts for the SNOM measurements of the EPs near the exciton resonance are taken along a direction parallel to the incident beam axis, near the centre of the suspended region as shown in Figure 4.12. This also minimizes the influence of complex boundary effects and ensures accurate determination of the fringe spacing. Once the polariton wavelength is obtained, it can be converted into the in-plane wavevector using,

$$\beta = \frac{2\pi}{\lambda_p} \tag{4.20}$$

The experimental polariton wavevectors were determined from the measured interference fringe periods using Equations. (4.19) and (4.20). The uncertainty in the extracted wavevector arises primarily from the determination of the fringe period from the near-field line profiles and the experimental incidence-angle uncertainty. Combining the wavelength-extraction relations gives $k_p = \frac{2\pi}{\rho} - k_0\cos(\alpha)$, where ρ is the measured fringe period and α is the incidence angle. Assuming independent uncertainties, the corresponding wavevector uncertainty can be estimated through standard error propagation as:

$$\sigma_{k_p} = \sqrt{\left(\frac{2\pi\sigma_p}{\rho^2}\right)^2 + (k_0 \sin\alpha\sigma_\alpha)^2}$$

Here, σ_p and σ_α represent the uncertainties in fringe spacing and incidence angle, respectively, with the angular uncertainty expressed in radians. These uncertainties determine the precision of the experimentally reconstructed dispersion, particularly near the excitonic resonance where the fringe contrast decreases and accurate period extraction become more challenging.

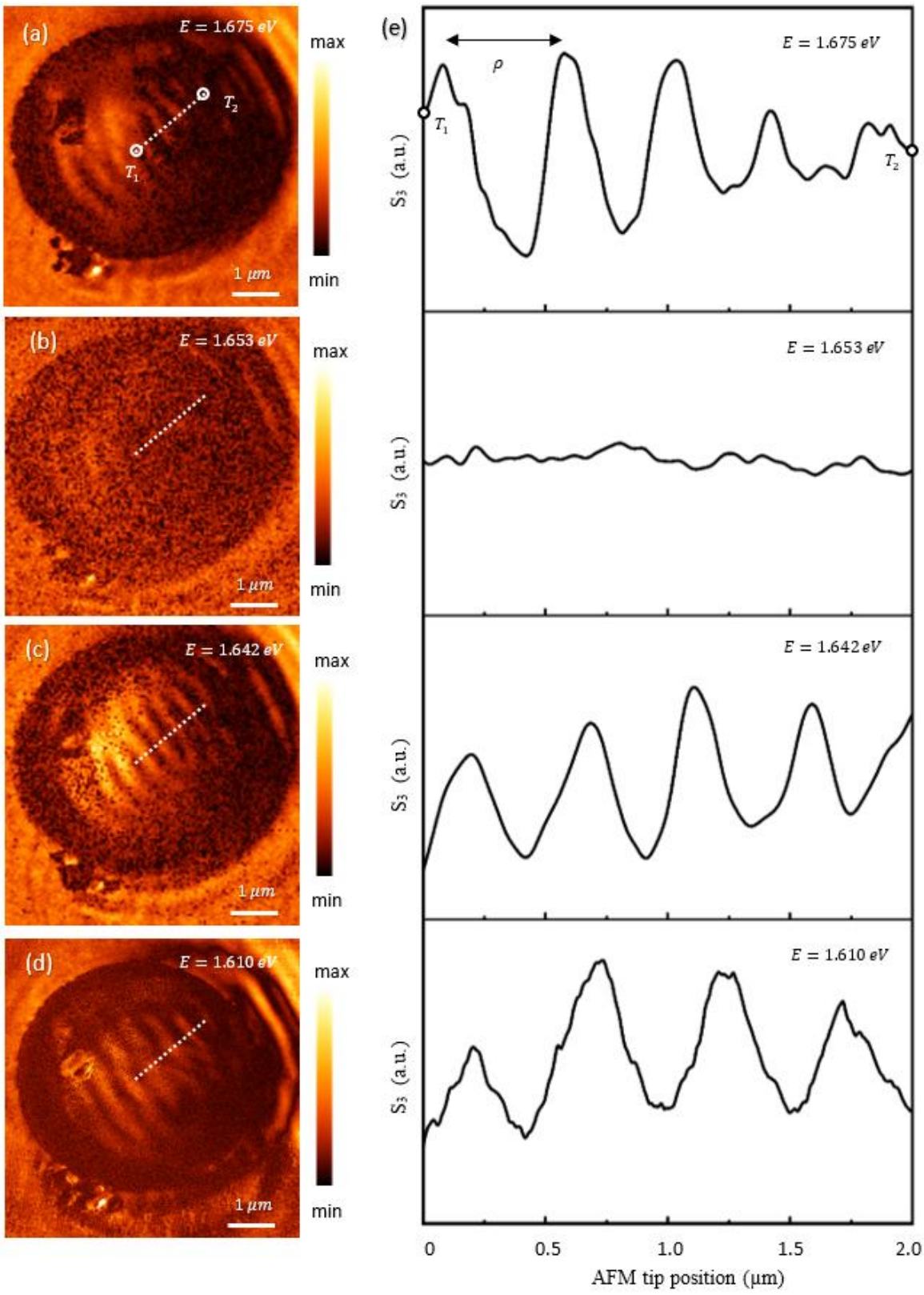


Figure 4.12 | Dispersion analysis of the guided mode from a free standing monolayer WSe_2. a-d, Experimental near-field images of guided modes in suspended monolayer WSe_2 at the excitation Energies of $E = 1.675, 1.653, 1.642$ and $1.610\ eV$. Colour bar represents the intensity of the s-SNOM amplitude signal S_3. T_1 and T_2 are the AFM tip positions at the

start, and the end of the line cut profile. **e,** Line cut profile data for the near field images a-d parallel to the d axis and closer to $d' = 0$. ρ is the measured experimental fringe period.

By repeating this procedure for excitation energies in the range of approximately 1.37 eV to 1.8 eV, the dispersion of the guided mode was reconstructed experimentally. An important observation is that at the exciton resonance energy, the fringe pattern becomes significantly suppressed or disappears entirely as shown in Figure 4.12 panel b. This is attributed to the strong absorption at resonance, which reduces the propagation length of the mode and prevents the formation of well-defined interference fringes. Away from resonance, however, the fringes are clearly visible for other excitation energies, allowing accurate extraction of the dispersion. The resulting data reveal a continuous variation of the propagation constant with energy, indicating the presence of a well-defined guided mode supported by the monolayer.

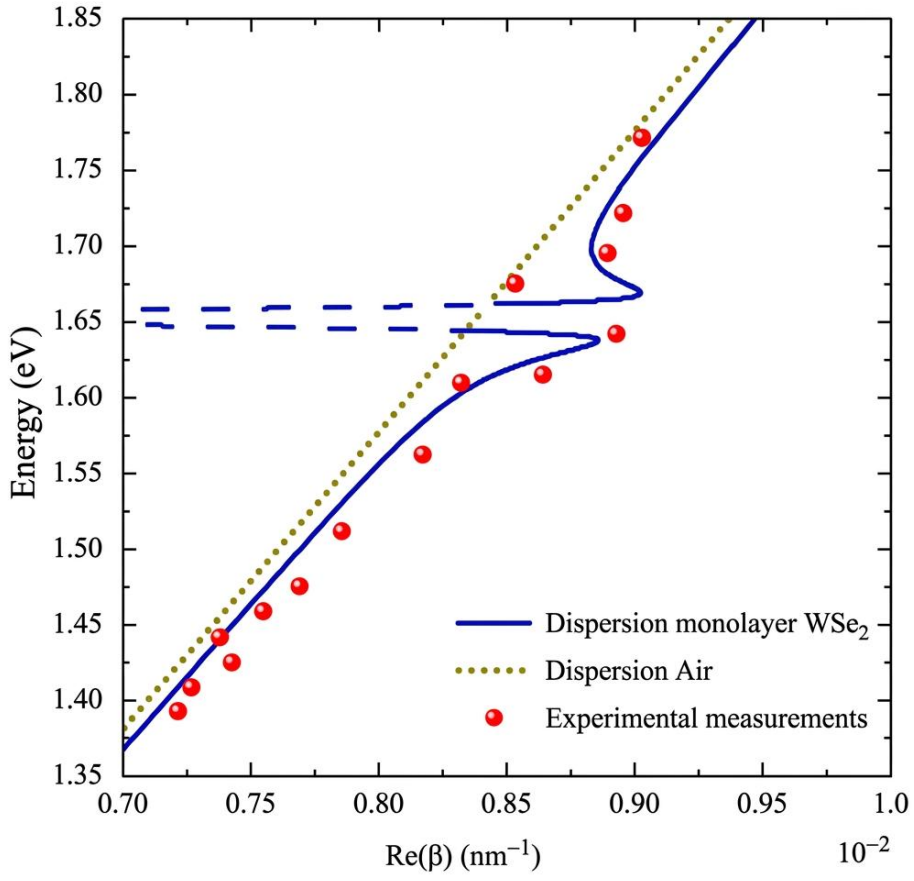


Figure 4.13 | Experimentally reconstructed dispersion of guided exciton polaritons in a free-standing WSe_2 monolayer. Simulated dispersion relation of a 2D guided exciton polaritons (blue curve) alongside experimentally measured wave vectors (red dots) obtained from near-field imaging results.

The experimentally obtained data for the in-plane wave vector and the theoretical dispersion curve is plotted in Figure 4.13. Here the experimentally calculated in-plane wavevectors are marked in alongside the derived dispersion curve in section 4.2.3.

For the quantitative dispersion analysis, wavelength-dependent near-field measurements were performed on two independently prepared suspended monolayer WSe_2 samples. The interference fringe periods were extracted from the corresponding line-cut profiles, and the resulting measurements were combined through averaging to determine the experimental polariton wavevectors presented in Figure 4.13. This approach reduces the influence of device-specific variations and improves the reliability of the experimentally reconstructed dispersion.

The experimentally reconstructed dispersion shows a clear transition from predominantly photon-like to exciton-polariton behaviour. At energies well below the exciton resonance, the dispersion closely follows the free-space light line, indicating a predominantly photonic response with relatively weak excitonic influence. As the excitation energy approaches the exciton resonance, a pronounced deviation from the light line is observed, accompanied by an increase in the in-plane wavevector. This demonstrates the growing influence of the excitonic response on the guided optical mode. A key feature of the measured dispersion is the pronounced back-bending near the exciton resonance, indicating a significant modification of the guided optical response. This behaviour, together with the deviation from the free-space light line and agreement with the surface-susceptibility model, provides evidence of exciton-photon hybridisation in the suspended monolayer waveguide. Unlike conventional cavity-polariton systems, discrete normal-mode splitting is not resolved in the present propagating geometry. Instead, the reconstructed dispersion exhibits a continuous, strongly dispersive response near the excitonic resonance. At the resonance energy, the near-field fringes are strongly suppressed, indicating increased absorption and reduced propagation, consistent with the expected damping of the guided mode.

As discussed in Section 1.2, a definitive identification of the strong-coupling regime requires the coherent exciton-photon interaction to be evaluated relative to the relevant optical losses and excitonic dephasing rates. In the present propagating monolayer geometry, the measurements do not independently determine the coherent coupling rate and the corresponding damping parameters required to establish a quantitative strong-coupling threshold. Therefore, although the observed back-bending and dispersion modification support exciton-photon hybridisation, they do not independently confirm that the strong-coupling condition has been satisfied. Further investigation of the complex mode dispersion, linewidths,

and damping characteristics would be required to evaluate the coupling regime quantitatively. Overall, these results demonstrate an exciton-modified guided polaritonic response in a suspended WSe_2 monolayer, with the dispersion evolving from predominantly photon-like behaviour away from resonance to pronounced excitonic influence near the resonance.

References

1. Hu, F., & Fei, Z.(s). Recent progress on exciton polaritons in layered transition-metal dichalcogenides. Advanced Optical Materials 2020, 8 (5), 1901003.

2. Ghosh, S., Su, R., Zhao, J., Fieramosca, A., Wu, J., Li, T., Zhang, Q., Li, F., Chen, Z., & Liew, T.(s). Microcavity exciton polaritons at room temperature. Photonics Insights 2022, 1 (1), R04-R04.

3. Sun, X., Zhu, Y., Qin, H., Liu, B., Tang, Y., Lü, T., Rahman, S., Yildirim, T., & Lu, Y.(s). Enhanced interactions of interlayer excitons in free-standing heterobilayers. Nature 2022, 610 (7932), 478-484.

4. Zhu, B., Chen, X., & Cui, X.(s). Exciton binding energy of monolayer WS2. Scientific reports 2015, 5 (1), 9218.

5. Hansen, K. R., Colton, J. S., & Whittaker-Brooks, L.(s). Measuring the exciton binding energy: learning from a decade of measurements on halide perovskites and transition metal dichalcogenides. Advanced Optical Materials 2024, 12 (3), 2301659.

6. Weisbuch, C., Nishioka, M., Ishikawa, A., & Arakawa, Y.(s). Observation of the coupled exciton-photon mode splitting in a semiconductor quantum microcavity. Physical review letters 1992, 69 (23), 3314.

7. Dhara, S., Chakraborty, C., Goodfellow, K., Qiu, L., O'Loughlin, T., Wicks, G., Bhattacharjee, S., & Vamivakas, A.(s). Anomalous dispersion of microcavity trion-polaritons. Nature Physics 2018, 14 (2), 130-133.

8. Kusch, P., Mueller, N. S., Hartmann, M. T., & Reich, S.(s). Strong light-matter coupling in MoS 2. Physical Review B 2021, 103 (23), 235409.

9. Hu, F., Luan, Y., Speltz, J., Zhong, D., Liu, C., Yan, J., Mandrus, D., Xu, X., & Fei, Z.(s). Imaging propagative exciton polaritons in atomically thin WSe 2 waveguides. Physical Review B 2019, 100 (12), 121301.

10. Hu, F., Luan, Y., Scott, M., Yan, J., Mandrus, D., Xu, X., & Fei, Z.(s). Imaging exciton–polariton transport in MoSe2 waveguides. Nature Photonics 2017, 11 (6), 356-360.

11. Fei, Z., Scott, M., Gosztola, D., Foley IV, J., Yan, J., Mandrus, D., Wen, H., Zhou, P., Zhang, D., & Sun, Y.(s). Nano-optical imaging of WS e 2 waveguide modes revealing light-exciton interactions. Physical Review B 2016, 94 (8), 081402.

12. Lee, S. W., Lee, J. S., Choi, W. H., & Gong, S. H.(s). Ultrathin WS2 polariton waveguide for efficient light guiding. Advanced Optical Materials 2023, 11 (16), 2300069.

13. Kondratyev, V. I., Permyakov, D. V., Ivanova, T. V., Iorsh, I. V., Krizhanovskii, D. N., Skolnick, M. S., Kravtsov, V., & Samusev, A. K.(s). Probing and control of guided exciton–polaritons in a 2D semiconductor-integrated slab waveguide. Nano Letters 2023, 23 (17), 7876-7882.

14. Alpeggiani, F., Gong, S.-H., & Kuipers, L.(s). Dispersion and decay rate of exciton-polaritons and radiative modes in transition metal dichalcogenide monolayers. Physical Review B 2018, 97 (20), 205436.

15. Hu, D., Yang, X., Li, C., Liu, R., Yao, Z., Hu, H., Corder, S. N. G., Chen, J., Sun, Z., & Liu, M.(s). Probing optical anisotropy of nanometer-thin van der waals microcrystals by near-field imaging. Nature communications 2017, 8 (1), 1471.

16. Khurgin, J. B.(s). Two-dimensional exciton–polariton—light guiding by transition metal dichalcogenide monolayers. Optica 2015, 2 (8), 740-742.

5. Induced Topological Phonon Polaritons

Engineering band structures to have non-trivial topological invariants (non-zero Chern numbers or valley-dependent Berry curvatures) is the foundation of realizing topological photonic[1-4] and polaritonic[5-9] systems. Most work carried out in the recent past has observed topological polaritonic systems, but almost all of this work relies on a photonic system designed to be topologically non-trivial and coupled to the material excitation either phonons[10] (lattice vibrations), excitons[9,11] (bound electron hole pairs), magnons, etc. in a wide range of electromagnetic spectrum based on the application and requirements[12,13]. These works have been demonstrated within the last 5 years, and topology is embedded in the photonic grating or metasurface[9-11]. This means it is introduced at the level of the photonic platform through techniques such as symmetry breaking, lattice engineering, or the design of artificial gauge fields, which are then coupled to the material excitations. The existence of these topological edge states or defect states is guaranteed by the geometry and the symmetry conditions of the photonic lattice design. So, in these kinds of systems, once the topological phase is structurally encoded into the photonic system, it remains fixed.

In contrast to all those works, the work discussed in this chapter explores a fundamentally different approach to realizing the topological polaritonic systems. Here, the photonic and material systems are topologically trivial when uncoupled. In this work, the two systems are coupled to introduce topological edge states, with the topology emerging solely from the strong light-matter interaction. The coupling of the systems induces band hybridization and inversion, leading to a topological phase transition. This new technique of realizing the topological state through an interaction-driven mechanism rather than depending on a pre-designed topological photonic lattice establishes a new paradigm for topological phase realization in photonic systems. In this work, the photonic system is designed to couple to phonon excitations, but the same principles and techniques can be applied to couple a similar photon-grating design to excitons or other material excitations. In this new framework, the topological transition is mainly induced by the hybridization of the two independent systems. Importantly, both systems individually show a Chern number C=0 (trivial topology), but still the interaction of the two systems gives rise to a topological system with non-trivial topological characteristics.

5.1. Theoretical Background of Induced Topology

5.1.1. Photonic system and trivial band structure

The system's starting point is a periodic dielectric photonic structure, implemented as a Si grating. The optical response of such a structure is governed by Maxwell's equations in a spatially periodic medium,

$$\nabla \times \left(\frac{1}{\mu_0}\nabla \times \mathrm{E}(\mathrm{r})\right) = \omega^2 \varepsilon(\mathrm{r})\mathrm{E}(\mathrm{r})$$

where E(r) is the electric field, ε(r) is the spatially periodic dielectric function, and ω is the angular frequency.

Due to the periodicity of the grating, the dielectric function satisfies

$$\varepsilon(\mathrm{r}) = \varepsilon(\mathrm{r} + \mathrm{R}),$$

for any lattice vector R. As a result, the eigenmodes of the system obey Bloch's theorem, and can be written as

$$\mathrm{E}_{n,\mathrm{k}}(\mathrm{r}) = e^{i\mathrm{k}\cdot\mathrm{r}}\mathrm{u}_{n,\mathrm{k}}(\mathrm{r}),$$

where k is the Bloch wavevector, n is the band index, and $\mathrm{u}_{n,\mathrm{k}}(\mathrm{r})$ is a periodic function with the same periodicity as the lattice. Solving this eigenvalue problem yields the photonic band structure $\omega = \omega_n(\mathrm{k})$, which describes how optical modes propagate within the periodic structure.

In the absence of coupling to material resonances, the silicon grating behaves as a purely photonic system. Its band structure is governed by the grating geometry and symmetry and remains topologically trivial. The system preserves time-reversal symmetry and does not exhibit band inversion, resulting in a zero topological invariant. While structural parameters such as period, duty cycle, and asymmetry modify the dispersion, they do not by themselves induce non-trivial topology. Instead, they produce distinct but still trivial band structures. These differences, however, play a crucial role when forming interfaces between domains, as they allow the system to be engineered toward topological transitions under additional interactions.

To understand the origin of the photonic bands and their interaction, we employ the guided-mode expansion (GME) method, which forms the theoretical foundation for deriving the effective Hamiltonian[14-17]. The structure is modelled as a combination of a lower homogeneous dielectric slab and an upper periodically modulated grating layer (Figure 5.1a-c). This

decomposition allows the system to be treated as a perturbation of a slab waveguide. The permittivities of the lower and the upper layer of the grating structure are defined as,

$$\widehat{\varepsilon_L} = \begin{cases} 0, & z < 0, z > L_2, \\ \hat{\varepsilon} - \varepsilon_0, & 0 < z < L_1, \end{cases} ; \widehat{\varepsilon_U} = \begin{cases} \hat{\varepsilon} - \varepsilon_0, & L_1 < z < L_2, \\ 0, & z > L_2, z < L_1, \end{cases} \quad (5.1)$$

Here ε_0 is the background (cladding) permittivity. The small asymmetry in low-index substrate and superstrate permittivities can be included as corrections to the refractive indices. First, the unpatterned dielectric slab (Figure 5.1c) is considered, which supports guided electromagnetic modes. For TE polarization, the electric field (with only y-component) can be written as

$$E_y(x, z) = \mathcal{E}_1(z) e^{ikx},$$

where the transverse mode satisfies

$$\mathcal{E}_1(z) \propto \begin{cases} \cos[k_z(z - L_1/2)], & \text{even modes} \\ \sin[k_z(z - L_1/2)], & \text{odd modes} \end{cases}$$

for $|z| < L_1$ with $k_z = \sqrt{k_x^2 - k_0^2 \varepsilon}$ and outside the slab, the field decays exponentially, indicating confinement as,

$$\mathcal{E}_1(z < 0) \propto e^{-\sqrt{k_0^2 \varepsilon_0 - k_x^2}\,|z|}$$

$$\mathcal{E}_1(z > L_1) \propto e^{-\sqrt{k_0^2 \varepsilon_0 - k_x^2}\,|z| - L_1}$$

By applying boundary conditions at the slab interfaces $z = 0$ and $z = L_1$, the dispersion relation $\omega(k_x)$of the guided modes is obtained. For small wavevectors near the Γ-point, this dispersion can be approximated as

$$\omega_1^{\pm}(\pm(k_x + \Delta k_x)) \approx \omega_1^0 \pm v_1 \Delta k_x \quad (5.2)$$

representing two counter-propagating modes with group velocity v_1 which is valid for small wavevectors k_x. These two counter-propagating modes are uncoupled.

Then, if we look at the upper grating, the total permittivity of the grating can be written as:

$$\varepsilon_2(x, z) = \varepsilon_0 + \hat{\varepsilon}_U(z) + \varepsilon_d(x, z)$$

The periodic permittivity modulation of the grating, $\varepsilon_d(x, z)$, is expressed as a Fourier series along the x-direction with spatial period Λ. This expansion decomposes the structure into discrete spatial harmonics, each corresponding to a diffraction order. Due to symmetry, the Fourier coefficients are real and satisfy $\varepsilon_d^{(-l)}(z) = \varepsilon_d^{(l)}$. The zeroth-order term defines the average permittivity of the structure, while higher-order terms describe the periodic

perturbation responsible for coupling between guided modes. Therefore, the periodic grating introduces a modulation in the dielectric function.

$$\varepsilon(x,z) = \varepsilon_{\text{av}}(z) + \sum_{l\neq 0} \varepsilon^{(l)}(z) e^{-i\frac{2\pi}{\Lambda}lx},$$

This periodic modulation couples modes with momenta differing by reciprocal lattice vectors ($k \to k \pm 2\pi/\Lambda$). This coupling leads to hybridization between forward and backward propagating modes, resulting in band folding and bandgap formation.

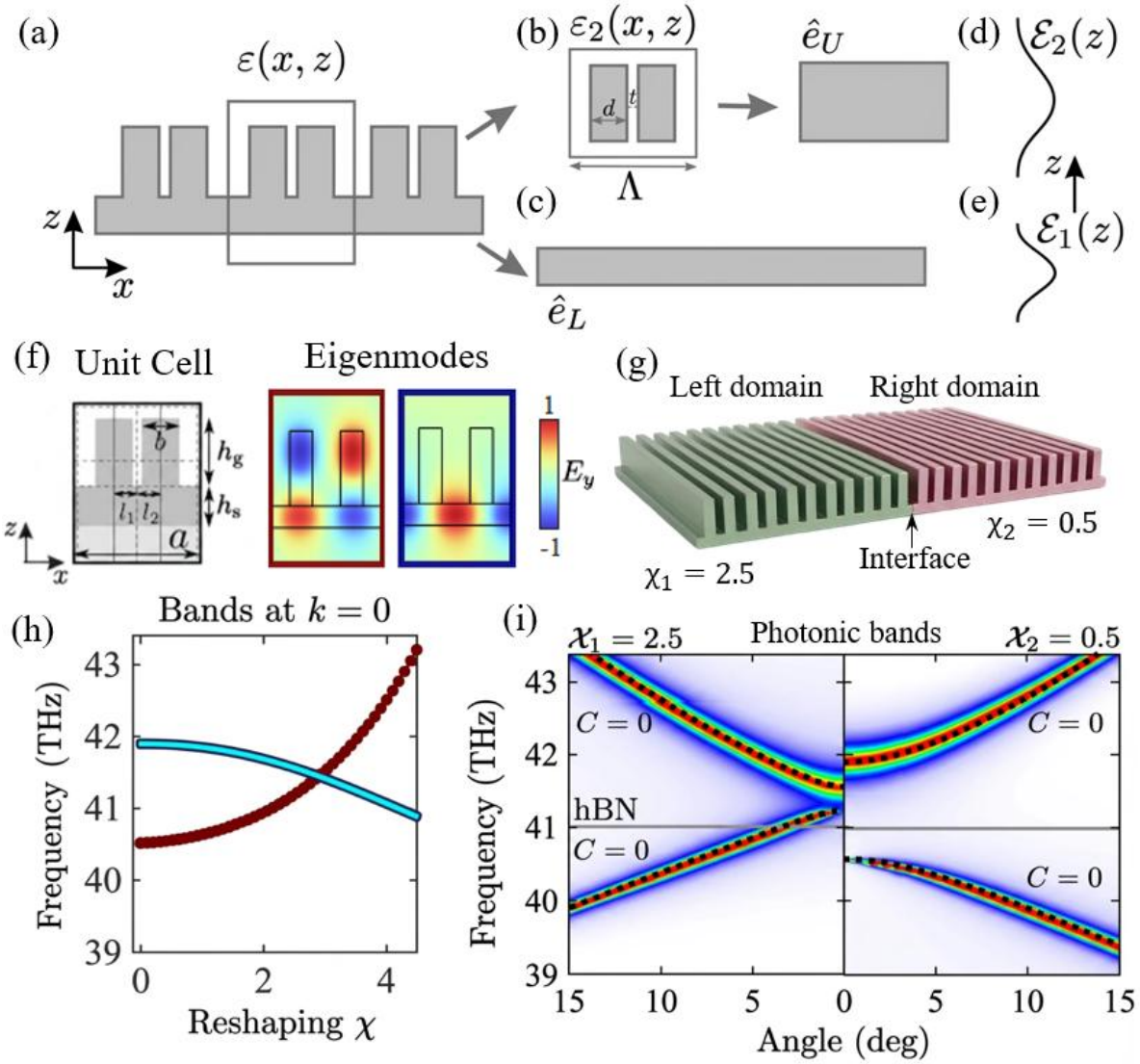


Figure 5.1 | Si grating-based photonic system. a, Schematic illustration of the photonic auxiliary lattices used for theoretical analysis. **b,** Upper grating and its corresponding homogeneous slab. **c,** Lower plain homogeneous dielectric slab. **d, e,** Transverse profiles of the bound even fundamental modes in the homogeneous slabs for the lower and upper structures, respectively. **f,** Left panel : Schematic of the unit cell of the Si photonic grating. The parameters

of the unit cell : a is the period, h_s represents the bottom slab thickness, h_g and b are the grating bar height and grating bar width respectively, $l_{1,2}$ are the bar off-centre shifts. **g,** 3D schematic of the photonic grating showing the two domains connected at the interface. **h,** Photonic bulk band dependence on reshaping factor χ at k = 0. Red curve indicates the high-Q mode, blue curve represents the low-Q mode. **i,** Numerically simulated electromagnetic energy spectrum.

Importantly, this process gives rise to two dominant photonic modes with distinct spatial and radiative characteristics. First being a high-Q mode (BIC-like), primarily localized within the grating bars and weakly radiative and secondly a low-Q mode, predominantly confined in the slab region and strongly radiative. This spatial separation directly determines their radiative properties. The slab-localized mode exhibits strong overlap with the radiation continuum and therefore experiences significant radiative losses, resulting in a short lifetime and low-quality factor. In contrast, the grating-localized mode is weakly coupled to free-space radiation and forms a BIC, leading to suppressed radiative losses and a high-Q resonance. This distinction is consistent with the mode profiles observed in the system as shown in Figure 5.1f.

Projecting the full Maxwell problem onto the reduced two-mode basis obtained from the GME method yields an effective Dirac-like Hamiltonian describing the photonic band structure near the Γ-point:

$$\widehat{H}_0 = \begin{pmatrix} \omega_0 + M + \beta_1 k^2 & v_D k \\ v_D k & \omega_0 + i\gamma_r - (M + \beta_2 k^2) \end{pmatrix} \tag{5.3}$$

Here ω_0 is the mid-gap frequency, M is the Dirac mass controlling band ordering, v_D is the coupling strength between counter-propagating modes, β_1, β_2 describe band curvature. The term $i\gamma_r$ accounts for radiative loss of the slab mode. The off-diagonal terms $v_D k$ arise from the periodic modulation, which couples modes of opposite momentum. This leads to hybridization and an avoided crossing between the bands.

Importantly, the parameters of this effective Hamiltonian are not fixed but are directly determined by the geometrical properties of the grating. The unit cell of the structure (Figure 5.1f left panel) is defined by parameters such as the slab thickness h_s, grating height h_g, period a, filling factor f, and lateral asymmetry δ. In particular, the period and filling factor are controlled through a reshaping parameter χ, where $a = 55\ \text{nm} \cdot (\chi - 1) + 2965\ \text{nm}$ and $f = 0.06 \cdot (\chi - 1) + 0.5$, while the bar positions are given by $l_{1,2} = -a/4 \pm \delta$. These geometrical parameters determine the modal confinement and coupling strength, and therefore directly influence the effective Hamiltonian. As a result, the Dirac mass becomes a function of the

structural deformation parameter $M = M(\chi)$, while the diagonal terms can be written in the form of a dispersive mass term $m(\chi) = M + \beta_{1,2}k^2$. This k^2 dependent contribution captures the curvature of the bands and plays an important role in determining the topological properties of the system. Here $\beta_{1,2}$ represents the effective band-curvature parameter (with $\beta_1, \beta_2 > 0$).

The Dirac mass M determines the ordering of the modes at the Γ-point ($k = 0$):

$$M > 0 \rightarrow \text{ trivial phase}$$

$$M < 0 \rightarrow \text{ band inversion}$$

Physically, the sign of M dictates the frequency ordering of the high-Q and low-Q modes at $k = 0$, such that a change in sign corresponds to an exchange of their modal character. The topological character of the bands can be captured by a winding number, which in this effective model depends on the sign of the Dirac mass term and the band-curvature coefficients. In particular, the invariant can be written as

$$C = \pm \frac{\text{sgn}(M) - \text{sgn}(\beta_{1,2})}{2} \tag{5.4}$$

Under this condition, $C = 0$ corresponds to the trivial phase when $M > 0$, while $C = \pm 1$ corresponds to a non-trivial phase when $M < 0$. This demonstrates that a sign change of the Dirac mass directly corresponds to a topological phase transition. In the uncoupled photonic system, the geometry is chosen such that $M > 0$, ensuring that the system remains topologically trivial.

5.1.2. Strong light-matter coupling with hBN and hybrid polaritons

To induce non-trivial topology, the photonic system is coupled to a material excitation. This is achieved using hBN, which supports phonon polaritons in the mid-infrared range. The dielectric response of hBN is described by

$$\varepsilon(\omega) = \varepsilon_\infty \frac{\omega^2 - \omega_L^2}{\omega^2 - \omega_T^2},$$

where ω_T and ω_L are the transverse and longitudinal phonon frequencies. Within the Reststrahlen band, the permittivity becomes negative, enabling strong confinement and subwavelength localization. Unlike the dispersive photonic modes of the grating, the phonon mode of hBN is nearly dispersion less over the relevant momentum range and can therefore be treated as a flat band, which plays a key role in the hybridization process. When the photonic

modes of the grating are tuned close to the phonon resonance, strong light-matter coupling occurs. This leads to hybrid polaritonic modes described by

$$\omega_{\pm}(k) = \frac{1}{2}\left[\omega_{\text{ph}}(k) + \omega_p \pm \sqrt{(\omega_{\text{ph}}(k) - \omega_p)^2 + 4q^2}\right] \tag{5.5}$$

where ω_{ph} and ω_{mat} represent the photonic and material dispersions, respectively, and q is the coupling strength. This results in the formation of an upper polariton branch and a lower polariton branch with an energy splitting proportional to the coupling strength. The hybrid modes inherit properties from both subsystems where photonic modes contribute dispersion and phonon modes provide confinement. This coupling modifies the underlying photonic band structure, which can be rigorously described using an effective Hamiltonian.

To rigorously describe the coupled system (Interaction with hBN), the photonic Hamiltonian is extended to include the phonon mode (three-mode coupled Hamiltonian),

$$\widehat{H}_3 = \begin{pmatrix} \widehat{H}_0 & \hat{Q} \\ \hat{Q}^{\dagger} & \omega_p + i\gamma_p \end{pmatrix} \tag{5.6}$$

where $\widehat{H}_0$ is the effective two-mode photonic Hamiltonian, ω_p is the phonon resonance frequency, and γ_p accounts for phononic losses. The coupling operator is given by

$$\hat{Q}^{\dagger} = (0 \quad q)$$

indicating that only one of the photonic modes couples efficiently to the phonon. This asymmetry arises due to spatial overlap, where the high-Q mode, localized within the grating bars, interacts more strongly with the hBN layer, while the slab-localized mode remains weakly coupled. The resulting system therefore consists of two dispersive photonic modes interacting with a nearly dispersion less phonon mode, forming three hybrid polaritonic branches (Figure 5.2). The hybridization leads to avoided crossings and significant reshaping of the band structure.

From a theoretical perspective, the effective photonic Hamiltonian can be mapped onto a lattice model analogous to the Rice-Mele chain, which describes a one-dimensional system with alternating onsite energies and hopping amplitudes. In this mapping, the two photonic modes correspond to orbitals of opposite parity (s- and p-like states), while their coupling arises from inter-orbital hybridization. The corresponding lattice Hamiltonian in momentum space can be written as

$$\hat{H}_{\mathrm{RM}} = \begin{pmatrix} \varepsilon_s - 2t_{ss}\cos(ka) + i\gamma_r & -2it_{sp}\sin(ka) \\ 2it_{sp}\sin(ka) & \varepsilon_p - 2t_{pp}\cos(ka) \end{pmatrix} \tag{5.7}$$

where the effective parameters are related to the continuum model through

$$\varepsilon_{s,p} = \omega_0 \pm M \mp \frac{2\beta}{a^2}, t_{ss,pp} = \pm\frac{\beta}{a^2} \; and \; t_{sp} = -\frac{iv_D}{2a}.$$

The curvature coefficients of the two bands are generally distinct. However, for simplicity, we assume that their difference is small, such that $| \beta_1 - \beta_2 | \ll \beta$, where $\beta = \frac{\beta_1+\beta_2}{2}$.

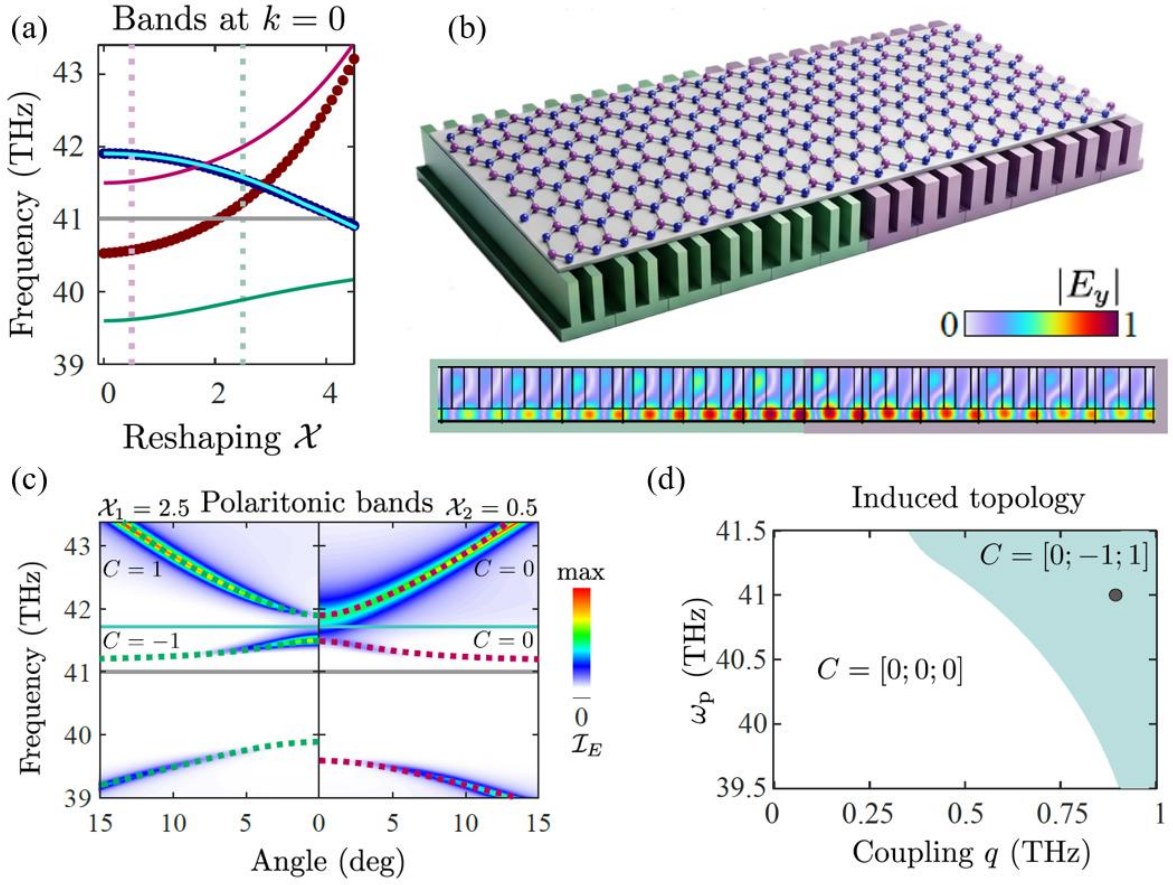


Figure 5.2 | Coupled topological polaritonic system. **a,** Bulk band evolution at $k = 0$ as a function of reshaping parameter χ. Thick curves represent the two photonic bands of the photonic grating. The three thin curves show the corresponding polaritonic bulk bands of the hBN-covered hybrid structure shown in b. Dashed vertical lines mark the selected values $\chi_1 = 2.5$ and $\chi_2 = 0.5$. **b,** Schematic of the hybrid structure with an hBN layer transferred onto the designed silicon grating. **c,** Numerically simulated electromagnetic energy spectra showing frequency bands labelled by the topological invariant C. The solid gray line denotes the hBN phonon resonance (corresponding to 7.3 μm in the mid-IR), while the cyan line highlights the edge-state frequency. **d,** Phase diagrams in the parameter space defined by the phonon

frequency ω_p and the coupling strength q. Each triplet of integers represents the winding numbers of the three polaritonic bands, ordered from lowest to highest frequency.

The effective Hamiltonian parameters were determined by fitting the two-band Dirac-like model in Eq. (5.3) to the photonic band structures obtained from full-wave finite-element simulations in COMSOL Multiphysics. The photon-phonon coupling coefficient (q) was subsequently estimated from the splitting of the hybrid polaritonic bands calculated for different hBN thicknesses. For the two selected domains, $\chi_1 = 2.5$ and $\chi_2 = 0.5$, the representative fitting parameters are summarized in Table 5.1 for an hBN thickness of 50 nm. The three hybrid polaritonic branches were obtained by diagonalizing the coupled Hamiltonian in Eq. (5.6), while the corresponding full-wave band structures were calculated using COMSOL Multiphysics. Their topological properties were determined by evaluating the quantized Zak phases and corresponding winding numbers from the Bloch eigenvectors across the Brillouin zone. These calculations provide the theoretical basis for the band evolution and the interaction-induced topological transition presented in Figure 5.2.

χ	β_1 (m^2Hz)	β_2 m^2Hz	ω_0 (THz)	V_D $10^6\ m.Hz$	M (THz)	γ_r (THz)	h_{hBN} (nm)	q (THz)	ω_p (THz)
$X_1 = 2.5$	20	10	41.394	7	0.1616	0.08	50	0.9	41
$X_2 = 0.5$	20	10	41.234	7	0.6608	0.06	50	0.76	41

Table 5.1 | Representative geometric and effective model parameters used in the numerical modelling. The total silicon thickness $h_g + h_s = 2.7\ \mu m$ is fixed, with $h_s = 0.6\ \mu m$ and $h_s = 2.1\ \mu m$.

As shown by the parameters in Table 5.1, both selected domains initially correspond to trivial photonic phases, with $M(X_1) > 0$ and $M(X_2) > 0$. Upon introducing the hBN layer, strong light-matter coupling modifies the hybrid polaritonic band structure. As the coupling strength increases, hybridization between the photonic and phononic modes drives a band inversion in one of the domains, leading to

$$M > 0 \rightarrow M < 0$$

as observed in the reversal of band ordering at the Γ-point. At an intermediate value of the deformation parameter, the bandgap closes and subsequently reopens, signalling a topological phase transition. As a result, the two interfaced domains become topologically distinct.

This transition can be detected through both near-field and far-field observables. In particular, the inversion of the bands is accompanied by a change in the polarization structure of the high-Q mode, which acquires a non-trivial polarization texture associated with a topological charge. The resulting bandgap hosts a hybrid edge state localized at the interface between the two domains.

The topological character of the system can be quantified by the winding number, which depends on the sign of the Dirac mass and the band curvature. For $M > 0$, the system remains in the trivial phase with $C = 0$, while for $M < 0$, it transitions to a non-trivial phase with $C = \pm 1$. This confirms that the sign change of the Dirac mass corresponds directly to a topological phase transition. The properties of the resulting edge states can be obtained by solving the effective Hamiltonian using an exponentially localized ansatz of the form $\sim e^{-\kappa|x|}$. This yields analytical expressions for the edge-state frequencies and decay rates:

$$\omega_{\pm} = \frac{\omega_0+\omega_p}{2} \pm \sqrt{\left(\frac{\omega_0-\omega_p}{2}\right)^2 + \frac{q^2}{2}} \tag{5.8}$$

$$\kappa_{\pm} = -\frac{M + \omega_0 - \omega_{\pm}}{v_D}.$$

A physically localized edge state corresponds to positive κ, indicating exponential decay away from the interface. The existence of such a solution is directly linked to the topological distinction between the two domains. When both decay constants are negative, the system remains topologically trivial, whereas the emergence of a positive decay constant corresponds to the appearance of a topological edge mode. In realistic structures, both photonic and phononic modes exhibit losses, characterized by γ_r and γ_p, respectively. However, in the regime where the hybridization strength exceeds the loss-induced broadening, the system can be well described by an effective Hermitian model. Under this condition, the topological bandgap remains open, and the edge states are robust against dissipation.

The resulting edge states are hybrid polaritonic modes, combining photonic dispersion with strong phononic confinement. These states are localized at the interface and form a synthetic potential well that traps both photons and phonons. Importantly, the topological phase in this system is not encoded in the geometry alone but emerges dynamically through light-matter interaction, providing a fundamentally new mechanism for realizing topological phases in photonic systems.

5.2. Experimental Design and Fabrication

For this work, Dr. Daria Smirnova performed the simulations in collaboration with her research group. Based on the theoretical framework and simulation results, an optimized grating design was established for the photonic system. A silicon-on-sapphire (Si/Al_2O_3) platform was selected as the substrate due to its high refractive index contrast where Si serves as the high-index photonic layer (permittivity ≈ 11.69) and sapphire as the low-index substrate (permittivity ≈ 2.05). This high refractive-index contrast enables efficient confinement of the guided modes within the designed Si grating.

This prevents leakage into the substrate and creates a well-defined photonic state, which is essential for the strong light-matter interaction expected to give rise to the polariton state. In addition to the refractive index contrast, the optical transparency of sapphire in the mid-IR range is crucial for the experimental realization, as the phonon reststrahlen band and resonance are around 7μm.

5.2.1. Proposed grating design and hybrid structure based on simulation results

The proposed hybrid structure and its design parameters are illustrated in Figure 5.3. The silicon grating consists of two domains with different geometrical parameters. As shown in the figure, the left-hand domain (green region) has a wider grating and a smaller unit-cell gap compared to the right-hand domain (pink region). As discussed in Section 5.1, both domains are designed to be topologically trivial in the uncoupled photonic system. However, upon coupling with the hBN layer, one of the domains transitions to a non-trivial phase due to strong light-matter interaction. Based on the simulation results and theoretical analysis for the selected hBN thickness, appropriate shaping factors were chosen for the two domains. For an hBN thickness of 50-100 nm, the left domain is designed with a shaping factor of 2.5, while the right domain uses a shaping factor of 0.5. The interface gap between the two domains is set to 925 nm, which defines the region where the topological edge mode is expected to be confined.

The total silicon thickness is 2.7 μm. To ensure proper confinement of the guided modes within the slab region beneath the grating, numerical simulations were used to determine an optimal slab thickness of 0.6 μm. Consequently, the grating height is defined as 2.1 μm. In addition, to accommodate formation of the topological edge mode and its associated decay length within the bandgap, the lateral dimensions of the grating were carefully selected. The grating width was chosen to be at least 180 μm ($M \geq 180\ \mu m$), ensuring sufficient spatial extent for mode localization. The grating length was designed to be larger than the width ($m \geq M$) to avoid

finite-size effects along the propagation direction. All these geometrical design parameters are illustrated in Figure 5.3.

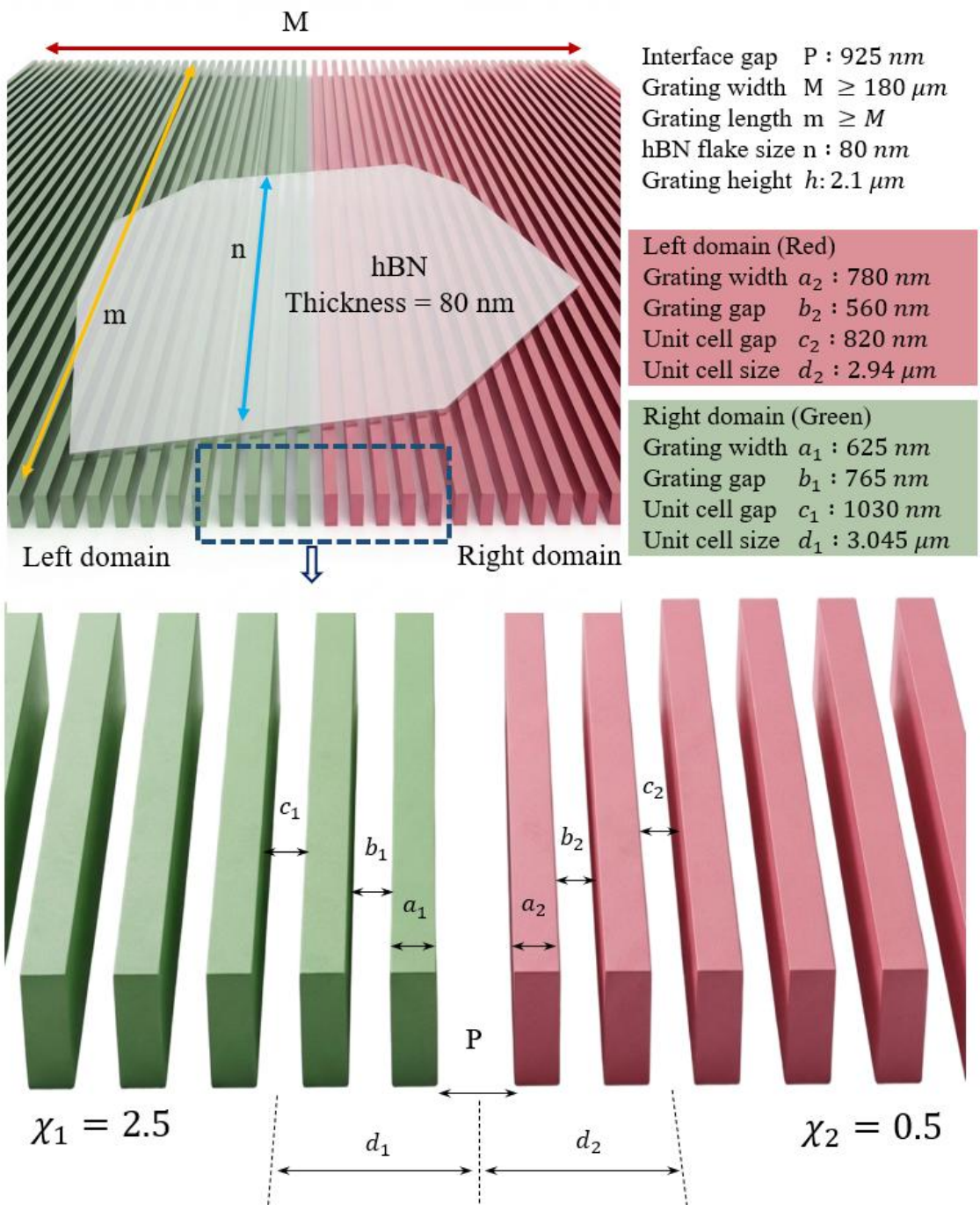


Figure 5.3 | Si grating design finalized parameters.

5.2.2. Device Fabrication

The first step of the fabrication is preparation of the silicon-on-sapphire substrate. The design of the Si grating was performed for a 2.7 μm deposited on a sapphire substrate. This is a challenging task since the adhesion of the Si layer onto the sapphire is not high enough. After

depositing Si onto the sapphire substrate, it tends to peel off within a few hours. To overcome this issue, a SiO_2 adhesion layer is introduced. First, the Sapphire substrate is subjected to an O_2 plasma clean at 150 W with an 8 sccm flow rate for 1 minute. This step treats the substrate surface and improves the adhesion of the SiO_2 layer to the sapphire substrate

After that, using PECVD, a 45 nm SiO_2 layer is deposited onto the substrate using the recipe discussed in chapter 2. After the SiO_2 layer deposition, the sample was kept inside the chamber without being exposed to the atmosphere and the temperature was reduced from the SiO_2 deposition temperature of $300^{\circ}C$ to $150^{\circ}C$. Then, again through PECVD, with the corresponding recipe a 2.7 μm Si layer was deposited on the Sapphire/SiO_2 substrate. The substrate is then spin coated with ARP 6200.13 resist with a spin speed of 1500 rpm for 1 minute. The ARP resist thickness is measured to be around 400 nm. The thicker resist is required for a proper lift-off since a thicker Al mask is needed for the ICP-F etching in subsequent steps due to ICP-F RIE etching selectivity of Si and Al etch rates. After the ARP resist deposition, the sample is coated with a 10 nm Au layer using thermal evaporation. This is just a conductive layer to assist the EBL process.

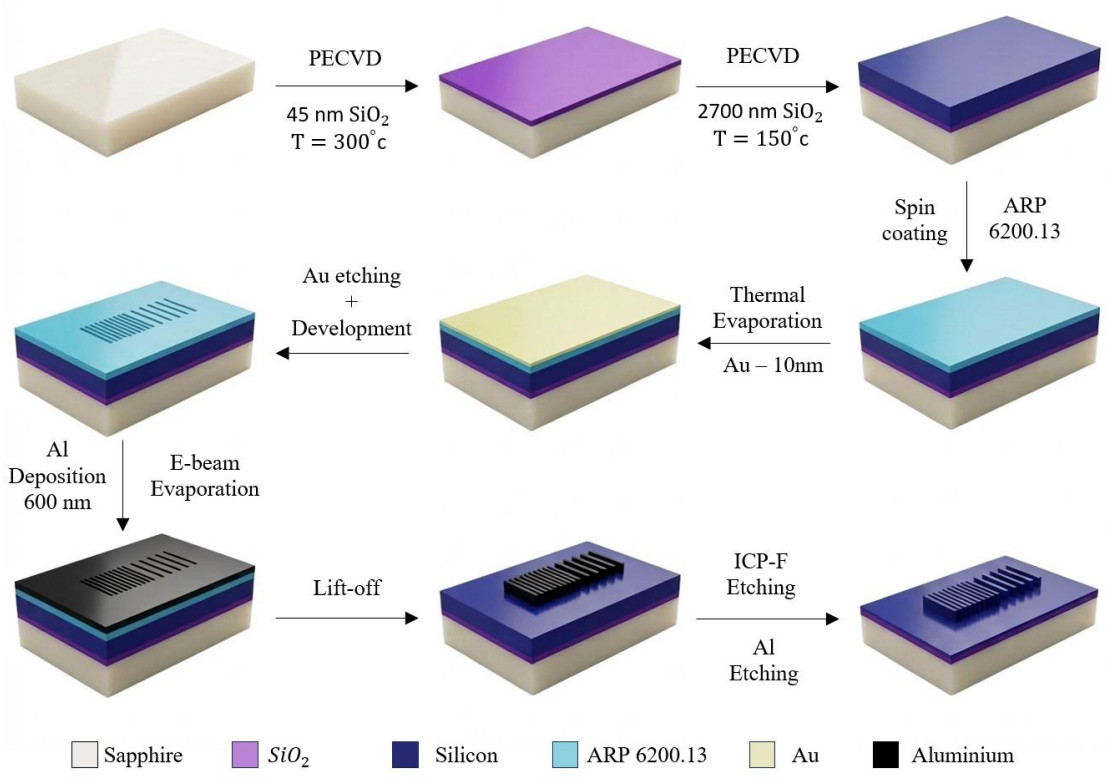


Figure 5.4 | Fabrication process of the silicon photonic grating.

The sample is then subjected to EBL patterning using Elionix EBL tool. After the EBL exposure, the sample is first dipped in an Au etchant to remove the 10nm Au conductive layer

followed by a DI water rinse and N_2 gas blow dry. Then the sample is developed using n-Amyl Acetate (AR 600 546) by dipping the sample in the developer for 1 minute followed by an IPA rinse and N_2 blow dry. After patterning the resist, a 600 nm Al layer is deposited using an e-beam evaporator. Then the sample is dipped in the ARP remover solution (Di-Methyl Acetate) overnight till the Al layer is lifted off to obtain the patterned Al mask for ICP-F etching. Then the sample is etched using ICP-F plasma RIE etching using gases SF_6 : CHF_3 : Ar with a ratio of flow rates 3.5 : 50 : 1 sccm for 16 minutes and 48 seconds (etching rate:24.9 nm/min). with an ICP forward power of 401 W and a RF forward power of 20 W with a DC bias of 214 V. The chamber was pressurized at 15 Torr.

One of the key fabrication challenges affecting the feature quality of the final grating structure arises from the limited etching selectivity between the metal mask and Si during the ICP-F etching process, which is approximately 5-6. Consequently, a relatively thick Al mask is required to achieve the desired etching depth without significant mask degradation. However, the use of a thick Al mask introduces additional challenges during EBL and the subsequent lift-off process. In particular, the resist thickness must be sufficiently large, typically at least comparable to the deposited Al thickness, to facilitate successful lift-off. The increased resist and metal thicknesses can compromise patterning fidelity, potentially leading to variations in feature dimensions, incomplete lift-off, residual material, and increased edge roughness of the Al mask. These imperfections may subsequently be transferred to the Si structure during ICP-F etching, resulting in increased sidewall roughness, deviations from the intended grating geometry, and reduced overall fabrication quality.

5.2.3. Final device

The fabricated Si grating is illustrated by the SEM images in Figure 5.5. As is evident, the grating is etched through consistently and the grating structures are well defined (Figure 5.5a). The 30-degree tilted image validates the etching depth of the grating to be around 2120 nm. When the total thickness of the underneath slab is considered, it was 530 nm. So, the total Si thickness deposited on the Sapphire substrate is 2650 nm. As measured in the two SEM images in panels c and d, the grating width, grating gap, unit cell gap and unit cell size (period) for both left and right-side domains are close to the designed values as shown in Figure 5.3.

After fabrication of the Si photonic grating with the designed geometrical features, an hBN flake of suitable size (as required by the design in Section 5.2.1) was transferred onto the grating. The hBN flake was first obtained via mechanical exfoliation (Figure 5.6a), and its

thickness was characterized using PSI measurements. The transfer process was carried out using a stacking stage.

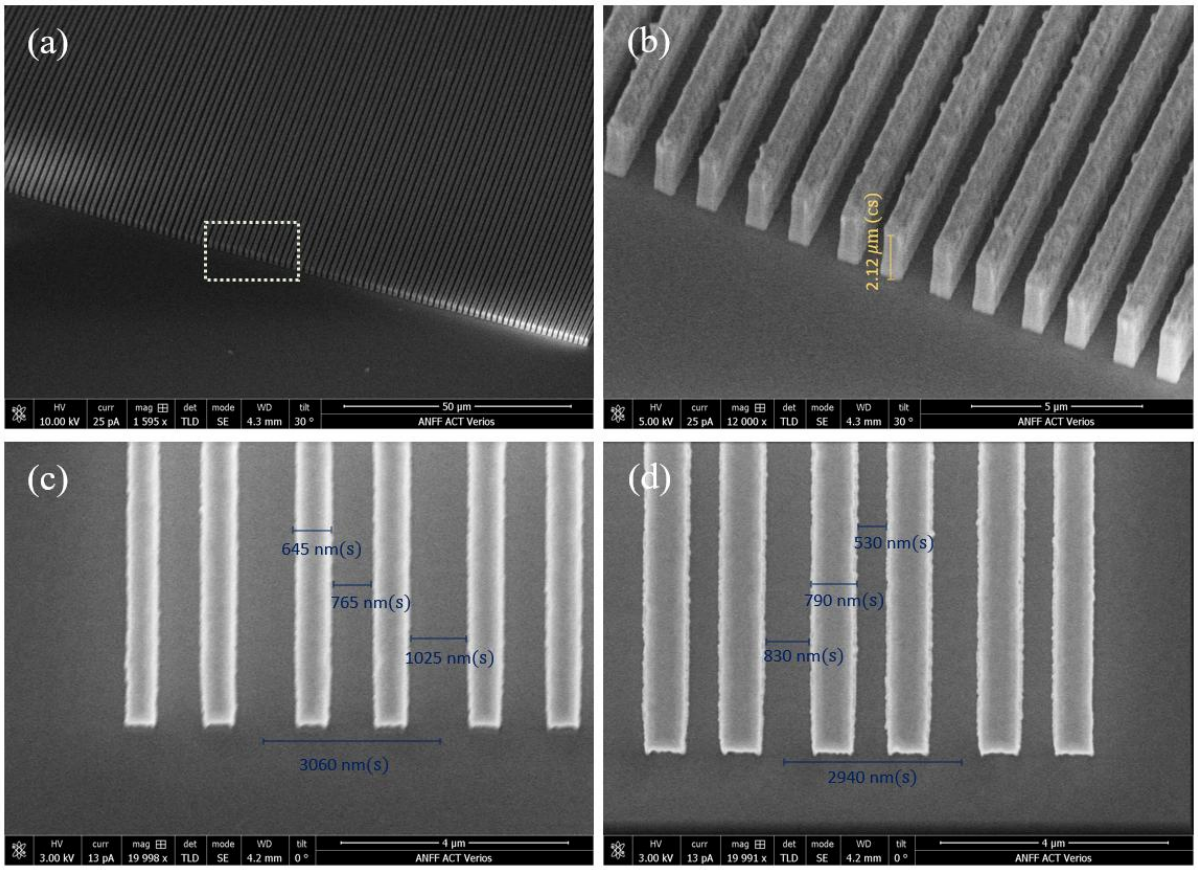


Figure 5.5 | SEM images of the fabricated silicon grating. a, Tilted-view SEM image showing a large-area overview of the grating structure. **b,** Higher-magnification tilted SEM image of the region indicated by the dashed outline in a, with the measured grating bar height. **c, d,** Top-view SEM images displaying the geometrical parameters of the left and right domains of the grating.

This step required careful handling due to the large aspect ratio of the grating, with bar heights of approximately 2120 nm, compared to the relatively thin (~80 nm) hBN flake. To ensure proper transfer, the flake was first precisely aligned with the grating using the transfer-stage microscope and then brought into contact with the structure using an xyz-controlled stage (Figure 5.6b). Gentle contact was initially established, followed by the application of slight pressure to ensure conformal contact between the flake, grating, and underlying substrate.

Then, the sample (substrate/grating with the PDMS-supported flake) was maintained on the stage at 110 °C for approximately 4 hours to promote adhesion. The sample and the PDMS layer as a unit were then removed from the stage and kept under an aluminium block to apply

additional pressure for over 24 hours to assist the transfer process. Without this extra pressure, the flake does not transfer completely since the grating aspect ratio is too high. Finally, the PDMS (gel film) was carefully peeled off, resulting in the successfully transferred hBN flake, as shown in Figure 5.6c-f.

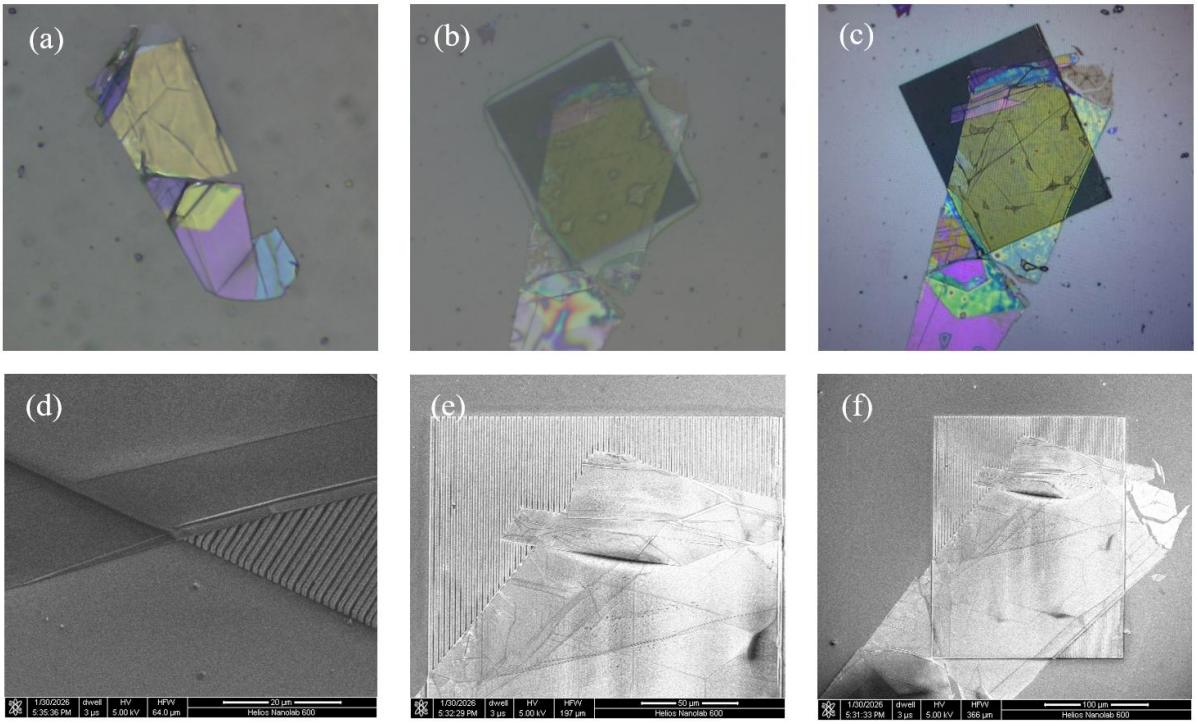


Figure 5.6 | Flake transferring onto the Si grating a, Optical microscope image of the exfoliated hBN flake on a PDMS layer. **b,** Optical microscope image of the hBN layer transferred onto the Si grating during the transfer process on the transfer stage. **c,** Optical microscopic image of the fully transferred hBN layer onto the Si grating. **d-f,** SEM images of the final device.

5.3. Near-field characterization and experimental realization of induced topological polariton mode

The primary objective of this work is to experimentally demonstrate the induced topological polariton in the coupled system. To justify this, the Si grating platform is first investigated in the uncoupled regime, where both grating domains are shown to be topologically trivial. Upon coupling to the hBN layer, the experimental measurements confirm that one domain becomes non-trivial and that an edge mode arises due to the two topologically distinct domains being coupled. The main signature of confinement of the electric field at the interface (topological edge state) was expected to be observed in the near-field images, and the sample was analysed using the s-SNOM setup. As discussed in Chapter 2, the same s-SNOM setup and mid-IR laser

were used over the wavelength range of 6700-7300 nm. This section first examines the coupled system, where hBN on the grating leads to interaction-induced topology and the emergence of an edge state, as observed by s-SNOM measurements. The uncoupled photonic system is then analysed, confirming that the grating domains are topologically trivial without coupling.

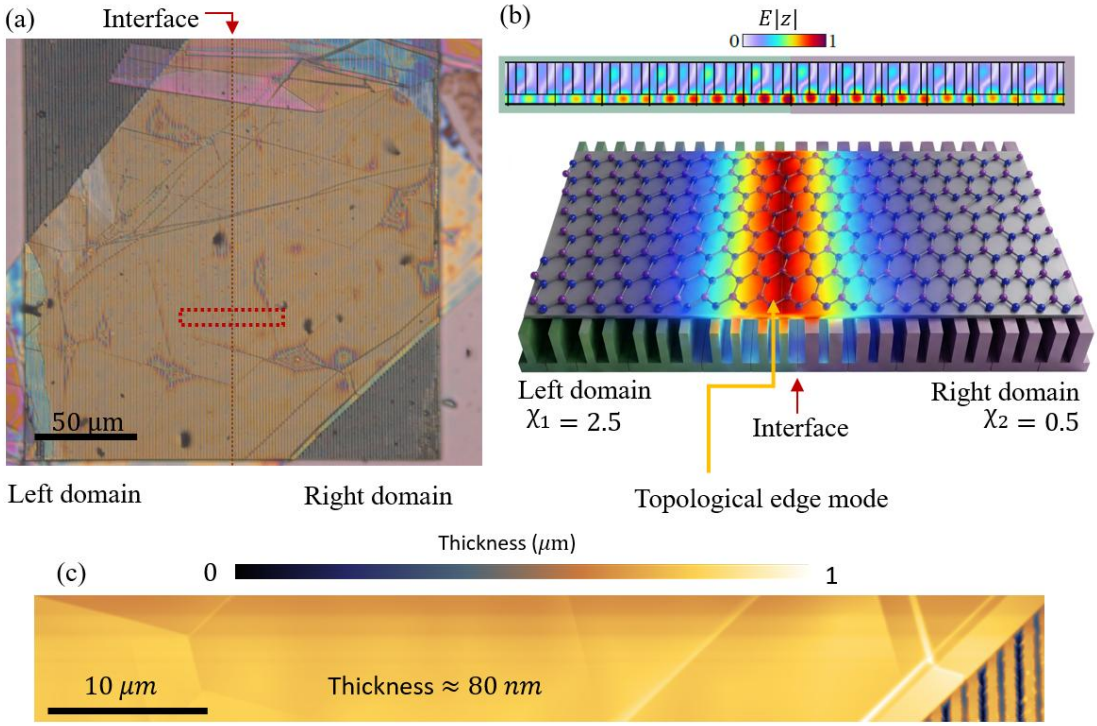


Figure 5.7 | Topological edge mode in the coupled hybrid system. a, Optical image of the fabricated sample with the hBN flake transferred onto the Si grating. **b,** Schematic showing the expected edge mode in the coupled system, arising from a topological transition in the left domain. **c,** AFM image of the transferred hBN flake used to verify its thickness.

5.3.1. Characterization of the coupled hybrid system to investigate the induced topological polariton edge mode

The grating with the transferred hBN flake was characterized using the s-SNOM setup. As shown in Figure 5.7a, a small central region (red dotted area) was selected for frequency-dependent near-field measurements. The coupled system is expected to support an edge mode (Figure 5.7b) if strong coupling induces a band inversion in the left domain, making it topologically non-trivial. The thickness of the transferred hBN flake was first verified using AFM (panel c) to ensure it meets the design requirements. Near-field measurements were then performed over an excitation wavelength range of 6600–7300 nm.

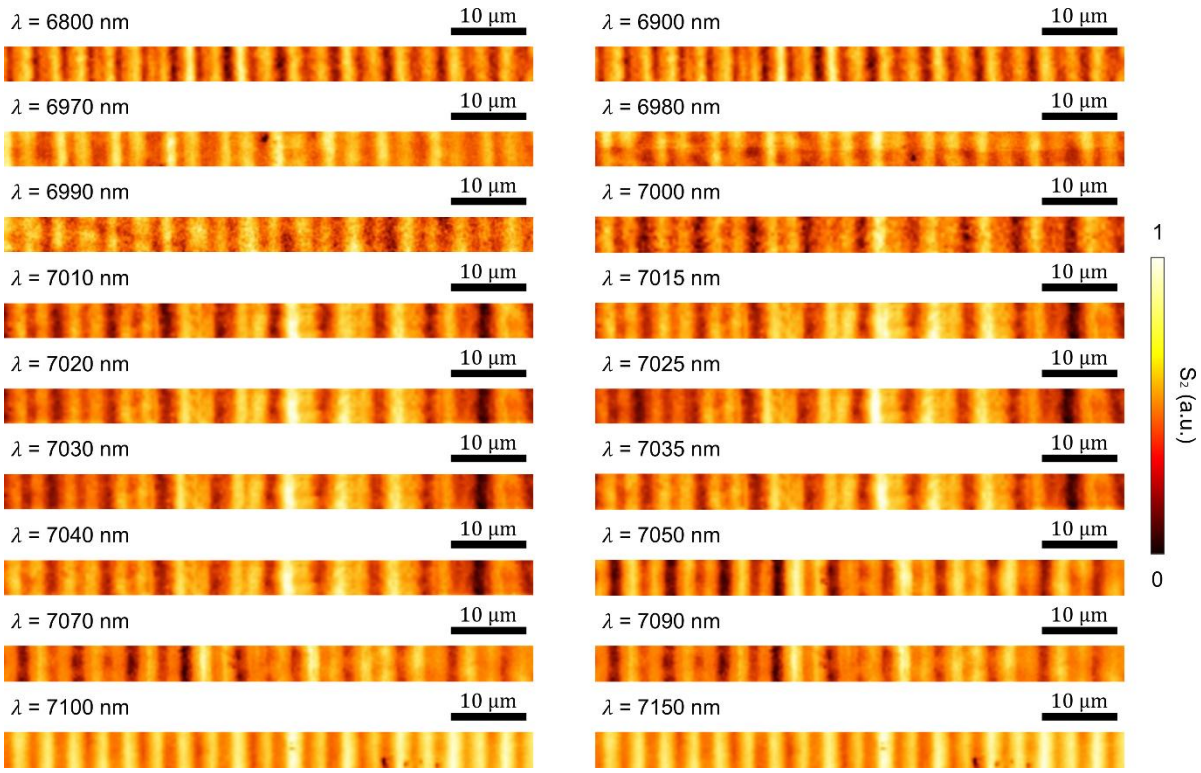


Figure 5.8 | Near-field measurements of a 70 × 5 µm regions across the interface, used to identify the topological band gap. s-SNOM near-field amplitude maps, S_2, measured over a broad excitation wavelength range covering the upper bulk band, the experimentally observed topological band gap, and the lower bulk band.

Based on the simulation results discussed in Section 5.1.2, the band gap of the coupled system is predicted to lie between 7182–7207 nm (41.4 - 41.745 THz), with a band gap width of 25 nm. However, the experimental results (Figure 5.8) show that the edge mode appears at shorter wavelengths, specifically between 7010-7040 nm, where a strong electric field is localized at the interface. As observed through the results in Figure 5.8 for wavelengths below approximately 7010 nm, the near-field response is dominated by the extended grating-modulated bulk modes, and no strong localization is observed at the interface. Within the wavelength range of approximately 7010-7040 nm, a pronounced near-field enhancement appears at the interface, with the strongest response near the center of the band gap. For wavelengths above approximately 7040 nm, the localized interface enhancement disappears, and the response returns to an extended bulk-like distribution.

Although the topological band gap is spectrally shifted, its measured width is ~30 nm, which is close to the simulated value. This shift can be attributed to differences between the simulated and experimental conditions. The simulations assume a silicon-on-sapphire structure under normal incidence, whereas the fabricated sample includes an additional SiO_2 layer between the

silicon and sapphire which was needed to increase the adhesion between the two layers. In addition, slight variations in grating parameters and fabrication imperfections are likely to further influence the position of the band gap.

The initial measurements, showing a high electric field at the interface, are not sufficient on their own to confirm the existence of an edge mode, nor to claim an induced topological polariton edge state. After identifying the band gap, a higher-resolution measurement over a larger area was performed. Figure 5.9a shows the optical microscope image of the hybrid sample after hBN transfer, where two regions were selected for frequency dependent s-SNOM measurements. The blue rectangle marks a scan region centered on the domain boundary, used to directly probe the emergence of an interface-localized response.

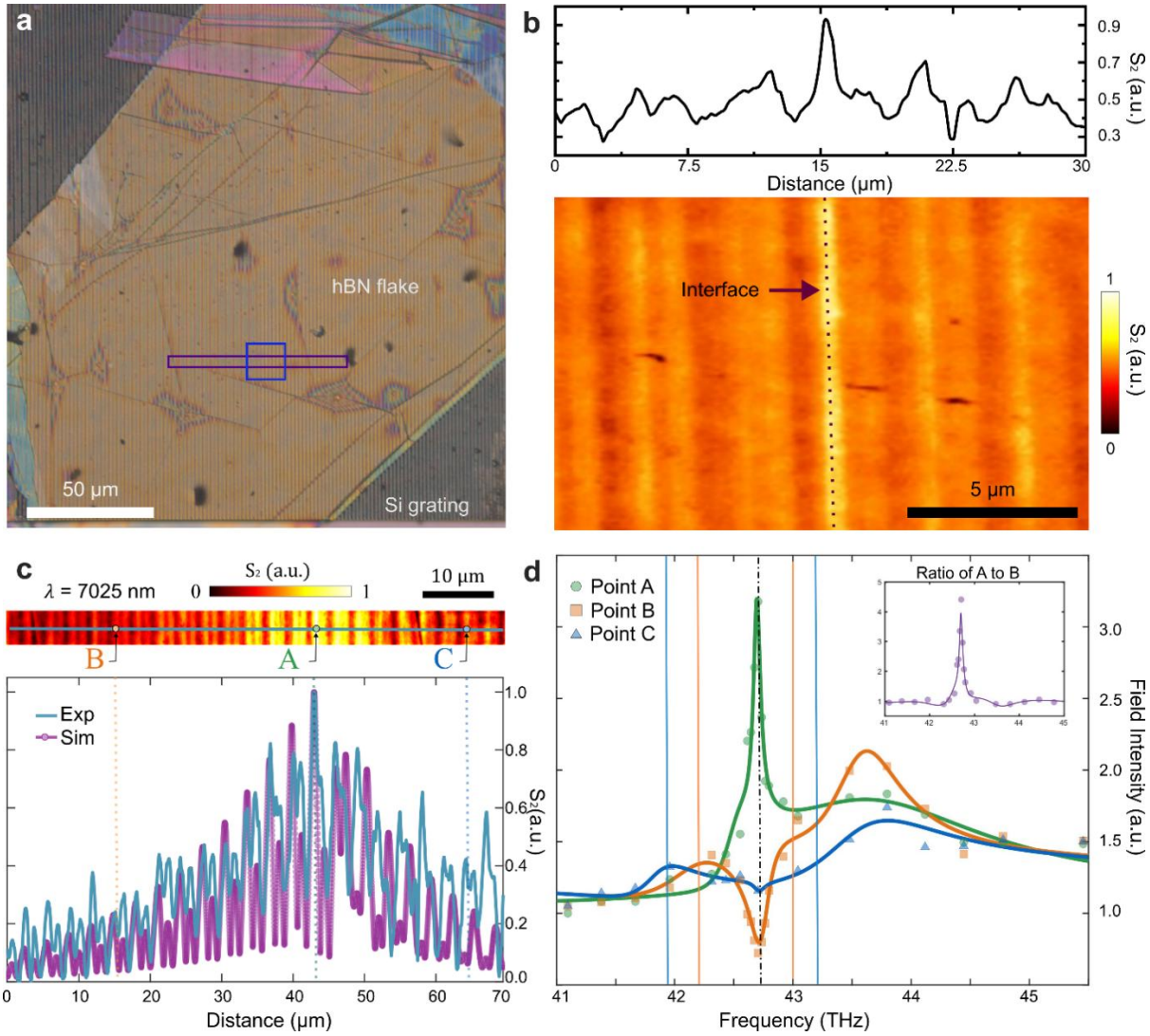


Figure 5.9 | Edge mode identification using s-SNOM measurements at the centre of the band gap. a, Optical microscope image of the hBN-integrated two-domain silicon grating. The blue rectangle marks the region used to acquire the s-SNOM image across the interface shown

in panel b, while the purple rectangle marks the 70 μm × 5 μm region used for the horizontal near-field scan shown in panel c. **b**, Experimental s-SNOM near-field image measured near the interface at $\lambda = 7025$ nm, corresponding to the centre wavelength of the experimentally observed topological band gap. The lower panel shows the measured near-field amplitude map, and the upper panel shows the corresponding horizontal line-cut profile. The vertical dotted line marks the interface, where a pronounced near-field maximum is observed. **c**, Horizontal 70 μm × 5 μm s-SNOM near-field measurement across the interface at $\lambda = 7025$ nm. The light-blue horizontal line in the upper panel indicates the line cut used to extract the experimental near-field profile shown in the lower panel as a solid light-blue curve. The simulated field-intensity profile of the coupled system is plotted in purple for comparison. The labelled positions B, A and C correspond to the left grating domain, interface and right grating domain, respectively, and are used to extract the frequency-dependent near-field intensities shown in panel d. **d**, Frequency-dependent near-field intensity extracted from points A, B and C, representing the interface, left-domain and right-domain responses, respectively. The inset shows the intensity ratio between the interface (point A) and the left grating domain (point B). The vertical black solid/dotted line marks the theoretically predicted edge-state resonance frequency. The vertical orange lines indicate the simulated bulk band-gap edges of the left domain at 42.2 and 43.0 THz, while the vertical blue lines indicate the simulated bulk band-gap edges of the right domain at 41.9 and 43.2 THz.

The purple rectangle marks a longer horizontal region extending across the interface and into both domains, enabling the spatial decay of the mode away from the boundary to be evaluated. Figure 5.9b shows the near-field response measured at $\lambda = 7025$ nm, corresponding to the center of the experimentally observed topological band gap. The near-field map exhibits a pronounced intensity maximum at the domain boundary, which is also resolved in the corresponding line-cut profile. This behavior is absent in the bare silicon control structure (discussed in section 5.3.2), indicating that the interface response emerges only after coupling the photonic grating to the hBN phonon resonance. The spatial localization of this mode is further confirmed by the long horizontal scan in Fig. 4c. The 70 μm × 5 μm s-SNOM map shows that the near-field intensity is strongest at the interface and decreases into both adjacent domains, consistent with the expected real-space profile of an edge-bound polaritonic mode in Fig. 5.2b. The light-blue line drawn through the center of the near-field map indicates the line-cut region used to extract the experimental spatial profile. The resulting average line-cut profile is shown as the light-blue curve in the lower panel of Fig. 5.9c, together with the simulated

field profile of the coupled system depicted as the purple dotted curve. Although the absolute resonance frequency is shifted relative to the idealized simulation, the experimental and simulated profiles show the same fringe periodicity and an interface-centered envelope, supporting the assignment of the measured response to the designed hybrid edge mode rather than to random local scattering.

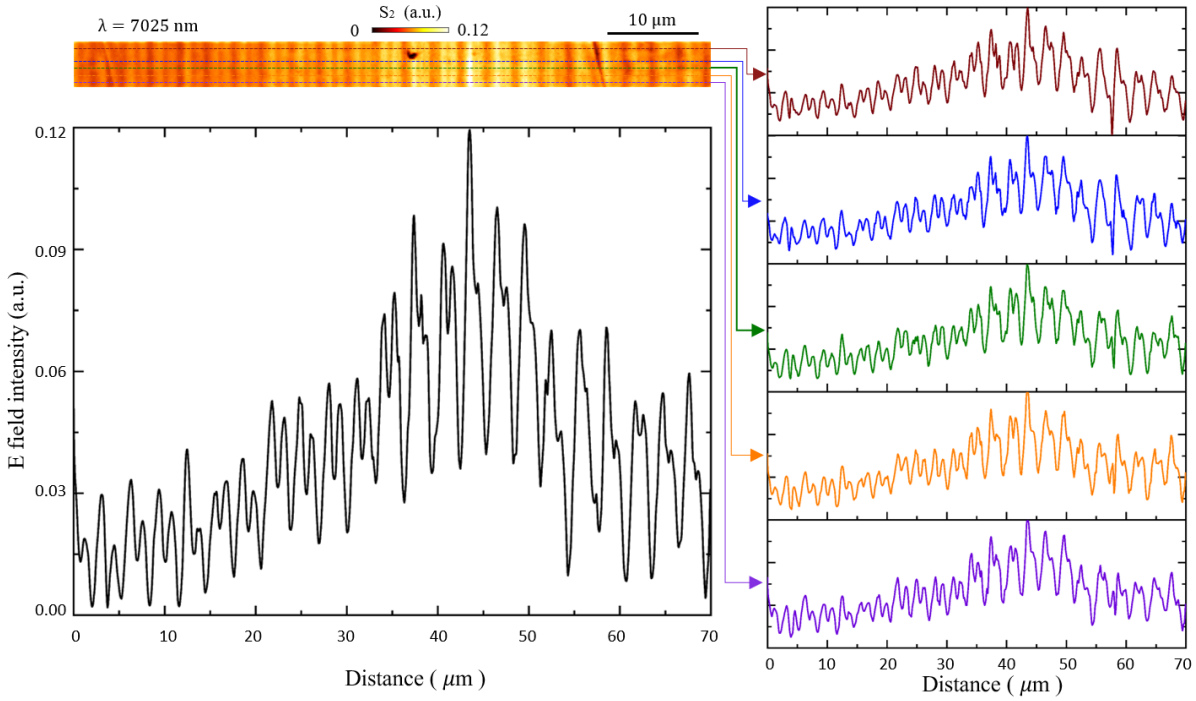


Figure 5.10 | Averaging method used to extract line profiles from experimental near-field images.

To ensure that this behaviour is not due to a random local feature, the horizontal line cut profiles shown are averaged profiles obtained by taking five-line cuts at different positions across the image, as illustrated in Figure 5.10. These lines cut profiles were analysed within the identified band gap to further confirm the confinement of the E-field at the interface, as shown in Figure 5.11. Within the band gap, a clear edge mode is observed, and its strength decreases as the excitation wavelength moves away from the centre of the band gap. At an excitation wavelength of 7025 nm, the line cut profile shows the highest intensity and the fastest decay. As the wavelength approaches 7010 nm and 7040 nm, the interface still exhibits higher intensity, but the decay of the E-field into the left and right domains becomes less pronounced.

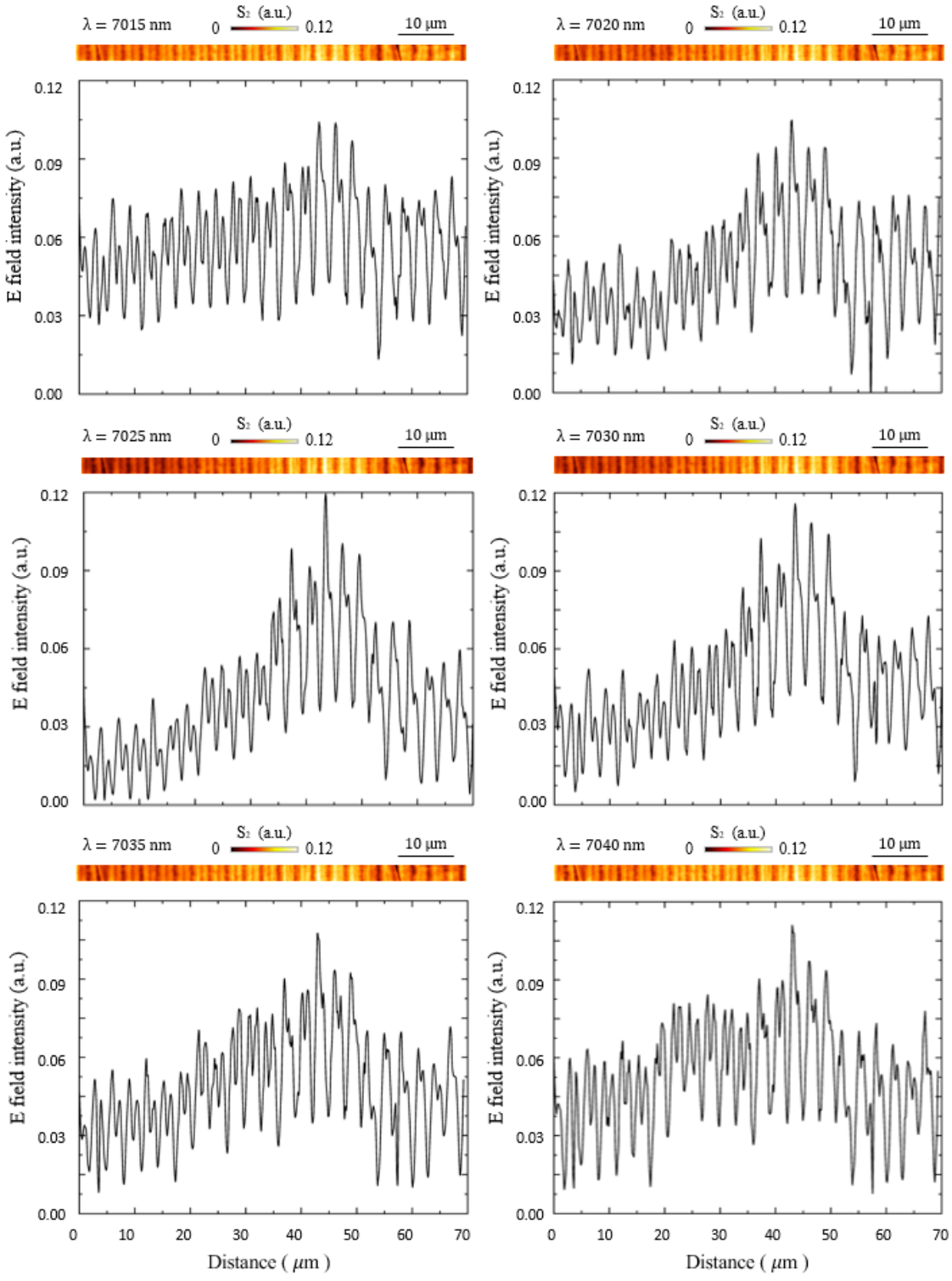


Figure 5.11 | Experimental near-field measurements within the topological band gap, with corresponding line-cut profile analysis.

While the line-cut analysis supports the presence of the interface-localized polaritonic mode, further frequency-dependent analysis was performed to quantify the relative near-field enhancement at the interface compared with the surrounding domains. For this purpose, a

normalised near-field enhancement factor $\eta(x,\lambda)$, was evaluated at three representative positions within the system, as shown in Figure 5.9d. This dimensionless quantity is defined as the ratio of the local near-field intensity to the spatially averaged intensity of the corresponding line-cut profile at each excitation wavelength,

$$\eta(x,\lambda) = \frac{I\,(x,\lambda)}{\langle I\,(x,\lambda)\rangle_x}$$

Here, $I\,(x,\lambda)$ represents the local near-field intensity at position (x) and wavelength λ, while $\langle I\,(x,\lambda)\rangle_x$ denotes the spatially averaged intensity of the corresponding line-cut profile. Since the measured second-harmonic demodulated s-SNOM amplitude S_2 is proportional to the local near-field magnitude, the intensity is evaluated as $I \propto S_2^2$. This normalisation enables comparison of the relative local field response at different excitation wavelengths while reducing variations in the overall measured signal level. Importantly, the normalised near-field enhancement factor provides an experimental measure of the relative local optical response.

To evaluate the near-field enhancement of the coupled system, a representative position at the interface, labelled A in Figure 5.9c, was selected. At each excitation wavelength, the near-field intensity at this position was normalised to the spatially averaged intensity of the corresponding line-cut profile. The resulting normalised enhancement factor, represented by the green curve in Figure 5.9d, exhibits a pronounced increase within the experimentally identified topological band gap, reaching its maximum near the centre of the band-gap region. This indicates a strong relative enhancement of the local near-field response at the interface, consistent with the presence of an interface-localized polaritonic mode.

For comparison, two additional positions were selected within the left and right domains(Point B and C), located approximately 10- and 7-unit cells away from the interface, respectively. The corresponding normalised near-field enhancement factors show weaker local responses within the relevant band-gap region, indicating that the measured enhancement is concentrated near the interface rather than uniformly distributed across the grating. This spatial and spectral contrast is consistent with the confinement of the hybrid polaritonic edge state predicted by the theoretical model.

To further quantify the relative interface enhancement, the ratio between the near-field intensities at points A and B is plotted in Figure 5.9d inset. Within the topological band gap, the intensity at the interface is significantly higher than that measured in the left domain, whereas outside the band-gap region the intensities become comparable. Together with the

spatial confinement observed in the near-field maps and the absence of interface localization in the uncoupled photonic control, these results provide experimental evidence supporting the existence of the interaction-induced topological polaritonic edge state.

The interaction-induced origin of the edge mode further implies that its strength can be controlled by the hBN thickness, which tunes the effective light-matter coupling. In the thin-layer regime, the photonic field varies weakly across the hBN thickness, leading to a linear scaling of the induced polarization and an effective coupling that follows $q \propto \sqrt{h_{\mathrm{hBN}}}$. This perturbative description holds as long as the phase accumulation across the layer remains small, $k_z h_{\mathrm{hBN}} \ll 1$. Thus, the coupling strength can be tuned via thickness, while the edge-state response remains well defined from its onset at ~ 15 nm up to ~ 110 nm. The thin-layer approximation breaks down when $k_z h_{\mathrm{hBN}} \sim 1$, marking the crossover to a finite-thickness waveguide regime. In the hyperbolic regime of hBN ($\varepsilon_{\parallel} < 0$, $\varepsilon_{\perp} > 0$), the dispersion gives $k_z \approx \sqrt{|\varepsilon_{\parallel}|/\varepsilon_{\perp}}\, k_{\parallel} \approx (1.0 - 1.2)\, k_{\parallel}$ around $1400\ \mathrm{cm}^{-1}$. For the present structure, with spatial frequencies set by a ~ 600 nm grating bar width and a ~ 3 μm period, the estimated $k_{\parallel} \sim 2 - 10\ \mu\mathrm{m}^{-1}$ suggests a crossover scale $h_{\mathrm{hBN}} \sim 100 - 500$ nm. This indicates a transition from a sheet-like anisotropic susceptibility regime to a finite-thickness hyperbolic waveguide regime.

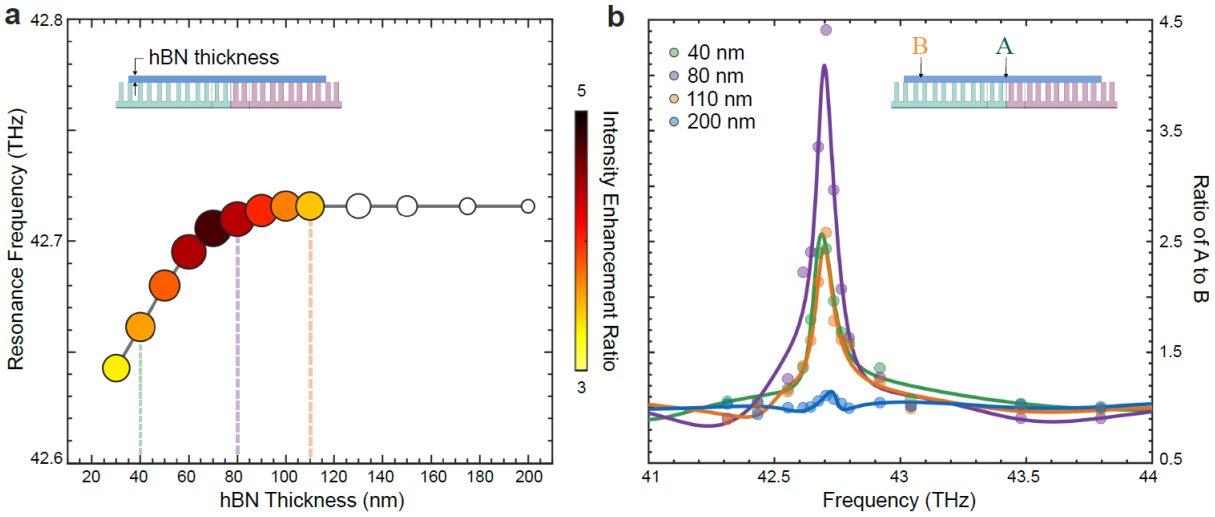


Figure 5.12 | Tunability of the interaction-induced topological phonon- polariton edge state through coupling strength. **a**, Calculated hBN-thickness dependence of the edge-state resonance frequency. The marker color and size indicate the estimated interface-to-bulk intensity enhancement ratio (evaluated approximately eight-unit cells away from the interface in the nontrivial hybrid domain), showing that the edge-mode response strengthens with increasing light-matter coupling before saturating and eventually weakening in the thick-hBN regime. The inset schematically shows the two-domain grating, with the left and right domains

indicated in light green and light pink, respectively. The blue layer represents the hBN flake, whose thickness controls the light-matter coupling strength between the silicon grating modes and the hBN phonon resonance. **b**, Frequency-dependent near-field intensity ratio between the interface (point A) and the left grating domain (point B) measured for hBN flakes with different thicknesses. The ratio I_A/I_B quantifies the relative enhancement of the near-field signal at the interface and therefore provides an experimental measure of edge-mode confinement. The inset indicates the positions of points A and B used to extract the near-field intensities for the ratio calculation.

In simulations, the edge-state dispersion curve can be reliably traced under plane-wave excitation up to a thickness of approximately 110 nm. Beyond this regime, the coupling to the edge state becomes inefficient. Consequently, the dispersion is continued by identifying the resonant enhancement under near-field excitation conditions. In Fig. 5.12a, the markers represent the estimated field enhancement $I(A)/I(B)$, obtained theoretically from the characteristic localization length of the edge state.

We experimentally verified this thickness dependence by transferring hBN flakes with different thicknesses onto nominally equivalent two-domain silicon gratings and measuring the near-field response using s-SNOM. For each thickness, the local near-field intensity was extracted at the interface, point A, and in the left grating domain, point B, as indicated in the inset of Fig.5.12b. The ratio $I(A)/I(B)$ was then used as an experimental measure of the relative interface enhancement. As shown in Fig. 5.12b, the edge-mode response is strongest for the 80 nm hBN flake, where a sharp enhancement appears near the edge-state frequency. For the thinner 40 nm flake, the interface enhancement is weaker, consistent with reduced light-matter coupling. For the thicker 110 nm flake, the enhancement is also reduced, indicating that the system has moved beyond the optimal coupling regime. When the hBN thickness is increased further to approximately 200 nm, the resonant interface enhancement disappears, consistent with inefficient excitation of the edge state in the finite-thickness hyperbolic regime.

5.3.2. Trivial Photonic system characterization

To confirm that the observed edge mode in the coupled system arises from strong light–matter interaction, the uncoupled photonic system (Si grating) was examined using the near-field setup. In order to confirm the trivial nature of the Si grating a frequency-dependent mid-infrared s-SNOM measurements were performed over the range of approximately 41-47 THz with a selected region as illustrated in Figure 5.13a,b. Measurements were performed at the

same excitation wavelengths used for the coupled system, enabling a direct comparison while three representative s-SNOM amplitude maps are selected for Figure 5.13c. These maps correspond to excitation frequencies in the lower bulk-band region, the spectral window where the hybrid topological band gap is expected after hBN integration, and the upper bulk-band region. In all three cases, the near-field signal follows the periodic modulation of the grating, but no interface-centered field enhancement or localized spatial envelope is observed. The stronger signal from one bar within each unit cell is attributed to the oblique illumination geometry of the s-SNOM measurement. (7 scans from the full spectral series of near-field scans are shown in Figure 5.14 panel c with the respective line cut profiles in panel d).

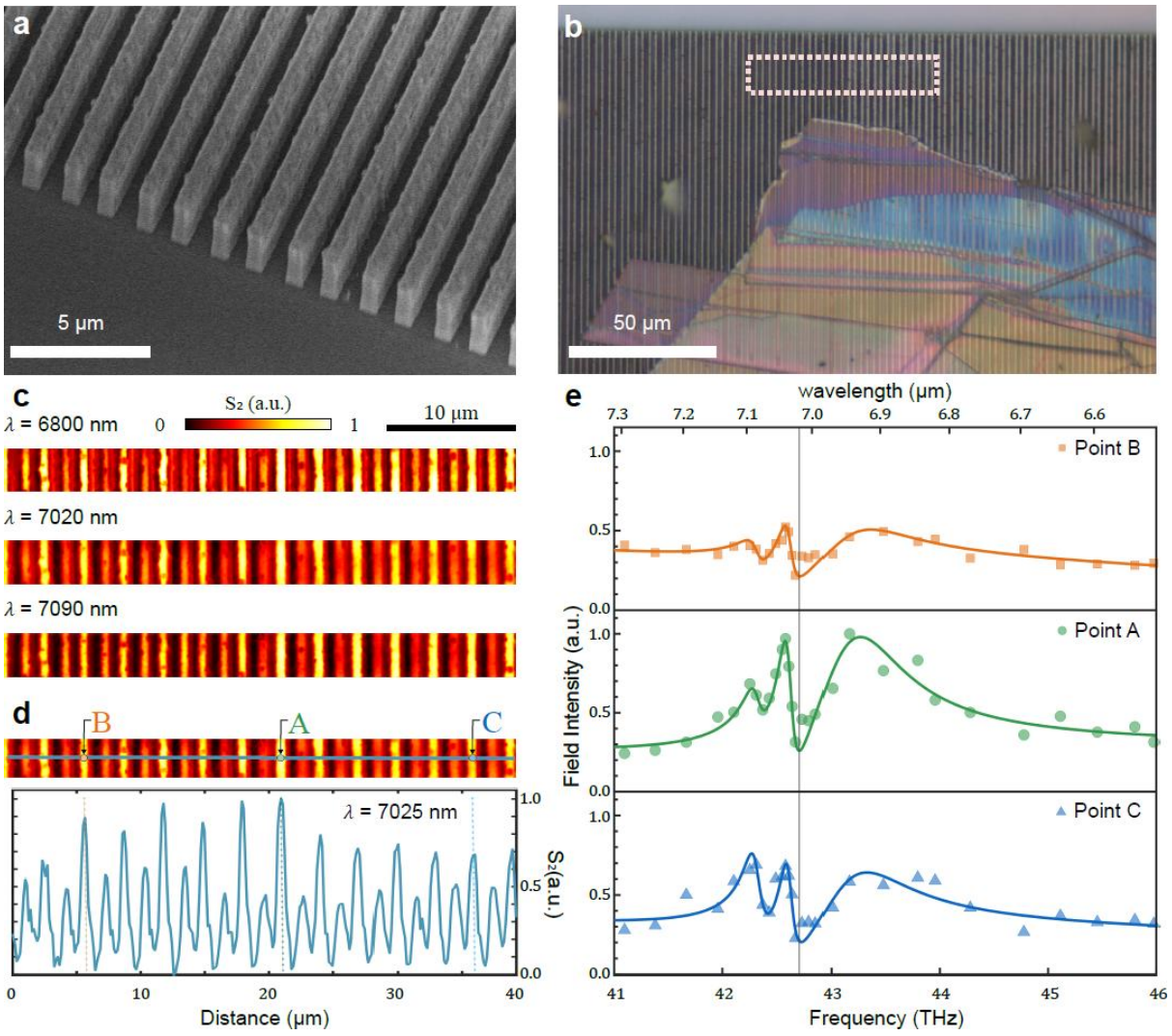


Figure 5.13 | Control near-field characterization of the uncoupled trivial photonic system. **a**, Tilted scanning electron microscope image of the fabricated two-domain silicon grating, showing the well-defined silicon bars and confirming the structural realization of the designed photonic domains. **b**, Optical microscope image of the fabricated bare silicon grating before

hBN integration. The white dashed rectangle marks the grating region selected for s-SNOM near-field imaging and used to generate the data shown in panels c-e. **c,** Experimental s-SNOM near-field amplitude maps recorded at three representative excitation wavelengths across the relevant mid-infrared spectral range. The top, middle and bottom panels correspond to the upper bulk-band region, the spectral region where the topological edge mode is expected only after hBN coupling, and the lower bulk-band region, respectively. No interface-localized enhancement is observed in the uncoupled photonic structure. **d**, Near-field map measured at $\lambda = 7025$ nm, corresponding to the centre wavelength of the experimentally relevant spectral window. The labelled points B, A and C correspond to the left-domain bulk, interface region and right-domain bulk positions, respectively. The light-blue horizontal line indicates the line cut used to extract the near-field intensity profile shown in the lower panel. The profile shows grating-period oscillations but no interface-centered envelope or monotonic decay away from the domain boundary. **e**, Frequency-dependent normalized near-field intensities extracted at points B, A and C, together with multi-channel Fano fits. The spectra are described by bulk resonant channels only, with no additional interface-localized pole.

To quantify this spatial response, we extracted a representative horizontal linecut profile from the near-field map, as shown below the s-SNOM images in Figure. 5.13d. The linecut captures the periodic grating response across both domains and was used to define three positions for spectral analysis: point A at the interface, point B in the left domain, and point C in the right domain. Using the frequency-dependent near-field data, we calculated the average local field magnitude at these positions across the measured spectral range.

The resulting spectra from the three selected positions are shown in Figure. 5.13e and were used to quantify the near-field scattering characteristics of the bare grating. We fit the demodulated s-SNOM intensity profiles ($I \propto |E|^2$, where the local near-field magnitude $|E|$ is directly proportional to the measured S_2 signal amplitude) to a multi-channel Fano interference framework. Experimental raw magnitude data were squared to represent optical intensity and normalized to the global maximum to preserve relative cross-domain amplitudes and baselines across the three spatial positions.

For a given spatial domain *d*, the total spectral intensity profile is modeled using the generalized multi-channel expression:

$$I_d(f) = I_{\mathrm{bg},d}(f) + \sum_j A_{j,d}\left[\frac{(q_{j,d}+\delta_{j,d})^2}{1+\delta_{j,d}^2} - 1\right], \tag{3}$$

where $d \in \{A, B, C\}$ serves as the spatial domain index corresponding to Point A (interface zone), Point B (left domain), and Point C (right domain), respectively. Here, $I_{\mathrm{bg},d}(f)$ represents the non-resonant continuum background, $A_{j,d}$ is the coupling amplitude, $q_{j,d}$ is the phenomenological Fano asymmetry parameter, and $\delta_{j,d} = (f - f_{0,j,d})/\gamma_{j,d}$ defines the normalized spectral detuning relative to the resonance frequency $f_{0,j,d}$ and damping half-width $\gamma_{j,d}$ of channel j.

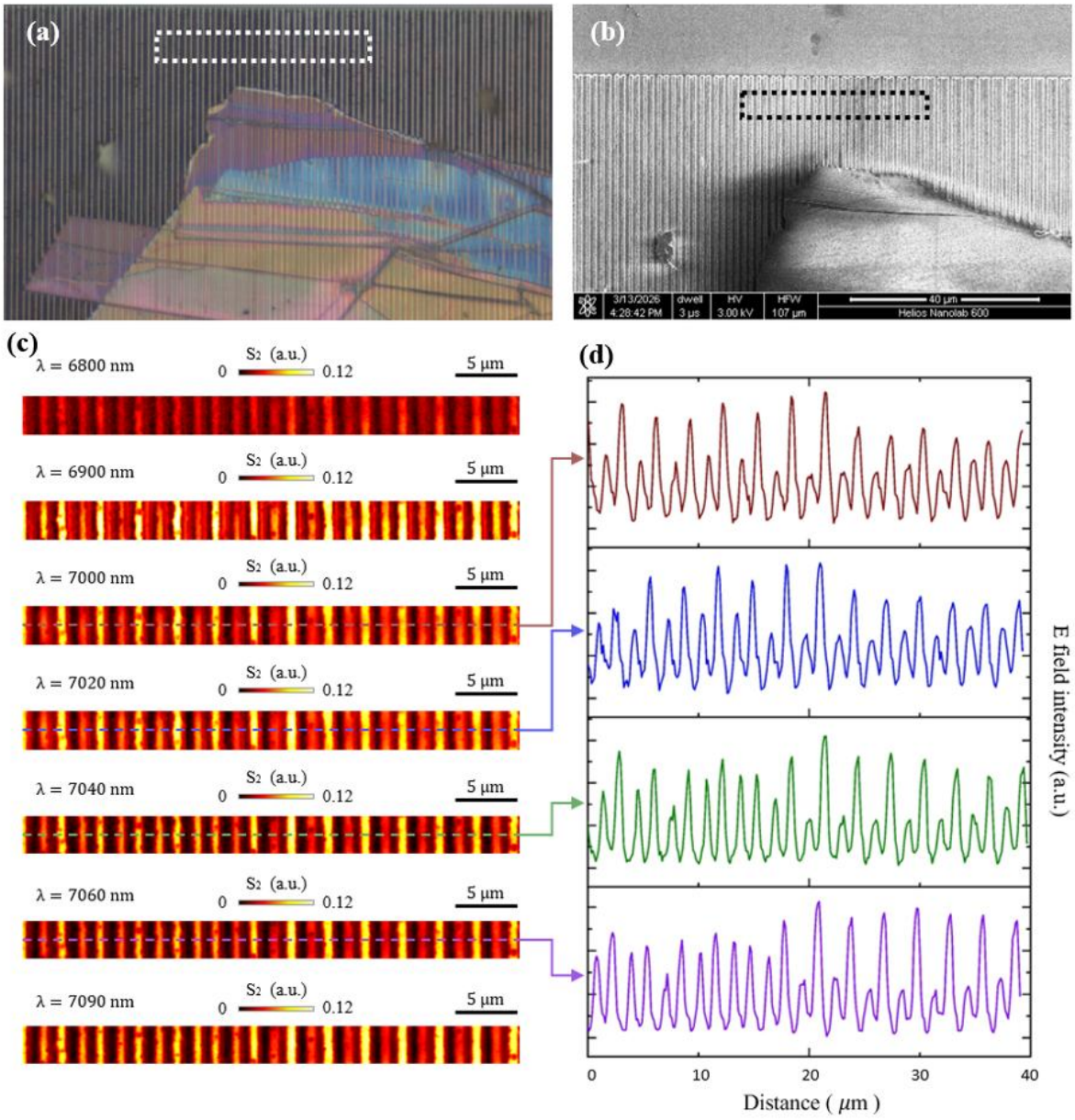


Figure 5.14 | Near-field response of the uncoupled photonic system. a, b, Optical and scanning electron microscope images of the Si grating, highlighting the region probed to verify the uncoupled system. **c, d,** s-SNOM near-field measurements of the uncoupled Si grating

across the topological bandgap, with corresponding line-cut profiles (right) showing selected measurements taken within and outside the bandgap.

In principle, a two-band description of the domains predicts four resonant states stemming from the bulk bands of the adjacent left and right trivial domains, which possess unequal bandgaps. However, in the fabricated sample, the resonances of two bulk modes are spectrally overlaid. We find that the generalized Fano framework restricted to three bulk channels ($j \in \{1,2,3\}$) yields a clean global fit to the collected data (Figure. 5.13e). To extract the shared pole structure of the system across spatial coordinates close to the interface, the central resonance frequencies ($f_{0,j}$) and linewidths (γ_j) were treated as global parameters across all domains ($\delta_{j,d} = \delta_j$), while the coupling amplitudes ($A_{j,d}$) and asymmetry parameters ($q_{j,d}$) varied locally. Optimization was performed using a multi-start Levenberg-Marquardt algorithm in MATLAB. This fitting configuration captures the defining spectral features of the system in Fig. 5.13e, notably the intensity drops between the upper bulk bands of the two domains (where a hybrid edge state is expected to reside) as well as the decay down to a baseline level of ~ 0.4 away from the resonance region for all three spatial positions.

This verifies that the uncoupled Si grating remains topologically trivial in the absence of strong light-matter coupling. Both domains behave as expected from the design and simulations, and the emergence of the edge state in the coupled system can therefore be directly attributed to interaction-induced topology.

5.4. Discussion and future work.

We have demonstrated that a topological polaritonic system can be created from a photonic structure that is initially trivial. In the absence of light-matter interaction, the system shows no topological features. However, once strong coupling with the phononic mode is introduced, the hybrid system becomes topological, confirming that the topology is induced by the light-matter interaction. This establishes a new paradigm that has not been experimentally demonstrated before.

The experimental results presented in this chapter establish the existence of an interaction-induced interface-localised polaritonic edge state through frequency-dependent near-field measurements, spatial confinement and decay analysis, and comparison with the uncoupled photonic control. However, the present experiments focus on the formation and localisation of the edge state rather than its directional transport properties. Consequently, unidirectional propagation, suppression of backscattering, and robustness against structural disorder have not

been independently verified experimentally. The theoretical analysis considers the influence of non-Hermitian losses on the topological properties of the hybrid system, but this should be distinguished from robustness against disorder-induced scattering. Furthermore, although the interaction-induced mechanism provides a potential route to actively tuning the topological phase, dynamic switching through externally applied strain or electrostatic gating has not yet been demonstrated experimentally. These aspects remain important directions for future investigation and device development.

Although this work focuses on phonon polaritons, the same concept can be extended to other material excitations, particularly exciton polaritons. A trivial photonic platform can be engineered to acquire topological properties through strong coupling, offering a powerful route to design tunable topological systems. A key advantage of this approach is the potential to actively control the topology using external stimuli.

To fully exploit this concept, further work is underway to investigate the dynamic tunability of the topological properties. One potential approach is strain engineering, which could modify the optical response and coupling conditions of the system, thereby influencing the emergence of topological transitions. However, implementing controlled and reversible strain in such hybrid structures presents significant experimental challenges, making this approach less practical for real-time modulation. A more promising direction is the development of electrically gated devices, where the optical properties and light-matter interactions could potentially be modified through an applied electric field. Such an approach could enable dynamic control over the topological phase and associated interface states. Introducing this additional temporal degree of freedom would represent an important step towards actively reconfigurable topological polaritonic devices, with potential applications in optical switching, modulation, and integrated photonic systems.

References

1. Wang, Z., Chong, Y., Joannopoulos, J. D., & Soljačić, M.(s). Observation of unidirectional backscattering-immune topological electromagnetic states. Nature 2009, 461 (7265), 772-775.

2. Hafezi, M., Demler, E. A., Lukin, M. D., & Taylor, J. M.(s). Robust optical delay lines with topological protection. Nature physics 2011, 7 (11), 907-912.

3. Rechtsman, M. C., Zeuner, J. M., Plotnik, Y., Lumer, Y., Podolsky, D., Dreisow, F., Nolte, S., Segev, M., & Szameit, A.(s). Photonic Floquet topological insulators. Nature 2013, 496 (7444), 196-200.

4. Gao, F., Gao, Z., Shi, X., Yang, Z., Lin, X., Xu, H., Joannopoulos, J. D., Soljačić, M., Chen, H., & Lu, L.(s). Probing topological protection using a designer surface plasmon structure. Nature communications 2016, 7 (1), 11619.

5. Karzig, T., Bardyn, C.-E., Lindner, N. H., & Refael, G.(s). Topological polaritons. Physical Review X 2015, 5 (3), 031001.

6. Sala, V., Solnyshkov, D., Carusotto, I., Jacqmin, T., Lemaître, A., Terças, H., Nalitov, A., Abbarchi, M., Galopin, E., & Sagnes, I.(s). Spin-orbit coupling for photons and polaritons in microstructures. Physical Review X 2015, 5 (1), 011034.

7. Milićević, M., Ozawa, T., Montambaux, G., Carusotto, I., Galopin, E., Lemaître, A., Le Gratiet, L., Sagnes, I., Bloch, J., & Amo, A.(s). Orbital edge states in a photonic honeycomb lattice. Physical review letters 2017, 118 (10), 107403.

8. Klembt, S., Harder, T., Egorov, O., Winkler, K., Ge, R., Bandres, M., Emmerling, M., Worschech, L., Liew, T., & Segev, M.(s). Exciton-polariton topological insulator. Nature 2018, 562 (7728), 552-556.

9. Liu, W., Ji, Z., Wang, Y., Modi, G., Hwang, M., Zheng, B., Sorger, V. J., Pan, A., & Agarwal, R.(s). Generation of helical topological exciton-polaritons. Science 2020, 370 (6516), 600-604.

10. Guddala, S., Komissarenko, F., Kiriushechkina, S., Vakulenko, A., Li, M., Menon, V. M., Alù, A., & Khanikaev, A. B.(s). Topological phonon-polariton funneling in midinfrared metasurfaces. Science 2021, 374 (6564), 225-227.

11. Li, M., Sinev, I., Benimetskiy, F., Ivanova, T., Khestanova, E., Kiriushechkina, S., Vakulenko, A., Guddala, S., Skolnick, M., & Menon, V. M.(s). Experimental observation of

topological Z2 exciton-polaritons in transition metal dichalcogenide monolayers. Nature communications 2021, 12 (1), 4425.

12. Yan, Q., Zhao, B., Zhou, R., Ma, R., Lyu, Q., Chu, S., Hu, X., & Gong, Q.(s). Advances and applications on non-Hermitian topological photonics. Nanophotonics 2023, 12 (13), 2247-2271.

13. Price, H., Chong, Y., Khanikaev, A., Schomerus, H., Maczewsky, L. J., Kremer, M., Heinrich, M., Szameit, A., Zilberberg, O., & Yang, Y.(s). Roadmap on topological photonics. Journal of Physics: Photonics 2022, 4 (3), 032501.

14. Kazarinov, R., & Henry, C.(s). Second-order distributed feedback lasers with mode selection provided by first-order radiation losses. IEEE Journal of Quantum Electronics 2003, 21 (2), 144-150.

15. Lee, S.-G., & Magnusson, R.(s). Band flips and bound-state transitions in leaky-mode photonic lattices. Physical Review B 2019, 99 (4), 045304.

16. Letartre, X., Mazauric, S., Cueff, S., Benyattou, T., Nguyen, H. S., & Viktorovitch, P.(s). Analytical non-Hermitian description of photonic crystals with arbitrary lateral and transverse symmetry. Physical Review A 2022, 106 (3), 033510.

17. Nguyen, H. S., Dubois, F., Deschamps, T., Cueff, S., Pardon, A., Leclercq, J.-L., Seassal, C., Letartre, X., & Viktorovitch, P.(s). Symmetry breaking in photonic crystals: on-demand dispersion from flatband to Dirac cones. Physical review letters 2018, 120 (6), 066102.

6. Spin-Selective coupling of SHG using 3R-WS_2 metasurface

The integration of nonlinear optical functions into compact photonic platforms is an important direction in modern nanophotonics, with relevance to on-chip light sources, signal processing, frequency conversion, and quantum photonics[1-3]. 2D TMDCs are attractive for this purpose because they combine strong light-matter interaction, excitonic resonances, and large nonlinear optical responses[1,4]. In monolayer TMDCs, the absence of inversion symmetry gives rise to a non-zero second-order nonlinear susceptibility, resulting in efficient SHG[4,5]. At the same time, the electronic band extrema at the inequivalent K and K′ valleys can be selectively addressed using circularly polarized light, which gives a direct relation between photon helicity and valley degree of freedom[1,6].

In conventional photonic systems, nonlinear generation and optical routing are often treated as separate functions. A nonlinear material generates light, while a separate photonic element, such as a grating, waveguide, or metasurface, controls its propagation. This separation increases fabrication complexity and can introduce additional losses, alignment constraints, and interface-related limitations. A more integrated approach is to combine nonlinear light generation and directional routing within the same photonic platform. This is the central motivation of the present chapter: to investigate a nonlinear valley-selective meta-waveguide platform in which helicity-dependent SHG generated in 3R-phase WS_2 is coupled directionally into guided modes of a Si_3N_4 waveguide.

The physical principle of the device combines three effects. First, the non-centrosymmetric crystal symmetry of WS_2 enables second-order nonlinear generation[4,5]. Second, valley-dependent optical selection rules link the helicity of circularly polarized excitation to the valley-dependent nonlinear optical response[1,6]. Third, a geometric-phase metasurface imposes a helicity-dependent in-plane momentum, allowing the generated nonlinear emission to be routed into different waveguide directions[7,8]. In this way, the platform converts polarization and valley information into spatially separated guided optical signals.

This concept is related to recent demonstrations by our collaborators of valley optoelectronic meta-waveguide device, where valley-dependent chiral SHG photons from monolayer WS_2 were routed through a chirality-selective meta-waveguide and electrically detected using WSe_2 photodetectors[9]. That work demonstrated near-unity valley-dependent chiral SHG and high polarization selectivity in a meta-waveguide platform. However, the device investigated in this chapter differs in its material and implementation strategy. Instead of relying on monolayer

WS_2 combined with separate photodetectors, the present work focuses on a 3R-phase WS_2 platform, where multilayer non-centrosymmetric stacking preserves a strong second-order nonlinear response while providing a larger optical interaction volume[10]. The aim is therefore not to reproduce the full optoelectronic readout architecture, but to establish a nonlinear meta-waveguide design in which the active TMDC layer itself participates in both nonlinear generation and metasurface-enabled routing.

6.1. Physical Principles of Valley-Selective Nonlinear Photonics

6.1.1. Valley dependent Optical Selection Rules in TMDCs

Monolayer TMDCs such as WS_2 possess a hexagonal lattice with broken inversion symmetry. This gives rise to two inequivalent valleys located at the K and K′ points of the Brillouin zone. These valleys represent distinct extrema in momentum space and can be treated as an additional degree of freedom for carriers. Because of the symmetry of the Bloch states at the band edges, optical transitions at the two valleys couple selectively to opposite circular polarizations[1,6].

This valley–helicity correspondence can be written schematically as

$$\sigma^+ \leftrightarrow K, \sigma^- \leftrightarrow K'$$

where σ^+ and σ^- denote right- and left-circularly polarized light, respectively.

For nonlinear processes, the relevant material response is described by the nonlinear polarization. For SHG, the second-order polarization at $2\omega$is

$$\mathbf{P}^{(2)}(2\omega) = \varepsilon_0 \chi^{(2)} : \mathbf{E}(\omega)\mathbf{E}(\omega)$$

where $\chi^{(2)}$is the second-order nonlinear susceptibility tensor and $E(\omega)$is the fundamental optical field. In centrosymmetric media, $\chi^{(2)}$vanishes under the electric-dipole approximation. In non-centrosymmetric TMDCs, however, $\chi^{(2)} \neq 0$, enabling efficient SHG[4,5].

Importantly, the valley selection rules are not limited to one-photon excitation. The two-photon transition amplitude involves a product of dipole matrix elements[9],

$$\langle \psi_c \mid \hat{P}^{\pm} \mid \psi_j \rangle \langle \psi_j \mid \hat{P}^{\pm} \mid \psi_v \rangle$$

which, under threefold rotational symmetry, leads to valley-selective SHG processes[9].

6.1.2. Geometric phase metasurfaces

For circularly polarized light, the geometric phase is given by

$$\phi = 2\sigma\theta$$

where θ is the meta-atom orientation angle and σ = ±1 represents helicity[7,8]. This expression shows that the phase acquired by light interacting with the metasurface depends not only on the structural orientation of the meta-atoms but also on the polarization state of the incident field. As a result, opposite circular polarizations experience opposite phase shifts.

The phase gradient produces an effective in-plane momentum:

$$k_G = \frac{d\Phi}{dx}$$

This momentum can be understood as arising from the spatial variation of the optical phase imposed by the metasurface, effectively modifying the propagation direction of the emitted light. In particular, for light incident under near-normal conditions, the in-plane component of the wavevector is negligible. Therefore, an additional in-plane momentum must be introduced to enable coupling into guided modes of a waveguide structure.

Coupling into guided modes occurs when the momentum matching condition is satisfied:

$$k_G \approx \beta_{wg}$$

where

$$\beta_{wg} = n_{eff} k_0$$

is the propagation constant of the waveguide mode. Here, n_{eff}represents the effective refractive index of the guided mode and $k_0$is the free-space wavevector. This condition ensures that the momentum of the emitted light matches that of the guided mode, enabling efficient coupling. This principle is widely used in metasurface–waveguide systems to achieve controlled and directional coupling of optical signals[9].

6.1.3. Spin-momentum locking and Directional coupling

Because the PB phase changes sign with helicity,

$$\sigma^+ \rightarrow +k_G, \sigma^- \rightarrow -k_G$$

leading to directional coupling into opposite waveguide modes[9]. This helicity-dependent momentum arises directly from the geometric phase response of the metasurface, which imparts opposite phase gradients to left- and right-circularly polarized light.

When the metasurface is integrated with a waveguide, this momentum asymmetry results in preferential coupling of different polarization components into opposite propagation directions. This phenomenon is commonly referred to as spin–momentum locking, where the spin angular momentum (polarization) of light determines its propagation direction within the structure.

In the context of the present system, this effect operates on the nonlinear emission generated within the 3R-WS_2 layer. Circularly polarized excitation first produces helicity-dependent second harmonic signals, which are then converted into directional propagation by the metasurface. This establishes a direct mapping between excitation helicity and guided propagation direction, enabling polarization-controlled routing of nonlinear optical signals within the device.

6.2. Device concept and numerical design

Building upon the physical principles discussed in the previous section, the implementation of a nonlinear valley-selective photonic system requires the integration of a nonlinear material with a structure capable of controlling light propagation at the subwavelength scale. In this work, a meta-waveguide platform is developed to achieve this functionality by combining a Si_3N_4 waveguide with a patterned metasurface region formed on a 3R-phase WS_2 flake. This configuration enables the generation, manipulation, and routing of polarization-dependent nonlinear optical signals within a compact, integrated structure.

The key idea of the proposed system is to exploit the intrinsic nonlinear response and valley-dependent optical properties of 3R-WS_2, while using a geometric phase metasurface to convert the polarization state of the generated light into directional propagation along a waveguide. This eliminates the need for separate nonlinear and photonic components, allowing both light generation and routing to be realized within a unified platform. Similar metasurface–waveguide architectures have been demonstrated for helicity-dependent routing of optical signals[9], where the metasurface provides the required phase gradient for coupling into guided modes.

The proposed device consists of three main components: a dielectric waveguide, a metasurface region, and input/output coupling structures. These elements are integrated on a fused silica (quartz) substrate to form a planar photonic platform capable of supporting guided optical modes and facilitating nonlinear light–matter interactions.

At the core of the structure is a Si_3N_4 waveguide with a thickness of approximately 350 nm, which is designed to support a fundamental guided mode in the near-infrared spectral range. Si_3N_4 is chosen due to its low optical loss, high refractive index contrast with the substrate, and compatibility with standard nanofabrication processes[7]. The waveguide provides a confined optical mode that enables efficient transport of the generated signal over micrometre-scale distances.

A 3R-phase WS_2 flake is transferred onto the central region of the waveguide, forming the active nonlinear layer. Due to its non-centrosymmetric stacking, the 3R-WS_2 maintains a strong second-order nonlinear response even in multilayer form[10]. This enables efficient generation of second harmonic signals under optical excitation, while also preserving valley-dependent selection rules that link the polarization state of the emitted light to the excitation helicity.

The metasurface is defined by patterning the 3R-WS_2 flake into an array of subwavelength nanostructures with spatially varying orientation. These structures act as anisotropic meta-atoms that impart a geometric phase to the generated optical field[7,8]. By introducing a controlled phase gradient across the metasurface region, an effective in-plane momentum is imposed on the emitted light, enabling coupling into the guided modes of the Si_3N_4 waveguide[9].

Because the geometric phase response is helicity-dependent, second harmonic signals generated under opposite circular polarizations are routed into opposite directions along the waveguide. This establishes a direct mapping between excitation helicity and propagation direction, consistent with the spin-momentum locking mechanism described earlier. As a result, the device enables polarization-controlled routing of nonlinear optical signals within a single integrated structure.

To enable optical readout of the guided signals, scattering gratings are incorporated at both ends of the waveguide. These gratings convert the guided modes back into free-space radiation, allowing the directionally routed signals to be detected experimentally. This approach provides a practical method for characterizing the device without requiring integrated photodetectors, while still capturing the essential directional coupling behaviour.

The design of the proposed meta-waveguide platform is based on the requirement of efficiently coupling the nonlinear optical signal generated within the 3R-WS_2 metasurface into the guided modes of the Si_3N_4 waveguide. This process is governed by momentum conservation and phase-matching conditions between the locally generated optical field and the supported waveguide modes.

For near-normal excitation, the in-plane component of the incident wavevector is negligible. Therefore, an additional in-plane momentum must be provided to enable coupling into the guided mode. This is achieved through the geometric phase gradient introduced by the metasurface:

$$k_G = \frac{d\Phi}{dx}$$

Efficient coupling occurs when this momentum matches the propagation constant of the waveguide mode:

$$k_G = n_{eff} k_0$$

where n_{eff} is the effective refractive index and k_0 is the free-space wavevector[9]. This condition ensures that the momentum of the emitted light matches that of the guided mode, enabling efficient coupling from the metasurface into the waveguide.

The metasurface is implemented by arranging anisotropic nanoantennas with spatially varying rotation angle θ, each imparting a phase shift

$$\Phi = \pm 2\theta$$

By introducing a linear variation in θ across the metasurface, a constant phase gradient is achieved, leading to a well-defined in-plane momentum:

$$k_G \approx \frac{2\theta}{p}$$

where p is the metasurface period. This relation provides a direct link between the metasurface geometry and the momentum required for coupling into the waveguide.

Numerical simulations were performed to validate this design approach. The nonlinear emission process was approximated using an array of in-plane electric dipoles positioned above the metasurface, representing localized second harmonic sources[9]. This approximation captures the essential coupling mechanism between the nonlinear emitter and the guided modes, while allowing efficient evaluation of the metasurface design.

The simulations confirm strong helicity-dependent directional coupling, where opposite circular polarizations result in propagation in opposite directions. This demonstrates that the metasurface provides both the required momentum matching and polarization-selective routing, consistent with the physical principles described earlier.

6.3. Fabrication of the Meta-waveguide platform and optical characterization

To fabricate the designed and proposed meta-waveguide device perfectly, careful integration of the dielectric waveguide and the patterned 3R-WS_2 metasurface is crucial. In this section, we detail the entire fabrication process, including the challenges and unique techniques used to fabricate the meta-waveguide device.

6.3.1. Substrate and waveguide fabrication

The first step in the fabrication is selecting the substrate and fabricating the Si_3N_4 waveguide on it. In addition to the Si_3N_4 waveguide, alignment markers were fabricated in this step for use in subsequent EBL processes. As a low-index cladding material, quartz was used as the substrate, providing a low-loss, optically transparent platform for guiding light in the near-infrared region. This helps with the transmission measurements at a later stage for optical characterization. The fabrication process began with depositing a 350 nm Si_3N_4 thin film using PECVD. Si_3N_4 is deposited by PECVD using SiH_4, NH_3, and N_2, with a 1500 mTorr Pressure and 40W forward RF power. This recipe deposits Si_3N_4 at a deposition rate closer to, and the deposition was carried out for 20 minutes and 48 seconds to achieve the desired thickness.

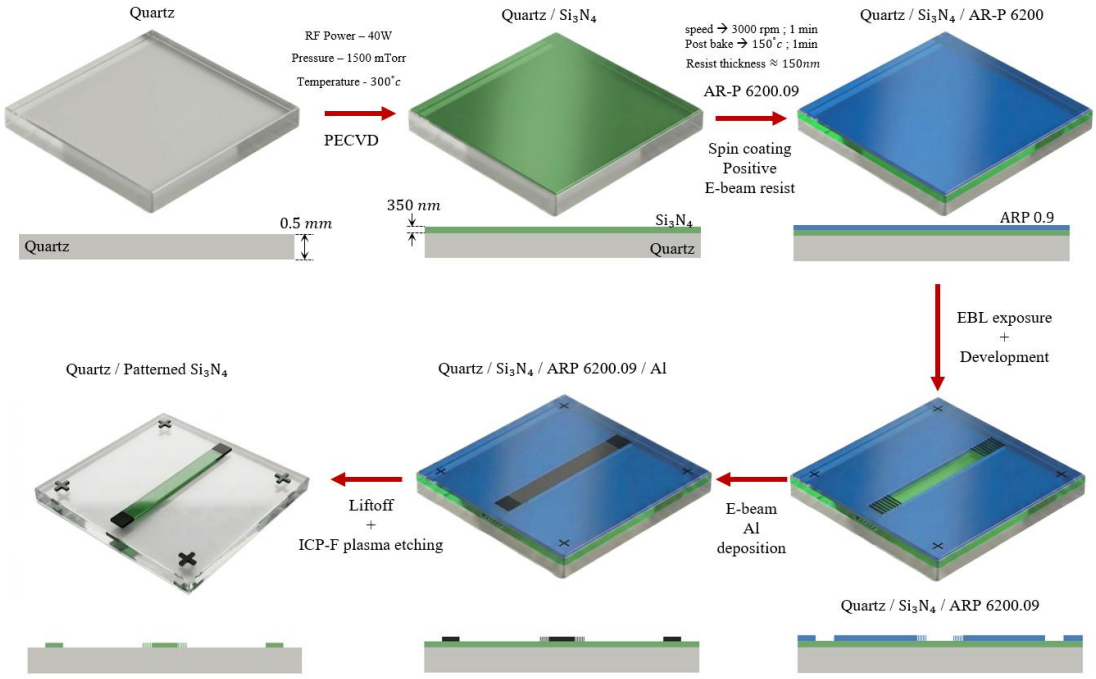


Figure 6.1 |Schematic of the fabrication process flow for the Si_3N_4 waveguide on a quartz substrate.

Then the substrate was prepared for the EBL process by spin-coating the positive e-beam resist ARP 6200.09 for 1 minute at 3000 rpm. The spin-coated sample contains a resist layer of 150-200nm in thickness, which is suitable for metal deposition and liftoff, as confirmed by ellipsometry and surface profiler measurements. To eliminate electron charging effects at the resist surface during lithography, a conductive polymer layer was spin-coated on the ARP 6200.09 resist. Then, using an Elionix EBL tool to pattern the alignment markers and the waveguide with the gratings. For the EBL process, a 5nA beam current and a dose factor of

400 are used. After exposure, the sample is developed using a set of solvents. First, the sample is dipped in DI water for 1 minute to remove the conductive polymer, then dried under N2. Then the sample is dipped in the developer solution n-Amyl Acetate (AR 600 546) for 1 minute, followed by an IPA rinse for 1 minute and N2 blow dry. After confirming successful development under an optical microscope, the sample is deposited with an Al mask layer using an e-beam evaporator. A 30nm Al layer is deposited at a rate of 0.2 nm/s. After that, the resist will be lifted off, leaving the Al mask with the waveguide and grating patterns and alignment markers on the quartz/Si_3N_4 sample. Then the waveguide is defined using an ICP-F etching process. The gases with flow rates of 4:2:6 sccm were used for ICP-F RIE etching with an ICP power of 50W, a Bias power of 25W, and a He pressure of 2000Pa. After etching, the remaining metal mask is removed using a suitable wet etchant, leaving behind the patterned Si_3N_4 waveguides on the fused silica substrate. The alignment markers are crucial for subsequent EBL steps and for accurately positioning the patterns on the flake in the proper regions. The fabricated waveguides are inspected using optical microscopy to verify the pattern fidelity and alignment markers. Ensuring high-quality waveguide structures at this stage is essential, as any defects or irregularities can significantly affect the propagation and coupling of optical signals in subsequent steps

6.3.2. Metasurface fabrication (with 3R-WS_2)

With the fabricated waveguides, the metasurface is fabricated. First, a Chromium protective layer is deposited on the waveguide. The metasurface should be placed in the middle of the waveguide. During metasurface fabrication, the TMDC flake needs to be etched using plasma; during this step, the waveguide or the scattering gratings should not be etched or damaged. Therefore, the Chromium protective layer is fabricated with a lithographic process. From steps 1 to 3 in Figure 6.2, the patterned waveguide on the substrate is spin-coated with the ARP 6200.04 resist and then patterned using EBL (Exposures and development). Then, from steps 3 to 4, Chromium is initially deposited using an e-beam evaporator to a thickness of 20 nm.

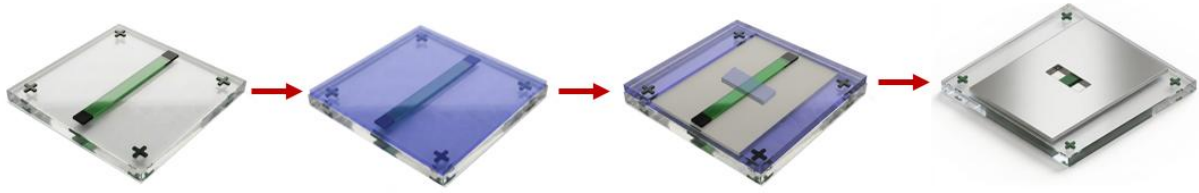


Figure6.2 | Fabrication process flow in creating the Cr protective layer for the Si_3N_4 waveguide.

Next, the metasurface fabrication process was carried out, which was the most challenging and critical step in realizing the circularly polarized-dependent meta-waveguide device. Unlike conventional metasurfaces patterned on uniform dielectric films or on random flakes on substrates (2D or bulk), this process involves fabricating subwavelength features directly on a mechanically transferred multilayer 3R-WS_2 flake at a predefined waveguide position. This makes the fabrication more challenging, particularly in ensuring good flake adhesion, achieving precise alignment, maintaining uniform resist coating, and preserving etching stability.

The fabrication of the metasurface begins with exfoliating a 3R-WS_2 flake to the desired thickness. As discussed in Chapter 2, we use mechanical exfoliation to produce the thin TMDC flake, and then, based on the optical contrast (experience) of the flakes that is transferred onto the gel film (PDMS), we roughly select the flakes that we believe have a thickness closer to 400nm. Then this flake is checked using PSI to obtain the optical thickness and confirm that the flake is 400nm or closer to that. The thickness measured by PSI on the gel film differs slightly from the actual flake thickness. To correct this, PSI measurements were performed on multiple flakes, which were then transferred to a substrate and measured using a surface profiler and AFM. This allowed calibration of the PSI optical thickness to the true flake thickness.

After selecting a ~400 nm thick flake on the gel film, the first critical step is transferring it onto the waveguide. This step must be done carefully due to several challenges. Since a 20 nm Cr protective layer is present, it is important to ensure that the TMDC flake is not just resting on the Cr layer but is in proper contact with the underlying Si_3N_4 waveguide. To achieve good adhesion, the substrate and waveguide are placed on the transfer stage and brought into contact with the PDMS flake. The stage is heated, and the sample is kept in contact for more than 24 hours. During the transfer, gentle pressure is applied multiple times with a slightly blunt tweezer or a curved-tip tool to improve contact and adhesion. This step is critical because the flake must withstand subsequent processes, such as EBL, plasma etching, cleaning, and wet etching, where poor adhesion could cause the flake or patterned structures to detach. After transfer, the sample is rinsed with IPA. This is not only for cleaning but also to test the adhesion quality, ensuring that the flake remains stable under liquid flow.

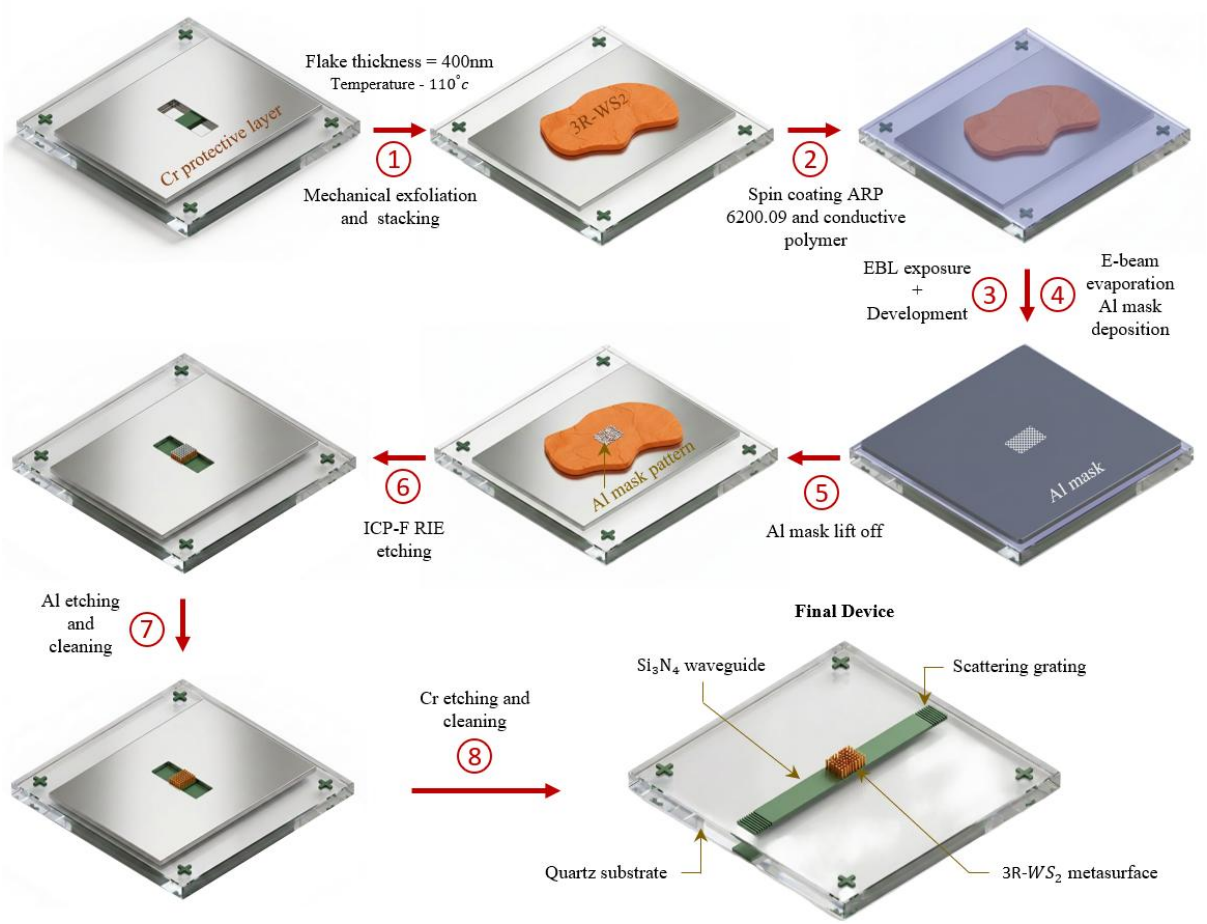


Figure 6.3 | Fabrication process flow for the 3R-WS_2 metasurface fabrication.

After that, the metasurface fabrication initiates with preparing the sample for the EBL exposure. The sample is first spin-coated with ARP 6200.09 resist at 3000 rpm for 1 minute and baked for 1 minute. The resultant resist coating is around 150 to 200nm thick, as confirmed by scratching the resist and measuring the thickness using the surface profiler. This is essential to ensure a proper lift-off. Then, a conductive polymer layer is spin-coated onto the resist to assist the EBL process and eliminate charging effects that can degrade the quality of the patterned features. Then we expose the sample and pattern the features to the positive photoresist using the Elionix EBL system. A 500-pA current and a dose of 400 were used in the EBL process. Then the samples were immediately developed by first removing the conductive polymer by dipping the sample in DI water for 1 minute, then blowing dry with N_2 gas. Then the sample was dipped in the ARP remover (n-Amy Acetate (AR 600 546)) for 1 minute, followed by a 1-minute IPA rinse (etch stopper) and a N_2 air blow-dry. After that, the sample was loaded into the e-beam evaporator, and an Al layer of 30 nm was deposited at a deposition rate of $1 A^{\circ}/s$. Then the sample was dipped in the ARP remover solution (Di-Methyl Acetate) overnight until the Al layer was lifted off, yielding the patterned Al mask for etching.

As shown in step 6 of Figure 6.3, the sample was etched using ICP-F plasma RIE with a flow rate ratio of 4:4:6 sccm for 8 minutes (etching rate was 50 nm/s). The higher ratio improved the quality of the sidewalls even though the etching rate was slightly reduced. After etching the 3R-WS_2 and fabricating the expected metasurface pillars, the AL mask is first etched with Type A aluminium etchant, followed by DI water cleaning. Finally, the Chromium layer is etched, the sample is cleaned with DI water and IPA, and it is N_2-blown-dried to finalize the fabrication. This wet etching process is much more complex and presents multiple challenges that were practically addressed. These details are discussed in the following section, along with the actual fabrication details.

6.3.3. Fabricated results and final devices

As fully detailed in section 6.3.2 the fabrication was carried out to realize the meta-waveguide devices. As a summary the entire set of steps associated with the actual fabrication (eliminating sample cleaning) is illustrated in Figure below.

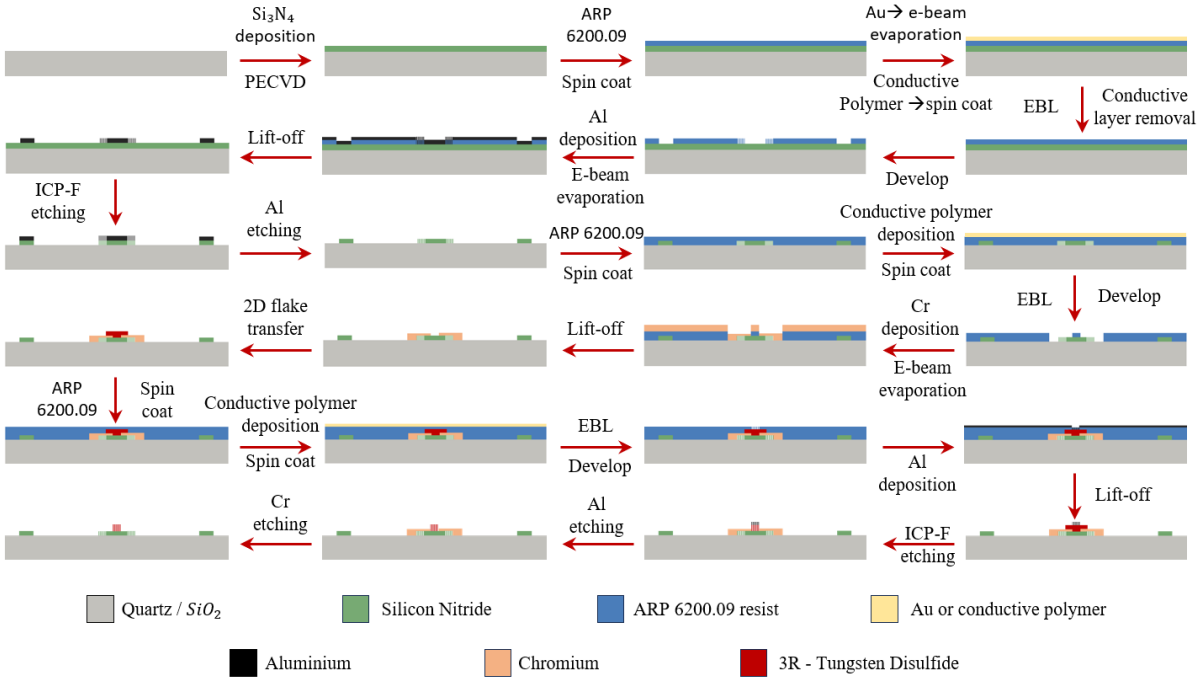


Figure 6.4 : Fabrication flow diagram for the complete meta-waveguide device.

A four-inch wafer was used to fabricate 38 sets of waveguide units as shown in Figure 6.5 panel a. Then the 38 units were cut into pieces using a micro diamond scriber setup to prepare squared shape unit (Figure 6.5b) sample which contains 10 waveguides fabricated with the Chromium protection layer and a window to transfer the TMDC flake onto the waveguide as shown in the optical microscopic image in Figure 6.5 panel c. Then the 3R phase WS2 flakes were exfoliated

onto a PDMS layer/gel film (Figure 6.5d), and the thickness of the flakes was measured using PSI, as shown in Figure 6.5 panels e and f.

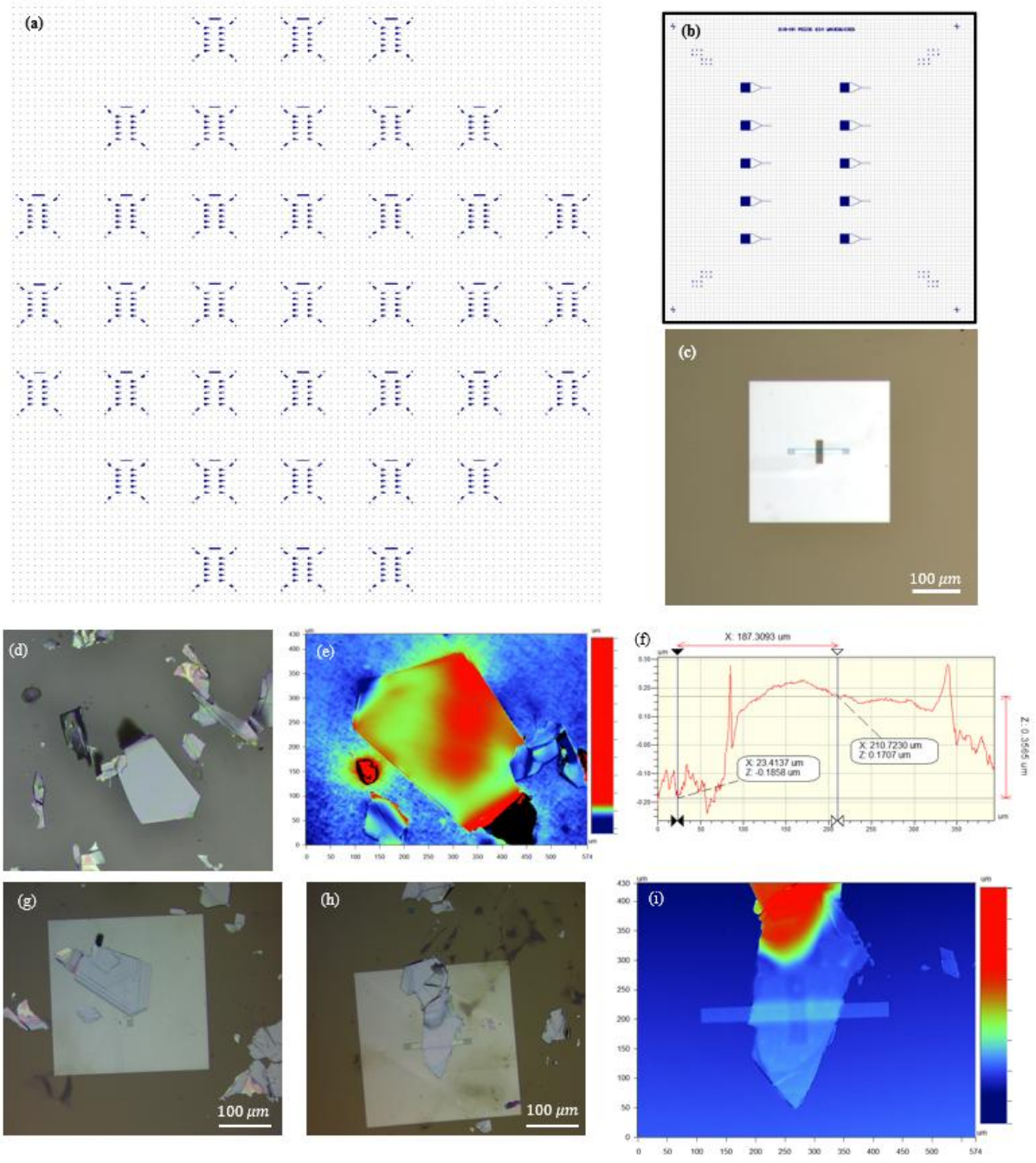


Figure 6.5 | Waveguide fabrication and flake transfer. a-c, Fabrication of waveguides on a 4-inch Si wafer and optical microscope image showing the waveguide with a Cr protective layer. **d,** Exfoliated 3R-WS_2 flake selected by optical contrast (~400 nm thick). **e, f,** PSI thickness measurements of the flake in (d). **g,** Optical microscope image of the flake after transfer onto the waveguide. **h, i,** Optical image of another transferred flake (see Fig. 6.6) and its corresponding PSI thickness measurement after transfer.

After identifying the region of the flake that has a thickness of 400 nm, the flake is mechanically transferred onto the waveguide while leaving the gel film on top of the waveguide properly aligned and subjected to a temperature of 110 degrees, and by applying force multiple times in between the transferring time of 1 to 24 to 48 hours.

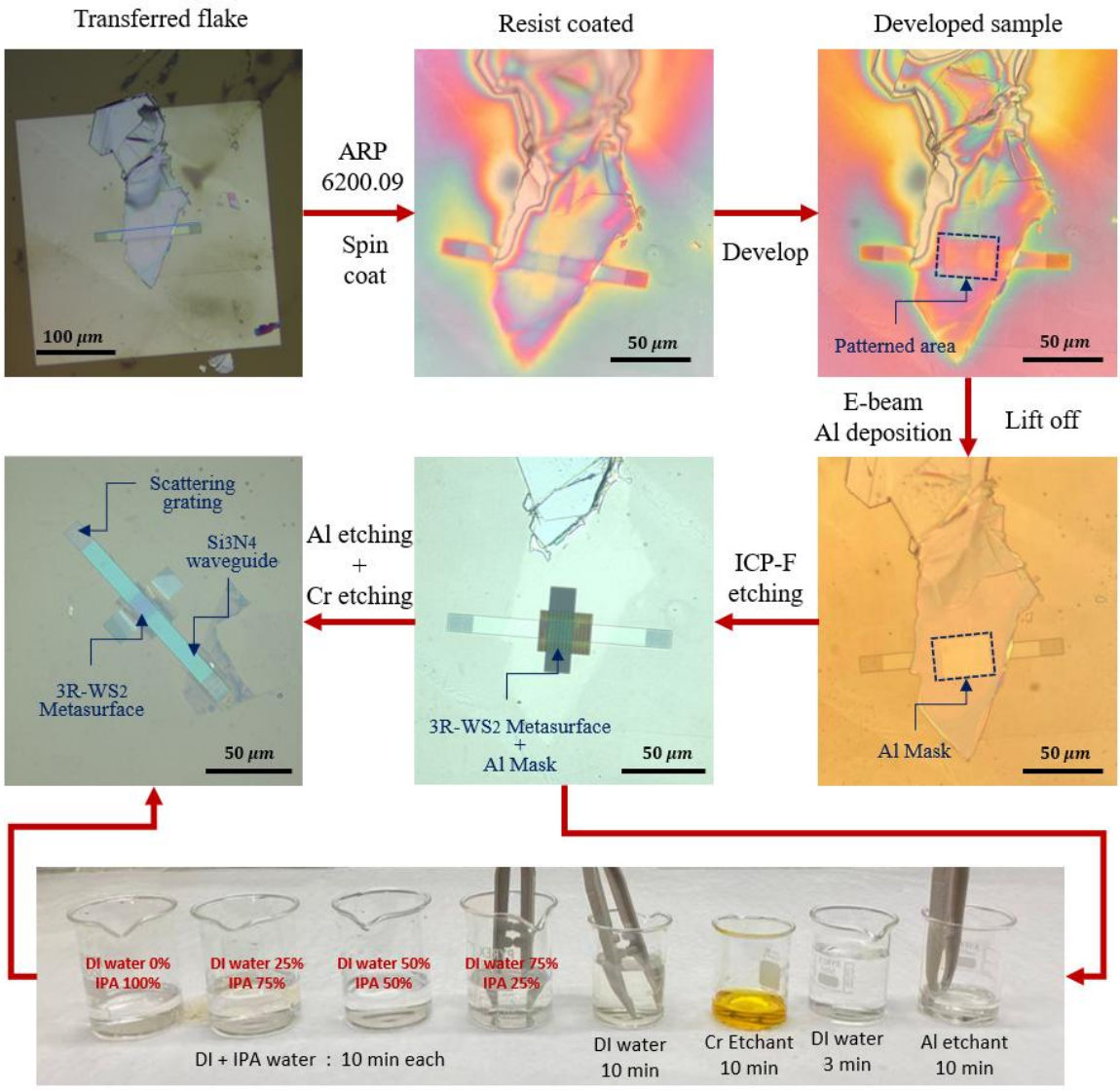


Figure 6.6 | Key EBL and etching steps used in the fabrication of the final device, highlighting the critical stages.

Two of the successfully transferred flakes onto the waveguide are shown in Figures g and h. Panel g is the transferred flake shown in panels d and e. After transferring to double-check the thickness of the flake on the substrate, another PSI measurement is taken, as illustrated in panel i of Figure 6.5. A small thickness contrast is visible on the transferred flake near the window and on the flake sitting on the Cr layer, confirming that the flake is in contact with the waveguide. The PSI measurement of the flake after transfer is very much closer to the actual

thickness, and for some samples, to confirm the thickness perfectly, an AFM scan or a surface profiler measurement was taken.

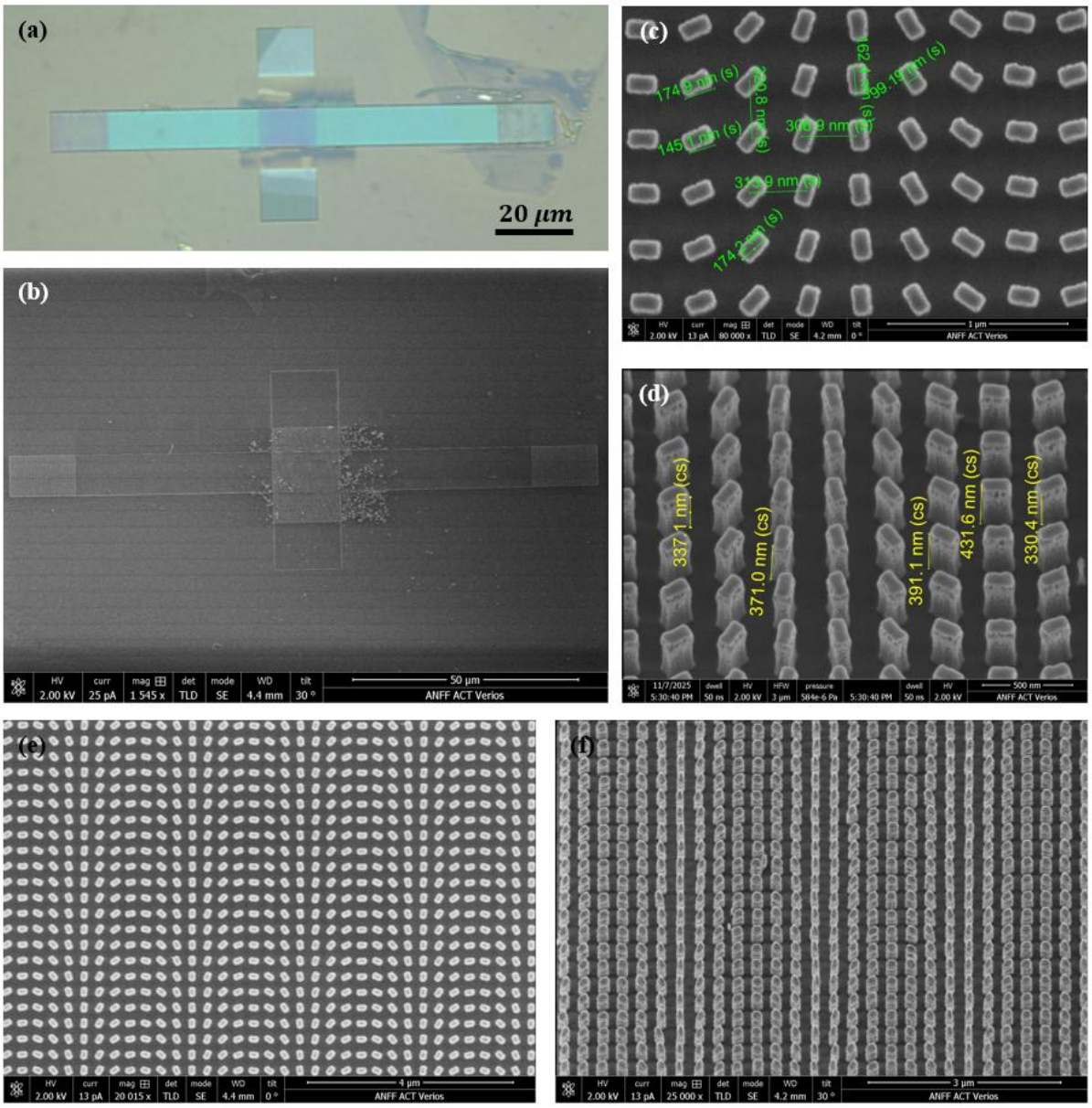


Figure 6.7 | Microscopic images of the final fabricated device. **a,** Optical microscope image of the meta-waveguide device. **b,** SEM image of the complete device. **c-f,** SEM images of the metasurface showing feature sizes.

After transfer, the sample is rinsed with IPA under flow to apply fluid force and test adhesion. If the flake remains in place, it is well attached to the waveguide and fabrication can proceed. As shown in Figure 6.6, the sample is then spin-coated, and the metasurface is patterned using EBL. After ICP-F RIE etching of the 3R-WS_2, it is important to follow a careful wet etching process. The final steps, including Al and Cr etching, are also carried out using wet processes.

Since the fabricated pillars have a high aspect ratio, they are prone to breaking or collapsing under strong liquid forces. To avoid this, the samples are not subjected to N_2 blow drying or agitation. Instead, they are cleaned by gently dipping them step by step in the required solutions, as illustrated in Figure 6.6. The final fabricated device is shown in figure 6.7.

6.3.4. Optical characterization

The fabricated meta-waveguide devices were characterized using a reflection SHG setup, as described in Chapter 2. The metasurface was excited with circularly polarized light to test spin-selective SHG modes guided along the waveguide (Figure 6.8a). To first confirm that the waveguide was not over-etched and could support light propagation, one grating was excited with a 775 nm laser, and the scattered signal was observed from the opposite grating (Figure 6.8b). Successful transmission confirmed that the waveguide was intact and not damaged.

Next, the ability of the waveguide to selectively couple circularly polarized light and guide it in different directions was tested, as shown in Figure 6.8c-f. The metasurface demonstrated clear spin selectivity for the fundamental beam under circularly polarized excitation at 775 nm.

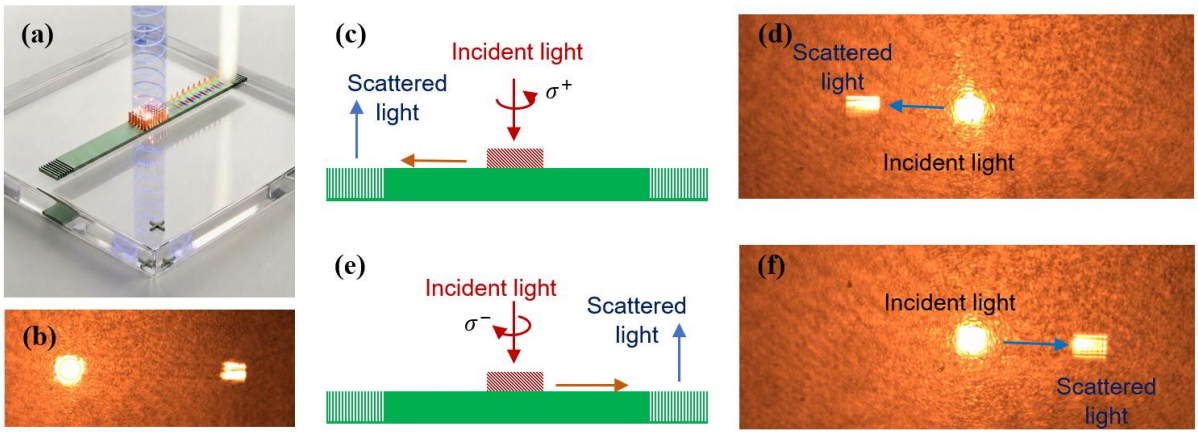


Figure 6.8 | Spin-selective coupling and guiding in the meta-waveguide device. a, Schematic of the expected spin-selective guided modes. **b,** CMOS image showing light coupled into the waveguide and guided from the left scattering grating to the right, confirming that the waveguide is intact. **c,d,** Metasurface excitation with LCP light, showing guided modes propagating toward the left scattering grating. **e,f,** Metasurface excitation with RCP light, showing guided modes propagating toward the right scattering grating.

The experimental results demonstrate the feasibility of helicity-dependent directional coupling in the fabricated 3R-WS_2 metasurface-integrated Si_3N_4 waveguide, providing an initial validation of the proposed spin-selective coupling mechanism. However, the second-harmonic

generation and guided-mode signals remain relatively weak in the current device, indicating that further optimisation is required to improve the overall nonlinear optical performance and coupling efficiency. In particular, improving the quality and uniformity of the fabricated metasurface structures, optimising their alignment and optical coupling with the underlying waveguide, and refining the excitation and collection conditions may help enhance the generated and guided optical signals. Therefore, the present work should be regarded as an exploratory proof-of-concept demonstration of the proposed meta-waveguide platform, rather than a fully optimised nonlinear photonic device. Further experimental investigation and device optimisation will be necessary to achieve more efficient SHG generation and directional coupling for practical integrated photonic and optoelectronic applications.

Beyond second-harmonic generation, the nonlinear meta-waveguide concept offers opportunities for investigating SPDC and integrated photon-pair generation using non-centrosymmetric 3R-phase TMDCs. Preliminary device development has also been explored using 3R-MoS_2 metasurface-integrated waveguide structures, with the aim of exploiting the material's second-order nonlinear response for guided photon-pair generation. However, experimental SPDC emission and photon-pair correlations have not been established as part of the work presented in this thesis. Further device fabrication, optical optimisation and quantum-optical characterisation will therefore be required to evaluate the feasibility of this approach for integrated quantum light sources.

References

1. Xiao, D., Liu, G.-B., Feng, W., Xu, X., & Yao, W.(s). Coupled spin and valley physics in monolayers of MoS_2 and other group-VI dichalcogenides. *Nature Physics* 2012, 8 (12), 899–903.

2. Boyd, R. W.(s). *Nonlinear Optics*, 3rd ed.; Academic Press: Burlington, MA, 2008.

3. Kauranen, M., & Zayats, A. V.(s). Nonlinear plasmonics. *Nature Photonics* 2012, 6 (11), 737–748.

4. Kumar, N., He, J., He, D., Wang, Y., & Zhao, H.(s). Second harmonic microscopy of monolayer MoS_2. *Physical Review B* 2013, 87 (16), 161403.

5. Malard, L. M., Alencar, T. V., Barboza, A. P. M., Mak, K. F., & de Paula, A. M.(s). Observation of intense second harmonic generation from MoS_2 atomic crystals. *Physical Review B* 2013, 87 (20), 201401.

6. Mak, K. F., He, K., Shan, J., & Heinz, T. F.(s). Control of valley polarization in monolayer MoS_2 by optical helicity. *Nature Nanotechnology* 2012, 7 (8), 494–498.

7. Yu, N., & Capasso, F.(s). Flat optics with designer metasurfaces. *Nature Materials* 2014, 13 (2), 139–150.

8. Lin, D., Fan, P., Hasman, E., & Brongersma, M. L.(s). Dielectric gradient metasurface optical elements. *Science* 2014, 345 (6194), 298–302.

9. Li, Z., et al.(s). Valley optoelectronics based on meta-waveguide photodetectors. *Nature* 2024, 629, 123–129.

10. Zhang, Y., et al.(s). Stacking-dependent second harmonic generation in layered MoS_2. *Nano Letters* 2016, 16 (4), 2485–2491.

7. Conclusion and Future works.

This dissertation explored different ways of light-matter interaction, mainly through polaritonics and nonlinear photonics to achieve light manipulation in ultra confined devices. The main focus was to develop engineered low dimensional, anisotropic material platforms to control the generation, propagation, and routing of optical signals at the nanoscale. The work presented here addresses several important challenges in nanophotonics, with a particular focus on controllable sub diffraction light propagation.

In the first part of this thesis, ghost hyperbolic phonon polaritons in calcite were investigated as a platform for long-range and directional mid-infrared light transport. We proposed a design strategy to engineer nano- and microstructures to selectively excite modes, preserving energy to couple to a single mode and enabling directional, long-range propagation. Although this was demonstrated for calcite and g-HPs, the method can be applied to any hyperbolic medium. Directionality, especially, is extremely important for many applications, and instead of relying on complex nanoscale structuring or techniques such as creating twisted layered structures, the proposed technique can be used to control and manipulate polariton systems. Since PhPs have long lifetimes and operate in the mid-IR, where many biological and other organic molecules have resonances, they can be used for biosensing applications. Since the propagation speed is considerably lower than that of other polaritons, this allows biological molecules to interact with light and produce effects that can be detected. Most importantly, in compact and ultrathin devices, surface phonon polariton assisted heat transfer is much more efficient and useful. Designing heat sources and heat sinks along desired pathways through structural engineering techniques we proposed and controlling these polaritons in a directional manner can be extremely useful for applications.

The thesis then extended the study of guided polaritons into the visible and near-IR regimes by investigating exciton polaritons in suspended monolayer WSe_2. Realizing guided modes in a true monolayer is extremely challenging due to the material's atomic thickness, weak optical confinement, and strong sensitivity to the surrounding dielectric environment. By using a suspended geometry, this work created a symmetric air-cladding condition that enabled the direct observation of guided exciton polaritons in a real spacer. Near-field imaging revealed clear interference fringes in the suspended monolayer region, while control regions without the suspended WSe_2 did not show comparable features. This confirmed the critical role of the free-standing geometry in supporting guided exciton-polariton propagation. The observation of

these modes in a monolayer platform is an important step toward ultrathin polaritonic waveguides and compact photonic devices based on atomically thin semiconductors.

Another key contribution of this thesis is the investigation of interaction-induced topological polaritons. Instead of relying on a photonic structure that is already designed to be topologically non-trivial, this work explores a different concept in which topology emerges from strong light–matter interaction itself. In this approach, the initial photonic structure is topologically trivial, and the non-trivial polaritonic phase is generated through coupling with material excitations. This provides a fundamentally different way of thinking about topological photonics, where topological behavior is not fixed solely by the geometry of the fabricated structure but can, in principle, be tuned by the strength and nature of the light-matter interaction. Such a platform offers a promising route toward reconfigurable topological photonic systems, in which external controls, such as strain, gating, optical pumping, or material tuning, can modify the polaritonic band structure after fabrication.

The final part of the thesis focused on nonlinear light-matter interactions in integrated van der Waals photonic platforms. In particular, this thesis developed a spin-selective second-harmonic generation platform based on 3R-WS_2 metasurfaces, combining the material's strong nonlinear response with valley dependent optical selection rules and directional coupling into guided modes. The non centrosymmetric 3R phase of WS_2 plays a key role by enabling strong second-order nonlinear generation, while the metasurface and waveguide geometry provide control over both the polarization and propagation direction of the generated second-harmonic signal. This shows how material symmetry and photonic design can work together to create a compact platform for controlled nonlinear light generation and routing. This work demonstrates a pathway toward on-chip generation and routing of chiral nonlinear optical signals, which is important for future valleytronic, optoelectronic, and quantum photonic devices.

Overall, this thesis shows that low dimensional materials and anisotropic crystals can provide highly versatile platforms for controlling light at deeply subwavelength scales. The studies presented here connect several areas that are often treated separately: hyperbolic phonon polaritons, guided exciton polaritons, topological polaritons, and nonlinear meta-waveguide systems. A common theme across all these works is that strong light–matter interaction can be shaped not only by material properties but also by geometry, boundary conditions, excitation configuration, and the photonic environment. By carefully engineering these factors, it becomes possible to control how optical energy is launched, confined, guided, converted, and routed. In conclusion, this thesis advances the development of nanoscale photonic and

optoelectronic systems by showing how polaritonic and nonlinear optical effects can be controlled in compact material platforms. Improvements in fabrication, loss reduction, and active tuning need to be explored. The work presented in this thesis provides a strong foundation for developing multifunctional photonic systems based on engineered light-matter interactions.